Responsive Gold Nano Particles for Biomedical Applications

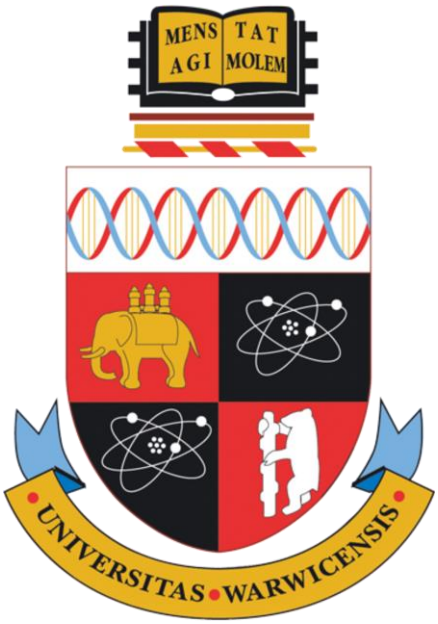

Sangho Won

A thesis submitted in partial fulfilment of the requirements for the degree of Doctor of Philosophy in Chemistry

University of Warwick

Department of Chemistry

November 2017

Table of Contents

List of Figures ..... **v**

List of Schemes ..... **xv**

List of Tables ..... **xvii**

Abbreviations ..... **xix**

Acknowledgements ..... **xxiii**

Declaration ..... **xxv**

Abstract ..... **xxvii**

Chapter 1: Introduction **1**

1.1 Nanotechnology: need and importance of gold nanoparticles for bio applications 1

1.1.1 Optical and electronic properties of gold nanoparticles 2

1.1.2 Applications for imaging, biosensing and, as functional scaffolds 4

1.2 Responsive polymer 8

1.2.1 Temperature responsive polymer 9

1.2.2 Influence factors on phase transition temperature 14

1.3 Reversible deactivation radical polymerization (RDRP) 18

1.3.1 RAFT polymerization 20

1.4 Temperature responsive gold nanoparticles 24

1.5 Carbohydrates 26

1.5.1 Protein-carbohydrates interaction: multivalency in protein-carbohydrate interactions 29

1.5.2 Lectins 31
1.5.3 Anti-adhesion therapy 35
1.6 Glycopolymers 37
1.6.1 Glycopolymers: post-polymerization modification 37
1.6.2 Glycopolymers for bacteria and lectin treatments (bio applications) 40
1.6.3 Glyconanoparticles for bacteria and lectin detection 43
1.7 Polymer grafting density 47
1.8 Aims and thesis summary 49
1.9 References 51

Chapter 2: Co-operative Transitions of Responsive-Polymer Coated Gold Nanoparticles; Precision Tuning and Direct Evidence for Co-operative Aggregation 68
2.1 Chapter summary 68
2.2 Abstract 69
2.3 Introduction 69
2.4 Result and Discussion 72
2.5 Conclusion 95
2.6 Experimental 95
2.6.1 Materials 95
2.6.2 Analytical and physical methods 96
2.6.3 Synthetic procedures 98
2.7 References 102

Chapter 3: Externally Controllable Glycan Presentation on Nanoparticle Surfaces to Modulate Lectin Recognition 108

3.1 Chapter summary 108

3.2 Abstract 109

3.3 Introduction 109

3.4 Result and Discussion 112

3.5 Conclusion 130

3.6 Experimental 130

3.6.1 Materials 130

3.6.2 Analytical and physical methods 131

3.6.3 Synthetic procedures 134

3.7 References 140

Chapter 4: Triggerable Multivalent Glyco-Nanoparticles for Probing Carbohydrate-Carbohydrate Interactions 143

4.1 Chapter summary 143

4.2 Abstract 144

4.3 Introduction 144

4.4 Result and Discussion 147

4.5 Conclusion 163

4.6 Experimental 164

4.6.1 Materials 164

4.6.2 Analytical and physical methods 165

4.6.3 Synthetic procedures 167

4.7 References 177

Chapter 5: Conclusions 181

Appendices 185

Appendix 1: Supplementary Information 186

Appendix 2: ‘Unsuccessful’ experiments 189

Appendix 3: Publications 197

List of Figures

Chapter 1	Introduction	
Figure 1.1	Global market trends for nanotechnology in drug delivery 2011-21.	1
Figure 1.2	Basics of localized surface plasmon resonance (LSPR) of gold nanoparticles due to collective oscillation of surface electrons with incident light at a specific wavelength.	3
Figure 1.3	Various colours of gold nanoparticles solutions depending on particle size.	4
Figure 1.4	Gold nanoparticles for use in cytodiagnostics products (pregnancy test).	5
Figure 1.5	TEM images of various types of gold nanoparticles: A) nanospheres, B) nanorods, C) silica/gold nanoshells, D) nanobowls with a gold seed on the bottom, E) nanocubes and nanocages, F) nanostars, G) bipyramids and H) octahedrals.	6
Figure 1.6	Versatility of gold nanoparticles.	7
Figure 1.7	'Galaxy' of nanostructured stimuli-responsive polymer materials. The phase behaviour of responsive polymer in versatile forms.	9
Figure 1.8	Schematic illustration of the 'coil-to-globule' polymer conformation change upon heating above the LCST.	10
Figure 1.9	Temperature vs. polymer volume fraction (ϕ). Schematic illustration of phase diagrams for polymer solution A) lower critical solution temperature (LCST) behaviour and B) upper critical solution temperature (UCST) behaviour.	11
Figure 1.10	Chemical structure of temperature responsive polymer exhibiting LCST or UCST.	13

Figure 1.11 Schematic illustration of phase diagrams for polymer solution exhibiting an isothermal LCST transition at a fixed temperature. 14

Figure 1.12 Polymer structure/solvent system for tuning the phase transition system. 15

Figure 1.13 Schematic illustration of incorporation end-group effect on the LCST of polymer with different molecular weight. 16

Figure 1.14 Three basic interactions among anions, pNIPAM, and hydration waters for effects of Hofmesiter anions on the LCST of pNIPAM. 17

Figure 1.15 General mechanism for RDRP, copper-mediated ATRP and NMP polymerization processes. 19

Figure 1.16 Chemical structure of the four main classes of RAFT agents. 20

Figure 1.17 The mechanism of RAFT polymerization process. 22

Figure 1.18 RAFT agent and resulting RAFT polymer, showing the α-end (R) and ω-end (Z). 23

Figure 1.19 Schematic illustration of the synthesis of pNIPAM coated AuNPs and their thermo-responsive behaviour in aqueous solution and their aggregation in the presence of various concentrations of NaCl. 24

Figure 1.20 Schematic representation and characterisation of the controlled-release system. A) Schematic illustrating how the system works, B) TEM images of pNIPAM-co-pAM covered Au nanocages. 25

Figure 1.21 Electron microscopy image of a cross section of a rat myocardial capillary showing the glycocalyx of the endothelial cells. 26

Figure 1.22 Isomerisation complexity of carbohydrates, the red colour indicates structural difference. 27

Figure 1.23 The ten mammalian monosaccharides chemical structures with symbols are the CFG nomenclature, the red colour indicates structural difference from the glucose unit. 28

Figure 1.24 A schematic drawing illustrating protein-carbohydrate interactions at the cell surface mediating cell-cell binding, cell-microbe adhesion and cell-antibody binding. 29

Figure 1.25 Carbohydrate-protein interactions. A) An oligomeric protein can interact with an individual cell-surface glycan or B) with multiple different cell-surface glycans simultaneously. C) Oligomeric proteins can also interact with soluble glycans or D) soluble oligomoeric lectins can interact with cell surface glycans. E) Soluble proteins can cluster cell-surface glycoproteins or F) soluble glycans can cluster cell-surface receptors to mediate signal transduction. 30

Figure 1.26 A) Schematic representation of the peanut agglutinin carbohydrate binding site, B) ricin with the toxic A chain (red), cell-targeting B chain and disulphide linkage (yellow). 32

Figure 1.27 Structure of a C-type carbohydrate-binding domain from an animal lectin. 33

Figure 1.28 Electron micrograph of type 1 fimbriated *E. coli*. 34

Figure 1.29 Schematic illustration of anti-adhesion therapy: inhibition of microbial adhesion using anti-adhesion agents (e.g. glyco-ligands). 35

Figure 1.30 Synthesis of functional polymers by post-polymerization modification. 38

Figure 1.31 Schematic of glycopolymers by post-polymerization modification from ‘clickable’ structure. 39

Figure 1.32 Schematic design of evaluating mannose and galactose functional polymers for DC-SIGN binding. 41

Figure 1.33 Schematic representation of the preparation of multifunctional biotinylated glyconanoparticles *via* a photochemical process. 44

Figure 1.34 Schematic representation of carbohydrate-functionalised gold nanoparticles for selective binding to different strains of bacteria. 45

Figure 1.35 Schematic comparing different grafting densities of polymers on particle surface as a function of polymer chain length and monomer type containing small side chain (PVP) / large (POEGMA) 48

Chapter 2 Co-operative Transitions of Responsive-Polymer Coated Gold Nanoparticles; Precision Tuning and Direct Evidence for Co-operative Aggregation

Figure 2.1 ^{1}H NMR spectra of 2-(dodecylthiocarbonothioylthio)-2-methylpropanoic acid in $CDCl_3$. 72

Figure 2.2 ^{13}C NMR spectra of 2-(dodecylthiocarbonothioylthio)-2-methylpropanoic acid in $CDCl_3$. 73

Figure 2.3 Infrared spectra of 2-(dodecylthiocarbonothioylthio)-2-methylpropanoic acid. IR cm^{-1}: 2917 (alkyl-H stretch); 1712 (C=O stretch); 1070(S-(C=S)-S stretch). 73

Figure 2.4 ^{1}H NMR spectra of poly(*N*-isopropylacrylamide) with DP100. 74

Figure 2.5 A) Synthetic route to pNIPAMs; B) SEC analysis of polymers. 75

Figure 2.6 Turbidimetry scans (absorbance at 700 nm) of homopolymer in A) pure water and B) PBS. In all cases the total polymer concentration of the solutions was 2.5 mg mL^{-1}. 77

Figure 2.7 Turbidimetry analysis of blends of $pNIPAM_{50}$ and $pNIPAM_{100}$ at 2.5 mg mL^{-1}. 78

Figure 2.8 Size characterisation of $pNIPAM_{100}@Au_{15}$ and $pNIPAM_{100}@Au_{40}$ nanoparticles. A + B) UV-Vis analysis 80

before and after polymer coating; C + D) DLS analysis before and after polymer coating.

Figure 2.9 TEM images of gold nanoparticles. A + B) 15nm and C + D) 40 nm sized gold nanoparticles before and after $pNIPAM_{100}$ coating. Polymer functionalised particles showing higher colloidal stability. 81

Figure 2.10 X-ray photoelectron spectroscopy analysis of pNIPAM functionalised gold nanoparticles. Representative high-resolution XPS spectrum of C 1s and N 1s region before and after various pNIPAM conjugation. A) Carbon (C 1s) peak and B) Nitrogen (N 1s) peak from the XPS analysis of polymer/gold hybrid nanoparticles (normalised to gold signal). 83

Figure 2.11 Solution properties of polymer coated nanoparticles. A) Zeta-potential analysis of nanoparticles in water, and in phosphate buffered saline; B) Example UV-Vis spectra showing effect of heating above the transition temperature. Inset images show red-blue colour shift upon aggregation. 84

Figure 2.12 Hydrodynamic diameter for the pNIPAM coated 15 nm and 40 nm gold nanoparticles in A) pure water and B) PBS buffer as a function of temperature. 86

Figure 2.13 Turbidimetry scans (absorbance at 700 nm) of $pNIPAM_{50}@Au_{15}$ and $pNIPAM_{100}@Au_{15}$ mixture of the particles with different mass fraction. The total gold core concentration of the solutions was 0.029 mg mL^{-1}. 87

Figure 2.14 Turbidimetry scans (absorbance at 700 nm) of pre-mixture of $pNIPAM_{50}$ and $pNIPAM_{100}$ with different mass fraction coated Au_{15} in PBS solution. The total gold core concentration of the solutions was 0.029 mg mL^{-1}. 88

Figure 2.15 Turbidimetry scans (absorbance at 700 nm) of blends with different mass fraction of $pNIPAM_{100}$ coated Au_{15} and Au_{40}. 89

The total gold core concentration of the solutions was 0.029 mg mL^{-1}.

Figure 2.16 Turbidimetry scans (absorbance at 700 nm) of $pNIPAM_{50}@Au_{15}$ and $pNIPAM_{100}@Au_{40}$ mixture in PBS solution. The total gold core concentration of the solutions was 0.029 mg mL^{-1}. 91

Figure 2.17 TEM analysis of co-operative particle mixture aggregation with different mass fraction. Left hand column shows nanoparticles at 25 °C (below their cloud point) and right hand column shows the same particles which were prepared at 58 °C, above cloud point of the 15 nm particles, but below that of the 40 nm particles. 93

Figure 2.18 Additional TEM analysis of co-operative particle mixture aggregation with different mass fraction. Left hand column shows nanoparticles at 25 °C (below their cloud point). Right hand column shows the same particles which were prepared above cloud point of the 15 nm particles (58 °C) and 40 nm particles (63 °C). 94

Chapter 3 Externally Controllable Glycan Presentation on Nanoparticle Surfaces to Modulate Lectin Recognition

Figure 3.1 ^{19}F NMR spectra of PFP-$pHEA_{15}$. 113

Figure 3.2 Infrared spectra of PFP-pHEA (red) and galactosamine-pHEA (blue). 113

Figure 3.3 SEC analysis of polymer. 114

Figure 3.4 Turbidimetry scans (absorbance at 700 nm) of pure pNIPAMs (1.0 mg mL^{-1}) and polymer functionalised gold nanoparticles (0.057 mg mL^{-1}). 117

Figure 3.5 UV-vis spectrum and photographs of colour changes of $pHEA_{15}$-Gal coated A) 40 nm and B) 60 nm sized gold 118

nanoparticles upon addition of serial dilution of SBA (0 – 10 μg mL^{-1}) following 30 mins of incubation at 20 °C.

Figure 3.6 TEM images of $pHEA_{15}$-Gal coated 60 nm gold nanoparticles A), C) non-aggregation without SBA B), D) aggregation with SBA (10 μg mL^{-1}) following 30 minutes of incubation at 20 °C and 40 °C, respectively. 119

Figure 3.7 X-ray photoelectron spectroscopy analysis of polymer functionalised gold nanoparticles. Representative high-resolution XPS spectrum of C1s, N1s and O1s region after $pHEA_{15}$-Gal (9)-$pNIPAM_{50}$ (1); $pHEA_{15}$-Gal; $pNIPAM_{50}$ conjugation. A) Carbon (C1s) peak, B) nitrogen (N1s) peak and C) Oxygen (O1s) peak from the XPS analysis of polymer/gold hybrid nanoparticles (normalised to gold signal). 121

Figure 3.8 UV-Vis traces of different nanoparticle formulations in presence of serial dilution of SBA (0 – 0.01 mg mL^{-1}) after 30 minutes incubation. Gold particles (60 nm) had [$pHEA_{15}$-Gal]:[$pNIPAM_{25}$] 2:8 at 20 °C A) and 40 °C B); [$pHEA_{15}$-Gal]:[$pNIPAM_{25}$] 5:5 at 20 °C C) and 40 °C D). An increase in Abs_{700} and decrease in Abs_{540} is indicative of binding. All curves normalise so Abs_{450} = 1. Arrow indicates increase concentration. 122

Figure 3.9 UV-Vis traces of different nanoparticle formulations in presence of serial dilution of SBA (10 – 1 μg.mL^{-1}) after 30 minutes incubation. All particles (60 nm) had [$pHEA_{15}$-Gal]:[$pNIPAM_x$] 8:2. $pNIPAM_{25}$ at 20 °C A) and 40 °C B); $pNIPAM_{50}$ at 20 °C C) and 40 °C D). An increase in Abs_{700} and decrease in Abs_{540} is indicative of binding. All curves normalise so Abs_{450} = 1. Arrow indicates increase concentration. 124

Figure 3.10 Dynamic light scattering (DLS) analysis of thermally gated lectin binding. $pHEA_{15}$-Gal:$pNIPAM_{50}$ ratio 9:1 @$AuNP_{60}$. A) Hydrodynamic diameter at 20 °C initially, and after 30 minutes incubation with SBA; B) Hydrodynamic diameter at 40 °C, initially and after 30 minutes incubation with SBA. All results are mean from a minimum of 3 independent repeats. TEM images of these particles after addition of SBA (10 μg mL^{-1}): C) at 20 °C for 30 mins; D) at 40 °C following 30 minutes incubation. 126

Figure 3.11 Assessment of specificity of thermally gated nanoparticles to a panel of lectins. Lectin concentration is 1 – 10 μg mL^{-1}. A – D) show UV-Visible traces (normalised to Abs_{450}) following 30 minutes incubation at 20 °C with indicated lectin. Arrow indicates increase concentration. 127

Figure 3.12 Assessment of specificity of thermally gated nanoparticles to a panel of lectins. Lectin concentration is 1 – 10 μg mL^{-1}. A – D) show UV-Visible traces (normalised to Abs_{450}) following 30 minutes incubation at 40 °C with indicated lectin. Arrow indicates increase concentration. 128

Figure 3.13 Control experiments for non-specific interactions with non-carbohydrate binding protein, BSA. A) $pHEA_{15}$-Gal@Au_{60} at 20 °C; B) $pHEA_{15}$-Gal (9)-$pNIPAM_{50}$(1) @Au_{60} at 20 °C; C) $pHEA_{15}$-Gal (9)-$pNIPAM_{50}$(1) @Au_{60} at 40 °C. 129

Chapter 4 Triggerable Multivalent Glyco-Nanoparticles for Probing Carbohydrate-Carbohydrate Interactions

Figure 4.1 SEC analysis of polymers. 149

Figure 4.2 Infrared spectra of PFP-$pHEA_{15}$ (black), GalNAc-$pHEA_{15}$ (red) and Lac-$pHEA_{15}$ (blue). Box indicate region where PFP ester group would be found. 150

Figure 4.3 Characterisation of polymer functionalised 60 nm gold nanoparticle A) UV-Vis spectra; B) DLS analysis; C) Transmission electron microscope (TEM) image of Lac-$pHEA_{15}$ (9) / $pNIPAM_{50}$ (1) coated 60 nm gold nanoparticles at 20 ^{o}C showing polymer 'halo'; D) at 40 ^{o}C in presence of Ca^{2+} when aggregated. 151

Figure 4.4 Turbidimetry scans (absorbance at 700 nm) of pure $pNIPAM_{50}$ (1.0 mg mL^{-1}) and polymer functionalised gold nanoparticles (0.0255 mg mL^{-1}) in different solution. 153

Figure 4.5 Zeta-potential analysis of nanoparticles in water, in HEPES without Ca 2^{+}, and in HEPES containing Ca^{2+} (100 mM). Polymer functionalised gold nanoparticles (0.0255 mg mL^{-1}). 154

Figure 4.6 Calcium and lectin triggered aggregation of homogenous glyco-nanoparticles. A) Lac-$pHEA_{15}$@Au_{60} with Ca^{2+}; B) GalNAc-$pHEA_{15}$@Au_{60} with SBA; C) Binding Isotherm with Ca^{2+} gradient. 155

Figure 4.7 Calcium and lectin triggered aggregation of homogenous glyco-nanoparticles. TEM analysis of Lac-$pHEA_{15}$@Au_{60} A) without and B) with Ca^{2+}. Scale bar = 500 nm. 156

Figure 4.8 Calcium and lectin triggered aggregation of homogenous glyco-nanoparticles. A) Lac-$pHEA_{15}$@Au_{60} with SBA; B) GalNAc-$pHEA_{15}$@Au_{60} with SBA; C) Binding isotherm with SBA gradient. 157

Figure 4.9 UV-Vis traces of different glycol-nanoparticle in presence of serial dilution of manganese (Mn^{2+}) after 30 minutes incubation at room temperature. A) Lac-$pHEA_{15}$@Au_{60} with Mn^{2+}; B) GalNAc-$pHEA_{15}$@Au_{60}; C) Binding isotherm with Mn^{2+} gradient. 158

Figure 4.10 Temperature–controlled gating off lactose expression at Lac-pHEA$_{15}$: pNIPAM$_{50}$ ratio 9 : 1 @Au$_{60}$ surfaces. Ca^{2+} addition at 20 °C showing full UV-vis A) and time-dependence B). Ca^{2+} addition at 40 °C showing full UV-Vis C) and time-dependence D). 159

Figure 4.11 TEM analysis of Lac-pHEA$_{15}$(9)/pNIPAM$_{50}$(1)@Au$_{60}$ to prove need for both collapse of the steric block and Ca^{2+}. 20 ºC without A) and with B) 100 mM Ca^{2+}. 40 ºC without C) and with D) 100 mM Ca^{2+}. 160

Figure 4.12 Interactions between glyco nanoparticles and GM-3 functional surface. UV-Vis analysis of GM-3 surface after incubation with particles, A) with 'static' nanoparticles at fixed temperature and B) with dynamic nanoparticles, in presence of Ca^{2+} at variable temperatures. SEM's of C) Lac-pHEA$_{15}$@Au$_{60}$ at 20 ºC; D) GalNAc-pHEA$_{15}$@Au$_{60}$ 20 ºC; E) Lac-pHEA$_{15}$(9)/pNIPAM$_{50}$(1)@Au$_{60}$ at 20 ºC; F) Lac-pHEA$_{15}$(9)/pNIPAM$_{50}$(1)@Au$_{60}$ at 40 ºC. False colour applied to SEM for clarity (non-coloured images are presented in the appendix 1). 162

List of Schemes

Chapter 2	**Co-operative Transitions of Responsive-Polymer Coated Gold Nanoparticles; Precision Tuning and Direct Evidence for Co-operative Aggregation**	
Scheme 2.1	Synthesis of thermo-responsive polymer (pNIPAM) and polymer/gold hybrid nanoparticles.	79
Scheme 2.2	The co-operative LCST transitions of two different homopolymers mixing.	86
Scheme 2.3	The possible co-operative and non-cooperative aggregates expected to guide TEM analysis.	92
Chapter 3	**Externally Controllable Glycan Presentation on Nanoparticle Surfaces to Modulate Lectin Recognition**	
Scheme 3.1	Synthesis of polymers by RAFT polymerization and polymer conjugation onto AuNPs.	112
Scheme 3.2	Concept of using responsive polymers to gate access to nanoparticles. Below the LCST of pNIPAM steric hindrance prevents lectin binding to glycans, but above the LCST, the polymer collapse to expose glycans enabling binding and aggregation of the particles.	115
Chapter 4	**Triggerable Multivalent Glyco-nanoparticles for Probing Carbohydrate-Carbohydrate Interactions**	
Scheme 4.1	Synthesis of a non-responsive/responsive polymer. A) Synthesis of glycosylated pHEA; B) Synthesis of pNIPAM. Initiator = 4,4′-Azobis(4-cyanovaleric acid).	147

Scheme 4.2	Concept of gated glycoparticles. A) Homo-and hetero-genous coating of gold nanoparticles; B) concept of thermo-responsive polymer gate to control expression of lactose at the nanoparticle surface.	148
Scheme 4.3	Schematic illustration of experimental concept and GM-3 structure.	161
Scheme 4.4	Synthesis of amino-propyl modified lactose.	171

List of Tables

Chapter 1	**Introduction**	
Table 1.1	Selected polymers temperature region exhibiting LCST or UCST behaviour.	13
Chapter 2	**Co-operative Transitions of Responsive-Polymer Coated Gold Nanoparticles; Precision Tuning and Direct Evidence for Co-operative Aggregation**	
Table 2.1	Characterisation of polymers.	75
Table 2.2	LCST values for each polymer and polymer mixture in different media.	78
Table 2.3	Characterisation of the polymer coated nanoparticles.	80
Table 2.4	XPS elemental ratios for pNIPAM/gold hybrid nanoparticles (normalised to gold signal).	83
Chapter 3	**Externally Controllable Glycan Presentation on Nanoparticle Surfaces to Modulate Lectin Recognition**	
Table 3.1	Polymer used in this study.	114
Table 3.2	Gold nanoparticles with pHEA-Gal and pNIPAM functionalisation.	116
Table 3.3	XPS elemental ratios for polymer/gold hybrid nanoparticles (normalised to gold signal).	120
Chapter 4	**Triggerable Multivalent Glyco-Nanoparticles for Probing Carbohydrate-Carbohydrate Interactions**	
Table 4.1	Polymer synthesis and characterisation.	149

Table 4.2	Nanoparticle characterisation.	152
Table 4.3	Solution properties of polymer coated gold nanoparticles.	154

Abbreviations

ACVA	4,4'-azobis(4-cyanovaleric acid)
ASGP-R	Asialoglycoprotein receptors
ATRP	Atom transfer radical polymerization
AuNP	Gold nanoparticle
BSA	Bovine serum albumin
CCI	Carbohydrate-carbohydrate interaction
$CDCl_3$	Deuterated chloroform
CFG	Consortium for Functional Glycomics
C(L)RP	Controlled living radical polymerization
Con A	Concanavalin A
CP	Cloud point
CRP	Controlled radical polymerization
CT	Cholera toxin
CTA	Chain transfer agent
Đ	Dispersity
DC-SIGN	Dendritic Cell-Specific Intercellular adhesion molecule-3-Grabbing Non-integrin
DLS	Dynamic light scattering
DMF	Dimethylformamide
DP	Degree of polymerization
DRI	Differential refractive index

E. coli	*Escherichia coli*
ESI	Electrospray ionisation
FTIR	Fourier transform Infrared spectroscopy
glycoAuNP	Glycosylated gold nanoparticle
GM-3	Monosialodihexosylganglioside
GPC	Gel permeation chromatography
hCG	Human chorionic gonadotropin
HEPES	4-(2-Hydroxyethyl)piperazine-1-ethanesulfonic acid, N-(2-Hydroxyethyl)piperazine-N′-(2-ethanesulfonic acid)
HepG2	Human liver hepatocellular carcinoma
HIV	Human immunodeficiency virus
K_d	Equilibrium dissociation constant
LCST	Lower critical solution temperature
LRP	Living radical polymerization
LT	Heat-labile enterotoxin
MAMs	More activated monomers
MeOD	Deuterated methanol
M_n	Number average molecular weight
MS	Mass spectrometry
M_w	Weight average molecular weight
NIPAM	*N*-isopropylacrylamide
NMP	Nitroxide-mediated polymerization
PAAC	Poly(acrylic acid)
PAAM	Poly acrylamide

PBS	Phosphate buffered saline
PDEAM	Poly(*N*,*N*-diethylacrylamide)
PDI	Polydispersity index
PEG	Poly(ethylene glycol)
PEtOx	Poly(*N*-ethyl oxazoline)s
PFP	Pentafluorophenyl
PGA	Poly(L-glutamic acid)
PHEA	Poly(hydroxyethyl acrylamides)
PMMA	Poly(methyl methacrylate)
PMVE	Poly(methyl vinyl ether)
PNA	Peanut agglutinin
PNIPAM	Poly(*N*-isopropylacrylamide)
POEGMA	Poly(oligo(ethylene glycol)methacrylate)
PPE	Poly(*p*-phenylene ethynylene)
PPEGMA	Poly(poly(ethylene glycol)methacrylate)
PPFMA	Poly(pentafluorophenyl methacrylate)
PVC	Poly(*N*-vinyl caprolactam)
PVP	Poly(*N*-vinylpyrrolidone)
RAFT	Reversible addition-fragmentation chain transfer
RCA_{120}	*Ricinus communis* agglutinin 120
RDRP	Reverisble deactivation radical polymerization
RP	Radical polymerization
SBA	Soybean agglutinin
SDS	Sodium dodecyl sulfate

SEC	Size exclusion chromatography
SEM	Scanning electron microscopy
SPR	Surface plasmon resonance
TEA	Triethylamine
TEM	Transmission electron microscopy
TGA	Thermogravimetric analysis
THF	Tetrahydrofuran
TMS	Tetramethylsilane
UCST	Upper critical solution temperature
UEA	*Ulex europaeus* agglutinin
UV-Vis	Ultraviolet-visible
WGA	Wheat germ agglutinin
XPS	X-ray photoelectron spectroscopy

Acknowledgements

I am profoundly grateful in all support that I have received on the path to this achievement and I am extraordinarily fortunate in having this great experience in my life with excellent people and environment. Firstly, I would like to a great deal of thank from the bottom of my heart to Prof. Matthew I. Gibson, my supervisor, for his support, careful concern, enthusiasm, patience, greater optimism and willingness to answer any odd questions and idea. He has made this thesis possible with his outstanding guidance. My great thanks go to the University of Warwick for their generous financial support through the Chancellor's scholarship.

I would like to express my deepest gratitude to all past and current members of the Gibson group, Dr. Daniel Phillips, Dr. Sarah-Jane Richards, Dr. Caroline Biggs, Dr. Lucienne Otten, Dr. Collette guy, Dr. Tom Congdon, Dr. Robert Deller, Dr. Daniel Mitchell, Ben Martyn, Richard Lowery, Laura Wilkins, Lewis Blackman, Chris Stubbs, Ben Graham, Marie Grypioti, Trisha Bailey, Alice Fayter and Julia Lipecki for their continual support and friendship they have shown during my studies. I am likewise deeply grateful to Dr. Gemma-Louise Davies for her kindness, assistance, honest advice and encouragement. My thanks also go to her group member Henry Lee and Jonathan Strong for their help and assistance.

I would furthermore like to thank Dr. Marc Walker for his assistance with the XPS analysis, Steven Hindmarsh for his assistance with the SEM analysis, Houari Amari and Steve York for their help with the TEM analysis.

I would particularly like to express appreciation to Prof. Sang Jun Sim who brought me in this amazing scientific world and his research group, also my previous colleagues for giving me this great fortune and all their support and help.

My heartfelt words of gratitude go to a number of friends for endless support, good wishes and friendship with very enjoyable moments. Dae Hee Park, Jungkyun Cheon, Jaekwang Lee, Dr. Yoonjeong Lee, Changmo Kang, Kyungroak Kang, Changwook Song, Dr. Chongyu Zhu, Wonseok Kim, Dr. Zunliang Zhang, Dr. Tum Nuttapol, Gyohee Baek, Heejun Yoo, Youngwoo Kim, Andrew Lee, Toto Zhang, Ali Mostaed, Zan Hua, Hajar Boughaza, Hoonjong Joo, Dr. Min Kim, Jong Uk Lee, Ho Joon Jun, Dr. Ho Seok Kwak, Dr. Xingyi Ma, Jae Joon Yoo, Ji Pyo Hong, Ji Min Hong, Jeongha Hwang, Young Seok Yoo and Jin Up Park. I will be forever thankful to all.

I truly and deeply appreciate to my best friend Sungwoo Lim, the road I had chosen of my own free became a less lonely path to follow thorough his great support, good humour and an everlasting friendship. Cheers!

A word of thanks is not enough to express my appreciation for the endless support and incredible love of my family and my running buddy. My partner Narae Won, her daily encouragement, trust, being always my side on good days and bad with true love and constant smile have helped me grow into a better person and strengthened my faith in this long journey. Finally, my dad Myungjong Won, mom Myungsook Hong, elder sister Jiyoon Won, aunt, uncle, cousin, grandparents and grandma, their profound love, devotion and faith in me have given me the courage and confidence to step forward and go after my dreams. I wouldn’t be here I am today without my family. I love you,

I love you all forever! ♥

Declaration

This thesis is submitted to the University of Warwick in support of my application for the degree of Doctor of Philosophy. It has been composed by myself and has not been submitted in any previous form for any degree in other University. The work presented was carried out by the author except for the XPS experiments in Chapter 2 and 3, which were carried out by Dr. Marc Walker at the University of Warwick and the SEM experiments in Chapter 4, which were carried out by Steven Hindmarsh at the University of Warwick.

Chapter 2 was published as:

S. Won, D. J. Phillips, M. Walker and M. I. Gibson, 'Co-operative transitions of responsive-polymer coated gold nanoparticles; precision tuning and direct evidence for co-operative aggregation', *J. Mater. Chem. B.*, 2016, 4, 5673-5682.

Chapter 3 was published as:

S. Won, S.-J. Richards, M. Walker and M. I. Gibson, 'Externally controllable glycan presentation on nanoparticle surfaces to modulate lectin recognition', *Nanoscale Horiz.*, 2017, 2, 106-109.

Chapter 4 was published as:

S. Won, S. Hindmarsh and M. I. Gibson, ‘Triggerable multivalent glyconanoparticles for probing carbohydrate-carbohydrate interactions’ *ACS Macro lett.*, 2018, 7, 178-183.

Abstract

Responsive polymer-based gold nanoparticles are capable of altering their unique optical properties, chemical and/or physical properties upon exposure to external stimuli, which allows these materials to use in a diverse range of biomedical applications.

Herein, the use of temperature responsive polymers and glycopolymers functionalised gold nanoparticles is given as sensors and biosensors, for controlled and triggered target detection. Chapter 2 investigates the transition characterisation and thermal aggregation co-operative behaviour of thermo-responsive polymer conjugated gold nanoparticles for a detailed understanding of fundamental features to apply in a biosensing system. Chapter 3 develops an optical, gold nanoparticle-based biosensor for the detection of specific biological target. Both temperature responsive and molecular recognizable polymers co-coated gold nanoparticles that change colour by protein-carbohydrate interaction mediated interparticular aggregation are controllable at desired condition. Optimisation of the particle coating is very essential to enhance the sensitivity and specificity of the biosensing system. Finally, this strategy is then extended and improved in Chapter4, with a larger glycans for probing control over the expression of particle surface glycans triggering carbohydrate-carbohydrate interactions with high specificity and selectivity, effectively. In summary, functionalised polymers and gold nanoparticles have been synthesized and developed as a biosensor. These gold nanoparticle conjugates may promise a powerful solution for rapid and reliable identification of disease and point-of-care treatment in modern healthcare issue.

Chapter 1

1. Introduction

1.1 Nanotechnology: need and importance of gold nanoparticles for bio applications

Modern healthcare needs rapid and reliable identification of disease for point-of-care treatment. To meet this strong demand, nanotechnologies dealing with in the range of 5 to 200 nanometer size materials have been rapidly expanding and developing in the last two decades. The current global market of nanotechnology used in drug development and drug delivery has been dramatically increasing. The total market size for all of these fields is expected to be over US$136 billion in 2021 with an annual growth of 15 %.[1]

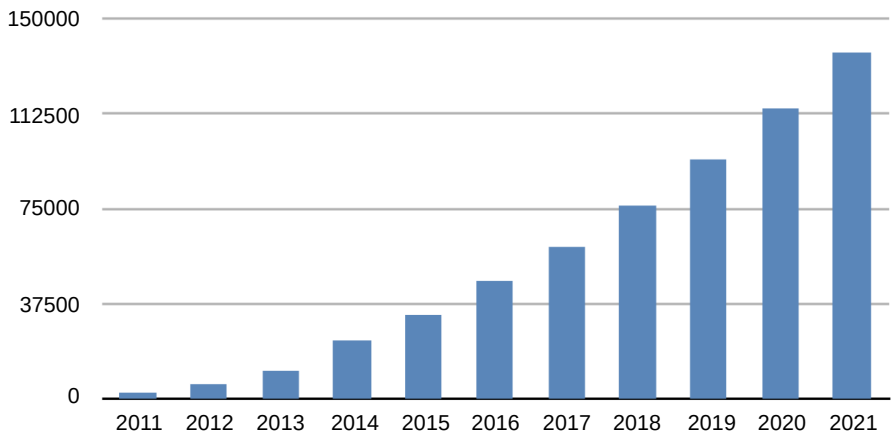

Figure 1.1 Global market trends for nanotechnology in drug delivery 2011-21, figure adapted from reference 1.

Metal nanoparticles are one of the most widely used forms among various materials in the clinical field (for therapeutics or diagnostics) due to their unique characteristics such as unique optical properties originates from the photophysical response, high surface-to-volume ratio, ease of synthesis, and straightforward surface chemistry and functionalization. Moreover, gold nanoparticles (AuNPs) based materials have been developed and showing therapeutic performance as advanced medical applications. For example, AuNPs can efficiently convert light or radiofrequencies into heat for hyperthermia treatment of targeted cancer cells[2,3] and form the basis of lateral flow assays such as those used in home pregnancy tests.[4]

1.1.1 Optical and electronic properties of gold nanoparticles

The interaction of light with surface free electrons of the gold nanoparticle (conduction band electrons) bestows unique electrical, conductive and optical properties of gold nanoparticle. Surface electron are forming a ‘cloud’ and electron clouds are excited and vibrated as a wave with a certain energy value by light at a specific wavelength (frequency). This electron oscillation causes a charge separation resulting in a collective dipole oscillation along the direction of the electric field of the light, called surface plasmon resonance (SPR). A strong absorption of the incident light induced by the SPR can be measured using an ultraviolet-visible (UV-Vis) absorption spectrometer.

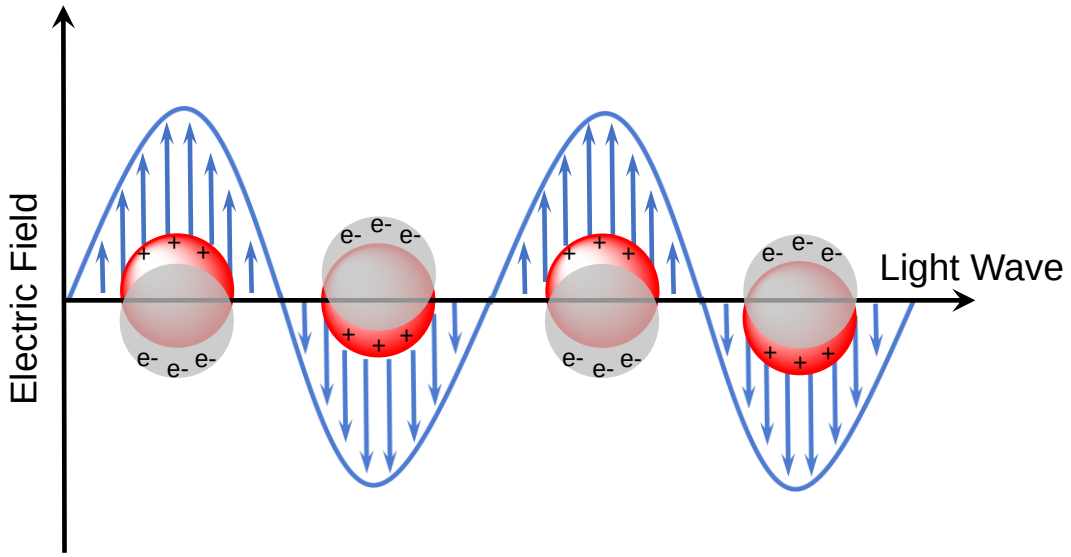

Figure 1.2 Basics of localized surface plasmon resonance (LSPR) of gold nanoparticles due to collective oscillation of surface electrons with incident light at a specific wavelength.

The SPR phenomenon of small (~30 nm) gold nanoparticle colloids causes an absorption of light at ~400-500 nm wavelength (blue-green portion of electromagnetic spectrum) while ~700 nm wavelength (red light) is reflected, yielding particle solutions with a red colour. The absorption wavelength of SPR shifts to longer wavelengths as increasing particle size, and consequently particles absorb red light and reflect blue light, giving blue-purple colour of nanoparticles. These properties have been used to create colourimetric biosensors based upon the target causing agglutination (aggregation) and hence generating a signal output.[5] Plasmon resonance associated-absorption wavelengths shift from blue to red while reflection light shifts from red to blue when particles aggregate together in the presence of analytes from individual small particle. Therefore, particle solutions exhibits visible colour change from red to blue on aggregation. Gold nanoparticles optical and electronic properties according to SPR phenomenon can be tuned by change particle characteristics for further applications. The electron charge density on the particle surface have an effect

on the SPR band intensity and wavelength and it depends on several factors such as the particle size, shape, structure, composition, surface chemistry, aggregation state and the dielectric constant surrounding medium as described by Mie theory.[6]

Figure 1.3 Various colours of gold nanoparticles solutions depending on particle size, figure adapted from reference 7.

1.1.2 Applications for imaging, biosensing and, as functional scaffolds

One of the most familiar bio applications is the home pregnancy test by using gold nanoparticles to generate signal in a lateral flow assay. Gold nanoparticles (< 50 nm) are conjugated with antibodies complementary to a target human chorionic gonadotropin (hCG) hormone in urine produced during pregnancy. Also, target analyte antibodies are immobilized in a line on a nitrocellulose or cellulose acetate membrane.

When the test stick is submerged in urine flow, if the hCG hormone is present it will bind to the gold nanoparticle first, and then be captured by antibodies on the membrane. This flow assay produces an observable coloured line due to particle aggregates using sandwich method.

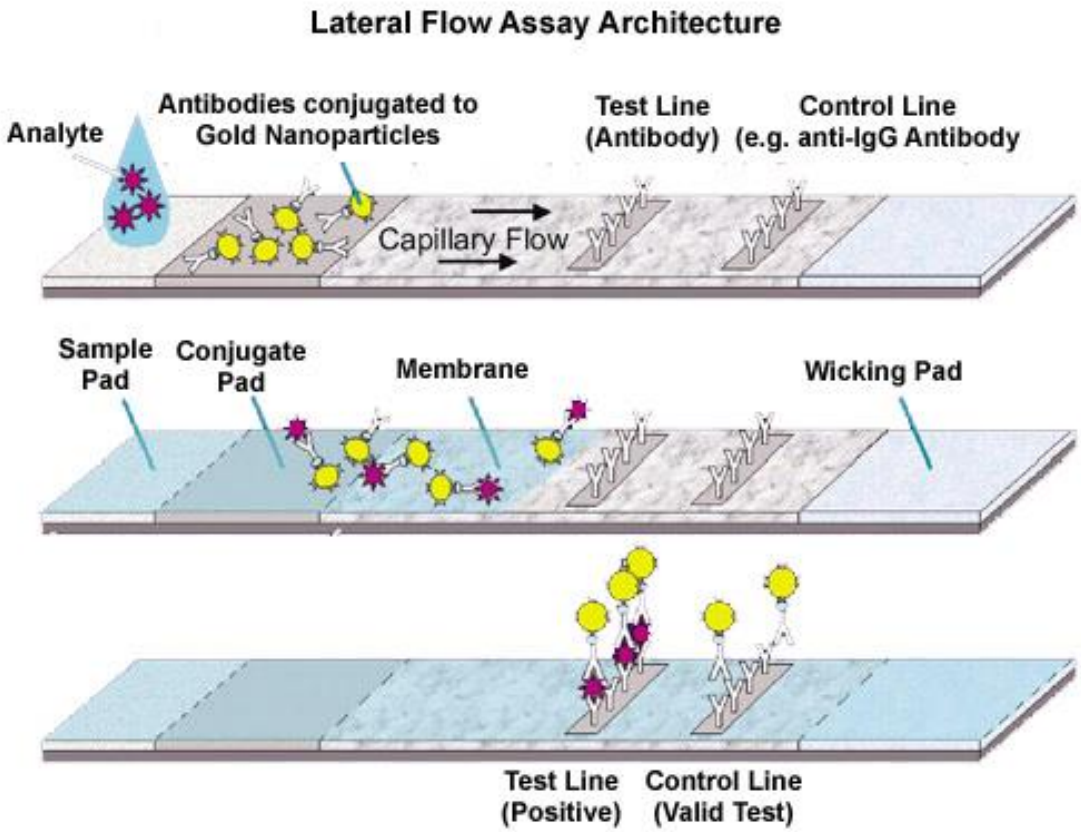

Figure 1.4 Gold nanoparticles for use in cytodiagnostics products (pregnancy test), figure adapted from reference 8.

Gold nanoparticles possess several physicochemical advantages allowing potential therapeutic and diagnostic applications. First, safety (intrinsic nontoxicity, low cytotoxicity) and biocompatibility both *in vitro* and *in vivo* with minimal inflammatory activation and few side effects.[9-13] Second, easy fabrication of particle with structure variation, spherical gold nanoparticles (nanospheres) can be easily synthesized in uniform size *via* classic Turkevich method using $HAuCl_4$ salt reduction by sodium

citrate in aqueous medium under reflux condition.[14] Also, different shapes such as nanorods, nanoshells, nanocages and nanostars can be obtained by various methods as shown in Figure 1.5.[15-21]

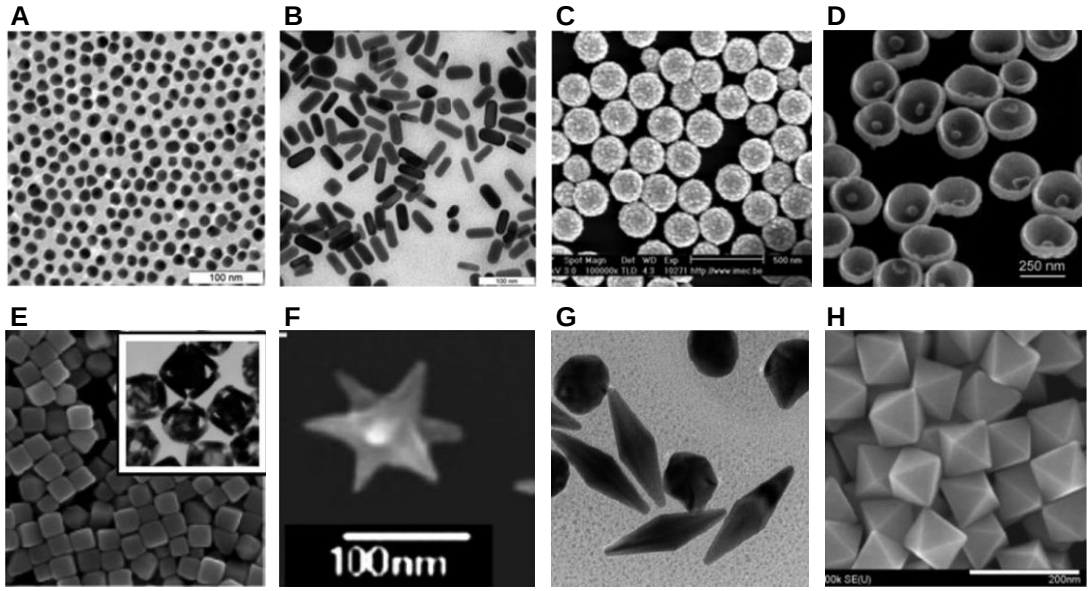

Figure 1.5 TEM images of various types of gold nanoparticles: A) nanospheres, B) nanorods, C) silica/gold nanoshells, D) nanobowls with a gold seed on the bottom, E) nanocubes and nanocages, F) nanostars, G) bipyramids and H) octahedrals, figure adapted from reference 22.

Third, various biologically useful materials including antibodies, DNA and RNA are capable of being conjugated and functionalised with gold nanoparticles by electrostatic interactions between particles and biological molecules.[23] This leads to improvement of stability, tumor-targeting, evade immune detection and crossing of biophysical barriers.[24,25] Fourth, surface plasmon resonance phenomenon and Raman scattering activity of gold nanoparticles have been exploited in non-radiation based imaging applications, tomography of tumors, drug delivery vehicles, tumor-specific photothermal therapy agents and molecular reporters.[15,26] Lastly, gold's high

absorption and enhancement of ionizing radiation can be used for radiation-based therapeutic to enhance the tumor-killing efficiency and diagnostic applications as well as X-ray contrast agent for imaging.[27-31]

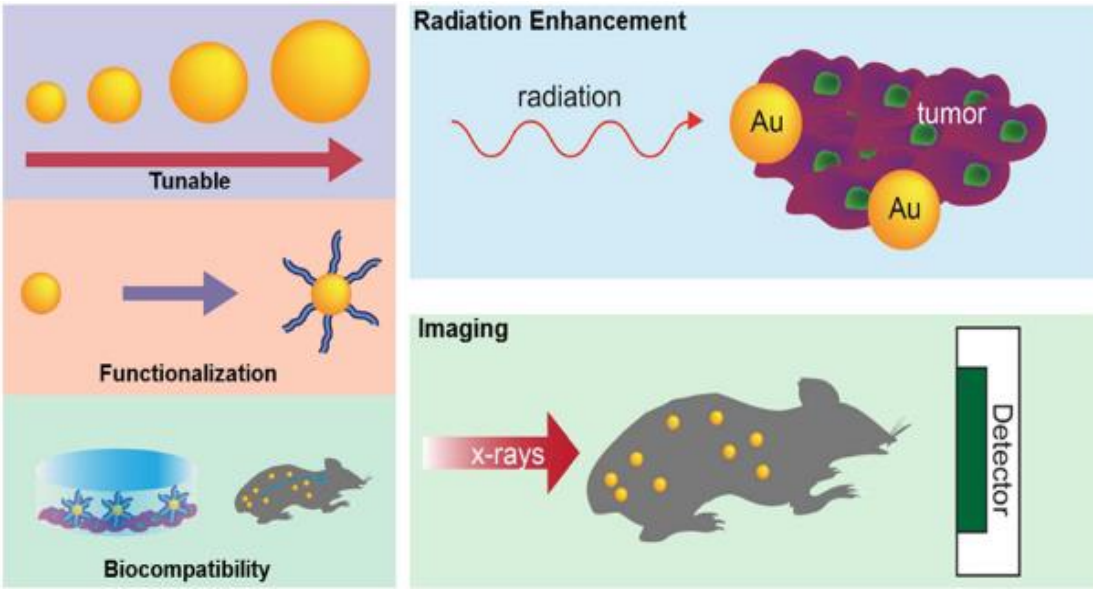

Figure 1.6 Versatility of gold nanoparticles, figure adapted from reference 32.

Therefore, various ligands and gold particle surface modifications have been employed to achieve better stability of gold nanoparticles, encapsulation of a therapeutic agent, imaging resolution and sensitivity, molecular recognition capabilities and stimulus responsive controlled release drug delivery.[33] Especially, responsive polymer based gold nanoparticle is a potential solution to increase the therapeutic performance and efficiency.

1.2 Responsive polymer

Polymers are described as covalently bonded macromolecular structure composed of many repeating subunits (monomers). Since the modern concept of polymer was defined by Staudinger,[34,35] these synthetic and nature material plays a crucial role in everyday our life due to their broad range of properties. Also, the development of a new class of polymers in the biomedical fields is desperate due to the higher living standard and the great concern for health care issue. As a result, a number of researchers have been developing new type of polymers called stimuli-responsive polymers (or smart/intelligent polymer), which are able to respond to environment by changing their chemical and/or physical properties.[36-38]

Stimulus-responsive polymers can change their conformation and exhibit their properties when a variety of external stimuli, such as temperature, pH, solvent, light, ions, mechanical force, the various small molecules and biomolecules and electric/magnetic fields are applied.[39-49] These unique properties and abilities can allow polymers to adapt to various biomedical fields including biosensor,[50] drug delivery[51] and many other applications[52-54] in a number of forms such as simple polymer solutions, hydrogels, micelles, films and layers.[55-59]

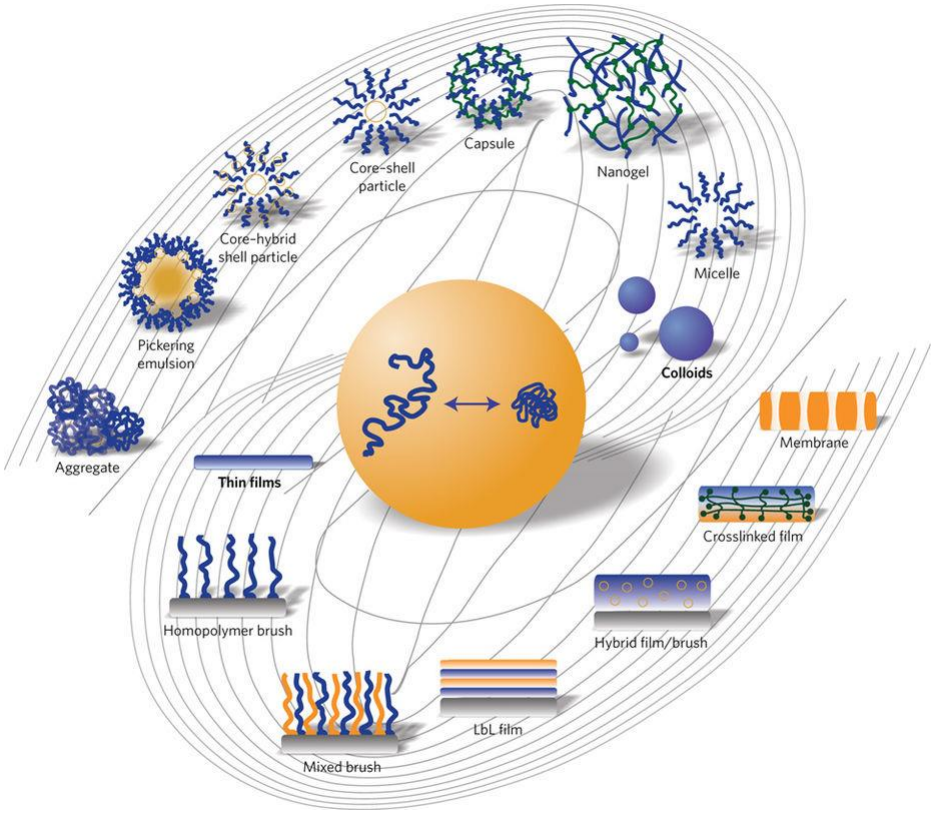

Figure 1.7 ‘Galaxy’ of nanostructured stimuli-responsive polymer materials. The phase behaviour of responsive polymer in versatile forms, figure adapted from reference 59.

1.2.1 Temperature responsive polymer

Temperature responsivity is the most extensively studied and widely investigated for biomedical applications. Temperature-responsive polymers in solution have a certain temperature exhibiting a phase transition which causes an abrupt change in their solvation. Some polymers are soluble and miscible below the certain temperature whereas polymers are insoluble and immiscible upon heating above the critical temperature which is called a lower critical solution temperature (LCST). On the contrary, polymers become soluble upon heating, have an upper critical solution temperature (UCST).

In the aqueous systems, polymer chains form an extended random coil in one homogeneous mixed phase by hydrogen bonding with surrounding water molecules. When heated above the LCST, polymer chains collapse to a compact (desolvated) globular conformation due to intra- and intermolecular hydrogen bonding of polymer molecules are favoured compared to a solubilisation by water molecule.[60-66] Also, intra- and intermolecular hydrophobic interactions of partially collapsed polymer chains enhance the phase transition (separation).[67,68]

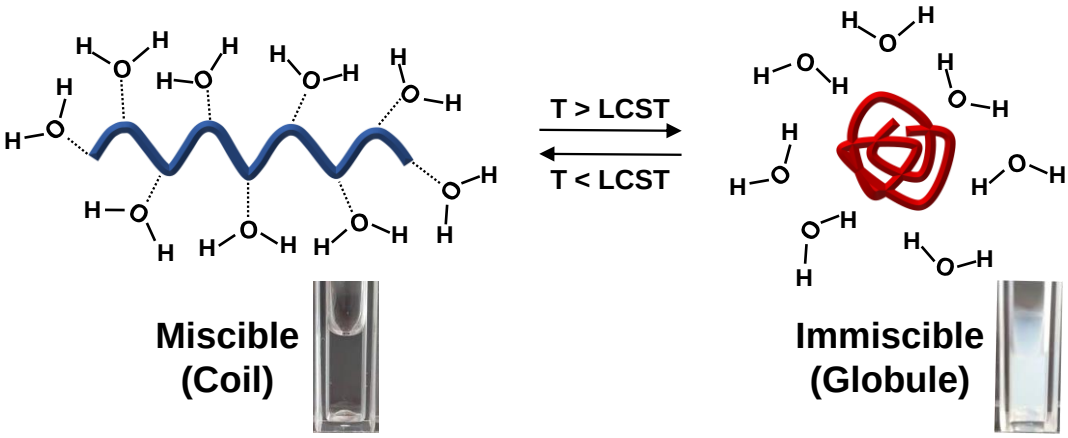

Figure 1.8 Schematic illustration of the 'coil-to-globule' polymer conformation change upon heating above the LCST.

The critical temperature should only be used as the terms of LCST/UCST at the minimum (LCST) or the maximum (UCST) point on the diagram respectively, when the phase diagram of a polymer/solvent mixture vs. temperature showing both one-phase and two-phase region (Figure 1.9). It is more suitable to use 'cloud point (CP)' term associated with macroscopic effect as transition temperature for any other transition from soluble to insoluble or vice versa at a given concentration (solution composition) without this phase diagram.[69] However, transition temperature of some

polymers like poly(*N*-isopropylacrylamide) (pNIPAM) is nearly identical to the LCST at any given concentration.[70]

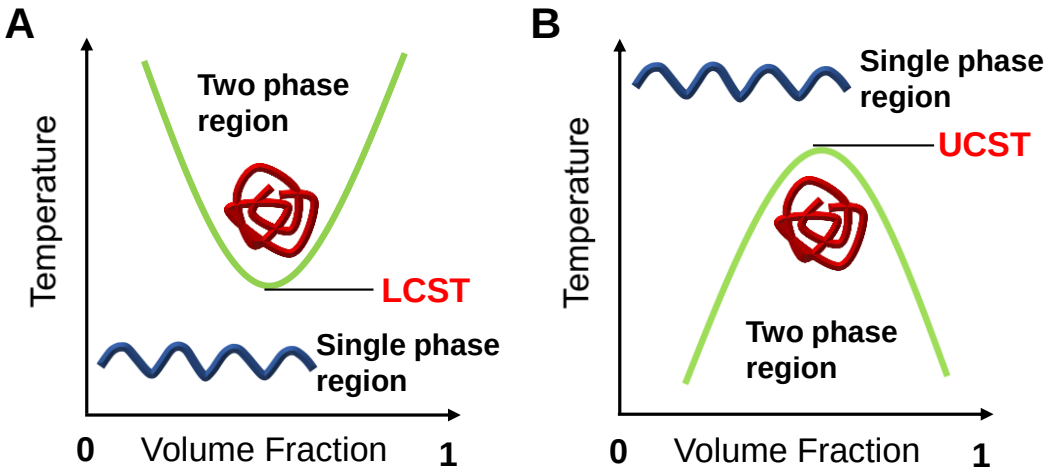

Figure 1.9 Temperature vs. polymer volume fraction (ϕ). Schematic illustration of phase diagrams for polymer solution A) lower critical solution temperature (LCST) behaviour and B) upper critical solution temperature (UCST) behaviour.

There are a variety of polymers exhibiting LCSTs properties, Table 1.1 and Figure 1.10 show either LCST or UCST of selected polymers in aqueous solution and their chemical structure. These polymers have the transition temperature in the region from 20 to 40 ^{o}C.[71]

First, poly(*N*-isopropylacrylamide) (pNIPAM) is one of the most well-known polymer having a LCST from 30 ^{o}C to 35 ^{o}C.[72-75] The LCST of pNIPAM allows this biocompatible material to use in controlled release applications and this transition temperature is almost independent of the concentration, molecular weight based on gel permeation chromatography (GPC) analysis (over ~ 10 kg mol^{-1}) and end group of pNIPAM.[70] Poly(*N*,*N*-diethylacrylamide) (pDEAM) has a nearly identical transition temperature at 32 – 34 ^{o}C which depends on the tacticity of the polymer.[76] Poly(*N*-

vinyl caprolactam) (pVC) also possesses temperature responsive properties including solubility in water and organic solvents, biocompatibility and high absorption ability for biomedical applications.[77] The transition temperature of poly(methyl vinyl ether) (pMVE) is exactly 37 ^{o}C. pMVE is synthesized by cationic polymerization using inert condition and this polymer showing different thermal demixing behaviour to pNIPAM.[78] Poly(*N*-ethyl oxazoline)s (pEtOx) have a high transition temperature around 62 ^{o}C. In order to decrease a transition temperature and obtain potential in drug delivery application, modification of pNIPAM backbone by grafting polymerization of EtOx have developed recently.[79] If hydrophobic and hydrophilic residues are well balanced then elastin like oligo-and polypeptides also show LCST behaviour. For example, poly(pentapeptide) of elastin consists of repeating peptide unit GVGVP (G: Glycine, V: Valine, and P: Proline) and poly(GVGVP) exhibits a phase transition temperature at 30 ^{o}C. Above this phase transition temperature, polymer is stable as a secondary supramolecular structure by hydrophobic folding and assembling transition.[80] A responsive doxorubicin-polypeptide conjugate for cancer therapy have been designed by Chilkoti et al.[81,82] Lastly, a combination of poly acrylamide (pAAm) and poly(acrylic acid) (pAAc) with an interpenetrating network has a transition temperature at 25 ^{o}C. The poly(acrylamide-co-acrylic acid) particularly shows UCST behaviour due to co-operative effects by hydrogen bonding between pAAm and pAAc.[83,84]

Table 1.1 Selected polymers temperature region exhibiting LCST or UCST behaviour.[71]

Polymer	Phase transition temperature in aqueous solution
LCST behaviour:	
Poly(*N*-isopropylacrylamide)	30 – 35 °C
Poly(*N*,*N*-diethylacrylamide)	32 – 34 °C
Poly(*N*-vinylcaprolactam)	30 – 50 °C
Poly(methyl vinyl ether)	37 °C
Block copolymer of poly(ethylene oxide) and poly(propylene oxide)s	20 – 85 °C
Poly(pentapeptide) of elastin	28 – 30 °C
UCST behaviour:	
Poly(acrylamide-co-acrylic acid)	25 °C

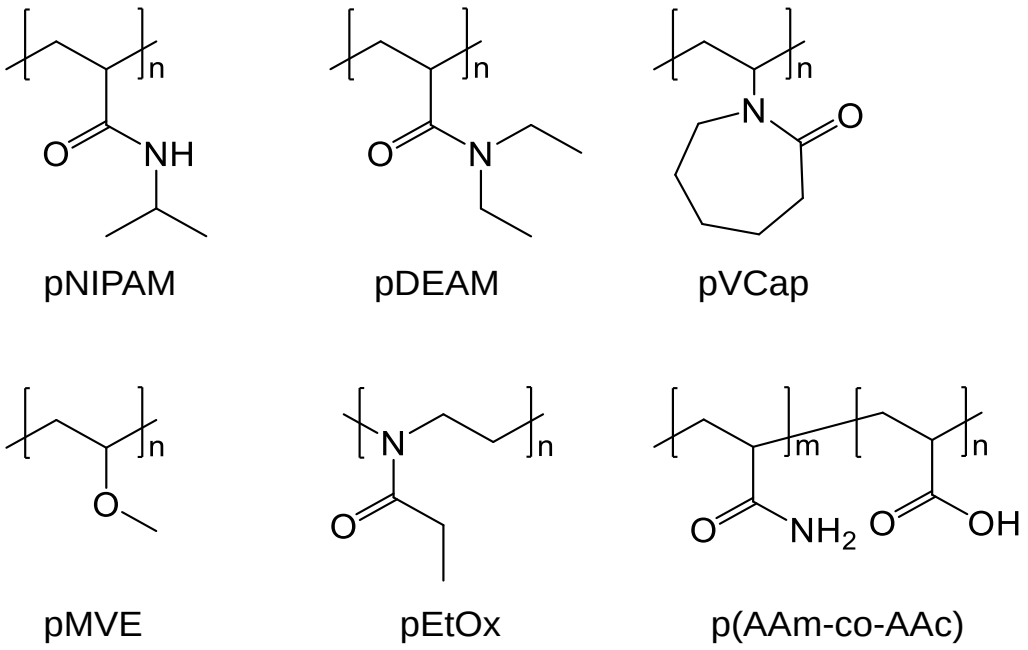

Figure 1.10 Chemical structure of temperature responsive polymer exhibiting LCST or UCST.

1.2.2 Influence factors on the phase transition temperature

Tuning the phase transition temperature of responsive polymers for cancer treatment and targeted drug delivery may have more benefits than conventional hyperthermic treatments or thermotherapy method. Because of the exact (desired) temperature where materials transition occurs for specific targeted tumour cell or tissue can be controlled without external heat energy sources. The LCST behaviour of temperature responsive polymer strongly depends on the hydrophilic/hydrophobic balance within the polymer molecules and the solvent interaction with the polymer. The phase separation boundary of a system can be increased or decreased such that an insoluble polymer globule can be a soluble coil (Figure 1.11A) or vice versa (Figure 1.11B) at a fixed temperature through hydrophilic/hydrophobic balance changes in the surrounding environment.

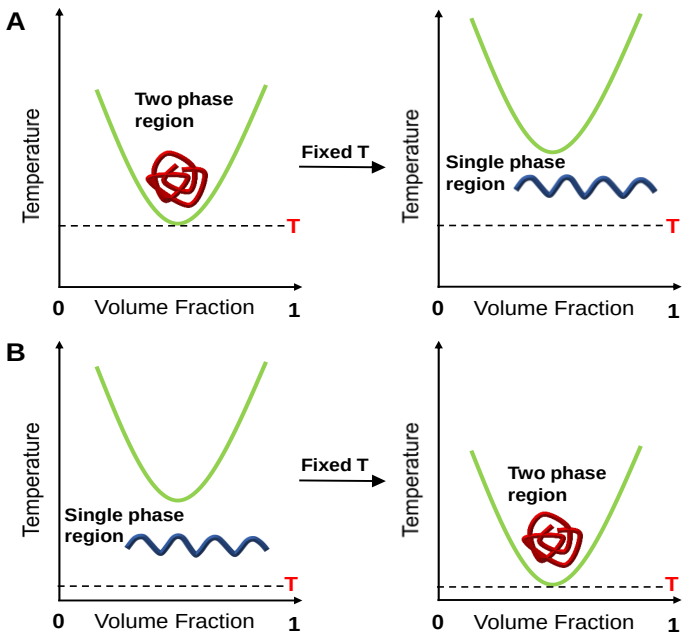

Figure 1.11 Schematic illustration of phase diagrams for polymer solution exhibiting an isothermal LCST transition at a fixed temperature.

It should be noted that the phase transition temperature of an aqueous polymer solution can be tailored by several factors affecting on hydrophilic/hydrophobic balance changes in polymer/solvent system, such as polymer composition (structure), molecular weight, end-group, concentration, solvent quality (presence of additives) and salt concentration.[85-87]

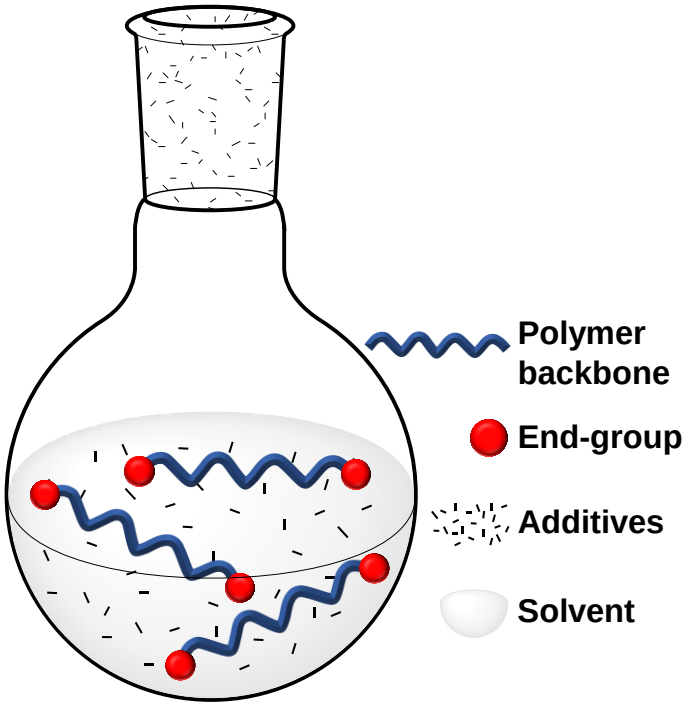

Figure 1.12 Polymer structure/solvent system for tuning the phase transition system.

The coil to globule phase transition of polymer can be affected by adjusting the polymer composition of hydrophilic or hydrophobic monomer. Copolymerization with more hydrophilic (less hydrophobic) monomer increases the LCST, while less hydrophilic (more hydrophobic) monomer decreases the LCST of polymer.[88-90] Also, the molecular weight and incorporation of polymer end groups have influence on the LCST. For instance, low molecular weight of pNIPAM (below ~ 10 kg mol^{-1} based on GPC analysis) displays molecular weight dependent LCSTs, but only within a narrow

M_w range.[91-93] The LCST is decreased as increasing the molecular weight due to pNIPAM with higher molecular weight shows much larger conformational change upon heating.[94] But this trend is reversed when the LCST is influenced by incorporation hydrophobic end groups. The LCST shifts lower when the proportion of hydrophobic end groups of pNIPAM oligomers become larger due to the relative influence for total hydrophobicity of polymer as shown in Figure 1.13.[95] However, the LCST of high molecular weight pNIPAM (over ~ 10 kg mol^{-1} based on GPC analysis) is almost independent of the molecular weight and end groups.[96]

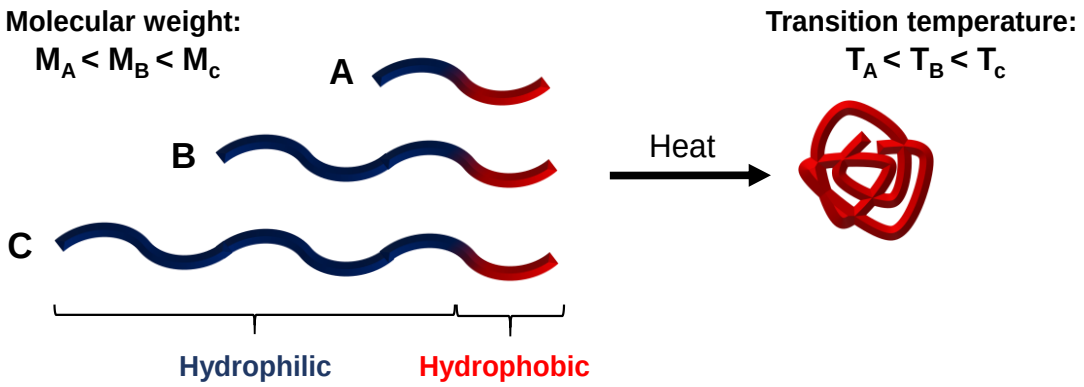

Figure 1.13 Schematic illustration of incorporation end-group effect on the LCST of polymer with different molecular weight.

Solvent system altered by additives (salt, surfactants, and co-solvent) can influence the phase transition through changes of polymer-solvent interactions. Salt effect on the LCST of temperature responsive polymer pNIPAM has been reported by some studies.[97,98] The addition of salt plays a pivotal role in the decrease of LCST called 'salting-out effect' due to increases of pNIPAM hydrophobicity through polymer structure changes and interaction with surrounded water molecules. Cremer and co-workers described three basic interactions among salt anions, polymer and water as shown in Figure 1.14.[99] A surface tension related to the LCST between hydrophobic

parts of polymer (hydrocarbon backbone and isopropyl group) and neighboring hydration water can be modulated by salts. The transition temperature can be shifted lower by direct binding of the anion from salt to the amide group of pNIPAM. Salt anions could polarize water molecule and destabilize hydrogen bonding of the amide group in pNIPAM. However, some other types of salt ions and salt concentration can increase the LCST of polymer described as 'salting-in effect' due to Hofmeister effect.

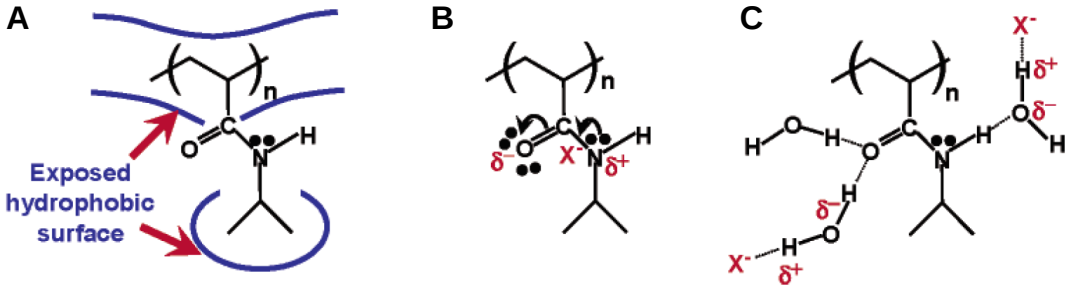

Figure 1.14 Three basic interactions among anions, pNIPAM, and hydration waters for effects of Hofmesiter anions on the LCST of pNIPAM, figure adapted from reference 99.

Amphiphilic surfactants absorbed by polymer molecules causes altered hydrophilic/hydrophobic balance within polymer. This leads to large shifts of transition temperature or even disappearance of transition temperature. Polymers can undergo other types of aggregation forms such as micellisation in contrast with coil-to-globule transition upon addition of surfactants.[77] Both pVC and pNIPAM show increased transition temperature with increasing concentration of ionic surfactant like sodium dodecyl sulfate (SDS).[77,100]

1.3 Reversible deactivation radical polymerization (RDRP)

In order to prepare the polymers for a number of biomedical applications, control over the polymer architecture including molecular weight, molecular weight distribution also referred to as a polydispersity index (PDI), functionality, and composition is highly desirable due to many useful properties of polymers result from their structure and molecular weight.

'Living' polymerization was developed by Michael Szwarc through the anionic polymerization of styrene with an sodium/naphthalene system in 1950s for using more precisely controlled polymers.[101,102] This technique is a form of chain growth polymerization defined as polymerization reactions where chain termination or chain transfer reaction is removed(absent)/minimized. Living polymerization offers precision and control in macromolecular synthesis through linear molecular weight process (growth) with time until all monomer is consumed or intentionally terminated.

Since 1970s, several new methods called reversible deactivation radical polymerization (RDRP) have been discovered which allowed living polymerization to use free radical chemistry, also referred to as living or controlled radical polymerization (C(L)RP). These techniques can be used with a wide range of vinyl monomers for various applications and the robust polymerization condition of RDRP provides benefits for new materials design (well-defined polymers) compared to conventional radical polymerization (RP).[103,104]

RDRP techniques include atom transfer radical polymerization (ATRP),[105] nitroxide-mediated polymerization (NMP),[106] and reversible addition-fragmentation chain

transfer (RAFT)[107] polymerization. All of these RDRP techniques work by establishing a dynamic equilibrium between a small fraction of active polymerizing chains (propagating radical) and a major fraction of dormant species. This leads to promote fast initiation with respect to propagation, and therefore reduce chain termination as a state of 'living'.[108,109]

ATRP is a catalytic process using a metal complex, typically copper (the two oxidation states are Cu^{I} and Cu^{II}) and *N*-containing ligands as catalysts which determine the rate of monomer addition to the propagating polymer chain end. One primary limitation of the ATRP is a requirement of long-time purification to remove high amounts of the catalyst.[110,111] In NMP, the polymerization is thermally initiated in the absence of an external radical source or a metal catalyst. An alkoxyamine is used for the initiating materials to generate the reversible end-capping of growing polymer chains with a nitroxide species and they are able to protect the growing chain end from termination steps.[112,113]

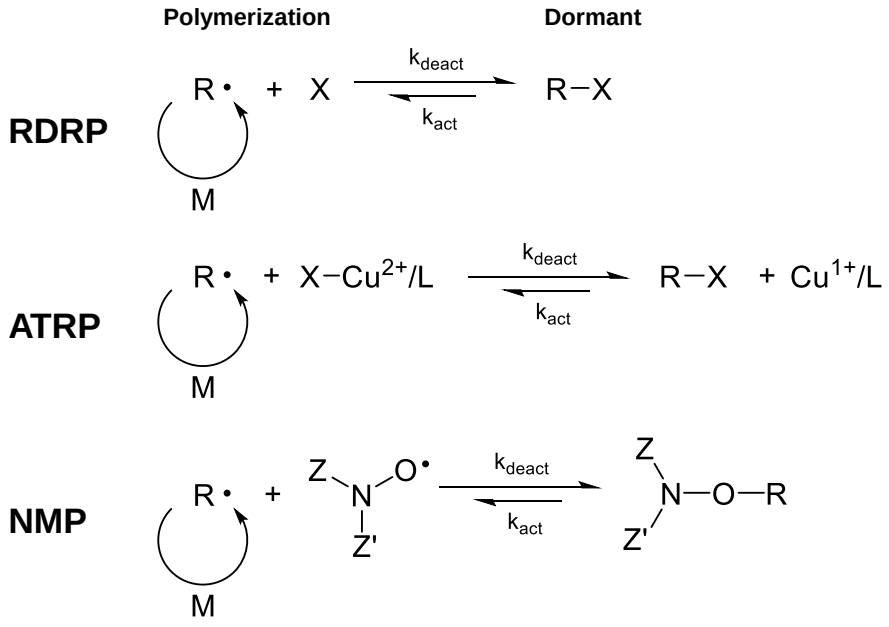

Figure 1.15 General mechanism for RDRP, copper-mediated ATRP and NMP polymerization processes.

1.3.1 RAFT polymerization

RAFT polymerization is a one of reversible deactivation radical polymerization processes discovered at CSIRO of Australia in 1998.[107] Currently, this polymerization is one of the most versatile and effective way of living free-radical polymerization with many benefits.

Major advantages of the RAFT polymerization process are demonstrated by its ability to control polymerization of most monomers including (meth)acrylates, (meth)acrylamides, acrylonitrile, styrenes, dienes, and vinyl monomers. In addition, its compatibility with a very wide range of reaction conditions (e.g. bulk, organic or aqueous solution, emulsion, suspension) and functional monomers such as acid, acid salt, hydroxy and tertiary amino groups.[114] It can also tolerate dithio-compounds and the initiator. This process offers a predetermined molecular weight and very narrow polydispersity polymers including functional end or side chain in a one step process without any need for protection and deprotection.[115] Furthermore, blocks, comb, brush, stars and polymers of more complex architectures can be tailored by RAFT polymerization.[116] The RAFT process involves RAFT agent or chain transfer agent (CTA) which mediate the polymerization *via* a reversible chain-transfer process, typically used RAFT agents have a thiocarbonylthio group (S=C-S) with substituents R and Z such as dithioesters,[107] trithiocarbonates,[117,118] ditihiocarbamates,[119] and xanthates [120] as shown in Figure 1.16.

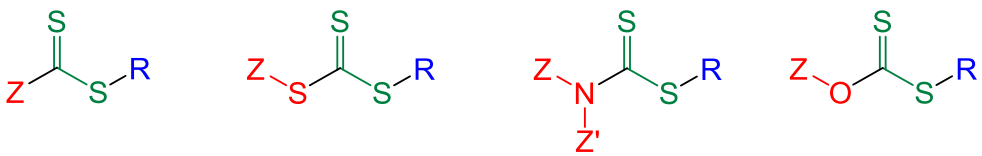

Figure 1.16 Chemical structure of the four main classes of RAFT agents.

A sequence of the RAFT polymerization mechanism consists of several key steps: initiation, propagation, initial equilibrium, re-initiation, main equilibrium, termination as shown in Figure 1.17.

First, the initiation step is started by a free-radical source through the thermal decomposition of radical initiator such as 4,4′-azobis(4-cyanovaleric acid) (ACVA). The decomposed radical fragment (I•) react with a single monomer (M) to form a propagating polymeric radical (P_n•) and propagating radical chains added to monomer to yield a longer propagating radicals. Following initiation, an initial equilibrium is achieved, the CTA (S=C(Z)S-R) reacts with a propagating polymeric radical with n monomer units (P_n•) to give an intermediate radical species. This radical species is broken down into a polymeric adduct of CTA (S=C(Z)S-P_n) and a new free radical (R•). This is a reversible step in which the intermediated CTA adduct radical can lose either the polymeric species (P_n•) or the R group (R•). The liberated radical (R•) reacts with a monomer (M) to form a new propagating radical (P_m•) (for initiating polymerization) in the re-initiation step. Then, the main equilibrium is established by the addition of the polymer radical (P_m•) to the CTA polymer adduct while releasing the other radical (P_n•) due to rapid exchange between the growing radical species (P_n•, P_m•) and the CTA polymer adduct (S=C(Z)S-P_n). In an ideal RAFT process, the radicals can add to (react with) all chains equally, causing equal chain growth and hence control over the narrow molecular weight distribution. Finally, the active propagating chains cannot react further *via* bi-radical termination process and the CTA adduct radical is suppressed to do not undergo termination reactions.

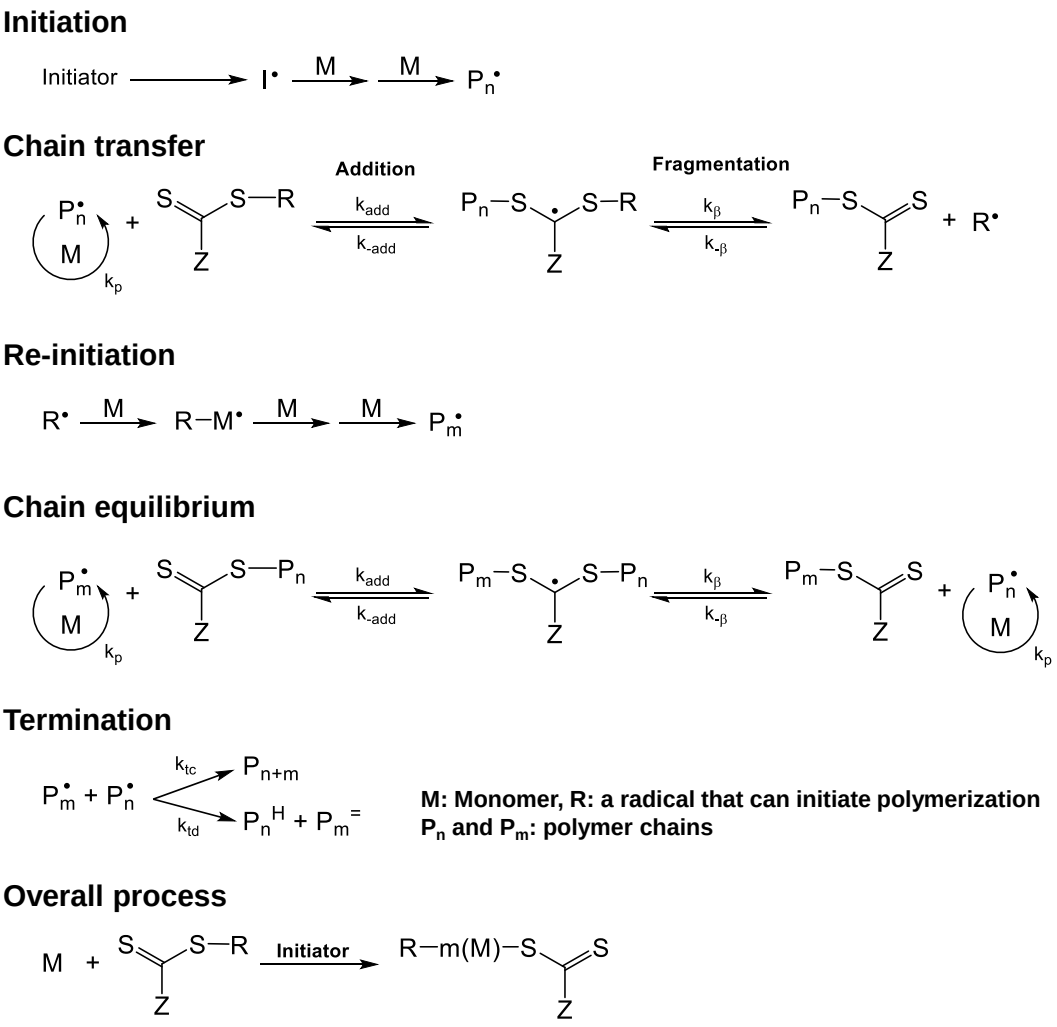

Figure 1.17 The mechanism of RAFT polymerization process.[121]

It is very important (should be highlighted) to use appropriate RAFT agents for the success of polymer synthesis with a high degree of functionality and narrow molecular weight distribution (less than 1.2). The effectiveness of RAFT agents depends on the R and Z groups that impact the polymerization reaction kinetics, reactivity and solubility. For an effective RAFT agent, the 'R' group must be able to reinitiate polymerization and be a good homolytic leaving group. The 'Z' group should control the reactivity of the C=S double bond which influences the rate of radical addition and fragmentation.

Moreover, the RAFT agent leads to the suitable polymerization process for functionalizing at both ends of the polymer chain. Polymers produced by RAFT polymerization possess a 'R' fragment where the site of polymer growth is at the alpha (α) terminus of the polymer. The omega (ω) terminus of the polymer contains a radical stabilizing functional group 'Z' fragment of the RAFT agent affected by covalent bond with thiocarbonylthio moiety (Figure 1. 18).[122]

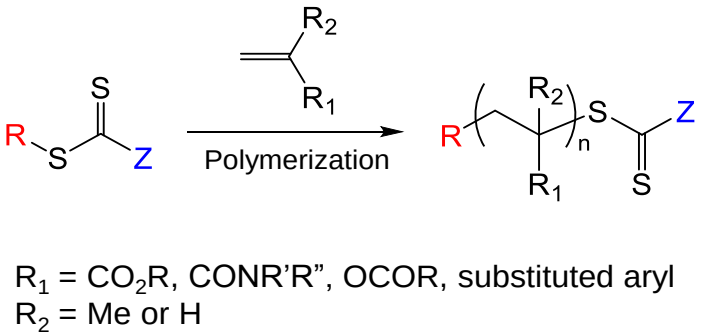

R_1 = CO_2R, CONR'R", OCOR, substituted aryl
R_2 = Me or H

Figure 1. 18 RAFT agent and resulting RAFT polymer, showing the α-end (R) and ω-end (Z).

Incorporated α-functional group onto polymer chain by designed of the R group of RAFT agent can produce carboxylic acid,[123] peptide[124] and lipid α-end functionalised polymers,[125] while the ω-end group can be controlled through modification of the Z group or by post-modification of the thiocarbonyl group after polymerization.[126]

For the major study in this thesis, a functionalised polymer containing a thiol end group at the ω-terminus is employed to react with a gold or an alkene functional group. The thiocarbonylthio group terminated RAFT polymers can be converted to a thiol terminal by use of excess amine to act as a nucleophile,[127] which allows for chemically attaching the thiol-terminated polymer on the gold surface due to high affinity of sulfur for gold.[128,129]

1.4 Temperature responsive gold nanoparticles

Temperature-responsive polymer modified gold nanoparticles have attracted significant attention in recent years for many versatile biomedical applications.[130-134] Unique optical properties of gold nanoparticles and conformational change of the surface bound responsive polymer producing observable optical property changes, which allows these hybrid material to use for biosensing and drug/gene delivery.

In one example, gold nanoparticles coated with thermo-responsive pNIPAM shell has been developed as a colourimetric temperature and salt sensor by Hoogenboom and co-workers.[135] A red coloured solution of citrate stabilized gold nanoparticle was obtained by the Turkevich method and pNIPAM was synthesized *via* RAFT polymerization. Different amount of salt was able to induce visible red to blue-purple colour change of the pNIPAM functionalised gold nanoparticles solution by particle aggregation at increased temperature, as shown in Figure 1.19. Furthermore, this particle shows higher temperature sensing regime in the presence of NaSCN compared to NaCl, indicating particle aggregation is not only due to charge screening, but also the Hofmeister effects.

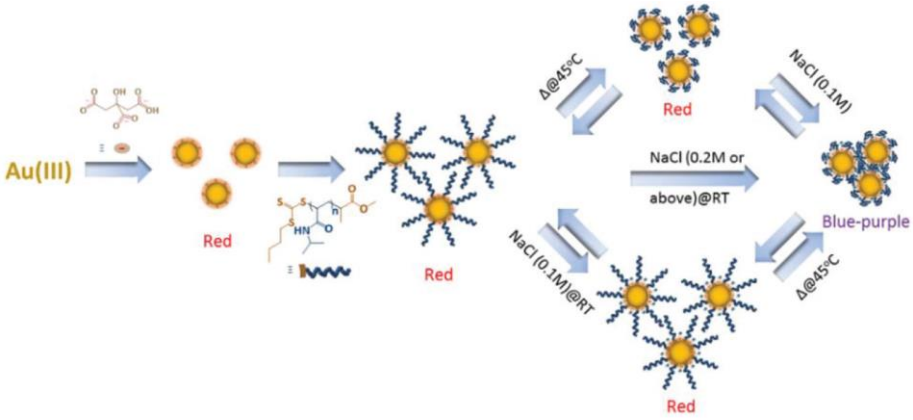

Figure 1.19 Schematic illustration of the synthesis of pNIPAM coated AuNPs and their thermo-responsive behaviour in aqueous solution and their aggregation in the presence of various concentrations of NaCl, figure adapted from reference 135.

Another example, Xia et al. has shown the novel drug cargo using thermal responsive pNIPAM copolymers by incorporating poly acrylamide (pAM) into pNIPAM polymer chain to control and release drug from gold nanocages.[136] As shown in Figure 1.20, pNIPAM-co-pAM copolymers were grafted on surfaces of gold nanocages. On exposure to a near-infrared laser, the gold nanocages absorbed this light and the light energy was converted into heat. Thus, the heat triggered the collapsed globule structure of thermo-responsive polymer on gold nanocage surfaces and pre-loaded drugs release. After turning off the laser, the polymer chain conformation is relaxed and extended with the termination of drug release. Therefore, this smart polymer hybrid gold nanoparticles can be the potential solution for real biomedical applications such as hyperthermic cell/tissue treatment and drug delivery.

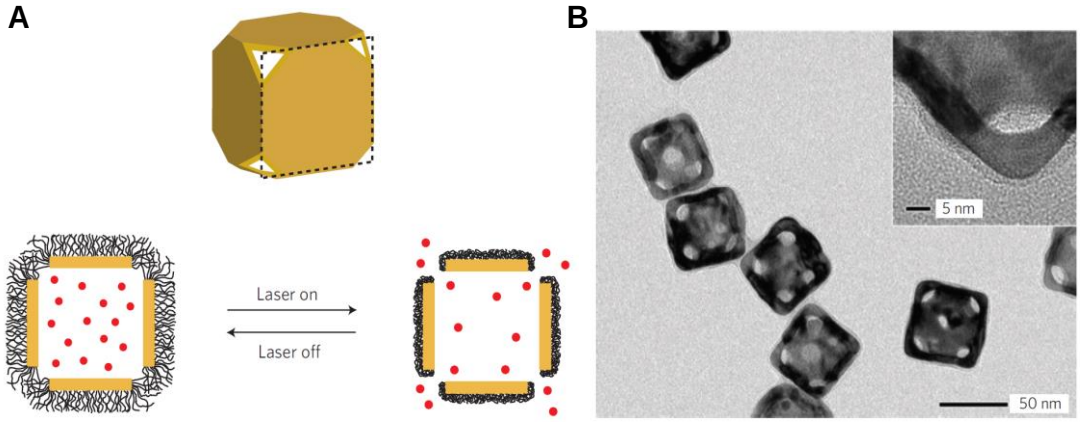

Figure 1.20 Schematic representation and characterisation of the controlled-release system. A) Schematic illustrating how the system works, B) TEM images of pNIPAM-co-pAM covered Au nanocages, figure adapted from reference 136.

1.5 Carbohydrates

A carbohydrate is a biological molecule performing many important roles in living organisms including energy source for metabolism, components of genetic molecule, immune system, fertilization, and preventing pathogenesis, etc.[137] Carbohydrates are also referred to as 'saccharide' consisting of four chemical groups such as monosaccharides, disaccharides, oligosaccharides, and polysaccharides according to their degree of polymerization. Carbohydrates exist mostly as polysaccharides (glycans) in nature. On the cell surface, carbohydrates are covalently bonded to membrane proteins and lipids to form a dense glycocalyx mediating cell-cell interaction, recognition process, and cell-protection (Figure 1.21).[138]

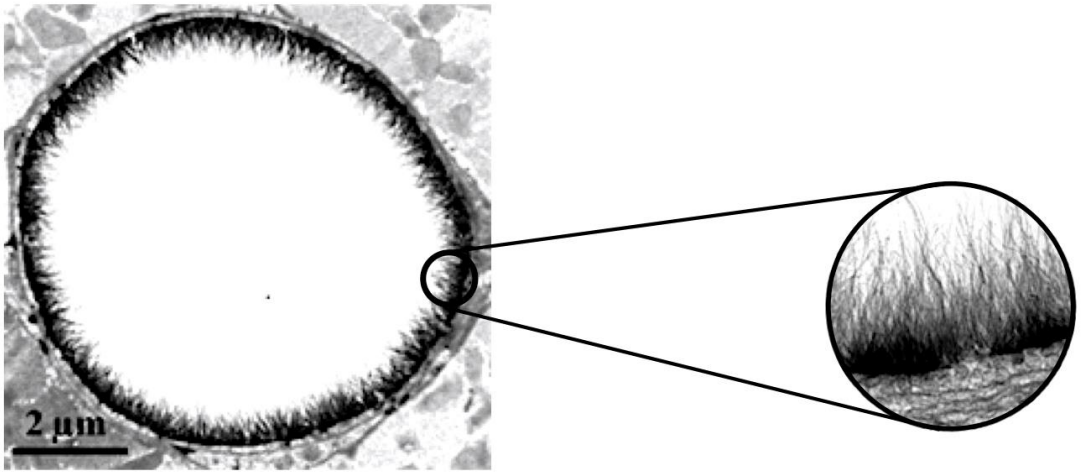

Figure 1.21 Electron microscopy image of a cross section of a rat myocardial capillary showing the glycocalyx of the endothelial cells, figure adapted from reference 138.

Polysaccharides or oligosaccharides are highly complex macromolecules linked by single monosaccharide units together in variety of ways, this results in numerous glycan structural and chemical diversity of carbohydrates molecules.[139] The most structural diversity comes from the differences of stereochemical configuration of

carbohydrate molecules such as enantiomers depending on the relative configuration by optical rotation (e.g. D/L-glucose), diastereoisomers depending on the configuration of one stereocenter that are also called epimers (e.g. glucose/galactose), anomers depending on the configuration of the anomeric carbon (α / β), different glycosidic linkages and branching between monomers (e.g. 1-4 / 1-6) as shown in Figure 1.22.[139,140]

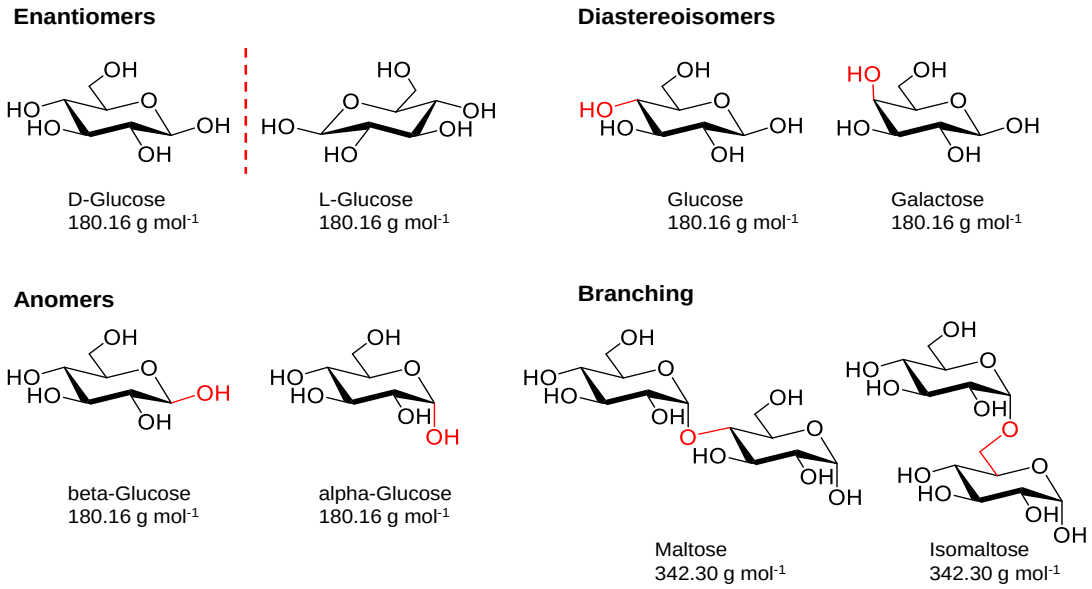

Figure 1.22 Isomerisation complexity of carbohydrates, the red colour indicates structural difference.

Also, the complexity of glycans are determined by various combinations from several monosaccharide building blocks containing through linkage between multiple functional groups.[141] Typically, mammalian glycans are composed of ten key mammalian monosaccharide units; glucose, galactose, mannose, *N*-acetyl glucosamine, *N*-acetyl galactosamine, fucose, xylose, glucuronic acid, iduronic acid and sialic acid which are able to assemble linear and branched structure (Figure 1.23).[139] These ten building blocks result in tremendous number of possible glycans with huge information density and very high degree of complexity due to many

different combinational structures by stereochemical linkages between the functional groups of units compared to linear macromolecules like proteins and nucleic acids (DNA). Theoretically, the number of possible hexasaccharides generates more than 10^{12} different structures, whereas the number of different hexamers of amino acids is calculated to 46656 structures.[142,143]

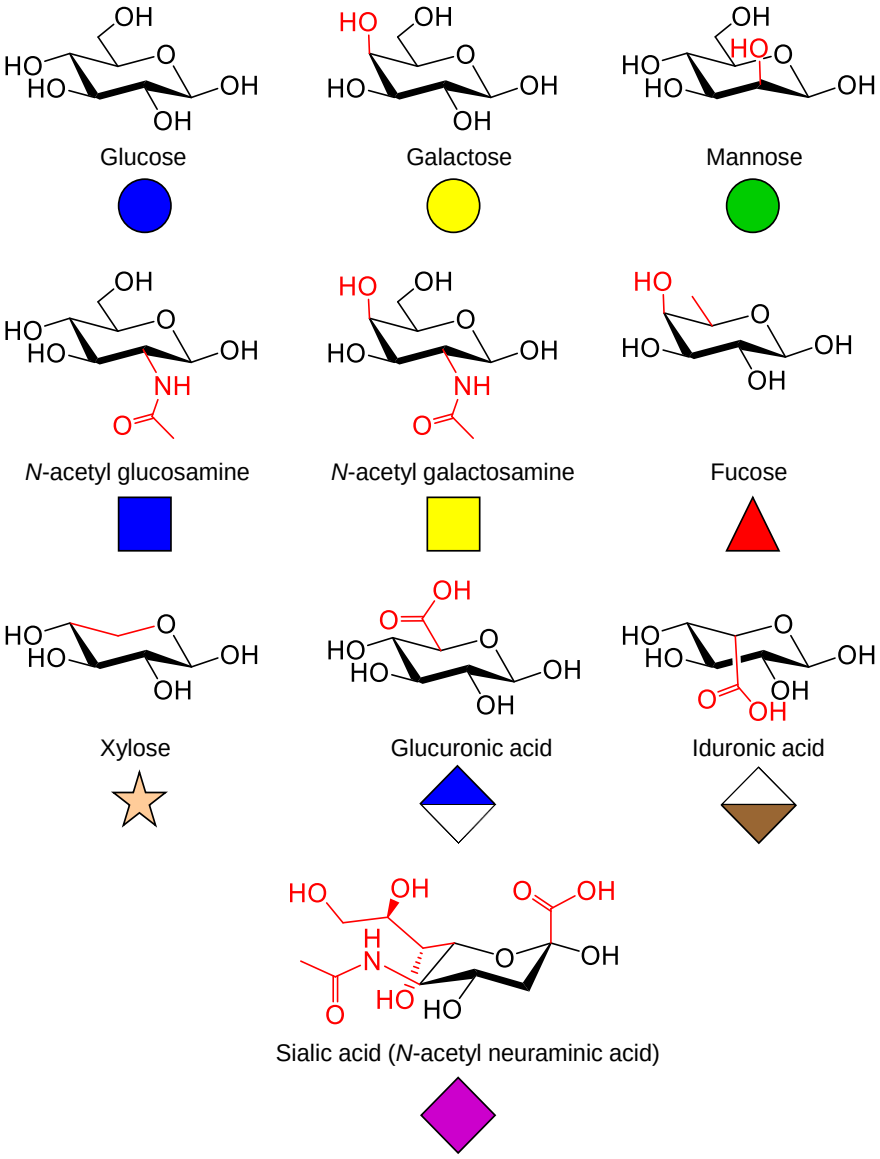

Figure 1.23 The ten mammalian monosaccharides chemical structures with symbols are the CFG[144] nomenclature, the red colour indicates structural difference from the glucose unit.

1.5.1 Protein-carbohydrates interaction: Multivalency in protein-carbohydrate interactions

A carbohydrate is existed as glycans, glycosylated proteins, glycolipids on the cell membrane and it is able to interact with protein receptors such as enzymes or lectins.[145] This specific protein-carbohydrate interaction mediate signal transduction for many important physiological/biological events, including cell-cell communication, cellular proliferation, fertilisation, cancer metastasis, pathogen recognition process and cell-microbe (bacterial, viral and bacterial toxin) adhesion, etc.[146-151]

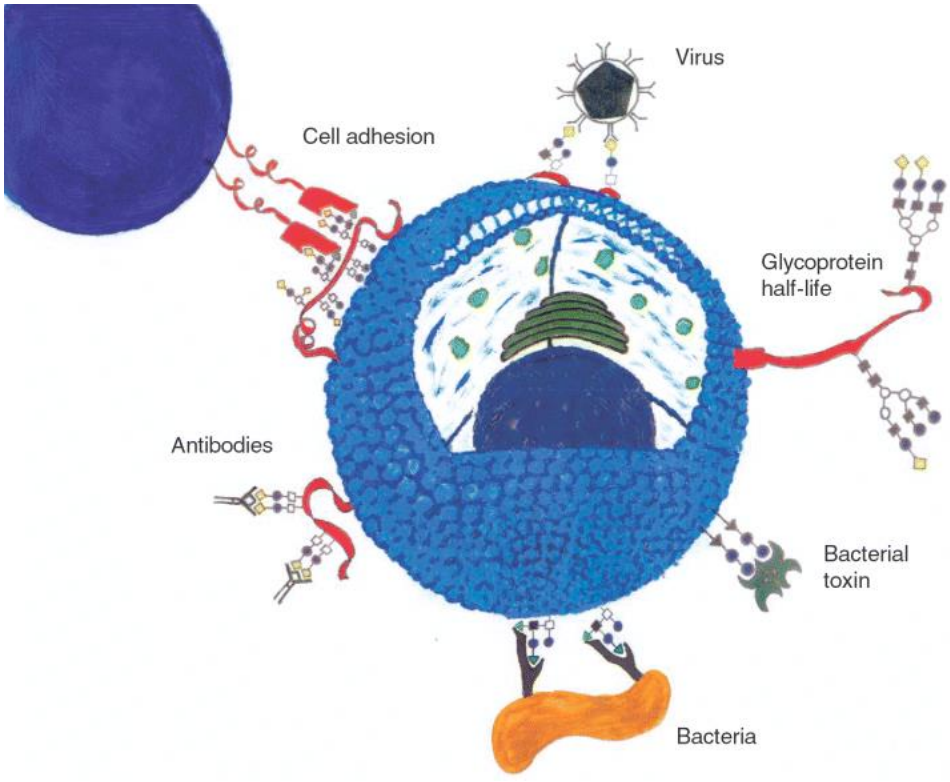

Figure 1.24 A schematic drawing illustrating protein-carbohydrate interactions at the cell surface mediating cell-cell binding, cell-microbe adhesion and cell-antibody binding, figure adapted from reference 152.

These interactions are typically so weak with a dissociation constant in the millimolar range ($K_d = 10^{-6} \sim 10^{-3}$ M) due to hydrogen bonds, van der Waals' interactions and hydrophobic stacking between the carbohydrate and the protein.[153] However, this recognition could be greatly enhanced by multivalent effect of densely packed carbohydrate molecules on the cell surface. The binding affinity of multiple carbohydrates is higher than the total sum of the individual carbohydrate binding, which is called as 'glycocluster effect'.[154-156]

This multivalent interaction is occurred through a variety of mechanisms; i) multiple carbohydrate residues within a glycan bind to corresponding oligomeric proteins on the cell surface or ii) secreted proteins, iii) a cluster of multiple glycans on the cell surface or iv) soluble glycans bind to (cell surface/soluble) proteins. (Figure 1.25).[157-161] Furthermore, binding potency of multiple ligands can be enhanced by several manners such as chelation, subsite binding, clustering and statistical rebinding.[162]

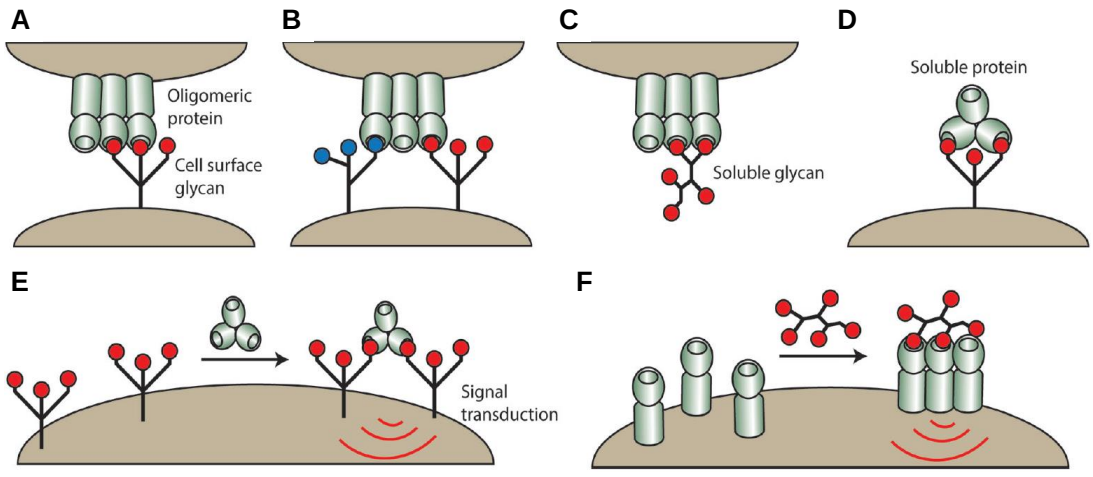

Figure 1.25 Carbohydrate-protein interactions. A) An oligomeric protein can interact with an individual cell-surface glycan or B) with multiple different cell-surface glycans simultaneously. C) Oligomeric proteins can also interact with soluble glycans or D) soluble oligomoeric lectins can interact with cell surface glycans. E) Soluble proteins can cluster cell-surface glycoproteins or F) soluble glycans can cluster cell-surface receptors to mediate signal transduction, figure adapted from reference 161.

1.5.2 Lectins

Lectins (from the Latin *legere*, 'to select') are carbohydrate-binding proteins playing a crucial role in many important biological activities as well as pathological processes for living organisms. They are ubiquitous, being found in animals, plants, microorganisms and also major components of the mammalian cells surface.[163-165] A lectin usually contains two or more binding sites, or even some lectins form oligomeric structures with multiple binding sites which enables to interact with the carbohydrate through the specific non-covalently interaction (hydrogen bonding and electrostatic interactions).

Legume lectins among plant lectins are the biggest family around 100 members have been isolated from plant seeds to investigate their binding characterisation. All legume lectins contain four invariant amino acid residues in the binding site for the protein-carbohydrates interaction, such as asparagine, aspartic acid, glycine, and leucine or an aromatic amino acid.[166]

The binding specificities of legume lectins have been well characterised. For example, concanavalin A (Con A) from the jack beans is the most popular legume lectin and used as a model system.[167] Con A has a binding site in the each subunit of dimer structure at low pH (< 5.5) and tetramer structure at neutral pH that having high affinity with mannose and glucose. Another example, peanut agglutinin (PNA) from *Arachis hypogaea* has amino acids (Asp83, Gly104, Asn127 and Tyr125) that binding to conjugates of galactose/*N*-acetyl galactosamine (Galβ1-3GalNAc) in the T-antigen as shown in Figure 1.26A.[166]

Several plant lectins are toxin, *ricinus communis* (ricin) is a toxin lectin isolated from castor beans and treated as a serious threat for use as a biological weapon. It is composed of the toxic portion of A chain and B chain for the cell-targeting (Figure 1.26B). B chain of ricin binds to carbohydrates on the surface of cell due to its galactose specificity. The A chain penetrates through into the cytoplasm and cleaves an adenine residue from the 28S ribosome after disulphide linkage between the chains is broken, this leads to stopping protein synthesis by inactivation of ribosomes and ultimately killing the cell.[168]

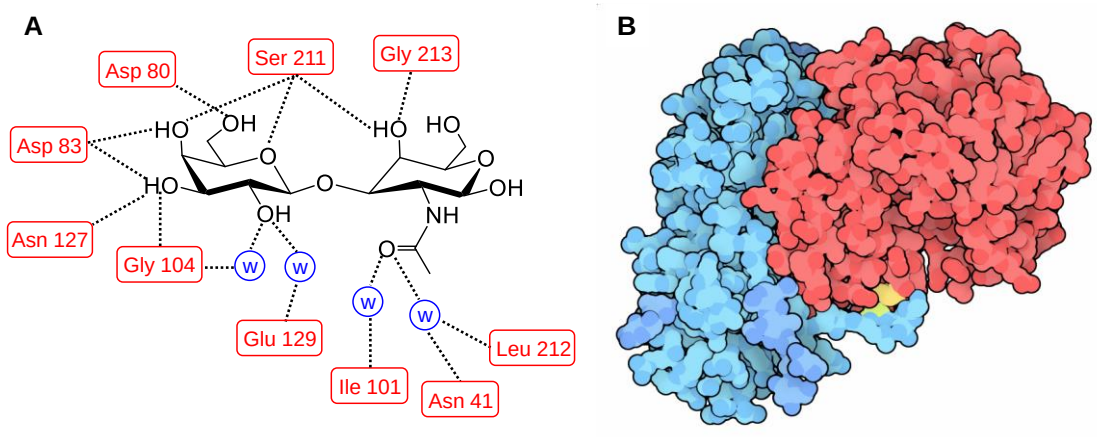

Figure 1.26 A) Schematic representation of the peanut agglutinin carbohydrate binding site figure adapted from reference 166, B) ricin with the toxic A chain (red), cell-targeting B chain and disulphide linkage (yellow), figure adapted from the reference 169.

Lectins can be divided into various classes in terms of their amino acid sequences and biochemical properties. One large class is the C-type lectins requiring calcium ion.[170] Ca^{2+} (Mn^{2+}, also a metallic cation) enhance the binding ability with carbohydrates by helping the positioning of amino acid residues in lectins. Animal C-type lectins have various subunits with 1-8 binding sites per each subunit and lectin folding has a

compact domain of 110 - 130 amino acids which are responsible for carbohydrate binding. As shown in Figure 1.27, a calcium ion directly links hydroxyl groups on the carbohydrate to amino acid residues in the protein, while other protein side chains form hydrogen bonding with other hydroxyl groups of carbohydrates.[171,172] Carbohydrate binding specificity can be altered by changes in the amino acid residues of the lectin.

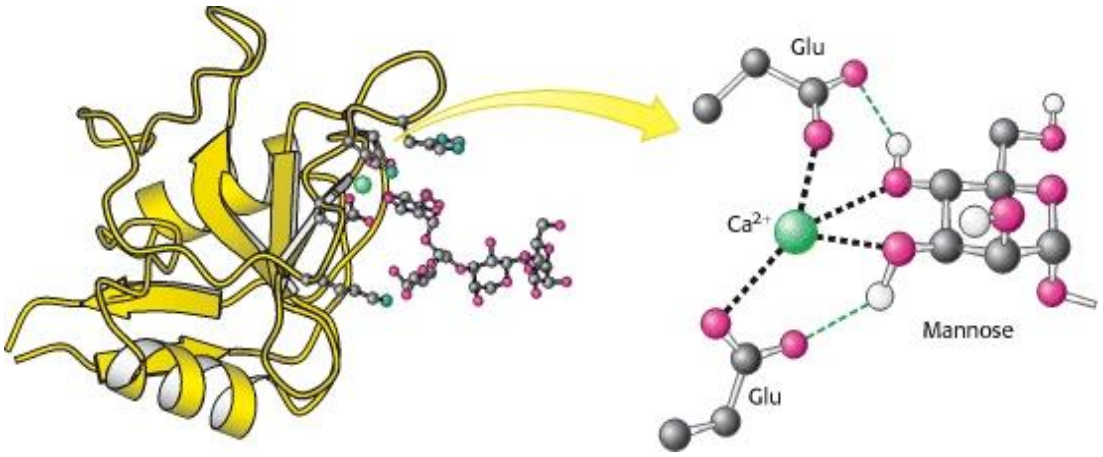

Figure 1.27 Structure of a C-type carbohydrate-binding domain from an animal lectin, figure adapted from reference 170.

Bacteria also contain carbohydrate-specific lectins that enable bacterial adhesion onto host cell surface by molecular interaction between cell surface carbohydrates and lectins of bacteria.[173] Particularly, bacteria produce surface lectins, commonly in the form of the fimbriae (or pili) that are hair-like assemblies of protein subunits and fimbriae are efficient adhesion tools to mediate colonization of various biotic and abiotic surfaces (Figure 1.28).[174]

Escherichia coli (*E. coli*) producing the type 1 fimbriae which are the most abundant structure both in pathogenic and non-pathogenic gram-negative bacteria. The FimH (type 1 fimbrial lectin) is mannose-specific and found at the tip of the fimbriae. The various bacterial surface lectins are able to initiate infectious diseases by mediating bacterial adhesion to epithelial cells in the urinary and gastrointestinal tracts thorough the specific and reversible non-covalently protein-carbohydrate interaction.[175]

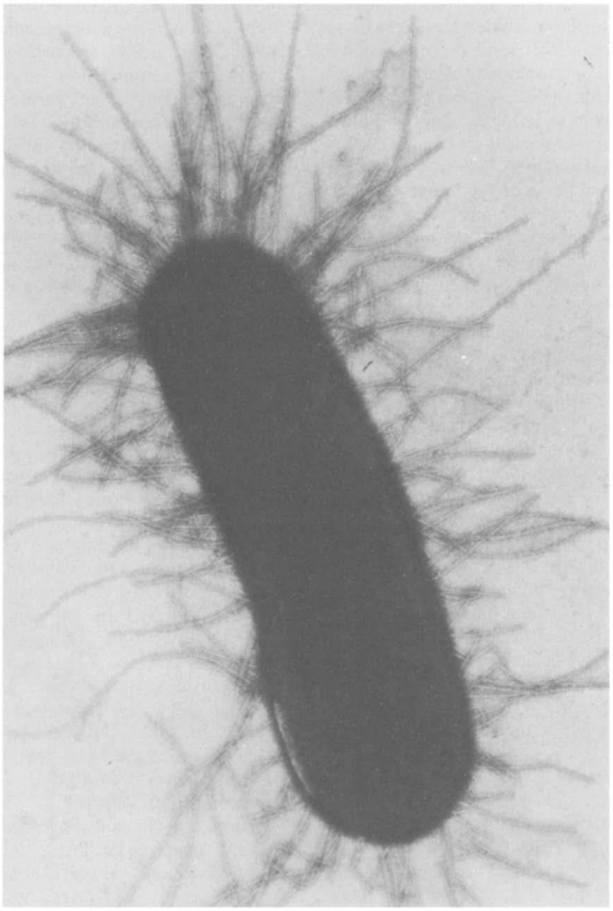

Figure 1.28 Electron micrograph of type 1 fimbriated *E. coli*., figure adapted from reference 174.

1.5.3 Anti-adhesion therapy

Anti-adhesion therapy is an attractive approach for fighting bacterial infections. The adherent state is a key step for bacterial survival and one of the initial stages for the infectious process. Therefore, it is very important to interfere the adhesion at an early stage following the exposure of the host to pathogens. Anti-adhesion method employs competitive inhibition agents that reduce ability of contact between host cells and pathogens. Carbohydrate or its analogues which are structurally similar to glycoprotein or glycolipid receptors for the adhesion bind the bacteria primarily, rather than the carbohydrates on the host cell in the competitive inhibition process.[176] The anti-adhesion strategy inhibits pathogenicity by interference agents rather than kill or arrest growth of the pathogen like antibiotics, this leads to significantly lower bacteria resistant to the anti-adhesion agent than bacteria resistant to antibiotics. Also, this agent do not disrupt normal microbiota within the organism.

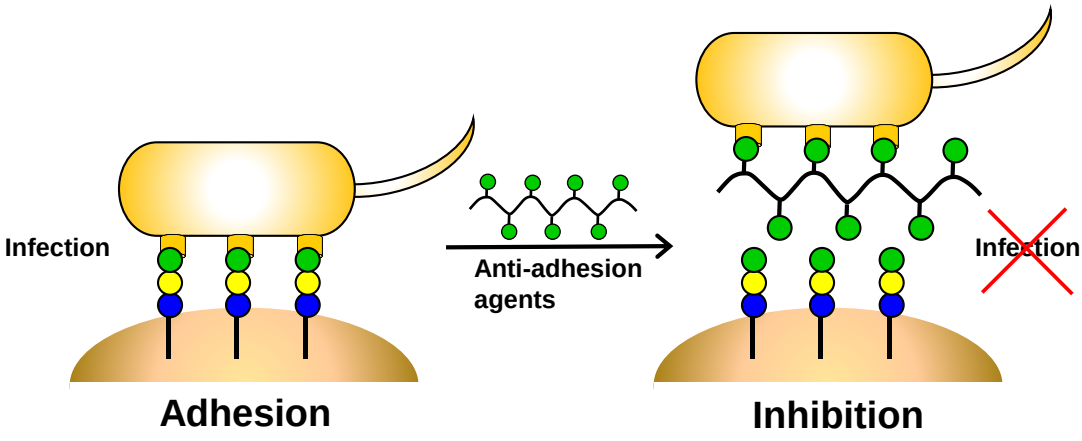

Figure 1.29 Schematic illustration of anti-adhesion therapy: inhibition of microbial adhesion using anti-adhesion agents (e.g. glyco-ligands).

Some drawbacks of anti-adhesion therapy are that pathogens express more than one type of adhesion during the infectious process due to their various adhesion encoding genes and low binding affinity of the carbohydrate for the proteins on the bacteria.[176] For an effective anti-adhesion therapy, multiple agents are required to inhibit each type of adhesion of the infecting pathogen or inhibitors should exhibit a broad range of anti-adhesion activity as well as high binding affinity for target pathogens.[177]

The use of synthetic oligosaccharides as multivalent adhesion inhibitors have been developed by attaching many copies of the saccharides, to increase the low binding affinities of monovalent glycoside.[178] Synthetic glycopolymers have also been exploited by functionalisation with terminal carbohydrates and linking branches with functional residues for effective inhibition of adhesion. Some examples demonstrated glycopolymer were successfully used as specific inhibitors for cholera toxin binding[179] and fimbriated strains of *E. coli* binding.[180]

1.6 Glycopolymers

Synthetic glycopolymers mimicking natural biomolecules have been extensively investigated for medical applications due to ease of synthesis, variable structure and chain length. Pendant sugar moieties along the polymer backbone or at the end of the chain are able to interact with target proteins through multivalent interactions.[181-183] The strength of binding strongly relies on the type of sugars, anomeric status, connecting linker type and linkage position between the carbohydrate and the polymer backbone, density of sugars, degree of polymerization and branching.[161,184] Therefore, the design of the glycopolymer for multivalent presentation (specific carbohydrate-protein interactions) is very important and essential. For example, glycopolymers can access to multiple binding sites in proteins by increasing the polymer chain length and hence increasing their binding affinity.

1.6.1 Glycopolymers: post-polymerization modification

Especially, glycopolymers have been successfully synthesized using post-polymerization modification processes, Figure 1.30. This method is a highly attractive for synthesis of functional polymers that can overcome the limited functional group tolerance compared to direct polymerization using controlled polymerization techniques. Monomers bearing functional groups that are inert to the polymerization conditions but able to introduce additional functionality. These monomers were polymerized directly through the controlled polymerization to generate reactive

polymer precursors still containing side-chain functionalities (chemoselective handles). Then in a subsequent step, polymer precursors converted into desired functional polymers with a broad range of bifunctional reagents.

The identical reactive polymer precursor results in diverse libraries of different functional polymers with same molecular weight and chain-length distribution by post-polymerization modification and this strategy is very useful to probe structure-property relationships of polymer.[185]

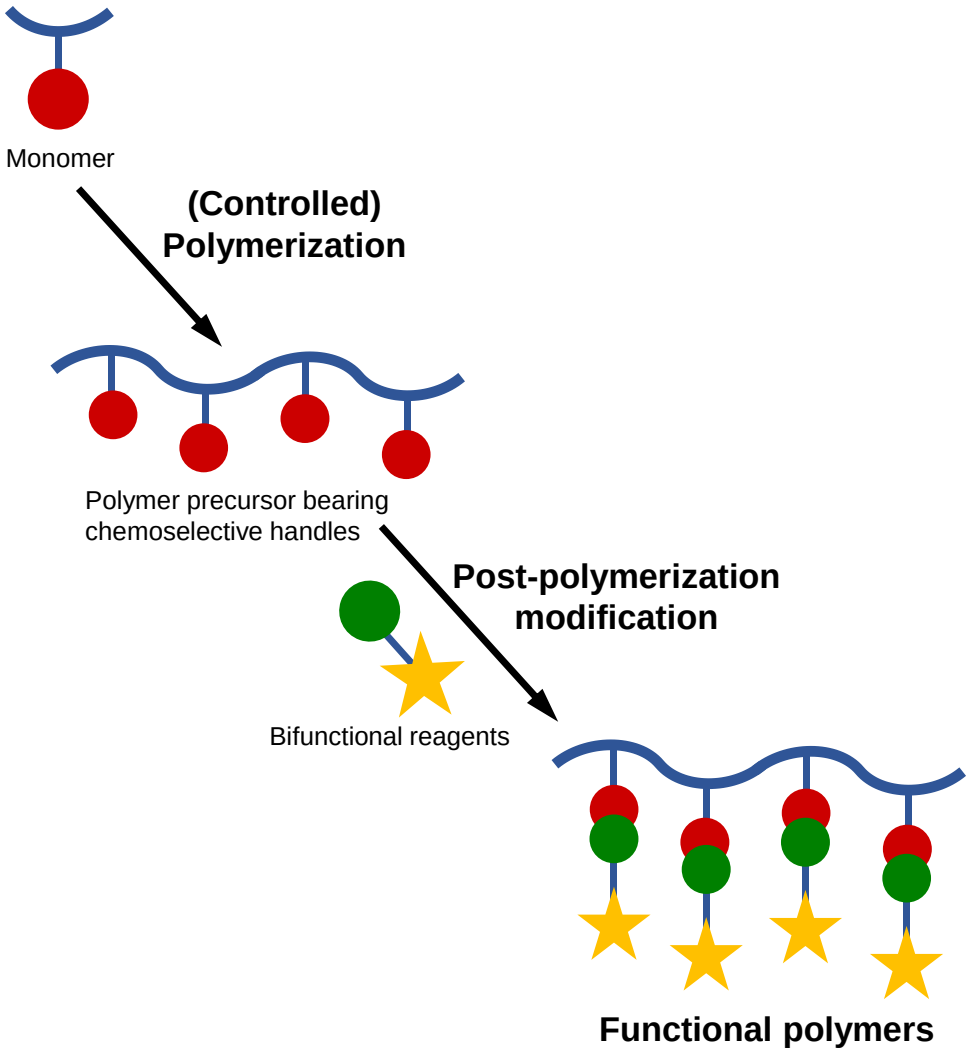

Figure 1.30 Synthesis of functional polymers by post-polymerization modification.

RAFT polymerization has been used to synthesis poly(pentafluorophenyl methacrylate) (pPFMA) backbones as reactive scaffolds for further functional modification with primary amines by Gibson et al.[186] Diverse libraries of functional polymers with same chain length distribution were prepared from the same starting polymer precursor *via* post-polymerization modification to determine structure-property relationships.[186] In order to obtain the bio functionality for glycopolymers, the pPFMA scaffolds were functionalised with allylamine to generate pendant alkene functionality, and then alkene/alkyne side chains were subsequently functionalised with thiolated carbohydrates in sequential addition procedure *via* thiol-ene 'click' chemistry[187,188] which describes highly efficient coupling reactions that proceed to quantitative conversion without any side products by Sharpless (Figure 1.31).[189]

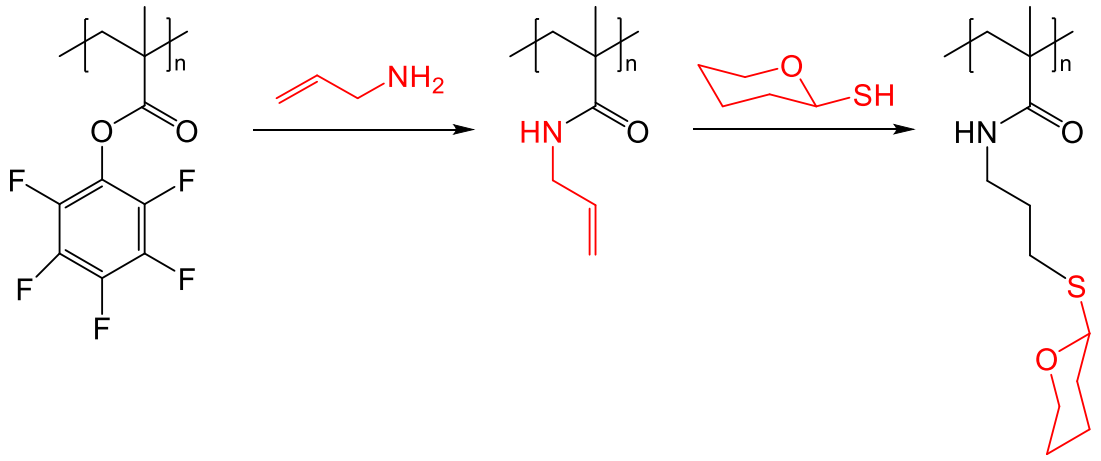

Figure 1.31 Schematic of glycopolymers by post-polymerization modification from 'clickable' structure.

1.6.2 Glycopolymers for bacteria and lectin treatments (bio applications)

In order to achieve and enhance the specific recognition of lectins from pathogens, bacteria and cancer cells, numerous investigations using glycopolymers have been focused. Various types of glycopolymers with carbohydrate moieties along the polymer backbone or at the end of the chain for mimicking natural biomolecules could be prepared by synthetic polymeric techniques including post-polymerization modification.

Polizzotti et al. and co-workers designed glycopolymers as an anti-adhesion agents to act against infections by the cholera toxin (CT), Shiga toxins, and the heat-labile enterotoxin (LT). Poly(L-glutamic acid) (PGA) backbone incorporated with different degrees of β-D-galactosylamine was obtained by post-polymerization modification. The binding of galactose-functionalised glycopolymers to bacterial toxins is improved due to higher accessibility of galactose as increasing the bearing proportion (composition) of functional carbohydrate moiety in polymer.[190,191]

Glycoconjugate polymers having oligosaccharides and amino group were synthesized to perform as Shiga toxins (Stx1 and Stx2) adsorbents by Hatanaka group. Glycopolymers bearing globotriose/lactose units and small amount of acrylamide exhibited inhibitory effects on cytotoxicity of Stx1 and Stx2, respectively.[192]

Haddleton et al synthesized a library of glycopolymers containing mannose and demonstrated that mannose in clustered polymeric structure showing the high-affinity binding to a human dendritic cell associated lectin (DC-SIGN) related to immune

responses. This simple structures effectively prevented interactions between the DC-SIGN and the human immunodeficiency virus (HIV) envelope glycoprotein gp120 as shown in Figure 1.32.[193]

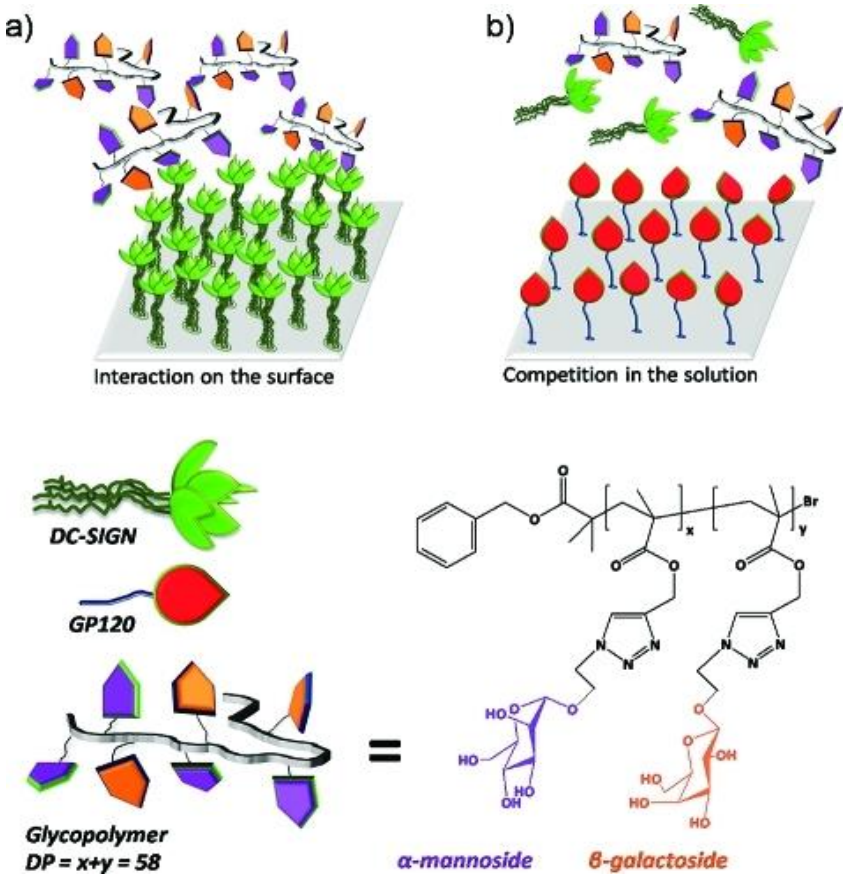

Figure 1.32 Schematic design of evaluating mannose and galactose functional polymers for DC-SIGN binding, figure adapted from reference 193.

Specific carbohydrates functionalised glycopolymers allow the potential sensing of a range of pathogens. Seeberger group used a water soluble fluorescent-conjugated glycopolymer to allow for multivalent detection of pathogens.[194] Poly(*p*-phenylene ethynylene) (PPE) was functionalised with mannosides by post-polymerization modification method. After incubation of the polymers with *E. coli*, brightly fluorescent cell clusters were shown due to multivalent interactions between the mannosylated glycopolymer and mannose receptors on the bacterial pili, which was confirmed by microscopy.

Glycopolymers can also be used as drug delivery systems. Suriano et al. have synthesized a family of amphiphilic block glycopolymers bearing D-glucose, D-galactose and D-mannose. Carbohydrates-bearing glycopolymers were able to self-assemble into micelles having a high density of sugar molecules in the shell with particle size of 100 nm and narrow size distribution, even after drug loading. Especially, galactose-containing micelles efficiently delivered doxorubicin (a drug used for liver cancer treatment) into targeted human liver hepatocellular carcinoma cells (HepG2) thorough interactions of galactose and the asialoglycoprotein receptors (ASGP-R) on the surface of hepatocytes.[195]

The results of these studies suggest strategies for optimising the binding of linear glycopolymers to bacterial toxins (protein-based materials). It is important to mention that the design of glycolpolymer structure in terms of molecular weight, multivalency of carbohydrate, spacing, linker length, branching and backbone rigidity can have a critical impact in a variety of biologically relevant (binding) events.

1.6.3 Glyconanoparticles for bacteria and lectin detection

Glyconanoparticles based on gold as a core metal have been extensively investigated as a part of biosensor systems due to their high stabilization, easy modification in size and composition, electronic and optical properties. Thiol-functionalised glycopolymer or saccharides (*via* RAFT polymerization) were efficiently attached onto gold nanoparticles and this particle demonstrated that the detection of some toxic lectins from other previous works successfully. Also, glyconanoparticles can mimic a globular shape of glycocalyx like shell to understand better than the functions of carbohydrates on the cell surface.

Penadés group first presented gold glyconanoparticles in 2001.[196] The thiol-ended disaccharide lactose or the trisaccharide were directly immobilized on gold nanoparticles surface. Gold salts ($AuCl_4^-$) were reduced in the presence of the desired thiol-functionalised glycoploymers with reducing agent ($NaBH_4$) through one-step preparation. In their another work, glyconanoparticles were obtained by multi-steps, gold nanoparticles were previously prepared by reducing gold salts ($HAuCl_4$), and then excess of thiol-armed carbohydrate derivatives were conjugated with gold nanoparticles in the subsequent step.[197]

Narain et al. reported biotinylated gold nanoparticles from well-defined biotinylated glycopolymers, pNIPAM, poly(ethylene glycol) (PEG), and HAuCl4 *via* a photochemical process. Multifunctional biotinylated glyconanoparticles underwent aggregation in the presence of the streptavidin due to the biotin-streptavidin interaction. These particles showed a high colloidal stability and high affinity for

bioconjugation to streptavidin, which are evaluated from surface plasmon resonance (SPR) curves by UV-vis spectroscopy.[198]

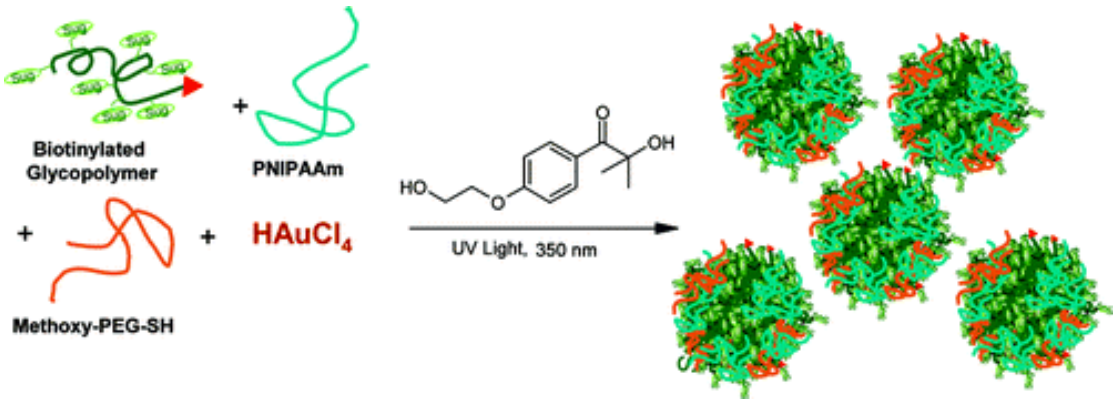

Figure 1.33 Schematic representation of the preparation of multifunctional biotinylated glyconanoparticles *via* a photochemical process, figure adapted from reference 198.

Furthermore, many researchers have recently developed efficiency of colourimetric sensing of toxic lectins by optimising various conditions such as length of the linker and polymer backbone, the density of ligands and size of core gold nanoparticles.

The influence of carbohydrate density on selective gold nanoparticles aggregation was investigated by Otsuka et al.[199] Lactose-conjugated gold nanoparticles exhibited selective aggregation when exposed to a bivalent lectin *Ricinus communis* agglutinin 120 (RCA_{120}), inducing significant changes in the absorption spectrum with visible colour change from red to purple. Further, more than 20 % lactose was required for aggregation to occur and the degree of aggregation was proportional to lectin concentration.

Lin et al. demonstrated that the multivalent interactions between mannose encapsulated gold nanoparticles and lectins/bacteria were affected by core particle size and the linker of ligands. The 20nm size gold nanoparticles with short mannopyranoside linker length showed the highest affinity to Con A as determined by SPR response curves[200] and 6 nm sized gold nanoparticles selectively bound to the mannose adhesion FimH of bacterial type 1 fimbriae, was observed by transmission electron microscopy (TEM).[201]

Richards et al. developed and optimised a versatile method to produce glyconanoparticles for lectins and lectin-expressing bacteria detection. Gold nanoparticles functionalised with galactose and mannose-ended poly(ethylene glycol) (PEG) discriminated between different strains of *E. coli* based on their different expression levels of the FimH adhesion. The use of the PEG chain increases the colloidal stability of particles retaining their bio-recognition properties. The optical properties of nanoparticles rapidly changed when bind to protein FimH positive bacteria, enabling the identification of bacteria strain by both the UV-absorbance peak and the visible colour shits.[202]

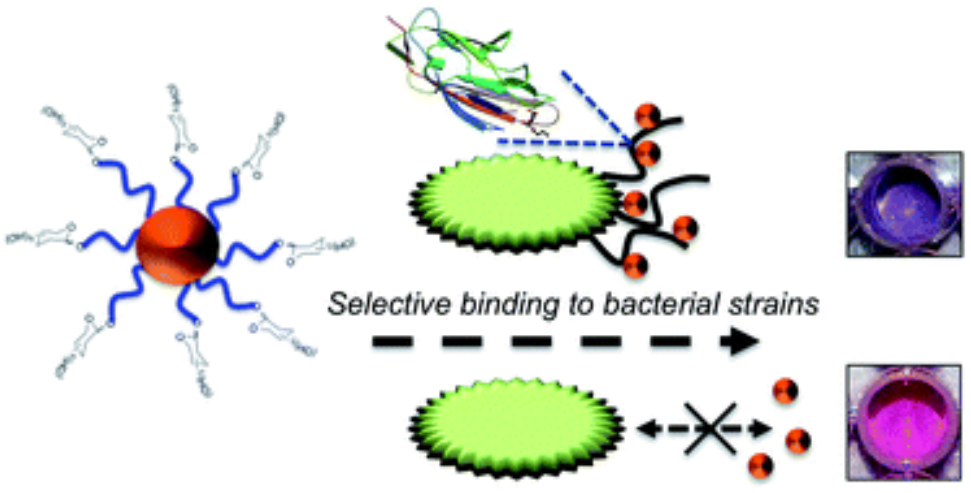

Figure 1.34 Schematic representation of carbohydrate-functionalised gold nanoparticles for selective binding to different strains of bacteria, figure adapted from reference 202.

In another work, glycosylated poly(hydroxyethyl acrylamides) (pHEA) with different degree of polymerization (DP) were immobilized onto 60 nm gold nanoparticles to evaluate the influence of glycopolymer chain length.[203] It is noted that long glycopolymer chain with a DP above 50 improved saline stability of particles, but particles were unable to generate a response upon addition of the lectins due to steric stabilization. Through an optimisation study, it was found that mixture of short glycopolymers with DP10 and DP20 gave rise to stable particles with rapid colourimetric response resulting from glyconanoparticle aggregation induced by correct lectins.

1.7 Polymer grafting density

The number of bound polymers per unit surface area (i.e. the grafting density) is a key parameter for design of nanoparticles in biological applications. This parameter directly affects the hydrodynamic diameter, colloidal stability of nanoparticles and drug loading capacity in the case of functionalised polymer incorporating drugs or sugars at the chain end.[204-207]

In general, thermogravimetric analysis (TGA) is a widely used tool for quantitative analysis of polymer grafting density and grafting density can be experimentally estimated from TGA of the carbon content in a solid nanoparticle-polymer sample. The grafting density (σ_{TGA}) of polymer on the surface of gold nanoparticle can be calculated from TGA analysis using following equation 1.[208]

$$\sigma_{TGA} = \frac{\frac{wt\%_{shell}}{wt\%_{core}} \rho_{core} \frac{4}{3} \pi r^3{}_{core} N_A}{MW_{polymer} 4\pi r^2{}_{core}} \qquad (1)$$

First, the relative mass of the polymer ($wt\%_{shell}$) and the residual mass of the total core gold particle ($wt\%_{core}$) are found form the TGA data. The number of polymer units per total sample is then derived by taking the polymer mass ($wt\%_{shell}$) and dividing by the polymer mass per chain (i.e. polymer molecular weight / avogadro's number). The total particle surface area in the sample is defined to be the total number of particles multipled by the surface area per particle ($4\pi r^2$). The number of nanoparticles is derived from the total core gold particle mass ($wt\%_{core}$) divided by the single core gold particle mass, which corresponded to the volume of a single particle ($4/3\pi r^3$) and the density of bulk gold (ρ_{core} = 19.6 g cm^{-3}). It is important to note that the radius of particle can be measured from TEM and both the surface area and volume calculations

require the assumption that the particle has a perfect spherical shape.

Gibson et al. estimated grafting density of thermo-responsive polymer poly(poly(ethylene glycol)methacrylate) (PPEGMA) coated gold nanoparticles from TGA measurement.[209] They assumed all particles have a grafting density of 0.3 chains of PPEGMA per nm^2 of gold particle surface. However, conventional TGA method requires a large amount of dried sample in order to provide sufficient quantity for analysis (i.e. milligrams).

For some polymers, X-ray photoelectron spectroscopy (XPS) can effectively measure the particle surface coverage of polymer. Ieong et al. calculated the relative grafting density (rather than the absolute) from the relative elemental compositions and MW information of polymer (equation 2) due to the penetration depth of the X-rays is estimated to be ~ 10 nm only.[210] Both longer poly(*N*-vinylpyrrolidone) (PVP) and poly(oligo(ethylene glycol)methacrylate) (POEGMA) had relatively lower grafting densities due to the increased steric hindrance of polymers, as shown in Figure 1.35.

$$\text{Relative grafting density} = \frac{I^C(Intensity\ of\ carbon\ signals)}{Number\ Carbons\ in\ Monomer\ \times DP} \qquad (2)$$

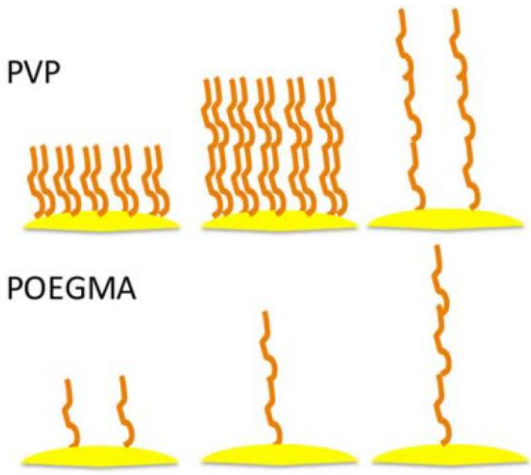

Figure 1.35 Schematic comparing different grafting densities of polymers on particle surface as a function of polymer chain length and monomer type containing small side chain (PVP) / large (POEGMA), figure adapted from reference 210.

1.8 Aims and thesis summary

Considering above, this thesis aimed to achieve two main targets: firstly the investigation of temperature responsive behaviour and co-operative behaviour for fine-tuning the transition temperature of thermo-responsive polymer tethered gold nanoparticles. The second aim was the development of a colourimetric detection method to probe protein-carbohydrate and carbohydrate-carbohydrate interactions based on stimuli response multivalent glyconanoparticles.

Chapter2 describes the fine-tuning of transition temperatures by blends of pNIPAM coated gold nanoparticles. pNIPAM with a thiol-functional terminal group was synthesized *via* RAFT polymerization and thermo-responsive gold nanoparticles were prepared by polymer grafting onto particle surface. Versitile approches were shown to mix nanoparticle components for co-operative thermal transitions; i) different polymers on same sized particles, ii) mixture of polymers on same sized particles, iii) same polymer on different sized particles and iv) different polymers on different sized particles. This provided precise control over the transitions of the responsive nanomaterials.

Chapter 3 develops a novel stimuli-responsive multifunctional gold nanomaterials as a colourimetric biosensor. Functional polymer tethered gold nanoparticles enabled temperature switchable target lectin detection based on combining the bio molecular recognition of galactose modified pHEA and the thermo-sensitivity based on the coil-to-globule phase transition of pNIPAM as a blocking agent. In order to increase sensitivity and selectivity for the rapid detection of lectins, several key conditions were optimised such as core particle size, blocking agent chain length and proportion between two different polymers. It was possible to achieve a smart polymer/gold

nanoparticle biosensor possesses temperature responsive phase transition and specific targeting multifunctional behaviour simultaneously.

Finally, **Chapter 4** shows an extended study that the previous methodology with larger glycans and the same polymers can used to demonstrate that larger sugar structures do not perturb the function of the thermo-responsive polymer or the efficient masking of the glycans. Multivalent glyco-nanostructures where the surface-expression of lactose can be triggered by an external stimulus, and a gold nanoparticle core enables colourimetric signal outputs to probe binding. Two different carbohydrate-carbohydrate interactions were investigated using this tool, which will enable their exploitation in biotechnology.

Chapter 5 is a conclusion chapter.

1.9 References

1 http://www.lex-innova.com.

2 W. P. Cheng and C. Thompson, PCT Int. Appl. WO 2008007092 A1.

3 R. Schulte, US 20070031337 A1

4 G. A. Psthuma-Trumpie, J. Korf and A. van Amerongen, *Anal. Bioanal. Chem.*, 2009, **393**, 569–582.

5 L. A. Dykman and N. G. Khlebtsov, *Acta Naturae*, 2011, **3**, 377–445.

6 G. A. Mie, *Ann Phys*, 1908, **25**, 377–445.

7 http://www.sigmaaldrich.com/technical-documents/articles/materials-science/nanomaterials/gold-nanoparticles.html.

8 http://www.cytodiagnostics.com/store/pc/Lateral-Flow-Immunoassays-d6.htm.

9 N. Khlebtsov and L. Dykman, *Chem. Soc. Rev.*, 2011, **40**, 1647–1671.

10 E. E. Connor, J. Mwamuka, A. Gole, C. J. Murphy and M. D. Wyatt, *Small*, **2005**, 1, 325–327.

11 C. Lasagna-Reeves, D. Gonzalez-Romero, M. A. Barria, I. Olmedo, A. Clos, V. M. Sadagopa Ramanujam, A. Urayama, L. Vergara, M. J. Kogan and C. Soto, *Biochem. Biophys. Res. Commun.*, 2010, **393**, 649–655.

12 J. A. Coulter, S. Jain, K. T. Butterworth, L. E. Taggart, G. R. Dickson, S. J. McMahon, W. B. Hyland, M. F. Muir, C. Trainor, A. R. Hounsell, J. M.

O'Sullivan, G. Schettino, F. J. Currell, D. G. Hirst and K. M. Prise, *Int. J. Nanomedicine*, 2012, **7**, 2673–85.

13 R. Shukla, V. Bansal, M. Chaudhary, A. Basu, R. R. Bhonde and M. Sastry, *Langmuir*, 2005, **21**, 10644–10654.

14 J. Turkevich, P. C. Stevenson and J. Hillier, *Discuss Faraday Soc.*, 1951, **11**, 55–75.

15 W. Cai, T. Gao, H. Hong and J. Sun, *Nanotechnol. Sci. Appl.*, 2008, **1**, 17–32.

16 M. Brust, M. Walker, D. Bethell, D. J. Schiffrin and R. Whyman, *J. Chem. Soc. Chem. Commun.*, 1994, **7**, 801–802.

17 J. Ye, P. Van Dorpe, W. Van Roy, G. Borghs and G. Maes, *Langmuir*, 2009, **25**, 1822–1827.

18 J. Chen, J. M. McLellan, A. Siekkinen, Y. Xiong, Z.-Y. Li and Y. Xia, *J. Am. Chem. Soc.*, 2006, **128**, 14776–14777.

19 C. L. Nehl, H. Liao and J. H. Hafner, *Nano Lett.*, 2006, **6**, 683–688.

20 M. Liu and P. Guyot-Sionnest, *J. Phys. Chem. B*, 2005, **109**, 22192–22200.

21 C. Li, K. L. Shuford, M. Chen, E. J. Lee and S. O. Cho, *ACS nano*, 2008, **2**, 1760–1769.

22 N. G. Khlebtsov and L. A. Dykman, *J. Quant. Spectrosc. Radiat. Transfer*, 2010, **111**, 1–35.

23 R. K. De Long, C. M. Reynolds, Y. Malcolm, A.Schaeffer, T. Severs and A. Wanekaya, *Nanotechnol. Sci. Appl.*, 2010, **8**, 53–63.

24 S. Jain, D. G. Hirst and J. M. O'Sullivan, *Br. J. Radiol.*, 2012, **85**, 101–113.

25 N. P. Praetorius and T. K. Mandal, *Recent Pat. Drug. Deliv. Formul.*, 2007, **1**, 37–51.

26 J. C. Kah, K. W. Kho, C. G. Lee, C. James, R. Sheppard, Z. X. Shen, K. C. Soo and M. C. Olivo, *Int. J. Nanomedicine*, 2007, **2**, 785–798.

27 R. I. Berbeco, W. Ngwa and G. M. Makrigiorgos, *Int. J. Radiat. Oncol. Biol. Phys.*, 2011, **81**, 270–276.

28 D. B. Chithrani, S. Jelveh, F. Jalali, M. van Prooijen, C. Allen, R. G. Bristow, R. P. Hill and D. A. Jaffray, *Radiat. Res.*, 2010, **173**, 719–728.

29 J. F. Hainfeld, D. N. Slatkin, T. M. Focella and H. M. Smilowitz, *Br. J. Radiol.*, 2006, **79**, 248–53.

30 D. Kim, S. Park, J. H. Lee, Y. Y. Jeong and S. Jon, *J. Am. Chem. Soc.*, 2007, **129**, 7661–7665.

31 M. Shilo, T. Reuveni, M. Motiei and R. Popovtzer, *Nanomedicine (Lond.)*, 2012, **7**, 257–269.

32 J. F. Dorsey, L. Sun, D. Y. Joh, A. Witztum, A. A. Zaki, G. D. Kao, M. Alonso-Basanta, S. Avery, A. Tsourkas and S. M. Hahn, *Trans. Cancer Res.*, 2013, **2**, 280–291.

33 W. S. Cho, M. Cho, J. Jeong, M. Choi, B. S. Han, H. S. Shin, J. Hong, B. H. Chung, J. Jeong and M. H. Cho, *Toxicol. Appl. Pharmacol.*, 2010, **245**, 116–123.

34 H. Staudinger, *From organic chemistry to macromolecules*, John Wiley &

Sons, New York, 1970.

35 R. Mülhaupt, *Angew. Chem., Int. Ed.*, 2004, **43**, 1054–1063.

36 P. Theato, *J. Polym. Sci., Part A: Polym. Chem.*, 2008, **46**, 6677–6687.

37 A. S. Hoffman, *Macromol. Symp.*, 1995, **98**, 645–664.

38 I. Galaev and B. Mattiasson, *Smart polymers: applications in biotechnology and biomedicine*, CRC Press, Taylor & Francis Group, Boca Raton, 2007.

39 M. Heskins and J. E. Guillet, *J. Macromol. Sci. Chem.*, 1968, **2**, 1441–1455.

40 S. Dai, P. Ravi and K. C. Tam, *Soft Matter*, 2008, **4**, 435–449.

41 D. A. Davis, A. Hamilton, J. Yang, L. D. Cremar, D. Van Gough, S. L. Potisek, M. T. Ong, P. V. Braun, T. J. Martínez and S. R. White, *Nature*, 2009, **459**, 68–72.

42 Y. L. Colson and M. W. Grinstaff, *Adv. Mater.*, 2012, **24**, 3878–3886.

43 T. Tanaka, I. Nishio, S.-T. Sun and S. Ueno-Nishio, *Science*, 1982, **218**, 467–469.

44 J. Thévenot, H. Oliveira, O. Sandre and S. Lecommandoux, *Chem. Soc. Rev.*, 2013, **42**, 7099–7116.

45 M. Irie, *Pure Appl. Chem.*, 1990, **62**, 1495–1502.

46 F. D. Jochum and P. Theato, *Chem. Comm.*, 2010, **46**, 6717–6719.

47 J. C. Grunlan, L. Liu and Y. S. Kim, *Nano Lett.*, 2006, **6**, 911–915.

48 R. S. Lee, Y. T. Huang and W. H. Chen, *J. Appl. Polym. Sci.*, 2010, **118**, 1634–

1642.

49 E. S. Gill and S. M. Hudson, *Prog. Polym. Sci.*, 2004, **29**, 1173–1222.

50 J. Hu and S. Liu, *Macromolecules*, 2010, **43**, 8315–8330.

51 A. Bajpai, S. K. Shukla, S. Bhanu and S. Kankane, *Prog. Polym. Sci.*, 2008, **33**, 1088–1118.

52 H. Koerner, G. Price, N. A. Pearce, M. Alexander and R. A. Vaia, *Nat. Mater.*, 2004, **3**, 115–120.

53 F. Wang, Y.-H. Lai and M.-Y. Han, *Macromolecules*, 2004, **37**, 3222–3230.

54 F. Seker, P. R. Malenfant, M. Larsen, A. Alizadeh, K. Conway, A. M. Kulkarni, G. Goddard and R. Garaas, *Adv. Mater.*, 2005, **17**, 1941–1945.

55 H. G. Schild, *Prog. Polym. Sci.*, 1992, **17**, 163–249.

56 T. Koga, F. Tanaka, R. Motokawa, S. Koizumi and F. M. Winnik, *Macromolecules*, 2008, **41**, 9413–9422.

57 J. E. Chung, M. Yokoyama, K. Suzuki, T. Aoyagi, Y. Sakurai and T. Okano, *Colloids Surf. B*, 1997, **9**, 37–48.

58 H. Wei, S. X. Cheng, X. Z. Zhang and R. X. Zhuo, *Prog. Polym. Sci.*, 2009, **34**, 893–910.

59 M. A. C. Stuart, W. T. S. Huck, J. Genzer, M. Müller, C. Ober, M. Stamm, G. B. Sukhorukov, I. Szleifer, V. V. Tsukruk, M. Urban, F. Winnik, S. Zauscher, I. Luzinov and S. Minko, *Nat. Mater.*, 2010, **9**, 101–113.

60 H. Feil, Y. H. Bae, J. Feijen and S. W. Kim, *Macromolecules*, 1993, **26**, 2496–

2500.

61 H. Vihola, A.-K. Marttila, J. S. Pakkanen, M. Andersson, A. Laukkanen, A. M. Kaukonen, H. Tenhu and J. Hirvonen, *J. Pharm. Sci.*, 2008, **97**, 4783–4793.

62 L. Klouda and A. G. Mikos, *Eur. J. Pharm. Biopharm.*, 2008, **68**, 34–45.

63 J. F. Lutz, *J. Polym. Sci. Part A*, 2008, **46**, 3459–3470.

64 G. Pasparakis and M. Vamvakaki, *Polym. Chem.*, 2011, **2**, 1234–1248.

65 F. Liu and M. W. Urban, *Prog. Polym. Sci.*, 2010, **35**, 3–23.

66 E. Ruel-Gariépy, J.-C. Leroux, *Eur. J. Pharm. Biopharm*, **2004**, *58*, 409-426.

67 Y. E. Kirsh, T. M. Karaputadze, V. V. Kobyakov, L. A. Sinitzina and S. A. Ostrovskii, *Vysokomol. Soed.*, 1979, **21**, 2734.

68 A. S. Dubovik, E. E. Makhaeva, V. Y. Grinberg and A. Khokhlov, *Macromol. Chem. Phys.*, 2005, **206**, 915–928.

69 D. Schmaljohann, *Adv. Drug Deliv. Rev.*, 2006, **58**, 1655–1670.

70 S. Fujishige, K. Kubota and I. Ando, *J. Phys. Chem.*, 1989, **93**, 3311–3313.

71 A. Gandhi, A. Paul, S. O. Sen and K. K. Sen, *Asian J. Pharm. Sci.*, 2015, **10**, 99–107.

72 M. Heskins and J. E. Guillet, *J. Macromol. Sci. Chem.*, 1968, **A2**, 1441–1455.

73 Y. Hirokawa and T. Tanaka, *J. Chem. Phys.*, 1984, **81**, 6379–6380.

74 C. Wu and S. Q. Zhou, *Macromolecules*, 1995, **28**, 5388–5390.

75 K. Akiyoshi, E. C. Kang, S. Kurumada, J. Sunamoto, T. Principi and F. M.

Winnik, *Macromolecules*, 2000, **33**, 3244–3249.

76 H. G. Schild, *Prog. Polym. Sci.*, 1992, **17**, 163–249.

77 E. E. Makhaeva, H. Tenhu and A. R. Khokhlov, *Macromolecules* 1998, **31**, 6112–6118.

78 R. Moerkerke, F. Meeussen, R. Koningsveld and H. Berghmans, *Macromolecules*, 1998, **31**, 2223–2229.

79 J. Rueda, S. Zschoche, H. Komber, D. Schmaljohann and B. Voit, *Macromolecules*, 2005, **38**, 7330–7336.

80 D. W. Urry, *J. Phys. Chem. B*, 1997, **101**, 11007–11028.

81 M. R. Dreher, D. Raucher, N. Balu, O. M. Colvin, S. M. Ludeman and A. Chilkoti, *J. Control. Release*, 2003, **91**, 31–43.

82 D. Y. Furgeson, M. R. Dreher and A. Chilkoti, *J. Control. Release*, 2006, **110**, 362–369.

83 T. Aoki, M. Kawashima, H. Katono, K. Sanui, N. Ogata, T. Okano and Y. Sakurai, *Macromolecules*, 1994, **27**, 947–952.

84 Y. M. Mohan, P. S. K. Murthy, J. Sreeramulu and K. M. Raju, *J. Appl. Polym. Sci.*, 2005, **98**, 302–314.

85 H. G. Schild and D. A. Tirrell, *J. Phys. Chem.*, 1990, **94**, 4352–4356.

86 S. Fujishige, K. Kubota and I. Ando, *J. Phys. Chem.*, 1989, **93**, 3311–3313.

87 Y. J. Zhang, S. Furyk, D. E. Bergbreiter and P. S. Cremer, *J. Am. Chem. Soc.*, 2005, **127**, 14505–14510.

88 D. Crespy and R. M. Rossi, *Polym. Int.*, 2007, **56**, 1461–1468.

89 R. Liu, M. Fraylich and B. R. Saunders, *Colloid Polym. Sci.*, 2009, **287**, 627–643.

90 L. D. Taylor and L. D. Cerankowski, *J. Polym. Sci., Polym. Chem. Ed.*, 1975, **13**, 2551–2570.

91 D. J. Phillips and M. I. Gibson, *Chem. Commun.*, 2012, **48**, 1054–1056.

92 J. V. M. Weaver, I. Bannister, K. L. Robinson, X. Bories-Azeau and S. P. Armes, *Macromolecules*, 2004, **37**, 2395–2403.

93 Z. Li, Y.-H. Kim, H. S. Min, C.-K. Han and K. M. Huh, *Macromol. Res.*, 2010, **18**, 618–621.

94 H. Yim, M. S. Kent, S. Mendez, G. P. Lopez, S. Satija and Y. Seo, *Macromolecules*, 2006, **39**, 3420–3426.

95 D. J. Mitchell, G. J. T. Tiddy, L. Waring, T. Bostock and M. P. McDonald, *J. Chem. Soc., Faraday Trans. 1*, 1983, **79**, 975–1000.

96 S. Furyk, Y. J. Zhang, D. Oritz-Acosta, P. S. Cremer and D. E. Bergbreiter, *J. Polym. Sci. Part A*, 2006, **44**, 1492–1501.

97 F. Eeckman, K. Amighi and A. J. Moes, *Int. J. Pharm.*, 2001, **222**, 259–270.

98 F. Eeckman, A. J. Moes and K. Amighi, *Int. J. Pharm.*, 2002, **241**, 113–125.

99 Y. Zhang, S. Furyk, L. B. Sagle, Y. Cho, D. E. Bergbreiter and P. S. Cremer, *J. Phys. Chem. C*, 2007, **111**, 8916–8924.

100 M. Meewes, J. Ricka, M. De Silva, R. Nyffenegger and T. Binkert,

Macromolecules, 1991, **24**, 5811–5816.

101 M. Szwarc, *Nature*, 1956, **178**, 1168–1169.

102 M. Szwarc, M. Levy and R. Milkovich, *J. Am. Chem. Soc*., 1956, **78**, 2656–2657.

103 K. Matyjaszewski and J. Spanswick, *Mater. Today*, 2005, **8**, 26–33.

104 W. A. Braunecker and K. Matyjaszewski, *Prog. Polym. Sci*., 2007, **32**, 93–146.

105 J. S. Wang and K. Matyjaszewski, *J. Am. Chem. Soc.*, 1995, **117**, 5614–5615.

106 C. J. Hawker, *J. Am. Chem. Soc.*, 1994, **116**, 11185–11186.

107 J. Chiefari, Y. K. Chong, F. Ercole, J. Krstina, J. Jeffery, T. P. T. Le, R. T. A. Mayadunne, G. F. Meijs, C. L. Moad, G. Moad, E. Rizzardo and S. H. Thang, *Macromolecules*, 1998, **31**, 5559–5562.

108 K. Matyjaszewski, *Advances in controlled/living radical polymerization*, American Chemical Society, Washington, DC, 2003.

109 A. Goto and T. Fukuda, *Prog. Polym. Sci.*, 2004, **29**, 329–385.

110 J. S. Wang and K. Matyjaszewski, *Macromolecules*, 1995, **28**, 7901–7910.

111 K. Matyjaszewski and J. Xia, *Chem. Rev.*, 2001, **101**, 2921–2990.

112 C. J. Hawker, G. G. Barclay and J. Dao, *J. Am. Chem. Soc.*, 1996, **118**, 11467–11471.

113 J. Nicolas, Y. Guillaneuf, C. Lefay, D. Bertin, D. Gigmes and B. Charleux, *Prog. Polym. Sci.*, 2013, **38**, 63–235.

114 C. L. McCormick and A. B. Lowe, *Acc. Chem. Res.*, 2004, **37**, 312–325**.**

115 Y. K. Chong, T. P. T. Le, G. Moad, E. Rizzardo and S. H. Thang, *Macromolecules*, 1999, **32**, 2071–2074.

116 T. P. Le, G. Moad, E. Rizzardo and S. H. Thang, PCT Int. Appl. WO 9801478 A1 980115.

117 R. T. A. Mayadunne, E. Rizzardo, J. Chiefari, Y. K. Chong, G. Moad and S. H. Thang, *Macromolecules*, 1999, **32**, 6977–6980.

118 M. Destarac, D. Charmot. X. Franck and S. Z. Zard, *Macromol. Rapid. Commun.*, 2000, **21**, 1035–1039.

119 R. T. A. Mayadunne, E. Rizzardo, J. Chiefari, J. Kristina, G. Moad, A. Postma and S. H. Thang, *Macromolecules*, 2000, **33**, 243–245.

120 R. Francis and A. Ajayaghosh, *Macromolecules*, 2000, **33**, 4699–4704.

121 G. Moad, E. Rizzardo and S. H. Thang, *Aust. J. Chem.*, 2005, **58**, 379–410.

122 G. N. Grover and H. D. Maynard, *Curr. Opin. Chem. Biol.*, 2010, **14**, 818–827.

123 J. Skey and R. K. O'Reilly, *Chem. Commun.*, 2008, **35**, 4183–4185.

124 J. Hentschel, K. Bleek, O. Ernst, J. F. Lutz and H. G. Borner, *Macromolecules*, 2008, **41**, 1073–1075.

125 M. Bathfield, D. Daviot, F. D'Agosto, R. Spitz, C. Ladaviere, M. T. Charreyre and T. Delair, *Macromolecules*, 2008, **41**, 8346–8353.

126 C. Boyer, V. Bulmus, T. P. Davis, V. Ladmiral, J. Liu and S. Perrier, *Chem.*

Rev., 2009, **19**, 5402–5436.

127 M. Deletre and G. Levesque, *Macromolecules*, 1990, **23**, 4733–4741.

128 Z. Merican, T. L. Schiller, C. J. Hawker, P. M. Fredericks and I. Blakey, *Langmuir*, 2007, **23**, 10539–10545.

129 A. B. Lowe, B. S. Sumerlin, M. S. Donovan, C. L. McCormick, *J. Am. Chem. Soc.*, 2002, **124**, 11562–11563.

130 M. Liang, I. C. Lin, M. R. Whittaker, R. F. Minchin, M. J. Monteiro and I. Toth, *ACS Nano*, 2010, **4**, 403–413.

131 C. Kim, Y. Lee, J. S. Kim, J. H. Jeong and T. G. Park, *Langmuir*, 2010, **26**, 14965–14969.

132 H. Wei, X. Zhang, C. Cheng, S. X. Cheng and R. X. Zhuo, *Biomaterials*, 2007, **28**, 99–107.

133 K. L. Hammer, C. M. Alexander, K. Coopersmith, D. Reishofer, C. Provenaza and M. M. Maye, *ACS Nano*, 2013, **7**, 7011–7020.

134 A. S. Hoffman, *Adv*. *Drug Delivery Rev*., 2002, **65**, 18–23.

135 S. Maji, B. Cesur, Z. Zhang, B. G. De Geest and R. Hoogenboom, *Polym. Chem.*, 2016, **7**, 1705–1710.

136 M. S. Yavuz, J. Cheng, C. M. Cobley, Q. Zhang, M. Rycenga, J. Xie, C. Kim, K. H. Song, A. G. Schwartz, L. V. Wang and Y. Xia, *Nat*. *Mater*. 2009, **8**, 935–939.

137 M. Anthea, J. Hopkins, C. W. McLaughlin, S. Johnson, M. Q. Warner, D.

LaHart and J. D. Wright, *Human Biology and Health*. Englewood Cliffs, Prentice Hall, New Jersey, 1993.

138 B. M. van den Berg, H. Vink and J. A. E. Spaan, *Circ. Res.*, 2003, **92**, 592–594.

139 A. Adibekian, P. Stallforth, M.-L. Hecht, D. B. Werz, P. Gagneux and P. H. Seeberger, *Chem. Sci.*, 2011, **2**, 337–344.

140 J. Hirabayashi, *Glycoconjugate J.*, 2004, **21**, 35–40.

141 Y. C. Lee and R. T. Lee, *Acc. Chem. Res.*, 1995, **28**, 321–327.

142 K. T. Pilobello and L. K. Mahal, *Curr. Opin. Chem. Biol.*, 2007, **11**, 300–305.

143 N. V. Bovin and H. J. Gabius, *Chem. Soc. Rev.*, 1995, **24**, 413–421.

144 CFG, http://www.functionalglycomics.org.

145 R. A. Dwek, *Chem. Rev.*, 1996, **96**, 683–720.

146 S. Schröter, C. Osterhoff, W. McArdle and R. Ivell, *Hum. Reprod. Update*, 1999, **5**, 302–313.

147 H. M. Florman and P. M.Wassarman, *Cell*, 1985, **41**, 313–324.

148 D. S. Kwon, G. Gregorio, N. Bitton, W. A. Hendrickson and D. R. Littman, *Immunity*, 2002, **16**, 135–144.

149 Y. v. Kooyk and G. A. Rabinovich, Nat. *Immunol.*, 2008, **9**, 593–601.

150 G. A. Rabinovich, Y. van Kooyk and B. A. Cobb, *Ann. N. Y. Acad. Sci*., 2012, **1253**, 1–15.

151 J. D. Hernandez and L. G. Baum, *Glycobiology*, 2002, **12**, 127–136.

152 J. Holgersson, A. Gustafsson and M. E. Breimer, *Immunol. Cell. Biol.*, 2005, **83**, 694–708.

153 D. Bundle and M. Young, *Curr. Opin. Struct. Biol.*, 1992, **2**, 666–673.

154 C. Fasting, C. A. Schalley, M. Weber, O. Seitz, S. Hecht, B. Koksch, J. Dernedde, C. Graf, E.-W. Knapp and R. Haag, *Angew. Chem. Int. Ed.*, 2012, **51**, 10472–10498.

155 C. R. Becer, Macromol. *Rapid Commun.*, 2012, **33**, 742–752.

156 K. Matsuura, M. Hibino, T. Ikeda, Y. Yamada and K. Kobayashi, *Chem. Eur. J.*, 2004, **10**, 352–359.

157 J. J. Lundquist and E. J. Toone, *Chem. Rev.*, 2002, **102**, 555–578.

158 J. C. Sacchettini, L. G. Baum and C. F. Brewer, *Biochemistry*, 2001, **40**, 3009–3015.

159 D. A. Mann, M. Kanai, D. J. Maly and L. L. Kiessling, *J. Am. Chem. Soc.*, 1998, **120**, 10575–10582.

160 T. K. Dam, R. Roy, D. Pagé and C. F. Brewer, *Biochemistry*, 2002, **41**, 1359–1363.

161 L. L. Kiessling and J. C. Grim, *Chem. Soc. Rev.*, 2013, **42**, 4476–4491.

162 L. L. Kiessling, J. E. Gestwicki and L. E. Strong, *Angew. Chem. Int. Ed.*, 2006, **45**, 2348–2368.

163 N. Sharon and H. Lis, *Science*, 1989, **246**, 227–234.

164 N. Sharon and H. Lis, *Glycobiology*, 2004, **14**, 53–62.

165 G. Ashwell and J. Harford, *Annu. Rev. Biochem.*, 1982, **51**, 531–554.

166 M. Ambrosi, N. R. Cameron and B. G. Davis, *Org. Bio. Chem.*, 2005, **3**, 1593–1608.

167 R. J. Pieters, *Org. Biomol. Chem.*, 2009, **7**, 2013–2025.

168 M. Fais, R. Karamanska, S. Allman, S. A. Fairhurst, P. Innocenti, A. J. Fairbanks, T. J. Donohoe, B. G. Davis, D. A. Russell and R. A. Field, *Chem. Sci.*, 2011, **2**, 1952–1959.

169 http://www.rcsb.org.

170 J. M. Berg, J. L. Tymoczko and L. Stryer, Biochemistry, 5th edn, 2002, ISBN-10: 0-7167-3051-0.

171 K. Drickamer, *Curr. Opin. Struct. Biol.*, 1999, **9**, 585–590.

172 W. I. Weis and K. Drickamer, *Annu. Rev. Biochem.*, 1996, **65**, 441–473.

173 G. Yilmaz and C. R. Becer, *Polym. Chem.*, 2015, **6**, 5503–5514.

174 N. Sharon, *FEBS Lett.*, 1987, **217**, 145–157.

175 N. Sharon, *Biochim. Biophys. Acta*, 2006, **1760**, 527–537.

176 I. Ofek, D. L. Hasty and N. Sharon, *FEMS Immunol. Med. Microbiol.*, 2003, **38**, 181–191.

177 N. Sharon, I. Ofek, *Glycoconjugate J.*, 2001, **17**, 659–664.

178 M. C. Galan, P. Dumy and O. Renaudet, *Chem. Soc. Rev.*, 2013, **42**, 4599–

4612.

179 M. Jones, L. Otten, S.-J. Richards, R. Lowery, D. Phillips, D. Haddleton and M. I. Gibson, *Chem. Sci.*, 2014, **5**, 1611–1616.

180 Z. Han, J. S. Pinkner, B. Ford, R. Obermann, W. Nolan, S. A. Wildman, D. Hobbs, T. Ellenberger, C. K. Cusumano and S. J. Hultgren, *J. Med. Chem.*, 2010, **53**, 4779–4792.

181 S. G. Spain and N. R. Cameron, *Polym. Chem.*, 2011, **2**, 60–68.

182 Y. Miura, D. Koketsu and K. Kobayashi, *Polym. Adv. Technol.*, 2007, **18**, 647–651.

183 G. Mulvey, P. I. Kitov, P. Marcato, D. R. Bundle and G. D. Armstrong, *Biochimie*, 2001, **83**, 841–847.

184 A. Muñoz-Bonilla and M. Fernández-García, *Materials*, 2015, **8**, 2276–2296.

185 M. A. Gauthier, M. I. Gibson and H.-A. Klok, *Angew. Chem. Int. Ed.*, 2009, **48**, 48–58.

186 M. I. Gibson, E. Froehlich and H.-A. Klok, *J. Polym. Sci. A Polym. Chem.*, 2009, **47**, 4332–4345.

187 S.-J. Richards, M. W. Jones, M. Hunaban, D. M. Haddleton and M. I. Gibson, *Angew. Chem. Int. Ed.*, 2012, **51**, 7812–7816.

188 A. Dondoni and A. Marra, *Chemical Society Reviews*, 2012, **41**, 573–586.

189 H. C. Kolb, M. G. Finn and K. B. Sharpless, *Angew. Chem. Int. Ed.*, 2001, **40**, 2004–2021.

190 B. D. Polizzotti and K. L. Kiick, *Biomacromolecules*, 2006, **7**, 483–490.

191 B. D. Polizzotti, R. Maheshwari, J. Vinkenborg and K. L. Kiick, *Macromolecules*, 2007, **40**, 7103–7110.

192 A. Miyagawa, M. C. Z. Kasuya and K. Hatanaka, *Carbohydr. Polym.*, 2007, **67**, 260–264.

193 C. R. Becer, M. I. Gibson, J. Geng, R. Ilyas, R. Wallis, D. A. Mitchell and D. M. Haddleton, *J. Am. Chem. Soc.*, 2010, **132**, 15130–15132.

194 M. D. Disney, J. Zheng, T. M. Swager and P. H. Seeberger, *J. Am. Chem. Soc.*, 2004, **126**, 13343–13346.

195 F. Suriano, R. Pratt, J. P. K. Tan, N. Wiradharma, A. Nelson, Y.-Y. Yang, P. Dubois and J. L. Hedrick, *Biomaterials*, 2010, **31**, 2637–2645.

196 J. M. de la Fuente, A. G. Barrientos, T. C. Rojas, J. Rojo, J. Cañada, A. Fernández and S. Penadés, *Angew. Chem., Int. Ed.*, 2001, **40**, 2257–2261.

197 A. G. Barrientos, J. M. Fuente, T. C. Rojas, A. Fernandez and S. Penadés, *Chem. Eur. J.*, 2003, **9**, 1909–1921.

198 R. Narain, A. Housni, G. Gody, P. Boullanger, M.-T. Charreyre and T. Delair, Langmuir, 2007, **23**, 12835–12841.

199 H. Otsuka, Y. Akiyama, Y. Nagasaki and K. Kataoka, *J. Am. Chem. Soc.*, 2001, **123**, 8226–8230.

200 C. C. Lin, Y. C. Yeh, C. Y. Yang, G. F. Chen, Y. C. Chen, Y. C. Wu and C. C. Chen, *Chem. Commun.*, 2003, **23**, 2920–2921.

201 C. C. Lin, Y. C. Yeh, C. Y. Yang, C. L. Chen, G. F. Chen, C. C. Chen and Y. C. Wu, *J. Am. Chem. Soc.*, 2002, **124**, 3508–3509.

202 S.-J. Richards, E. Fullam, G. S. Bersa and M. I. Gibson, *J. Mater. Chem. B*, 2014, **2**, 1490–1498.

203 S.-J. Richards and M. I. Gibson, *ACS Macro Lett.*, 2014, **3**, 1004–1008.

204 Y. Liu, M. K. Shipton, J. Ryan, E. D. Kaufman, S. Franzen and D. L. Feldheim, *Anal. Chem.*, 2007, **79**, 2221–2229.

205 S. Stolnik, B. Daudali, A. Arien, J. Whetstone, C. R. Heald, M. C. Garnett, S. S. Davis and L. Illum, *BBA-Biomembranes*, 2001, **1514**, 261–279.

206 V. C. F. Mosqueira, P. Legrand, J. L. Morgat, M. Vert, E. Mysiakine, R. Gref, J. P. Devissaguet and G. Barratt, *Pharm. Res.*, 2001, **18**, 1411–1419.

207 P. Jiemvarangkul, W. X. Zhang and H. L. Lien, *Chem. Eng. J.*, 2011, **170**, 482–491.

208 D. N. Benoit, H. Zhu, M. H. Lilierose, R. A. Verm, N. Ali, A. N. Morrison, J. D. Fortner, C. Avendano and V. L. Colvin, *Anal. Chem.*, 2012, **84**, 9238–9245.

209 M. I. Gibson, D. Paripovic and H.-A. Klok, *Adv. Mater.*, 2010, **22**, 4721–4725.

210 N. S. Ieong, C. I. Biggs, M. Walker and M. I. Gibson, *J. Polym. Sci., Part A: Polym. Chem.*, 2017, **55**, 1200–1208.

Chapter 2

2. Co-operative Transitions of Responsive-Polymer Coated Gold Nanoparticles; Precision Tuning and Direct Evidence for Co-operative Aggregation

2.1 Chapter summary

In this chapter, the thermal properties of the pNIPAM polymer with various molecular weights and salt effect on LCST of the polymer will be described first, and then the characterisation and thermal aggregation behaviour of gold nanoparticles conjugated with these polymers will be reported.

2.2 Abstract

Responsive polymers and polymer-coated nanoparticles have many potential applications with the crucial parameter being the exact temperature where the transition occurs. Chemical modification of hydrophobic/hydrophilic or ligand binding sites has been widely explored. This study reports an extensive investigation into the use of blending as a powerful tool to modulate poly(*N*-isopropylacrylamide) (pNIPAM) coated gold nanoparticles. By simply mixing nanoparticles of different compositions precise control over the transition temperature can be imposed. This was shown to be flexible to all possible mixing parameters (different polymers on different particles, different polymers on same particles and different sized particles with identical/different polymers). For the first time, direct evidence of the co-operative aggregation of differently sized nanoparticles (with different cloud points) is shown using transmission electron microscopy; particles with higher cloud points preferentially aggregate with those with lower cloud points with homo-aggregates not seen, unequivocally demonstrating the co-operative behaviour.

2.3 Introduction

Stimuli-responsive polymers can change their conformation and exhibit their properties when external stimuli, such as temperature,[1] pH,[2] light,[3] ions,[4] electric,[5,6] magnetic field[7] and biochemical agents[8] are applied. These unique properties and abilities have been formulated with polymers for various biomedical fields in a number of forms including simple polymer solutions,[9] hydrogels,[10,11] micelles,[12] films and layers.[13,14] Especially, thermo-responsive polymers are the most commonly used for

both *in vitro*[15-18] and *in vivo*[19-21] biomedical applications. Thermo-responsive polymers in solution display a lower critical solution temperature (LCST) or upper critical solution temperature (UCST). The LCST is the point where the polymer phase separates such that the polymer solution is miscible below the critical temperature whereas polymer solution is immiscible (precipitates) above it.

Poly(*N*-isopropylacrylamide) (pNIPAM) is one of the most well-known temperature-responsive polymers.[22-24] The mechanism of pNIPAM phase transition has been studied from many research groups and the most possible theory of temperature dependent phase transition is hydrogen-bonding interactions between pNIPAM and water.[25-28] In general, the LCST transition of pNIPAM is exhibited from 30 °C to 45 °C.[29-32] Several factors including molecular weight of polymer,[33] terminal group of polymer,[34] polymer concentration,[35] pH in solution and the presence of salt[36] as well as self assembly[37] have significant effects on the observed transition temperatures.

By employing reversible addition fragmentation and transfer (RAFT) polymerization, pNIPAM (and indeed many other classes of polymers) can be directly incorporated onto the surface of gold nanoparticles due to the quantitative installation of a (masked) thiol at each ω-chain end. Responsive polymer coated gold nanoparticles retain sensitivity to external stimuli[38-40] and can be applied in wide range of therapeutic applications including a catalysis, diagnosis, imaging and photoelectronic device.[41-47] It has been reported that pNIPAM coated gold nanoparticles can be used to drive cellular uptake upon increasing the temperature above the solution temperature due to a shift in the lipophilicity of the particle promoting membrane interactions[46,48] and is an attract route to gain entry into cells for delivery applications. However, to achieve this (or other) goals, precise control over the transition temperature is essential. It has

been reported by Fernández-Trillo et al that the cloud point of elastin-mimetic polymers could be tuned by simple mixing polymers with different cloud points.[49,50] This has been shown to be the case for some polymers but also polymer-grafted nanoparticles.[51,52] However, other classes of polymers failed to show any cooperativity with distinct 'steps' seen in mixtures of polymers such as elastin peptides or poly(oligo[ethyleneglycol methacrylates]).[53]

This raises questions about the scope of the blending approach but also the mechanism – for a single transition to occur, the particle/polymer with the higher cloud point must preferentially interact with the particle/polymer with a lower cloud point (otherwise it would not aggregate at temperatures below its own transition temperature). This implies a more complex inter-relationship between the entities than is often considered, and thus far there is no direct evidence of these interactions, as only turbidimetry is employed.

In this study, the co-operative aggregation of pNIPAM coated nanoparticles is studied in detail and the limits and scope of the blending (using all possible mixing parameters of particles and polymers) is studied using a range of techniques. Crucially, the size-dependant co-operative transitions are studied using electron microscopy, enabling the identity of each interacting component to be assigned to direct observe the cooperativity for the first time.

2.4 Result and Discussion

To access the range of well-defined pNIPAM's required for this study RAFT (reversible addition fragmentation chain transfer) polymerization was employed, Scheme 2.5A. It is curcial to select appropriate RAFT agents for a successful RAFT polymerization. Monomer (meth)acrylamides is classified in 'more activated' monomers (MAMs) which have their vinyl group conjugated to a carbonyl group and produce more stabilized radicals. A Z-group of the RAFT agent should help with the stabilization of the intermediate radical from monomers and promote the reactivity of the C=S bond toward radical addition.[54] Therefore, a trithiocarbonate (Z = S-alkyl) RAFT agent was chosen, and synthesized, based on its reported utility for control over the RAFT polymerization of NIPAM, which also inserts the desired thiol end-group and carboxyl acid at the each ω- and α- end of polymer for later immobilization onto gold nanoparticles and particle colloidal stabilities. Furthermore, this RAFT agent can be mass-produced and commercially purchased with low cost. The acid functionalised 2-(dodecylthiocarbonothioylthio)-2-methylpropanoic acid RAFT agent was characterised by ^{1}H NMR, ^{13}C NMR and Fourier transform infrared (FT-IR) spectra.

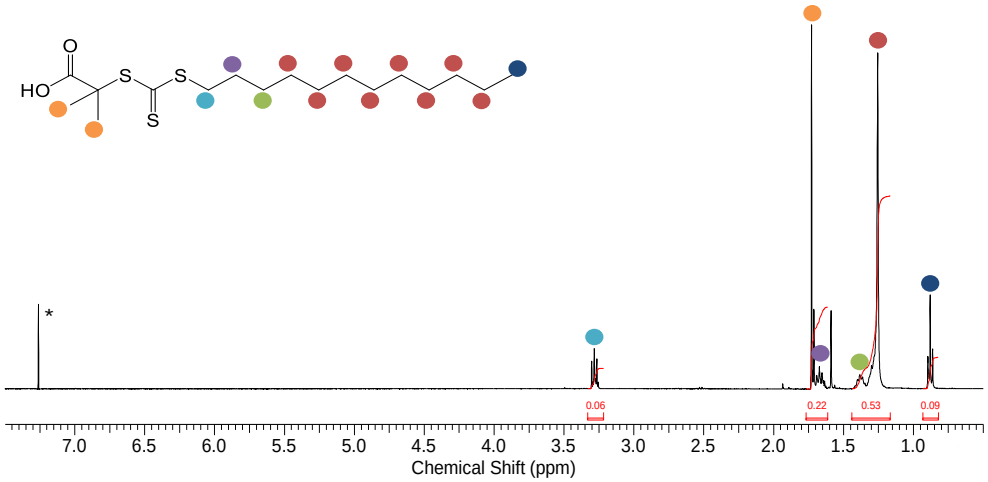

Figure 2.1 ^{1}H NMR spectra of 2-(dodecylthiocarbonothioylthio)-2-methylpropanoic acid in $CDCl_3$. *=solvent

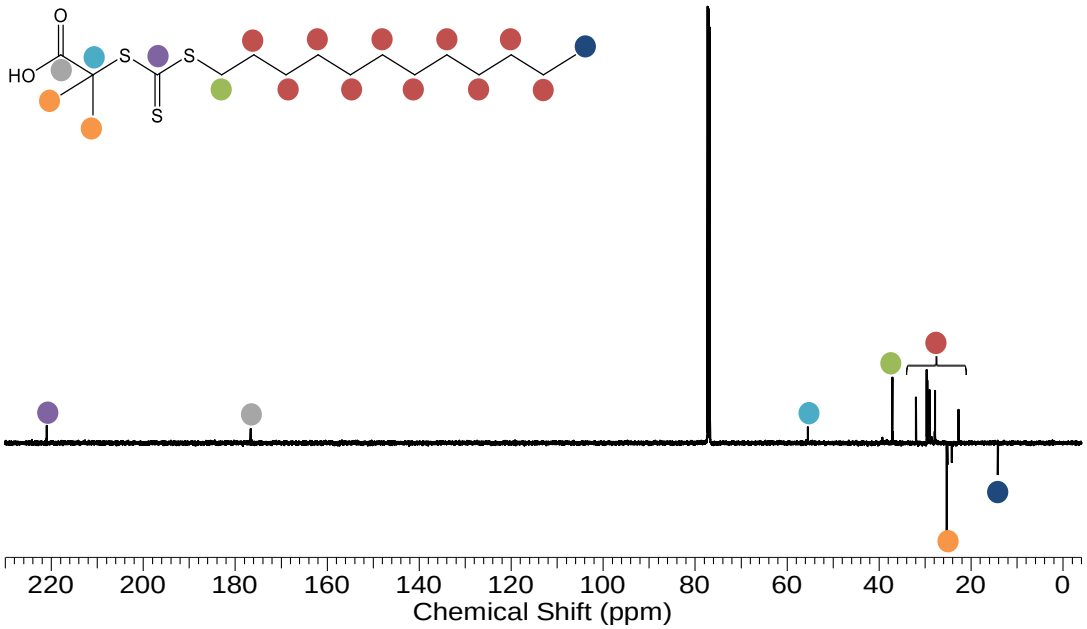

Figure 2.2 ^{13}C NMR spectra of 2-(dodecylthiocarbonothioylthio)-2-methylpropanoic acid in $CDCl_3$. *=solvent

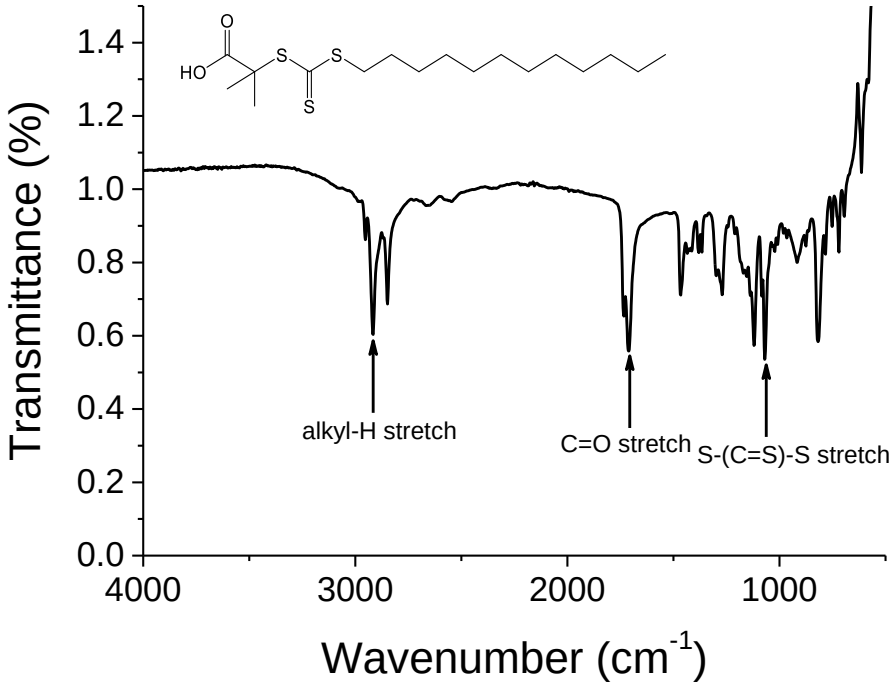

Figure 2.3 Infrared spectra of 2-(dodecylthiocarbonothioylthio)-2-methylpropanoic acid. IR cm^{-1}: 2917 (alkyl-H stretch); 1712 (C=O stretch); 1070(S-(C=S)-S stretch).

Three different molecular weight of NIPAM were polymerized in an optimal condition (methanol/toluene solution system at 70 ^{o}C) for a higher radical generation rate and polymerization rate with a narrow degree of polymerization (DP). The number of living and dead products polymer chain can be calculated from the number of RAFT agent moieties and the number of radicals generated from the initiator.[54] From the RAFT agent : initiator feed ratio (10 : 2), two radicals are introduced in a system containing ten RAFT agents, this leads to twelve chains comprising ten living chains and two dead chains by assuming the disproportionation termination. Therefore, our system has *L* (% of livingness) = 10/(10 + 2) × 100 = 83 % of living polymer with the trithiocarbonate end-group at the ω-end. It is noteworthy that using lower amounts of initiator is more effective way to reach much higher conversion of polymer.

Isolated polymer precipitates were characterised by ^{1}H NMR spectroscopy and size exclusion chromatography (SEC). The resonance peaks related to the methine proton of *N*-isopropyl group are observed at 4.0 ppm as shown in Figure 2.4, along with those associated with the C_{12} end group at 1.2 ppm.

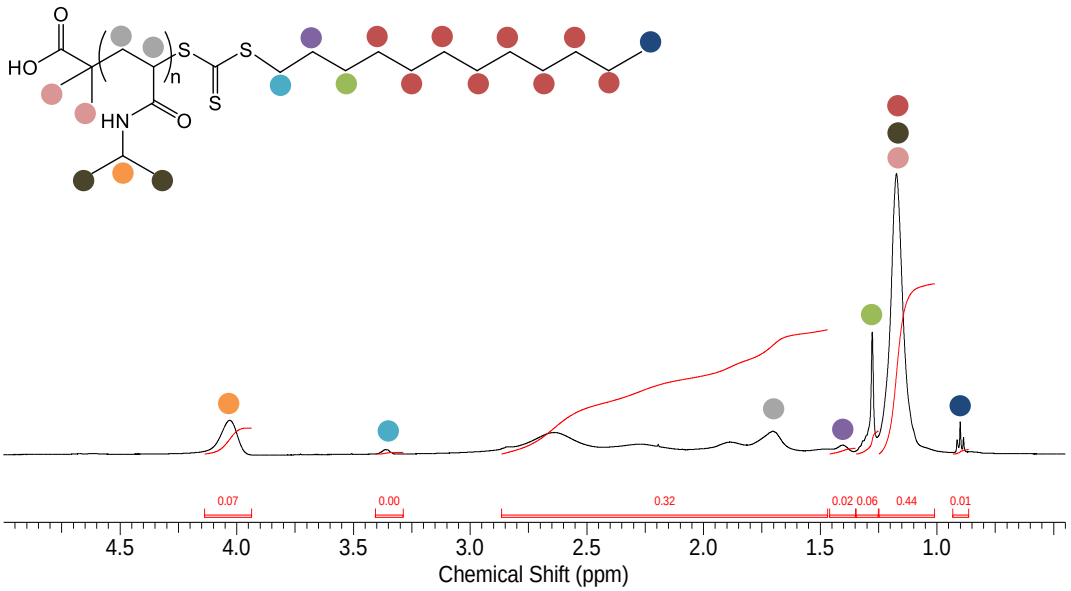

Figure 2.4 ^{1}H NMR spectra of poly(*N*-isopropylacrylamide) with DP100.

SEC confirmed a controlled polymerization with narrow dispersity values and the observed molecular weights agreeing well with those predicted from the monomer : initiator feed ratio, conversion was calculated by ^{1}H NMR spectrum with reference to a mesitylene standard and each sample was found to have more than 70 % conversion. The polymers are labelled from here based on their targeted degree of polymerization; pNIPAM$_{25}$, pNIPAM$_{50}$ and pNIPAM$_{100}$ as shown in Table 2.1 and Figure 2.5B.

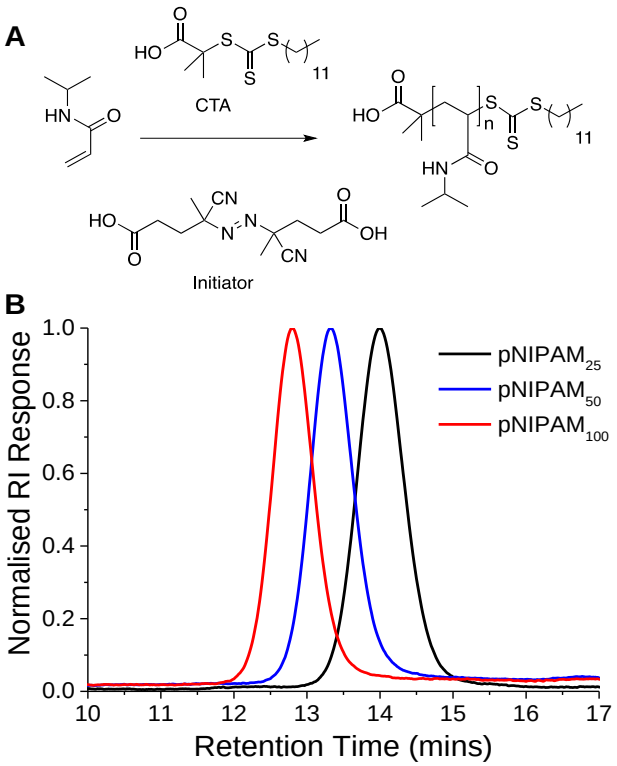

Figure 2.5 A) Synthetic route to pNIPAMs; B) SEC analysis of polymers.

Table 2.1 Characterisation of polymers.

Polymer	[M]/[CTA]/[I] [mol]	$M_{n\ Target}$ [g mol^{-1}]	Conversion[a)] [%]	$M_{n\ Theo}$ [g mol^{-1}][b)]	$M_{n\ SEC}$ [g mol^{-1}][c)]	M_w / M_n [-]
pNIPAM$_{25}$	25/1/0.2	2800	87 %	2500	2900	1.07
pNIPAM$_{50}$	50/1/0.2	5700	84 %	4800	4900	1.07
pNIPAM$_{100}$	100/1/0.2	11300	72 %	8100	7700	1.10

pNIPAM$_{xxx}$ = poly(*N*-isopropylacrylamide) where average degree of polymerization indicated by xxx.; [a)]Determined ^{1}H NMR; [b)]Calculated from the [monomer]:[CTA] ratio and of conversion; [c)]Determined by SEC in DMF using poly(methylmethacrylrate) PMMA standards.

The polymers were then evaluated for their thermo-responsive behaviour both in water and in phosphate buffered saline (PBS), as this is crucial for the measurements later in this study. 'Grafted to' gold nanoparticle polymer hybrids require salt to screen their overall net negative charge (*vide infra*).[55] UV-Vis spectroscopy was used to determine the cloud point (CP) of polymer defined as being the point of 50 % transmittance and the results of this (at 2.5 mg mL^{-1}) are shown in Figure 2.6 and Table 2.2. (Note, the cloud point is distinct from, and is the macroscopic effect associated with, an LCST). In water the polymers all had CPs close to the expected 32 °C (Figure 2.6A), but in buffer an unexpectedly high cloud point was observed with the shortest polymer having a transition above 60 °C as shown in Figure 2.6B. Previous work on pNIPAM (and indeed most thermo-responsive polymers) has shown that shorter polymers tend to have a higher cloud point, but saline normally depresses this value.[56-58] We ascribed this to partial self assembly of the shortest polymers into micelles due to the hydrophobic end group, and hence the transitions are for nanostructures (e.g. micelles) rather than the polymers with the C12 acting as the hydrophobic core. This effect has been observed by O'Reilly and co-workers showing that C12 end-groups can essentially function as a second hydrophobic block.[59] Once a micelle, the LCST will change due to conferment effects in the corona.[37,60,61] As the key aim of this work was to investigate the co-operative behaviours of gold nanoparticle (AuNP) hybrid materials, where the end group effects become less signficant, this was not explored any further.

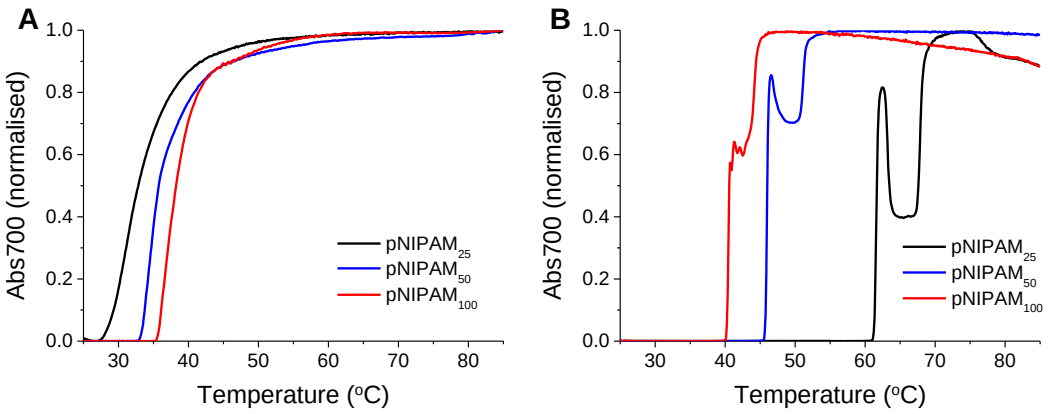

Figure 2.6 Turbidimetry scans (absorbance at 700 nm) of homopolymer in A) pure water and B) PBS. In all cases the total polymer concentration of the solutions was 2.5 mg mL^{-1}.

As the key aim of this study is to assess the co-operative CP transitions of hybrid nanoparticles, the co-operative aggregation of mixtures of these nanoparticles were studied. To observe this co-operative property, a pair of polymers having different molecular weights below ~10 kg mol^{-1} were tested as pNIPAM does not have a strong molecular weight dependence on its LCST above this value.[57,62] $pNIPAM_{50}$ (4.9 KDa) and $pNIPAM_{100}$ (7.7 KDa) were prepared at 2.5 mg mL^{-1} in PBS solution. Table 2.2 and Figure 2.7 also show transition temperature for blends of $pNIPAM_{50}$ and $pNIPAM_{100}$ at various weight fraction compositions. There are two independent transition temperature of each pure polymer, $pNIPAM_{50}$ has a transition temperature of 47 °C whereas $pNIPAM_{100}$ has a transition temperature of 41 °C. Blends of these polymers at all weight fractions shows a clear transition between 41 - 47 °C. The CPs of polymer mixture were shifted towards higher as increasing amounts of $pNIPAM_{50}$ to $pNIPAM_{100}$ with a cloud point of 42 °C, 43 °C and 45 °C, respectively. Previous reports on the shorter pNIPAMs showed that blends of these polymers underwent a single transition, based on the average molecular weight (MW) of the blend, but that longer polymers, or those with a great difference between their CPs had multiple

transitions.[52] This is in agreement with what was seen here, but with some shifting of the cloud point, albeit with two steps in the transition by the partial self assembled nanostructures transtion rather than the polymers due to incorporated hydrophobic end group.

Table 2.2 LCST values for each polymer and polymer mixture in different media.

Polymer	**Weight Fraction [%]**	**Cloud point$_{water}$ [°C]$^{a)}$**	**Cloud point$_{PBS}$ [°C]$^{b)}$**
pNIPAM$_{25}$	100	33	61
pNIPAM$_{50}$	100	36	47
pNIPAM$_{100}$	100	38	41
pNIPAM$_{50}$: pNIPAM$_{100}$	25 : 75	-	42
pNIPAM$_{50}$: pNIPAM$_{100}$	50 : 50	-	43
pNIPAM$_{50}$: pNIPAM$_{100}$	75 : 25	-	45

Cloud point was measured in $^{a)}$pure water and $^{b)}$PBS buffer upon heating from 25 °C to 85 °C, 2.5 mg mL^{-1} polymer concentration. CPs of pNIPAM mixture were not measured in water due to the very narrow gap between each polymers CP.

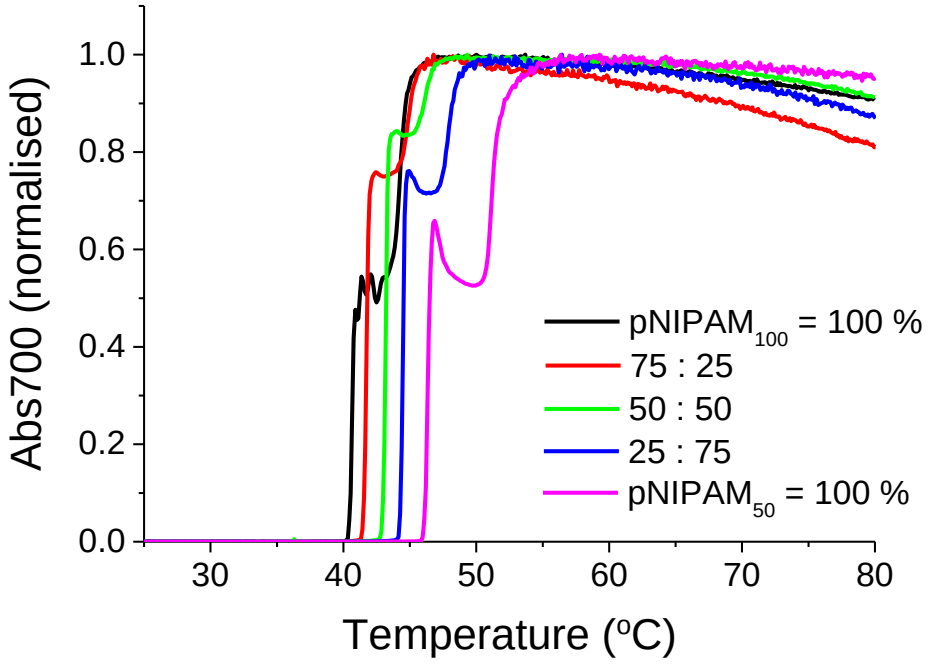

Figure 2.7 Turbidimetry analysis of blends of pNIPAM$_{50}$ and pNIPAM$_{100}$ in PBS buffer at 2.5 mg mL^{-1}.

With the function of the polymers and their co-operative nature confirmed, pNIPAM coated gold nanoparticles were synthesized as shown in Scheme 2.1. Terminal thiol functionality of pNIPAM can be prepared by nucleophilic cleavage of the trithiocarbonate end-group using nucleophiles (e.g. amines, thiols, hydroxide).[63-65] Briefly, thiol-terminated RAFT polymers were mixed onto pre-made citrate stabilized gold nanoparticles (15 nm and 40 nm) by a simple mixture procedure, which we have used previously. Excess polymer was removed by repeated centrifugation of samples to ensure only polymer-coated nanoparticles were investigated and not free polymer.

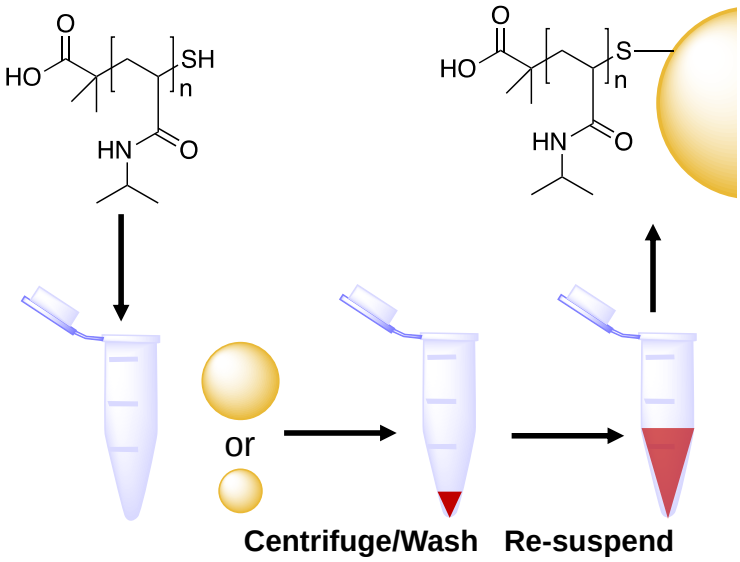

Scheme 2.1 Synthesis of thermo-responsive polymer (pNIPAM) and polymer/gold hybrid nanoparticles.

The nanoparticles were characterised by a range of techniques including transmission electron microscopy (TEM), dynamic light scattering (DLS) and X-ray photoelectron spectroscopy (XPS). The hydrodynamic diameter of uncoated gold nanoparticles was 17.5 nm and 42.4 nm by DLS measurements while after pNIPAM coating diameter were increased to 37.2 nm and 60.7 nm, respectively confirming the surface-tethering of the polymer chains. The surface plasmon resonance bands were also red shifted to longer wavelengths from 520 to 525 nm for 15 nm of gold nanoparticles and 526 to

531 nm for 40 nm of gold nanoparticles consistent with successful functionalisation as shown in Table 2.3 and Figure 2.8.

Table 2.3 Characterisation of the polymer coated nanoparticles.

Particle [a]	**SPR_{max} [nm]**	**d_{DLS} [nm]** [b]	**Cloud point [°C]** [c]
Bare Au 15nm	520	17.5	-
$pNIPAM_{25}@Au_{15}$	524	24.1	-
$pNIPAM_{50}@Au_{15}$	524	32.3	74
$pNIPAM_{100}@Au_{15}$	525	37.2	55
Bare Au 40 nm	526	42.4	-
$pNIPAM_{25}@Au_{40}$	530	49.6	-
$pNIPAM_{50}@Au_{40}$	531	55.5	80
$pNIPAM_{100}@Au_{40}$	531	60.7	60

[a] $X@Au_m$: X = polymer coating used; m=diameter of gold nanoparticle; [b] d_{DLS}(nm): Z-average diameter as determined by DLS; [c] measured in PBS upon heating from 25 °C to 85 °C, 0.029 mg mL^{-1} total gold concentration.

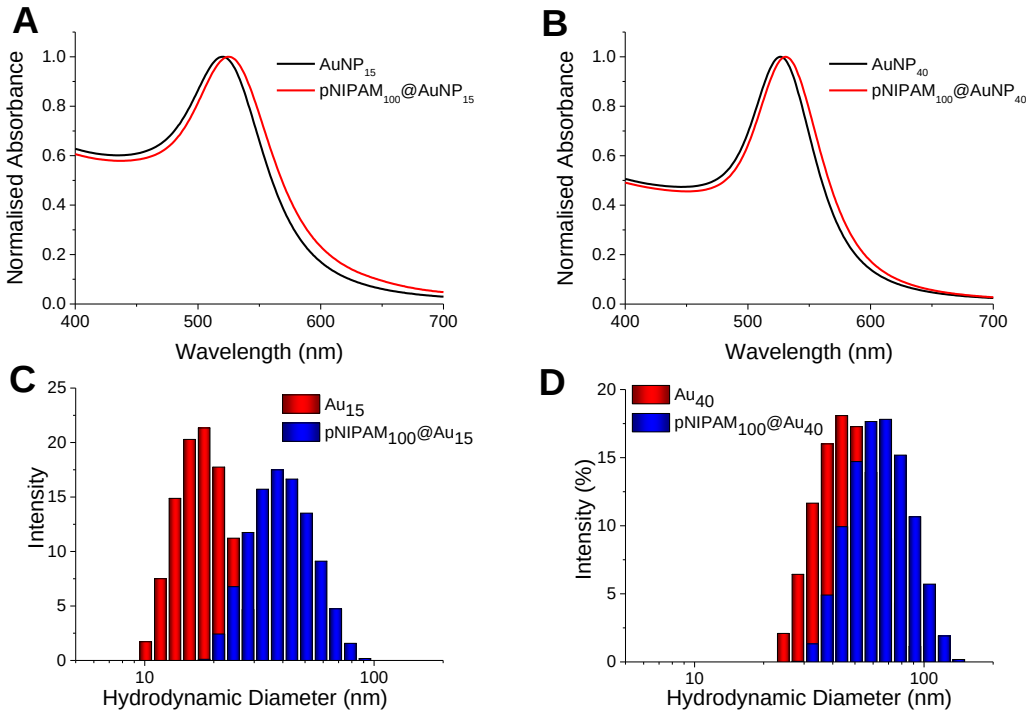

Figure 2.8 Size characterisation of $pNIPAM_{100}@Au_{15}$ and $pNIPAM_{100}@Au_{40}$ nanoparticles. A + B) UV-Vis analysis before and after polymer coating; C + D) DLS analysis before and after polymer coating.

The particles were also imaged by TEM after functionalization with the polymers (the non-coated polymers tended to aggregate on the TEM grid, see Figure 2.9). A uniform distribution of spherical core nanoparticles with an average particle size of 15.2 ± 1.4 nm and 40.7 ± 4.0 nm were observed in TEM and there was no evidence of agglomeration or ripening of the gold supporting the conclusion that the polymers were coating the gold particles.

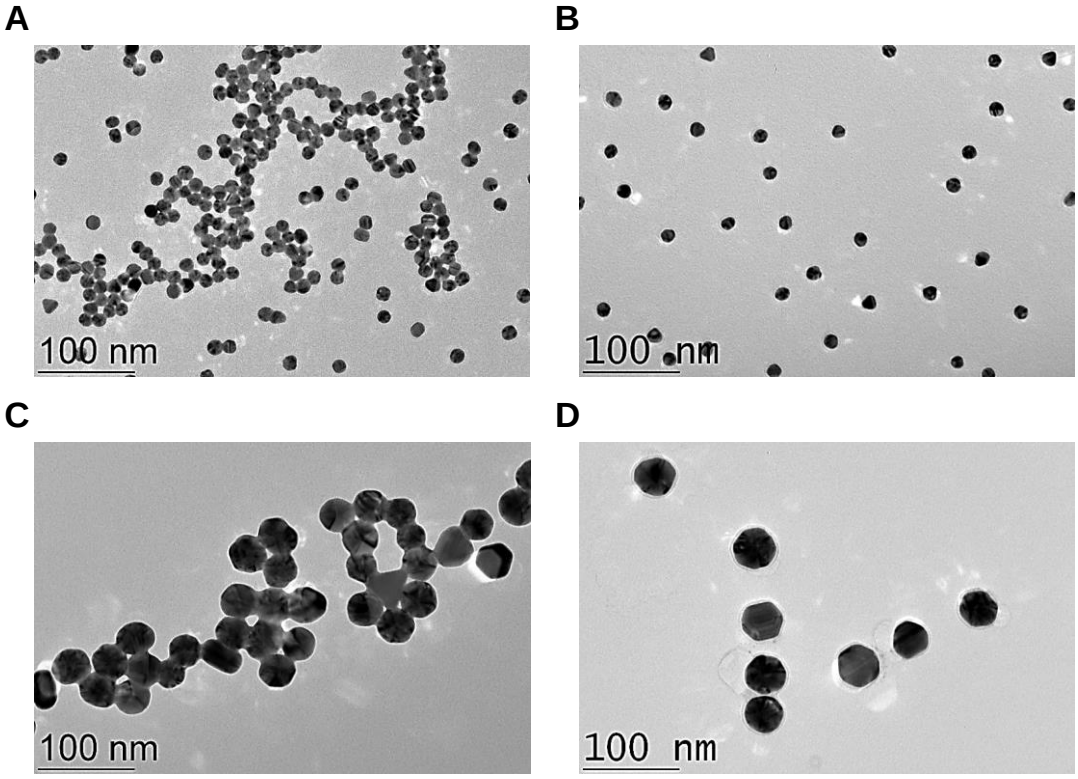

Figure 2.9 TEM images of gold nanoparticles. A + B) 15nm and C + D) 40 nm sized gold nanoparticles before and after $pNIPAM_{100}$ coating. Polymer functionalised particles showing higher colloidal stability.

Chemical characterisation was conducted using surface X-ray photoelectron spectroscopy (XPS) using gold particles deposited on silicon supports. As can be seen in Figure 2.10 and Table 2.4, both carbon (C1s) and nitrogen (N1s) region (at around 400.0 eV) of the spectra for the pNIPAM coated gold nanoparticles is broader than the bare gold nanoparticles. This is due to the C - N peak at around 286.0 eV. The presence of the C = O peak at around 288.0 eV indicates clear evidence of the presence of pNIPAM on the gold surface. Also, the intensity of both carbon and nitrogen peak increased higher after conjugation of longer pNIPAM polymer chain because of the higher concentration of carbon and nitrogen are incorporated in longer pNIPAM chain.

Furthermore, the XPS elemental ratio result could be used to calculate remaining citrate ligands at surface of gold nanoparticle after polymer coating. The C : O ratio of citrate stabilised bare gold nanoparticle is almost equal (Table 2.4) in agreement with theoretical 1 : 1 ratio due to trisodium citrate has 7 carbon and 7 oxygen. In the case of pNIPAM coated on gold nanoparticle surface, the C : N ratio should be approximately 6 : 1 (NIPAM monomer has 6 carbon and 1 nitrogen), if there is no residual citrate on particles surface after polymer grafting. However, the actual C : N ratios of three different pNIPAM coated nanoparticles were 15 : 1 – 20 : 1 rather than 6 : 1 as shown in Table 2.4, this result clearly indicated that the gold nanoparticle surface still has citrate residues in the presence of pNIPAM with similar ratio between pNIPAM and citrate.

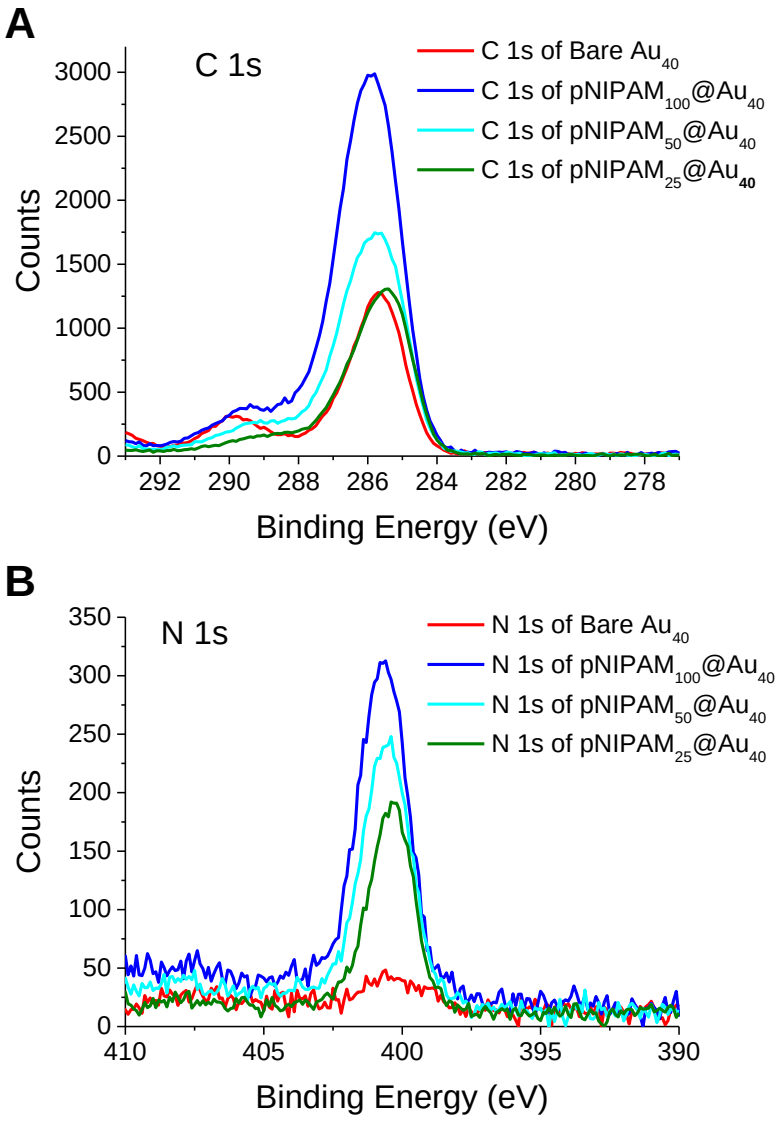

Figure 2.10 X-ray photoelectron spectroscopy analysis of pNIPAM functionalised gold nanoparticles. Representative high-resolution XPS spectrum of C 1s and N 1s region before and after various pNIPAM conjugation. A) Carbon (C 1s) peak and B) Nitrogen (N 1s) peak from the XPS analysis of polymer/gold hybrid nanoparticles (normalised to gold signal).

Table 2.4 XPS elemental ratios for pNIPAM/gold hybrid nanoparticles (normalised to gold signal).

Sample	Au 4f [%]	C 1s [%]	O 1s [%]	N 1s [%]	Cu 2p [%]	S 2p [%]
Bare Au_{40}	1.00	17.81	16.27	0.03	4.26	-
$pNIPAM_{100}@Au_{40}$	1.00	45.41	10.72	2.29	0.82	0.012
$pNIPAM_{50}@Au_{40}$	1.00	27.06	7.63	1.86	0.91	0.008
$pNIPAM_{25}@Au_{40}$	1.00	20.02	5.10	1.36	0.85	0.003
Cu foil reference	-	-	-	59.94	40.06	-

These well characterised pNIPAM$_{100}$@Au$_{15}$ particles could now be tested for their responsive behaviour. As reported by Hoogenboom et al.,[55] in water no transition was seen in the temperature range tested (25 – 85 °C), but when repeated in PBS clear transition could be seen. These observations were attributed to the residual citrate on the nanoparticle surface, which was still negative charged (measured by zeta-potential) even after polymer coating, but approached neutrality in PBS as shown in Figure 2.11A. The residual charge prevents aggregation due to electrostatic repulsions, but not in PBS due to the salt effects. Figure 2.11B shows the effect of heating the particles in PBS above their CP, with a clear red shift (long wavelength) in their absorption spectra, with an increase at 700 nm and red-blue colour shift.

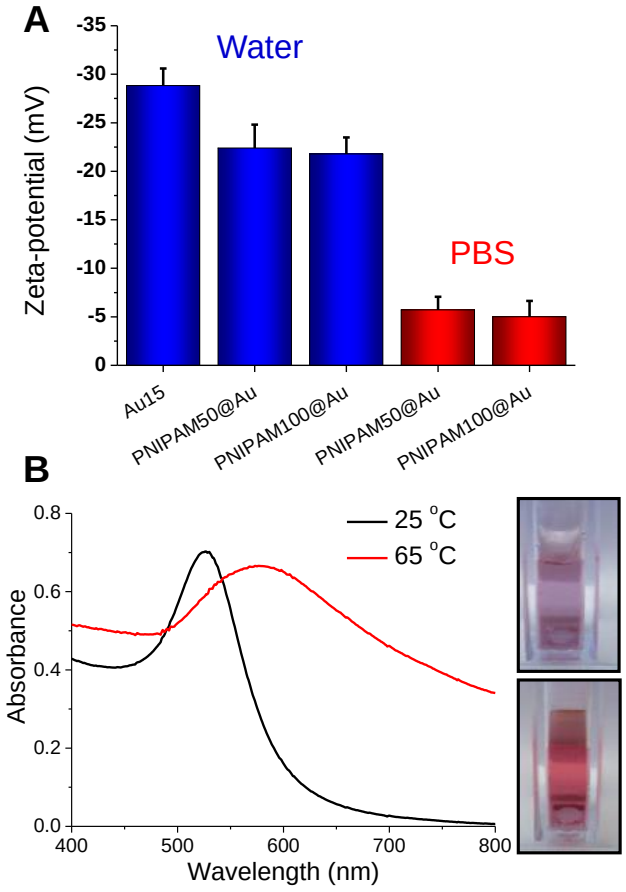

Figure 2.11 Solution properties of polymer coated nanoparticles. A) Zeta-potential analysis of nanoparticles in water, and in phosphate buffered saline; B) Example UV-Vis spectra showing effect of heating above the transition temperature. Inset images show red-blue colour shift upon aggregation.

The thermal aggregation property of pNIPAM coated gold nanoparticles was confirmed by DLS measurement with increasing temperature. The hydrodynamic diameter for both $pNIPAM_{100}$ coated 15 nm gold nanoparticles and 40 nm gold nanoparticles in pure water (~0.029 mg mL^{-1}) were slightly decreased as increasing the temperature from 25 °C to 80 °C as shown in Figure 2.12A. The reason of reduced hydrodynamic diameter of pNIPAM coated gold nanoparticles is associated with the coil-to-globule phase transition of the immobilized polymer by dehydration as temperature change.

On the contrary, when the pNIPAM coated gold nanoparticles were dispersed in PBS buffer with presence of salt (0.137 M of NaCl), the temperature responsive behaviour was exhibited in Figure 2.12B. As the temperature is increased from 25 °C to 80 °C, the hydrodynamic diameter for the pNIPAM coated gold nanoparticles increased. This is due to nanoparticle aggregation (due to hydrophobic pNIPAM above its CP) and hence an apparent increase in diameter and serves to highlight the importance of running responsive polymer/particle experiments in both pure water and saline solutions. The transition temperature of 55 °C for 15 nm gold nanoparticles and 60 °C for 40 nm gold nanoparticles were determined at significantly increasing point of diameter. The presence of certain level of salt in water may reduce electrostatic repulsion due to the charges are screened. This leads to induce the dehydrated pNIPAM chains to associate, and thereby interparticle aggregation is enhanced.

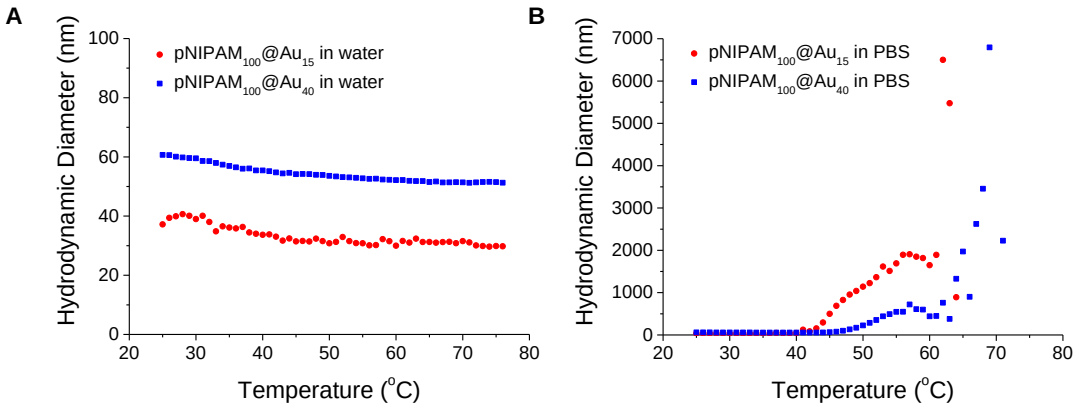

Figure 2.12 Hydrodynamic diameter for the pNIPAM coated 15 nm and 40 nm gold nanoparticles in A) pure water and B) PBS buffer as a function of temperature.

The main aim of this study was to probe, and provide direct evidence for the co-operative LCST transitions of polymer coated gold nanoparticles as a route to not only fine-tune their transition temperatures but also a way to enhance biosensing or generate complex assemblies of mixed particles. We have previously shown that pNIPAM homopolymers and various soft and hard nanoparticles show 'co-operative LCST' behaviour (scheme 2.2), but the scope and limitations of this property has not been fully investigated nor direct evidence for non-identical polymers or particles interacting.[51,52,61,66,67] To probe the potential for mixing, we investigate here a range of different combinations of polymers and nanoparticles.

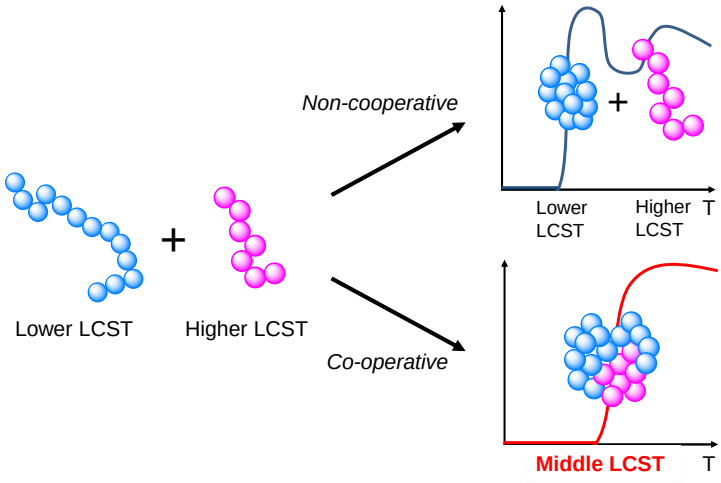

Scheme 2.2 The co-operative LCST transitions of two different homopolymers mixing.

Firstly, $pNIPAM_{50}$ and $pNIPAM_{100}$ were immobilised onto Au_{15}, using the methods described above. These nanoparticles solutions were then mixed with different weight ratio of 25 : 75, 50 : 50 and 75 : 25 respectively and their responsive transitions measured by UV-Vis, Figure 2.13. For the above mixtures, in each case a single transition temperature was observed which fell between that of the pure gold nanoparticles, and controlled by the mass fraction of the mixture. If independent transitions were occurring, two separate transitions would be expected, and the particle with a lower CP would not see a delay in its aggregation. This is also the first example of co-operative aggregation of nanoparticles with different coatings and implies that their responsive transitions involve interaction between the different sized nanoparticles rather than isolated events.

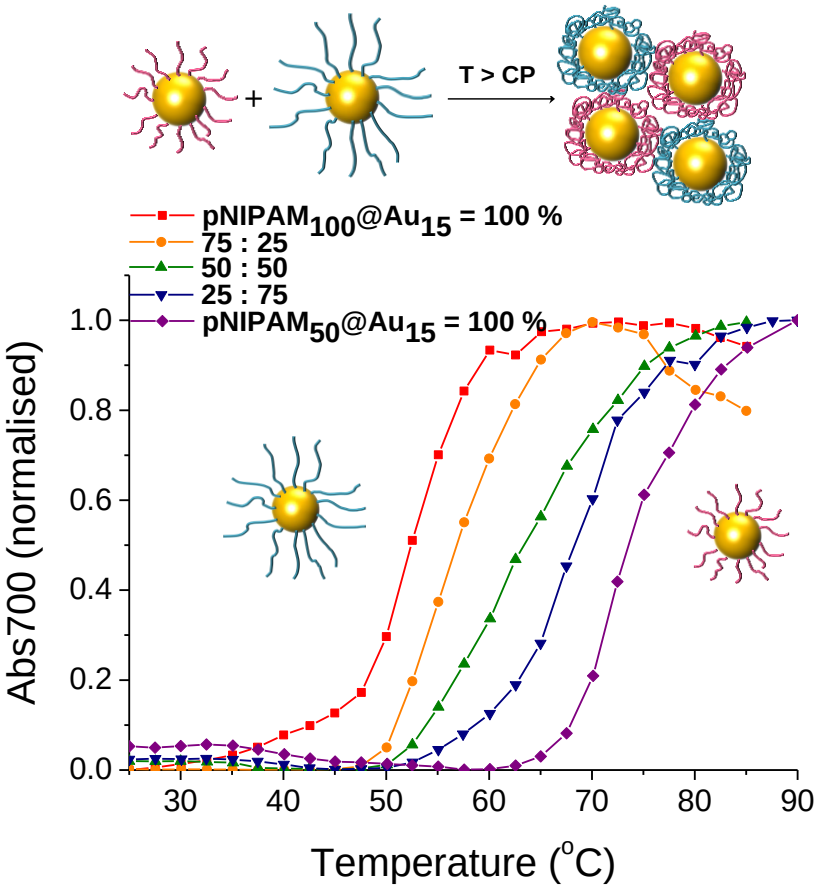

Figure 2.13 Turbidimetry scans (absorbance at 700 nm) of $pNIPAM_{50}@Au_{15}$ and $pNIPAM_{100}@Au_{15}$ mixture of the particles with different mass fraction. The total gold core concentration of the solutions was 0.029 mg mL^{-1}.

As a control experiment, the same pNIPAMs were first mixed in the same weight ratios as above (25 : 75, 50 : 50 and 75 : 25) and then added to the surface of gold particles following the same procedure as described above to give particles with surface heterogeneity. Whilst the homopolymer coated gold nanoparticles have sharp transition temperature of 55 °C and 74 °C, respectively. The CP of each particle conjugated with pre-mixed polymer lying between that of the two pure polymer coated nanoparticles are shown in Figure 2.14 and in agreement with what was seen in the single component nanoparticles mixtures. Taken together this shows that the transition of nanoparticles is highly dependent on the whole mixture and that more complex interactions between particles of different coatings take place.

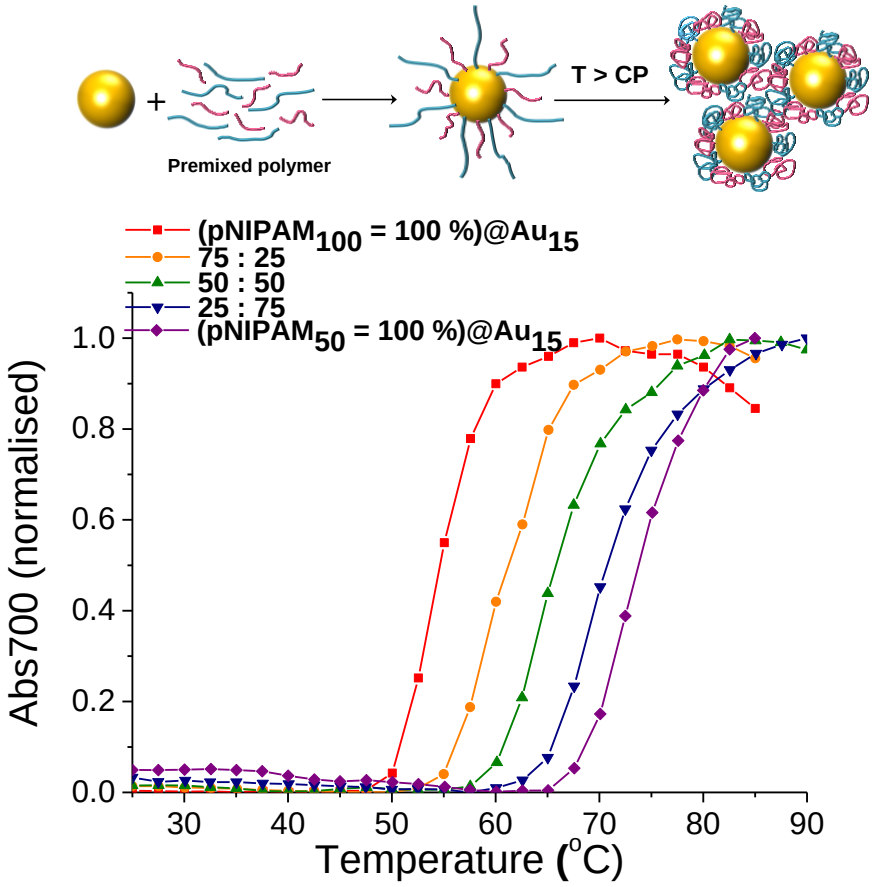

Figure 2.14 Turbidimetry scans (absorbance at 700 nm) of pre-mixture of $pNIPAM_{50}$ and $pNIPAM_{100}$ with different mass fraction coated Au_{15} in PBS solution. The total gold core concentration of the solutions was 0.029 mg mL^{-1}.

The above data confirms that cooperativity occurs, in that the observed transitions temperatures are shifted depending on the mass balance (e.g. overall MW) of the coating. For this hypothesis to be true, it must be that the lower CP particles preferentially interact (or aggregate) with the higher CP ones, or else the transition would not be affected; for example, if the lower CP particles interacted with each other, then a transition at lower temperature would be observed, followed by a step for the second type of particle. To enable us to probe and visualise this directly, a different co-operative system was required which enables discrimination between particles. Therefore mixtures of differently sized nanoparticles were chosen, as this would give an observable co-operative behaviour of nanoparticles in the TEM image (*vide infra*). As shown in Figure 2.15, with the same polymer $pNIPAM_{100}$ coating, transition of 15 nm gold nanoparticles occurs at 55 °C, while 40 nm gold nanoparticles shifted the transition to 60 °C. The solution containing a 50 : 50 % mixture of the particles shows a single transition at 57 °C.

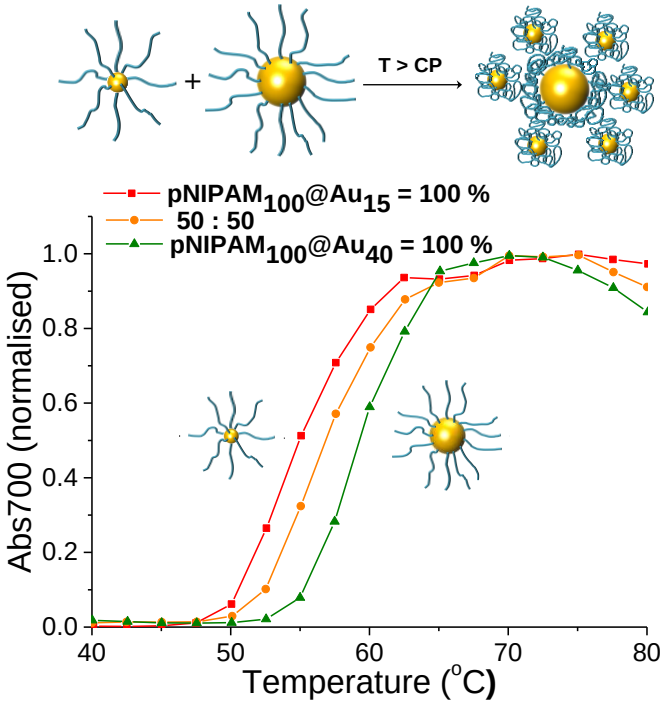

Figure 2.15 Turbidimetry scans (absorbance at 700 nm) of blends with different mass fraction of $pNIPAM_{100}$ coated Au_{15} and Au_{40}.

This result also shows dependency of cloud point on particle size. Previous researches higilighted that the change in curvature at the surface of particle has dramatic influences on cloud points, which is not universally observed.[66,68] Assuming equal grafting density and chain elongation, the degree of curvature decreses leading to a free space per polymer chain decrease, as nanoparticle size increases. Therefore, more crowded polymer chains decrease the cloud point of particle due to increased polymer-polymer interactions.

In order to explain our conflicting experimental result with the above theory, we can hypothesize that 15 nm gold nanoparticles actually have higher grafting density of pNIPAM than 40 nm gold nanoparticles, this leads to lower cloud point for small particle, which fits with previous research and experimental result in a similar manner.[69,70]

Figure 2.16 shows turbidimetry scans for blends of different particle with the different polymer coating. The $pNIPAM_{100}$ coated 40nm gold nanoparticle had a CP of 60 °C, whereas the $pNIPAM_{50}$ coated 15 nm gold nanoparticle had a CP of 74 °C. CPs of particle mixture for 25 :75 %, 50 : 50 % and 75 : 25 % with relative weight percent of $pNIPAM_{50}$ coated 15nm gold nanoparticles and $pNIPAM_{100}$ coated 40 nm gold nanoparticles were measured. In all cases, a single transition of particle mixture was observed 64 °C, 69 °C and 72 °C, showing that the CP is controlled by the relative weight fraction of each particles. This result proved process successfully and the CP of mixture particle solution is determined as a consequence of relative weight proportion of individual polymer coated nanoparticles. This strategy can be useful to control and predict CPs of polymer coated nanoparticles for desired condition.

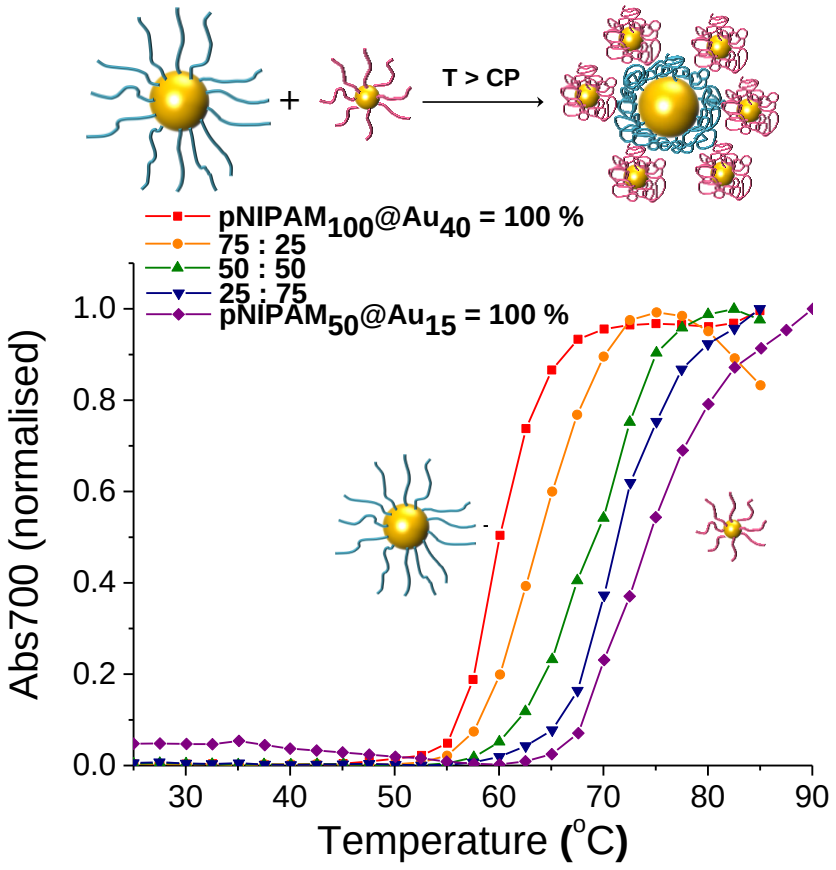

Figure 2.16 Turbidimetry scans (absorbance at 700 nm) of $pNIPAM_{50}@Au_{15}$ and $pNIPAM_{100}@Au_{40}$ mixture in PBS solution. The total gold core concentration of the solutions was 0.029 mg mL^{-1}.

The above data shows the highly co-operative nature of the nanoparticle transitions, but to it is desirable to be able to quantify the cooperativity and provide direct evidence that different nanoparticles are actually interacting preferentially with their partners. Scheme 2.3 shows the possible outcomes which would be expected for co-operative and non-cooperative transitions with different size/CP particles. In the non-cooperative case, heating above the CP of the smaller particle (lower CP) would be expected to only lead to aggregates of small particles forming, as the larger (Higher CP) particles would still be well dispersed. Conversely, if co-operative aggregation was occurring, then mixed aggregates containing both particles should be formed, explaining the modulation.

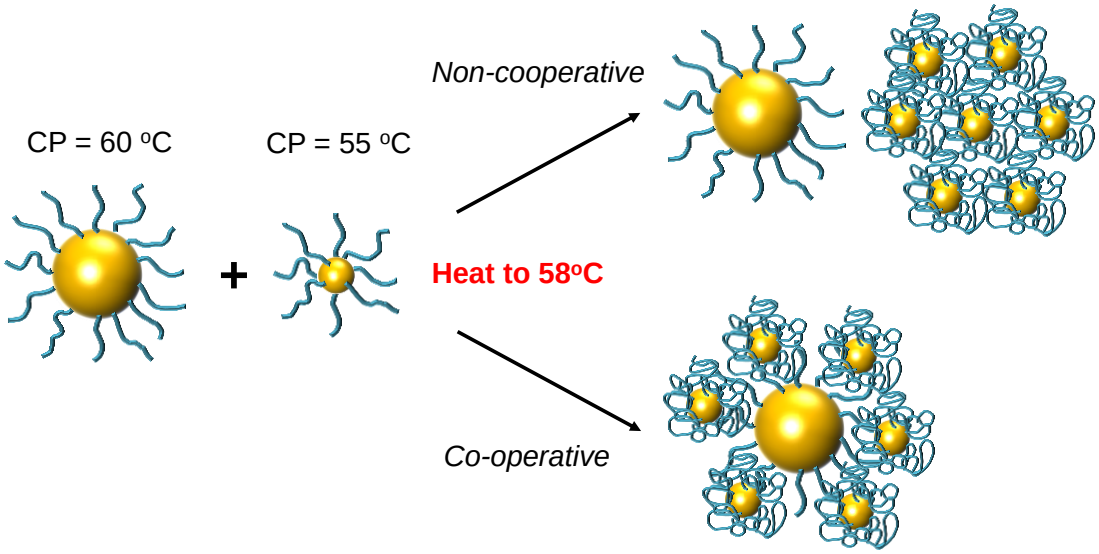

Scheme 2.3 The possible co-operative and non-cooperative aggregates expected to guide TEM analysis.

To probe this effect a range of nanoparticle samples (both pure and mixed) were prepared at a range of temperatures both below the CP but also at the CP. By choosing at temperature at the CP the larger gold nanoparticles (with high CPs) if they are not interacting should not aggregate at this temperature, providing a read out for the cooperativity. A range of mixtures were prepared of $pNIPAM_{100}@Au_{15}$: $pNIPAM_{100}@Au_{40}$ with weight ratios of 3 : 1, 1 : 1 and 1 : 3 at both 25 °C and 58 °C (i.e. below and at CP) and the TEM images are shown in Figure 2.17 and 2.18.

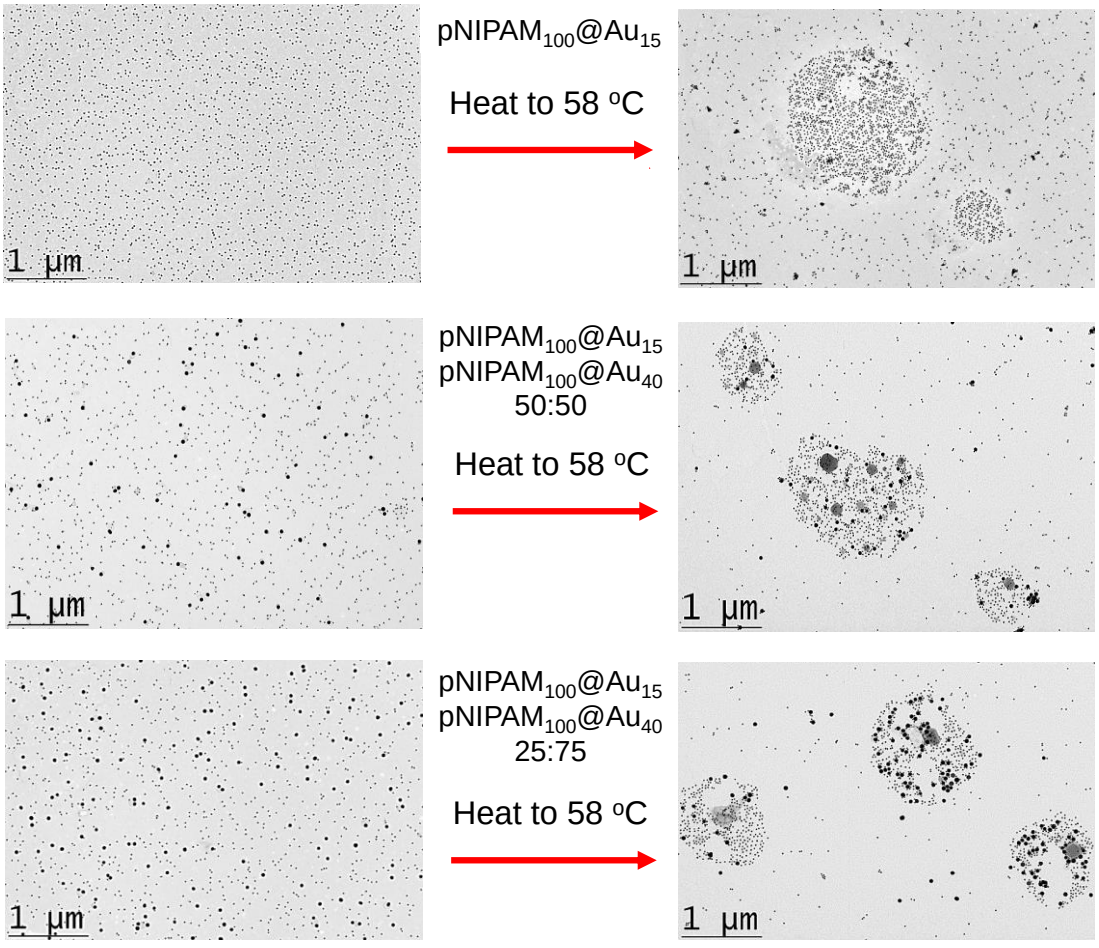

Figure 2.17 TEM analysis of co-operative particle mixture aggregation with different mass fraction. Left hand column shows nanoparticles at 25 °C (below their cloud point) and right hand column shows the same particles which were prepared at 58 °C, above cloud point of the 15 nm particles, but below that of the 40 nm particles.

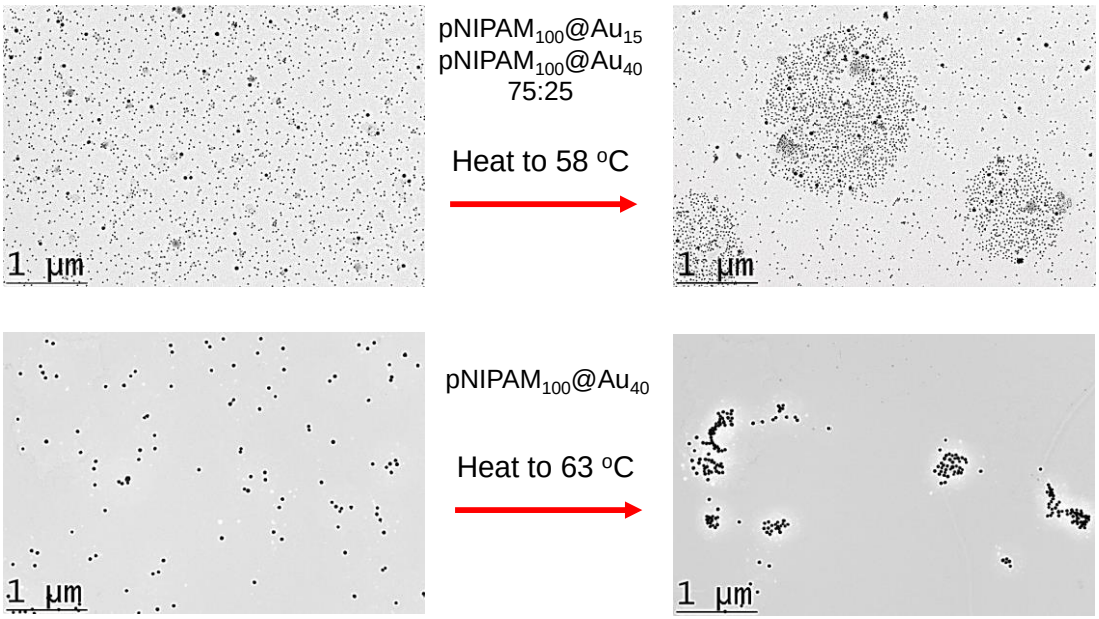

Figure 2.18 Additional TEM analysis of co-operative particle mixture aggregation with different mass fraction. Left hand column shows nanoparticles at 25 °C (below their cloud point). Right hand column shows the same particles which were prepared above cloud point of the 15 nm particles (58 °C) and 40 nm particles (63 °C).

Figure 2.17 and 2.18 clearly revealed that in the mixed nanoparticle solutions mixed aggregates are forming containing both small and large particles, rather than just those of the lower CP material, which would be expected in a non-cooperative environment. In addition to be a useful method for fine-tuning transition temperatures this shows that the particles aggregation is clearly dependant on the other particles which they are in contact with and may offer opportunities particularly in biosensing where the aggregation of a small fraction of a sample could be enhanced by other, non-interacting fractions of particles.

2.5 Conclusions

Here we have investigated the co-operative aggregation of a range of thermo-responsive polymer coated gold nanoparticles. It was shown that these particles were tolerant to almost all possible mixing parameters to still produce a single transition; i) different polymers on same sized particles, ii) mixture of polymers on same sized particles, iii) same polymer on different sized particles and iv) different polymers on different sized particles in all cases enabling a route to fine-tune the transition temperature. Crucially, using the co-operative aggregation of differently sized nanoparticles it was possible to obtain direct evidence for the preferential interaction of large/small nanoparticles with different cloud points *via* the formation of mixed aggregations in TEM, rather than the single-sized aggregates which are found in the absence of cooperativity. Such observations not only provide insight in the mechanism of these aggregation processed but provide an opportunity to create nanomaterials which are capable of interacting with their environment, and also communicating this to other particles in the mixture, which could offer new opportunities in biosensing.

2.6 Experimental Section

2.6.1 Materials

All chemicals were used as supplied unless otherwise stated. Methanol, hexane, hydrochloric acid, dichloromethane, toluene, acetone, tetrahydrofuran and diethyl ether were purchased from Fisher Scientific at laboratory reagent grade unless otherwise stated. Deuterochloroform (99.9 atom % D), 4,4'-azobis(4-cyanovaleric

acid) (> 97.0 %), dodecane thiol (≥ 98.0 %), potassium phosphate tribasic (reagent grade, ≥ 98.0 %), carbon disulfide (≥ 99.9 %), 2-bromo-2-methylpropionic acid (98.0 %), *N*-isopropylacrylamide (97.0 %), ethanolamine (≥ 99.0 %), magnesium sulfate (≥ 99.5 %) and mesitylene (analytical standard) were all purchased from Sigma-Aldrich. Ultrahigh quality water with a resistance of 18.2 MΩ cm (at 25 °C) was obtained from a Millipore Milli-Q gradient machine fitted with a 0.22 μm filter. Gold nanoparticle solutions for 15nm (0.242 mmol L^{-1}) and 40nm (0.296 mmol L^{-1}) were purchased from BBI Solutions. Pre-formulated, powdered, phosphate buffered saline was purchased from Sigma-Aldrich, and the desired solution made by addition of ultrahigh quality water to give [NaCl] = 0.137 M, [KCl] = 0.0027 M, [Na_2HPO_4] = 0.01M, [KH_2PO_4] = 0.0018 M and pH = 7.4.

2.6.2 Analytical and physical methods

^{1}H and ^{13}C NMR spectra were recorded for analysis of monomer conversions and polymer compositions on Bruker DPX-400 spectrometer using deuterated solvents obtained from Sigma-Aldrich. All chemical shifts are reported in ppm (δ) relative to tetramethylsilane (TMS). FTIR spectra were acquired using a Bruker Vector 22 FTIR spectrometer with a Golden Gate diamond attenuated total reflection cell. A total 64 (or 128) scans with resolution of 4 cm^{-1} were collected. Samples were pre-dried as a thin film for FTIR analysis. SEC analysis was conducted on Varian 390-LC MDS system equipped with a column, two PL-AS RT/MT auto sampler, a PL-gel 3 mm (50 × 7.5 mm) guard column, two PL-gel 5 mm (300 × 7.5 mm) mixed-D columns using dimethylformamide (DMF) with 1 mg mL^{-1} LiBr at 50 °C as the eluent at a flow rate of 1.0 mL min^{-1}. The GPC system was equipped with ultraviolet (UV) (set at 280 nm)

and differential refractive index (DRI) detections. Narrow molecular weight poly(methyl methacrylate) (PMMA) standards (200-1.0 × 10^6 g mol^{-1}) were used for calibration using a second order polynomial fit. Polymer solutions at 1 mg mL^{-1} were prepared in the eluent and filtered through 0.45 mm filters prior to injection. UV-vis spectra were recorded in a disposable cuvette using a Cary 60 UV-vis spectrometer from Agilent at 25 °C. Lower critical solution temperatures of free pNIPAM and pNIPAM nanoparticles were also analyzed using a Agilent Cary 60 UV-vis spectrometer equipped with a temperature controller at 700 nm with a heating/cooling rate of 1 °C min^{-1}. The cloud point of pNIPAM and pNIPAM nanoparticles were determined by normalising the turbidimetry curve such that the values were in the range of 0 to 1, and the transition temperature was defined as being the temperature corresponding to a normalised absorbance of 0.5. A polymer concentration of 2.5 mg mL^{-1} was used in all experiments. Dynamic light scattering (DLS) and Zeta potential measurements were performed using a Nano-Zs from Malvern Instruments, UK running DTS software (4 mW, He-Ne laser, λ = 633 nm) and an avalanche photodiode (APD) detector. The scattered light was measured at an angle of 173° for DLS measurement and at 12.8° for zeta potential measurements. The temperature was stabilized to ± 0.1 °C of the set temperature. All samples were prepared at the concentration of 0.029 mg mL^{-1} gold nanoparticles. Hydrodynamic diameter and zeta potential were determined using the manufacturer's software. The size and morphology of the synthesized gold nanoparticles and polymer coated gold nanoparticles were estimated by JEOL 2000FX transmission electron microscopy (TEM) at an accelerating voltage 200 kV. A drop of sample solution was deposited onto a copper grid and the water was evaporated under air. No staining was applied. The x-ray photoemission spectroscopy (XPS) data were collected at the Warwick

Photoemission Facility, University of Warwick, more details of which are available at reference.[71] The samples investigated in this study were deposited on to Cu foil, mounted on to a sample bar and loaded in to a Kratos Axis Ultra DLD spectrometer which possesses a base pressure of ~ 5 × 10^{-10} mbar. XPS measurements were performed in the main analysis chamber, with the sample being illuminated using an Al kα x-ray source. The measurements were conducted at room temperature and at a take-off angle of 90° with respect to the surface parallel. The core level spectra were recorded using a pass energy of 20 eV (resolution approx. 0.4 eV). The spectrometer work function and binding energy scale were calibrated using the Fermi edge and $3d_{5/2}$ peak recorded from a polycrystalline Ag sample immediately prior to the commencement of the experiments. The data were analysed in the CasaXPS package, using Shirley backgrounds, mixed Gaussian-Lorentzian (Voigt) lineshapes. For compositional analysis, the analyser transmission function has been determined using Ag, Au and Cu foils to determine the detection efficiency across the full binding energy range.

2.6.3 Synthetic procedures

Synthesis of 2-(dodecylthiocarbonothioylthio)-2-methylpropanoic acid (DMP)

Dodecane thiol (4.00 g, 4.73 mL, 19.76 mmol) was added dropwise to a stirred suspension of K_3PO_4 (4.20 g, 19.76 mmol) in acetone (60 mL) over 25 minutes. CS_2 (4.10 g, 3.24 mL, 53.85 mmol) was added and the solution turned bright yellow. After stirring for ten minutes 2-bromo-2-methylpropionic acid (3.00 g, 17.96 mmol) was added and a precipitation of KBr was noted. After stirring for 16 hour, the solvent was removed under reduced pressure and the residue was extracted into CH_2Cl_2 (2 × 200

mL) from 1M HCl (200 mL). The organic extracts were washed with water (200 mL) and brine (200 mL) and further dried over $MgSO_4$. The solvent was removed under reduced pressure and the residue was purified by recrystallization in hexane.

^{1}H NMR (400 MHz, $CDCl_3$) δ_{ppm}: 3.28 (2H, t, $J_{12\text{-}11}$= 7.54 Hz, H^{12}); 1.71 (6H, s, H^{13}); 1.67 (2H, p, $J_{11\text{-}10,\ 11\text{-}12}$ = 7.53 Hz, H^{11}); 1.38 (2H, p, $J_{10\text{-}9,\ 10\text{-}11}$= 7.78 Hz, H^{10}); 1.26 (16H, m, $H^{2\text{-}9}$); 0.88 (3H, t, $J_{1\text{-}2}$= 7.03 Hz, H^1).

^{13}C NMR (400 MHz, $CDCl_3$) δ_{ppm}: 196.00 (C^{13}); 177.56 (C^{16}); 64.69 (C^{14}); 37.09 (C^{12}); 31.92, 29.71, 29.63, 29.56, 29.45, 29.35, 29.12, 22.70 ($C^{2\text{-}9}$); 28.97 (C^{10}); 27.81 (C^{11}); 25.25 (C^{15}); 14.13 (C^1).

IR cm^{-1}: 2916 (alkyl-H stretch); 1710 (C=O stretch); 1068 (S-(C=S)-S stretch).

HRMS (ESI +) m/z: 365.1632 $[M+H]^+$; expected 365.1637 ($C_{17}H_{33}O_2S_3$).

Polymerization of *N*-isopropylacrylamide using 2-(dodecylthiocarbonothioylthio)-2-methylpropanoic acid (DMP)

Polymers with three different molecular weights were synthesised in typical procedure.[72] *N*-isopropylacrylamide (1 g, 8.84 mmol), 2-(dodecylthiocarbonothioylthio)-2-methylpropanoic acid (32.22 mg, 88.4 μmol), and 4,4'-azobis(4-cyanovaleric acid) (ACVA) (4.95 mg, 17.7 μmol) were dissolved in methanol/toluene (1 : 1; 4mL) in a glass vial containing a stir bar giving [monomer] : [chain transfer agent] : [initiator] = 100 : 1 : 0.2. Mesitylene (150 μL) was added as an internal reference and the mixture was stirred (5 mins). An aliquot of this starting mixture was removed for ^{1}H NMR analysis. The vial was fitted with a rubber septum

and degassed by bubbling with nitrogen gas (30 mins). The vial was then placed in an oil bath thermostated at 70 °C. After 35 minutes, the reaction mixture was opened to air and quenched in liquid nitrogen. An aliquot was removed and conversion determined by ^{1}H NMR. The remainder was precipitated into diethyl ether (45 mL). The polymer was re-precipitated and purified from THF to diethyl ether three times. The product was purified three times by precipitation from toluene into diethyl ether, isolated centrifugation, and dried under vacuum overnight to give a yellow solid. The overall monomer conversion was determined from the ^{1}H NMR spectrum by measuring the decrease in intensity of the vinyl peaks associated with the monomer relative to mesitylene. Conversion (NMR): 72 %; M_n (theoretical), 8100 g mol^{-1}; M_n (SEC), 7700 g mol^{-1}; M_w/M_n (SEC), 1.10.

General procedure for the synthesis of polymer-coated gold nanoparticles

Approximately 1 mg of the pNIPAM was added to a microcentrifuge tube, and dissolved in 100 μL of high-purity water. For the desired thiol-terminated polymer, ethanolamine (50 mol equiv of pNIPAM) was also added. To this tube 900 μL of the citrated-stabilized gold nanoparticle solution was added (15 nm: 0.242 mmol L^{-1}, 40 nm: 0.296 mmol L^{-1} total gold concentration), which was then agitated overnight in the absence of light. To remove excess polymer, the particles were centrifuged for 30 minutes at 10000 rpm. Following careful decantation of the supernatant, the particles were then re-dispersed in 1 mL of high-quality water and the centrifugation-resuspension process repeated for a total of 3 cycles. After the final cycle the particles were dispersed in 1 mL of high-quality water for future use. Assuming complete incorporation of the citrate coated gold particles into the final polymer coated particles

the total gold concentration in the final solution was 0.242 mmol L^{-1}, 0.048 mg mL^{-1} and 0.296 mmol L^{-1}, 0.058 mg mL^{-1}.

2.7 References

1 R. S. Lee, Y. T. Huang and W. H. Chen, *J. Appl. Polym. Sci.*, 2010, **118**, 1634–1642.

2 E. S. Gill and S. M. Hudson, *Prog. Polym. Sci.*, 2004, **29**, 1173–1222.

3 F. D. Jochum and P. Theato, *Chem. Comm.*, 2010, **46**, 6717–6719.

4 A. Kumar, I. Y. Galaev and B. Mattiasson, *Biotechnol. Bioeng.*, 1998, **59**, 695–704.

5 T. Shiga, *Adv. Polym. Sci.*, 1997, **134**, 131–163.

6 G. Filipcsei, J. Feher and M. Zrinyi, *J. Mol. Struct.*, 2000, **554**, 109–117.

7 M. Zrinyi, *Colloid Polym. Sci.*, 2000, **278**, 98–103.

8 T. Miyata, N. Asami and T. Uragami, *Nature*, 1999, **399**, 766–769.

9 B. Jeong, K. M. Lee, A. Gutowska and Y. H. An, *Biomacromolecules*, 2002, **3**, 865–868.

10 A. Hatefi and B. Amsden, *J. Control Release*, 2002, **80**, 9–28

11 B. Jeong, Y. H. Bae, D. S. Lee and S. W. Kim, *Nature*, 1997, **388**, 860–862.

12 H. Wei, S. X. Cheng, X. Z. Zhang and R. X. Zhuo, *Prog. Polym. Sci.*, 2009, **34**, 893–910.

13 S. Y. Yang and M. F. Rubner, *J. Am. Chem. Soc.*, 2002, **124**, 2100–2101.

14 X. Z. Shu, K. J. Zhu and W. Song, *Int. J. Pharm.*, 2001, **212**, 19–28.

15 M. Ebara, M. Yamato, M. Hirose, T. Aoyagi, A. Kikuchi, K. Sakai and T. Okano, *Biomacromolecules*, 2003, **4**, 344–349.

16 M. Yamato, C. Konno, A. Kushida, M. Hirose, M. Utsumi, A. Kikuchi and T. Okano, *Biomaterials*, 2000, **21**, 981–986.

17 M. A. Nandkumar, M. Yamato, A. Kushida, C. Konno, M. Hirose, A. Kikuchi and T. Okano, *Biomaterials*, 2002, **23**, 1121–1130.

18 K. Uchida, K. Sakai, E. Ito, O. H. Kwon, A. Kikuchi, M. Yamato and T. Okano, *Biomaterials*, 2000, **21**, 923–929.

19 A. Chilkoti, M. R. Dreher, D. E. Meyer and D. Raucher, *Adv. Drug. Deliv. Rev.*, 2002, **54**, 613–630.

20 J. Weidner, *Drug. Discov. Today*, 2001, **6**, 1239–1241.

21 D. E. Meyer, G. A. Kong, M. W. Dewhirst, M. R. Zalutsky and A. Chilkoti, *Cancer Res.*, 2001, **61**, 1548–1554.

22 J. M. Hu, X. Z. Zhang, D. Wang, X. L. Hu, T. Liu, G. Y. Zhang and S. Y. Liu, *J. Mater. Chem.*, 2011, **21**, 19030–19038.

23 Y. Z. You, K. K. Kalebaila, S. L. Brock and D. Oupicky, *Chem. Mater.*, 2008, **20**, 3354–3359.

24 M. R. Islam, A. Ahiabu, X. Li and M. J. Serpe, *Sensors*, 2014, **14**, 8984–8995.

25 H. G. Schild, *Prog. Polym. Sci.*, 1992, **17**, 163–249.

26 F. M. Winnik, *Polymer*, 1990, **31**, 2125–2134.

27 F. Meersman, J. Wang and Y. Q. Wu, *Macromolecules*, 2005, **38**, 8923–8928.

28 G. LunaBarcenas, D. G. Gromov, J. C. Meredith, I. C. Sanchez, J. J. dePablo and K. P. Johnston, *Chem. Phys. Lett.*, 1997, **278**, 302–306.

29 M. Heskins and J. E. Guillet, *J. Macromol. Sci. Chem.*, 1968, **A2**, 1441–1455.

30 Y. Hirokawa and T. Tanaka, *J. Chem. Phys.*, 1984, **81**, 6379–6380.

31 C. Wu and S. Q. Zhou, *Macromolecules*, 1995, **28**, 5388–5390.

32 K. Akiyoshi, E. C. Kang, S. Kurumada, J. Sunamoto, T. Principi and F.M. Winnik, *Macromolecules,* 2000, **33**, 3244–3249.

33 H. G. Schild and D. A. Tirrell, *J. Phys. Chem.*, 1990, **94**, 4352–4356.

34 Y. Xia, X. Yin, N. A. D. Burke and H. D. H. Ströver, *Macromolecules,* 2005, **38**, 5937-5943.

35 S. Fujishige, K. Kubota and I. Ando, *J. Phys. Chem.*, 1989, **93**, 3311–3313.

36 Y. J. Zhang, S. Furyk, D. E. Bergbreiter and P. S. Cremer, *J. Am. Chem. Soc.*, 2005, **127**, 14505–14510.

37 L. D. Blackman, D. B. Wright, M. P. Robin, M. I. Gibson and R. K. O'Reilly, *ACS Macro Lett.*, 2015, **4**, 1210–1214.

38 N. Nath and A. Chilkoti, *J. Am. Chem. Soc.*, 2001, **123**, 8197–8202.

39 R. A. Sperling, P. Rivera Gil, F. Zhang, M. Zanella and W. J. Parak, *Chem. Soc. Rev.*, 2008, **37**, 1896–1908.

40 A. Kumar, X. Zhang and X.-J. Liang, *Biotechnol. Adv.*, 2013, **31**, 593–606.

41 A. N. Shiway, E. Katz and I. Willner, *Chem. Phys. Chem.*, 2000, **1**, 18–52.

42 F. Remacle and R. D. Levine, *Chem. Phys. Chem.*, 2001, **2**, 20–36.

43 A. C. Templeton, W. P. Wuelfing and R. W. Murray, *Acc. Chem. Res.*, 2000, **33**, 27–36.

44 S.-J. Richards and M. I. Gibson, *ACS Macro Lett.*, 2014, **3**, 1004–1008.

45 S.-J. Richards, L. Otten and M. I. Gibson, *J. Mater. Chem. B*, 2016, **4**, 3046–3053.

46 F. Mastrotto, P. Caliceti, V. Amendola, S. Bersani, J. P. Magnusson, M. Meneghetti, G. Mantovani, C. Alexander and S. Salmaso, *Chem. Commun.*, 2011, **47**, 9846–9848.

47 S. Lv, C. Cehng, Y. Song and Z. Zhao, *RSC Adv.*, 2015, **5**, 3248–3259.

48 M. S. Yavuz, J. Cheng, C. M. Cobley, Q. Zhang, M. Rycenga, J. Xie, C. Kim, K. H. Song, A. G. Schwartz, L. V. Wang and Y. Xia, *Nat. Mater.*, 2009, **8**, 935–939.

49 F. Fernández-Trillo, J. C. M. van Hest, J. C. Thies, T. Michon, R. Weberskirch and N. R. Cameron, *Chem. Commun.*, 2008, **19**, 2230–2232.

50 F. Fernández-Trillo, J. C. M. van Hest, J. C. Thies, T. Michon, R. Weberskirch and N. R. Cameron, *Adv. Mater.*, 2009, **21**, 55–59.

51 M. I. Gibson, D. Paripovic and H.-A. Klok, *Adv. Mater.*, 2010, **22**, 4721–4725.

52 N. S. Ieong, M. Hasan, D. J. Phillips, Y. Saaka, R. K. O'Reilly and M. I. Gibson, *Polym. Chem.*, 2012, **3**, 794–799.

53 R. L. M. Teeuwen, F. A. de Wolf, H. Zuilhof and J. C. M. van Hest, *Soft Matter*,

2009, **5**, 4305–4310.

54 S. Perrier, *Macromolecules*, 2017, **50**, 7433–7447.

55 Z. Zhang, S. Maji, A. B. da F. Antunes, R. De Rycke, Q. Zhang, R. Hoogenboom and B. G. De Geest, *Chem. Mater.*, 2013, **25**, 4297–4303.

56 J. V. M. Weaver, I. Bannister, K. L. Robinson, X. Bories-Azeau and S. P. Armes, *Macromolecules*, 2004, **37**, 2395–2403.

57 Z. Li, Y.-H. Kim, H. S. Min, C.-K. Han and K. M. Huh, *Macromol. Res.*, 2010, **18**, 618–621.

58 Y. Zhang, S. Furyk, L. B. Sagle, Y. Cho, D. E. Bergbreiter and P. S. Cremer, *J. Phys. Chem. C*, 2007, **111**, 8916–8924.

59 J. Du, H. Willcock, J. P. Patterson, I. Portman and R. K. O'Reilly, *Small*, 2011, **7**, 2070–2080.

60 L. D. Blackman, M. I. Gibson and R. K. O'Reilly, *Polym. Chem.*, 2017, **8**, 233–244.

61 M. I. Gibson and R. K. O'Reilly, *Chem. Soc. Rev.*, 2013, **42**, 7204–7213.

62 D. J. Phillips and M. I. Gibson, *Chem. Commun.*, 2012, **48**, 1054–1056.

63 G. Moad, Y. K. Chong, E. Rizzard, A. Postma and S. H. Thang, *Polymer*, 2005, **46**, 8458–8468.

64 S. Harrisson, *Macromolecules*, 2009, **42**, 897–898.

65 C. Schilli, M. G. Lanzendoerfer and A. H. E. Mueller, *Macromolecules*, 2002, **35**, 6819–6827.

66 N. S. Ieong, K. Bebis, L. E. Daniel, R. K. O'Reilly and M. I. Gibson, *Chem. Commun.*, 2011, **47**, 11627–11629.

67 D. J. Phillips and M. I. Gibson, *Polym. Chem.*, 2015, **6**, 1033–1043.

68 M. I. Gibson and R. K. O'Reilly, *Chem. Soc. Rev.*, 2013, **42**, 7204–7213.

69 S. Mendez, J. G. Curro, J. D. McCoy and G. P. Lopez, *Macromolecules.*, 2005, **38**, 174–181.

70 M. -Q. Zhu, L. -Q. Wang, G. J. Exarhos and A. D. Q. Li, *J. Am. Chem. Soc.*, 2004, **126**, 2656–2657.

71 http://go.warwick.ac.uk/XPS

72 D. J. Phillips and M. I. Gibson, *Biomacromolecules*, 2012, **13**, 3200–3208.

Chapter 3

3. Externally Controllable Glycan Presentation on Nanoparticle Surfaces to Modulate Lectin Recognition

3.1 Chapter summary

In this chapter, polymer tethered gold nanoparticles as a temperature-controlled colourimetric detector of target lectins based on the molecular recognition of galactose modified pHEA and the thermo-sensitivity based on the coil-to-globule phase transition of pNIPAM as a blocking agent will be reported.

3.2 Abstract

Nature dynamically controls carbohydrate expression on cells rather than static presentation. Here we report synthetic glycosylated nanoparticles that contain polymeric 'gates' to enable external control (*via* temperature changes) of glycan surface expression, as an alternative to enzymatic control in Nature. This approach offers a new dynamic multivalent scaffold for glycan recognition.

3.3 Introduction

Glycans (sugars) mediate a diverse range of biological recognition and signal transduction pathways and are implicated in diseases such as cancer (aberrant glycosylation) or as sites for pathogen adhesion. The 'readers' of glycosylation state are lectins; carbohydrate binding proteins which are neither antibodies nor enzymes.[1] The typical affinity for a glycan to a lectin is rather weak (K_d: ~ mM), so Nature presents multiple copies of glycans on cell surfaces to benefit from the cluster glycoside effect – a non-linear enhancement in binding affinity when multiple glycans are present in proximity to each other (K_d: ~ nM).[2] Inspired by this, multivalent systems such as polymers, peptides, surfaces or nanoparticles functionalised with glycans have been used to generate high avidity binders. Due to their high affinity, glycopolymers[3,4] have been explored as anti-adhesive agents against, HIV,[5] cholera,[6] Shiga toxins[7] and also to recruit growth factors to control stem cell fate[8] with affinities on the nM scale.

Despite this vast range of structures synthesized, most glycomaterials are static entities

with the sugars always accessible for binding. This is in stark contrast to cell-surface glycans which are highly dynamic with the glycans presented changing depending on disease state and for protein folding quality control.[9,10] Current synthetic materials do not enable control over glycan expression to be modulated, and hence do not fully mimic the natural environment. Dynamic chemical bonds have been used to generate glycopolymers which reconfigure due to the action of lectin binding (i.e. internal trigger), but not to an external trigger.[11,12,13] In contrast, externally addressable polymers (often termed as 'smart' or 'responsive') have been extensively studied where an external stimulus, such as light, heat, pH, radiation, metal ions *etc.*, can trigger a (reversible) change in material properties. In particular, thermo-responsive polymers have attracted attention as due to their easy synthesis and diverse range of applications from triggered cellular uptake, trypsin-free cell release[14] and drug delivery.[15] Polymers which display an LCST (lower critical solution temperature) undergo a chain collapse (soluble – insoluble) upon heating providing a macroscopic effect from the external trigger.[16,17] Typical thermo-responsive polymers with an LCST include poly(*N*-isopropylacrylamide) (pNIPAM) and poly[(oligoethylene glycol) methacrylates] (pOEGMAs) due to their transitions being close to 37 °C. Many other classes have been developed and extensively reviewed.[18,19] Immobilization of responsive polymers onto metal or soft nanoparticle enables dynamic control over aggregation state based on an external trigger.[20,21] Mastrotto *et al*. used pNIPAM collapse to expose folate moieties on gold nanoparticle surfaces to enable temperature triggered uptake into cancerous cell lines.[22] Temperature gating has also been used to control access to biotin functionality on glass surfaces.[23] Gold nanoparticles (AuNPs) are widely used due to their easy functionalization with thiols and unique optical properties which make them excellent contrast agents in electron microscopy, or dark

field microscopy, but also as colourimetric sensors due to the coupling of their SPR bands when aggregated leading to a red-blue colour shift.[24] Immobilization of glycans onto AuNPs has been used as biosensors. Field *et al,* used α2,6-thio-linked sialic acid to detect human influenza,[25] and Richards *et al.* have used glycosylated gold nanoparticles libraries as multiplex sensors.[26]

Considering the above, we reasoned that if a nanoparticle surface could be formulated correctly, a responsive polymer could be used as an externally addressable 'gate' which upon application of a stimulus, is 'opened' (*via* chain collapse) to enable access to a glycan and hence enable binding. This can be considered as a synthetic alternative to enzyme expression levels, which *in vivo* control glycan expression based upon biological triggers.

3.4 Result and Discussion

To provide the desired gating mechanism on the nanoparticle surface pNIPAM was selected as the thermo-responsive polymer due to its well characterised switchable behaviour and high grafting density onto gold.[27] Well-defined poly(hydroxyethyl acrylamide) (pHEA) was selected as a non-responsive co-coating as we have previously demonstrated it to be an excellent stabilizing polymer for glyco-nanoparticles.[28] RAFT (reversible addition fragmentation chain transfer) polymerization[29] was employed as it enables control over molecular weight and also installs sulfur containing end-groups. Finally, nucleophiles treated pNIPAM and glycan modified pHEA (glycans act as nucleophiles through post-polymerization modification process) were achieved as an outcome of trithiocarbonate end-group removal and these thiol functionalised polymers allow direct conjugation onto AuNPs[29] as shown in Scheme 3.1.

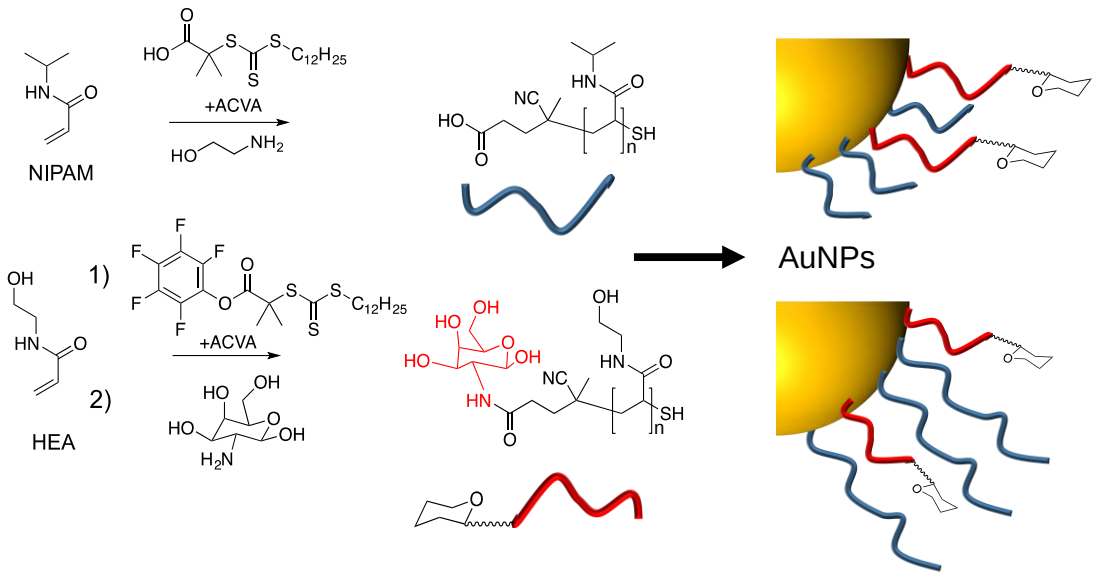

Scheme 3.1 Synthesis of polymers by RAFT polymerization and polymer conjugation onto AuNPs.

pHEA was synthesized using a pentafluorophenyl (PFP) ester RAFT agent, which enabled quantitative installation of 2-deoxy, 2-amino galactose post-polymerization, confirmed by ^{19}F NMR (Figure 3.1) and FT-IR. Infrared analysis of pHEA was conducted before and after reaction of pentafluorophenol end-group with galactosamine. Disappearance of C=O at around 1750 cm^{-1} attributable to the carbonyl associated with the PFP end-group being removed as shown in Figure 3.2.

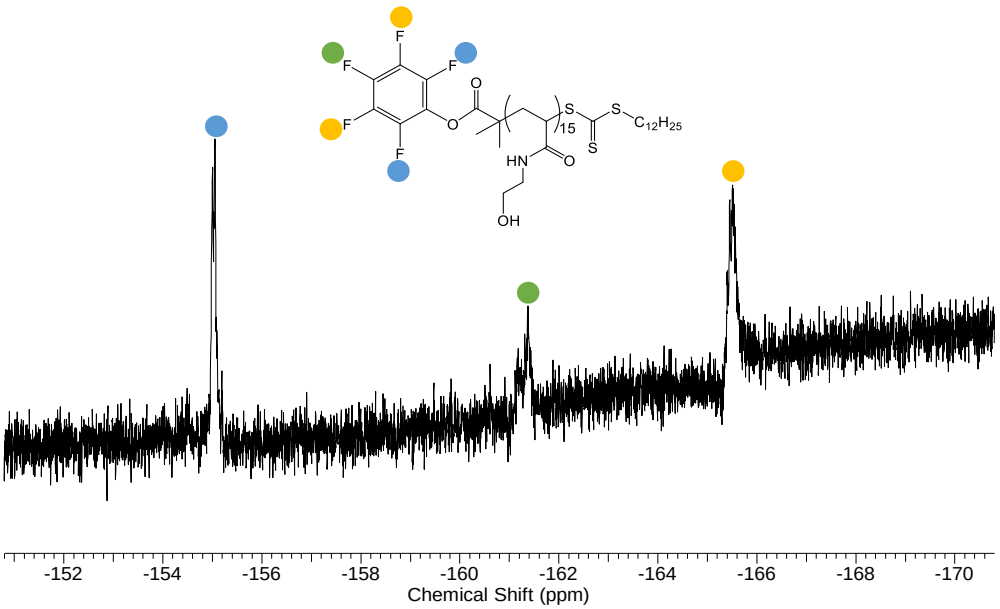

Figure 3.1 ^{19}F NMR spectra of PFP-pHEA$_{15}$.

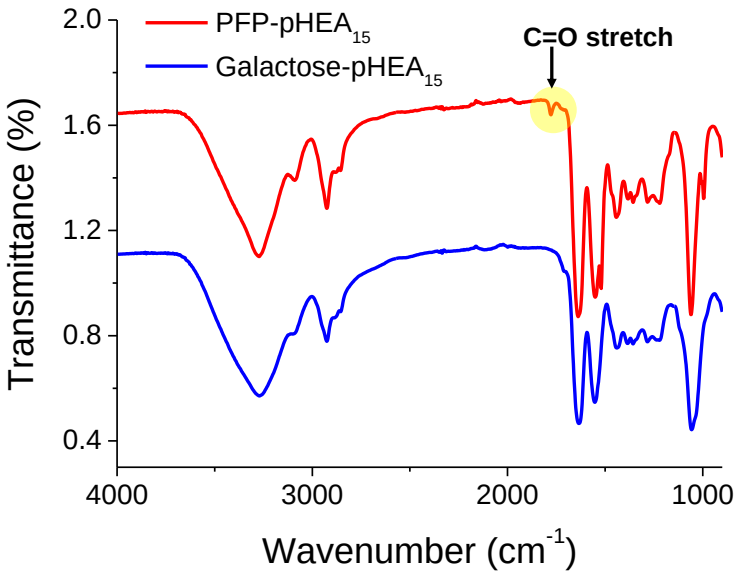

Figure 3.2 Infrared spectra of PFP-pHEA (red) and galactosamine-pHEA (blue).

Well-defined pHEA with DP = 15 was synthesised, along with two different pNIPAMs with DP 25 or 50, confirmed by size exclusion chromatography (SEC) and NMR, as shown in Table 3.1 and Figure 3.3. Molecular weight of all polymers determined by SEC are slightly higher than the theoretical values (were in decent agreement with the theoretical values), indicating well-defined polymerization with narrow poly dispersity below 1.1. As expected, the pNIPAMs displayed a lower critical solution temperature in solution (Table 3.1) of approximately 36 °C, which is essential for the gating concept, (below). All polymers were purified by dialysis against water prior to use.

Table 3.1 Polymer used in this study.

Polymer	**[M]/[CTA]/[I]**	**$M_{n\ Target}$**	**Conversion[a)]**	**$M_{n\ Theo}$[b)]**	**$M_{n\ SEC}$[c)]**	**M_w/M_n**	**Cloud Point[d)]**
	[mol]	**[gmol^{-1}]**	**[%]**	**[gmol^{-1}]**	**[gmol^{-1}]**	**[-]**	**[°C]**
pNIPAM$_{25}$	25/1/0.2	3200	87 %	2800	2900	1.07	36
pNIPAM$_{50}$	50/1/0.2	6000	86 %	5200	7100	1.10	38
PFP-pHEA$_{15}$	15/1/0.2	2300	93 %	2100	4800	1.10	-

pNIPAM$_{xxx}$ / pHEA$_{xxx}$ = poly(*N*-isopropylacrylamide) / poly(hydroxyethyl acrylamide) where average degree of polymerization indicated by xxx; [a)]Determined ^{1}H NMR; [b)]Calculated from the [monomer]:[CTA] ratio and of conversion; [c)]Determined by SEC in DMF using PMMA standards; [d)]Cloud point was measured in water upon heating from 25 °C to 80 °C, 1.0 mg mL^{-1} polymer concentration.

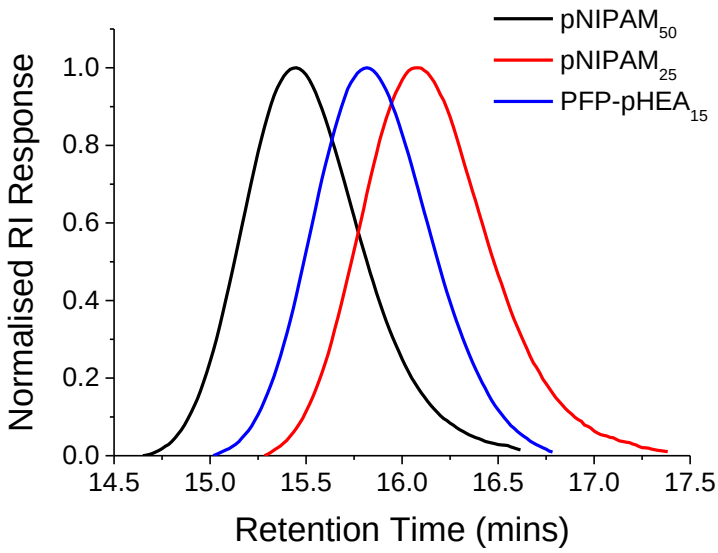

Figure 3.3 SEC analysis of polymer.

The gating concept, whereby increasing the temperature leads to selective collapse of the pNIPAM chains and consequently exposing the glycan is shown in Scheme 3.2. The polymer coatings had to fulfil several criteria for this concept to be successful i) long enough to promote colloidal stability; ii) correct ratio of responsive and glycan bearing polymer to ensure multivalent enhancement, but retain colloidal stability after pNIPAM collapse; iii) provide enough steric bulk to block glycan access below collapse temperature.

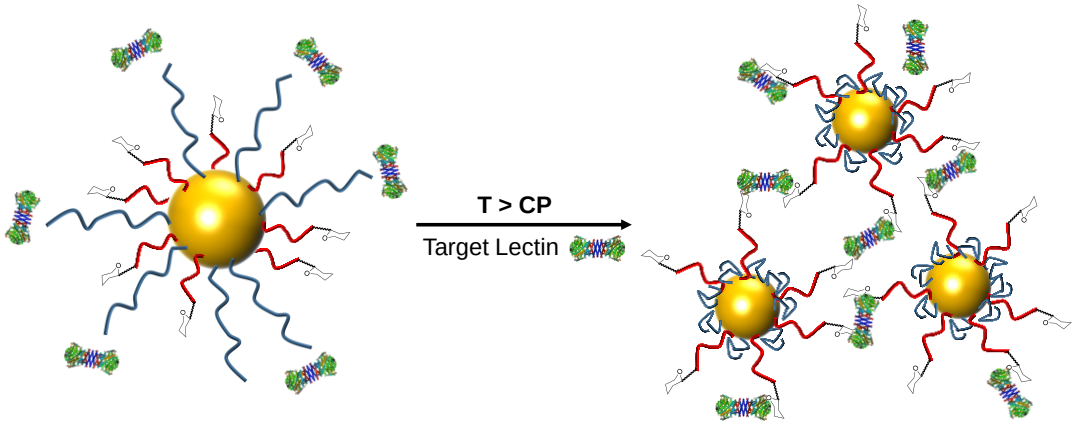

Scheme 3.2 Concept of using responsive polymers to gate access to nanoparticles. Below the LCST of pNIPAM steric hindrance prevents lectin binding to glycans, but above the LCST, the polymer collapse to expose glycans enabling binding and aggregation of the particles.

The thiol-terminated $pHEA_{15}$-Gal (galactose functional pHEA) and pNIPAM with different molar ratio was attached onto pre-formed gold nanoparticles directly by a simple mixing procedure and excess polymer removed by centrifugation-resuspension dialysis. The increase in diameter and red-shifted spectrum of wavelength measured by both DLS and UV-Vis spectrum indicating that gold nanoparticles (in 4-(2-Hydroxyethyl)piperazine-1-ethanesulfonic acid, N-(2-Hydroxyethyl)piperazine-N′-(2-ethanesulfonic acid) (HEPES) buffered solution) successfully functionalised by each polymer as shown in Table 3.2.

Table 3.2 Gold nanoparticles with pHEA-Gal and pNIPAM functionalisation.

Particle	**SPR $_{particle}$ [nm][a)]**	**Diameter [nm][b)]**	**Cloud point $_{HEPES}$ [°C][c)]**
Bare gold 40 nm	527	42	-
pHEA$_{15}$-Gal@Au40	530	50	-
Bare gold 60 nm	534	58	-
pHEA$_{15}$-Gal@Au60	537	66	-
pNIPAM$_{25}$@Au60	537	64	64
pHEA$_{15}$-Gal(2)/pNIPAM$_{25}$(8)@Au$_{60}$	537	64	67
pHEA$_{15}$-Gal(5)/pNIPAM$_{25}$(5)@Au$_{60}$	537	66	72
pHEA$_{15}$-Gal(8)/pNIPAM$_{25}$(2)@Au$_{60}$	538	66	78
pNIPAM$_{50}$@Au60	538	75	61
pHEA$_{15}$-Gal(8)/pNIPAM$_{50}$(2)@Au$_{60}$	538	68	50
pHEA$_{15}$-Gal(9)/pNIPAM$_{50}$(1)@Au$_{60}$	538	67	52

[a)]SPR maximum of gold nanoparticles after coating with polymer; [b)]Z-average diameter determined by DLS; [c)]Cloud point was measured in HEPES buffer upon heating from 25 °C to 80 °C, 0.057 mg mL^{-1} total particle concentration. The CP (cloud point) of particles defined as being the point of 50% transmittance by UV-Vis spectroscopy.

In addition, CPs of each particle was determined by turbidimetry curves using UV-vis. We observed each pNIPAM coated gold nanoparticle has over 60 °C of CPs, whereas glycopolymer coated nanoparticle has no CP due to its none-thermal responsivity (see Figure 3.4). From particles characterisation, our polymer coated particles are stable at saline condition in HEPES buffer confirmed by no aggregates of particles and no changes of UV-vis absorbance peaks even after long period of incubation (data not shown).

Also, particles are perfectly matched to this work because if gold particles are decorated with both thermo-responsive pNIPAM and non-thermal responsive $pHEA_{15}$-Gal, then CP of particles would be increased above only pNIPAM coated gold particles CPs (higher than 60 °C). But unlike our expectation, both $pHEA_{15}$-Gal and $pNIPAM_{50}$ (9:1 molar ratio) coated 60 nm sized gold nanoparticle has a lower CP of 52 °C, compared to the pNIPAM coated particles. However, the CP is the temperature where the particles aggregate, and the actual collapse of the pNIPAM will occur below this. The data (below) shows that the desired switching behaviour between 20 and 40 ^{o}C can occur, even though the observed $pHEA_{15}$-Gal(9)/$pNIPAM_{50}$ particle's CP (52 °C). This is a crucial component of our system, to ensure there are no false positives due to temperature induced particle aggregation, rather than the desired glycan-induced assembly.

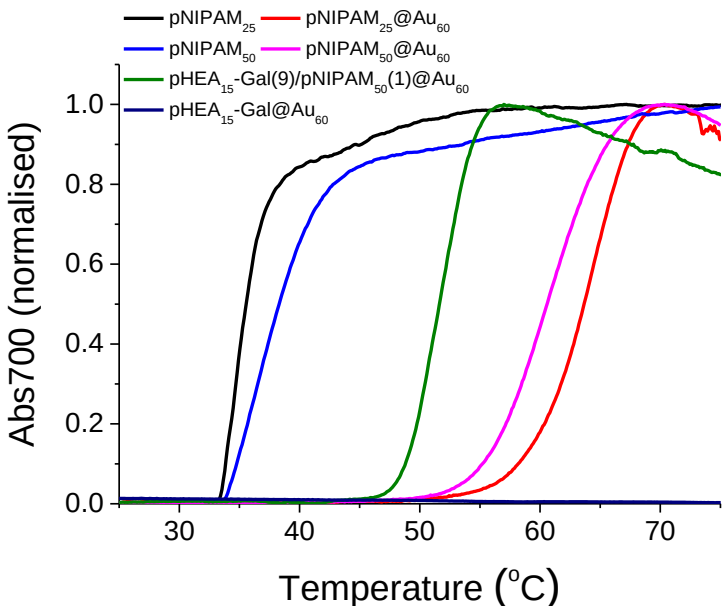

Figure 3.4 Turbidimetry scans (absorbance at 700 nm) of pure pNIPAMs (1.0 mg mL^{-1}) and polymer functionalised gold nanoparticles (0.057 mg mL^{-1}).

At the very first stage, 40 and 60 nm sized gold nanoparticles were functionalised with only $pHEA_{15}$-Gal to confirm the gold core size dependency for protein binding

efficiency. These particles were evaluated for binding with Soybean agglutinin (SBA) which has a preference for GalNAc binding and as it has 2 binding sites,[30] can hence lead to aggregation of glycosylated gold nanoparticles (glycoAuNPs). The binding interaction result in crosslink (aggregation) of particles and can be confirmed by analysis of the red to blue solution colour change and UV-spectra shifts due to coupling of the particle SPR bands, as shown in Figure 3.5. Both 40 and 60 nm particles were rapidly aggregated and changed solution colour from red to blue upon addition of highest concentration of SBA (10^{-2} mg mL^{-1}). This leads to significant change of the SPR peak to broader peak and longer wavelength in UV-vis spectrum. However, core 60 nm gold nanoparticles clearly showed dose-dependent response to the serial SBA dilution through increasing in absorbance at 700 nm than 40 nm core gold nanoparticles (see Figure 3.5B). This initial screens using $pHEA_{15}$-Gal coated nanoparticles in lectin aggregation assays indicated that 60 nm nanoparticles gave larger and faster responses than 40 nm particles due to theoretically higher grafting density for larger particle and hence is the diameter used from this point onwards.[28]

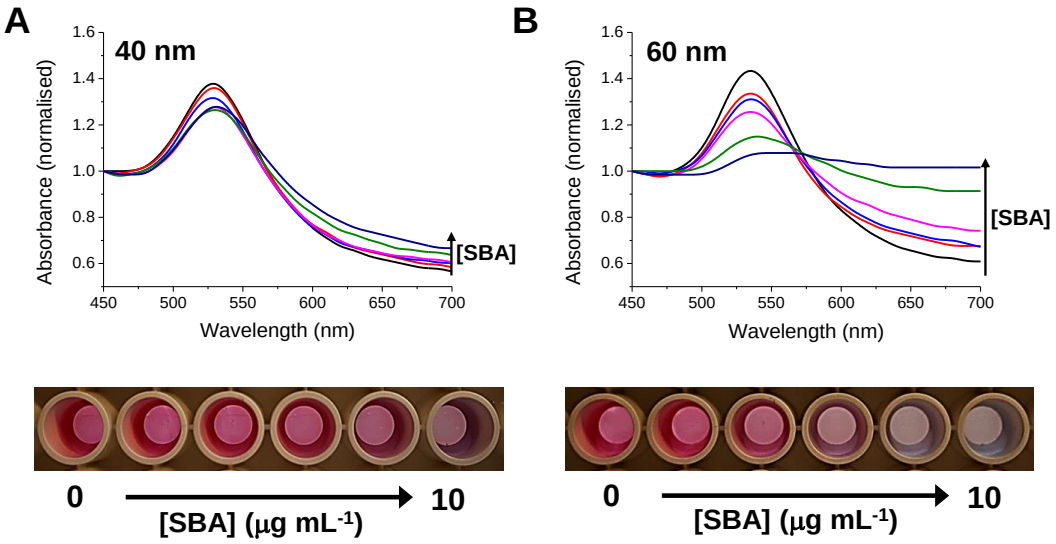

Figure 3.5 UV-vis spectrum and photographs of colour changes of $pHEA_{15}$-Gal coated A) 40 nm and B) 60 nm sized gold nanoparticles upon addition of serial dilution of SBA (0 – 10 μg mL^{-1}) following 30 mins of incubation at 20 °C.

To investigate the morphology of particle aggregation, TEM analysis was conducted. TEM images of Figure 3.6A and 3.6C clearly prove that $pHEA_{15}$-Gal coated gold nanoparticles have high colloidal stability at both 20 °C and 40 °C without addition of SBA and hence that any pNIPAM collapsed does not lead to aggregation for these mixed nanoparticles. Figure 3.6B shows the morphology of particle aggregates due to SBA particle binding at 20 °C. Also, the function (glycan binding) of SBA was not affected by the increased temperature to 40 °C as shown in particle aggregates of Figure 3.6D .

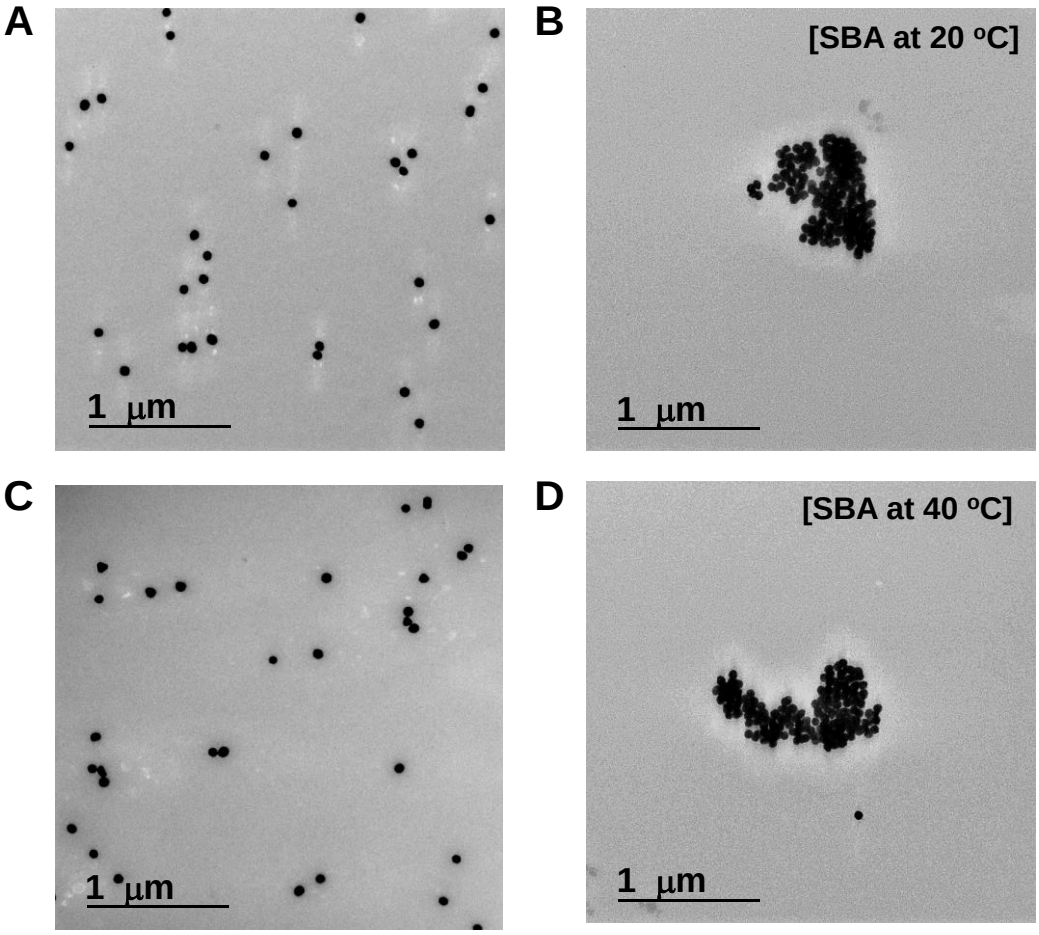

Figure 3.6 TEM images of $pHEA_{15}$-Gal coated 60 nm gold nanoparticles A), C) non-aggregation without SBA B), D) aggregation with SBA (10 μg mL^{-1}) following 30 minutes of incubation at 20 °C and 40 °C, respectively.

X-ray photoelectron spectroscopy (XPS) was used to provide additional chemical characterisation of the grafting-to success, as shown in Table 3.3 and Figure 3.7. The appearance of nitrogen and sulphur peaks which are not present in the citrate-stabilised precursor particles demonstrates addition of the polymers. No significant differences in density were seen between the polymers used on their own, suggesting that the feed ratio will be close to the obtained ratio on the particle surface. It is important to note that we cannot obtain exact polymer grafting densities for the particle from the XPS analysis in this study. Assuming 0.3 chains nm^{-2} from thermogravimetric analysis (TGA) in the previous work in a similar manner to producing thermo-responsive particle,[31] this gives ~ 3000 chains of polymer ($0.3 \times 4\pi r^2$) per gold nanoparticle.

Table 3.3 XPS elemental ratios for polymer/gold hybrid nanoparticles (normalised to gold signal).

Sample	Au 4f [%]	C 1s [%]	O 1s [%]	N 1s [%]	S 2p [%]
$pHEA_{15}$-Gal (9) / $pNIPAM_{50}$ (1) @Au_{60}	0.35	57.76	34.92	6.18	0.79
$pHEA_{15}$-Gal (9) @Au_{60}	0.52	60.54	34.37	3.75	0.81
$pNIPAM_{50}$ (1) @Au_{60}	1.48	64.37	27.87	5.77	0.50

Sample	Au 4f [%]	C 1s [%]	O 1s [%]	N 1s [%]	S 2p [%]
$pHEA_{15}$-Gal (9) / $pNIPAM_{50}$ (1) @Au_{60}	1.00	165.03	99.77	17.66	2.26
$pHEA_{15}$-Gal (9) @Au_{60}	1.00	116.42	66.10	7.21	1.56
$pNIPAM_{50}$ (1) @Au_{60}	1.00	43.49	18.83	3.90	0.34

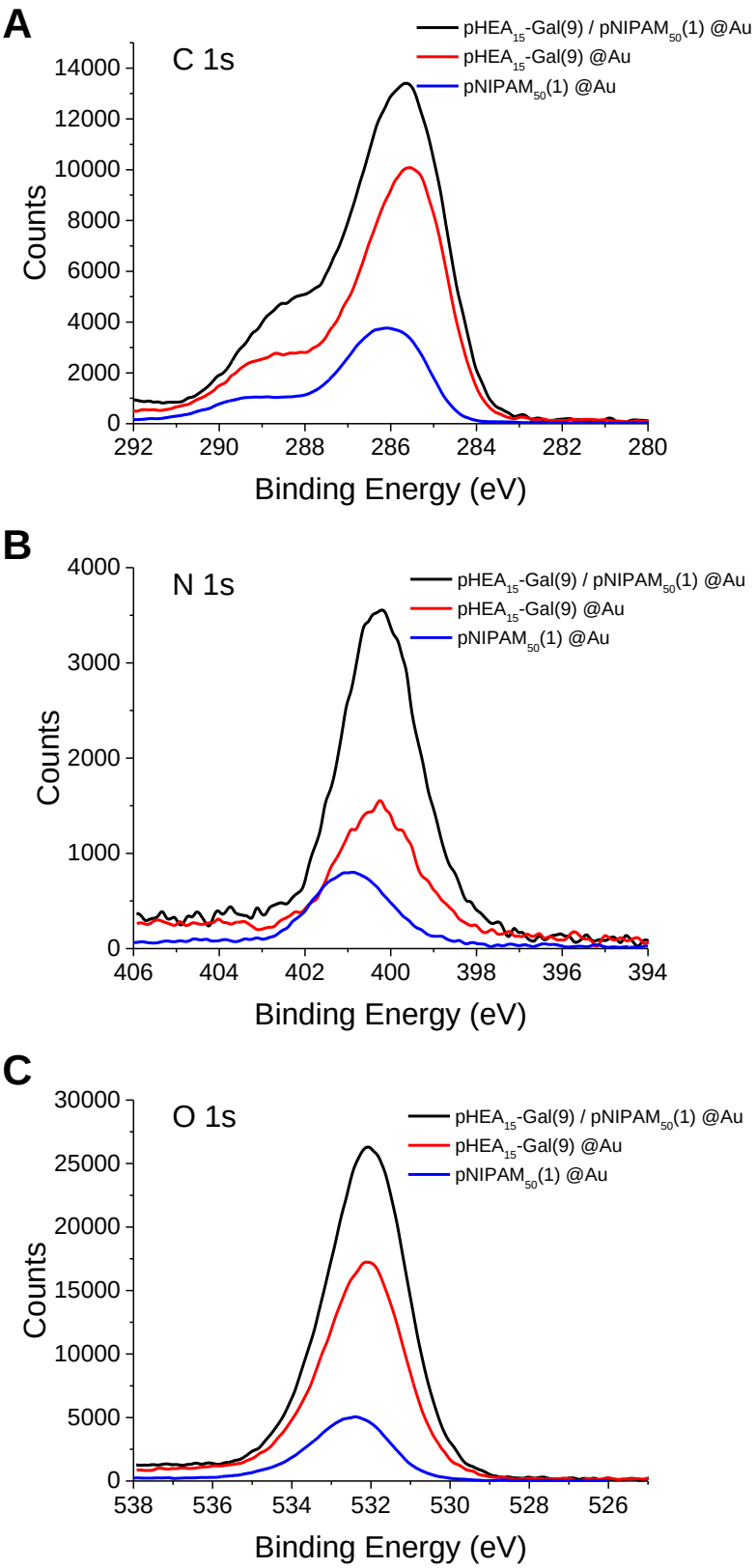

Figure 3.7 X-ray photoelectron spectroscopy analysis of polymer functionalised gold nanoparticles. Representative high-resolution XPS spectrum of C1s, N1s and O1s region after $pHEA_{15}$-Gal (9)-$pNIPAM_{50}$ (1); $pHEA_{15}$-Gal; $pNIPAM_{50}$ conjugation. A) Carbon (C1s) peak, B) nitrogen (N1s) peak and C) Oxygen (O1s) peak from the XPS analysis of polymer/gold hybrid nanoparticles (normalised to gold signal).

In a first series of experiments $pHEA_{15}$-Gal was mixed with $pNIPAM_{25}$ in three different molar ratios of 8:2, 5:5 and 2:8 used to functionalise 60 nm AuNPs. Particle responses were measured by UV-vis after 30 mins incubation at 20 °C and 40 °C (i.e. above and below the collapse temperature of pNIPAM) in the presence of SBA. Spectra are shown for 2:8 and 5:5 molar ratio of $pHEA_{15}$-Gal and $pNIPAM_{25}$ particles at both different temperature (see Figure 3.8). From this result, the fraction of pHEA-Gal is too small, relative to pNIPAM to enable SBA-induced aggregation and that the gating concept requires precision tuning of the glycan/blocking polymer ratio.

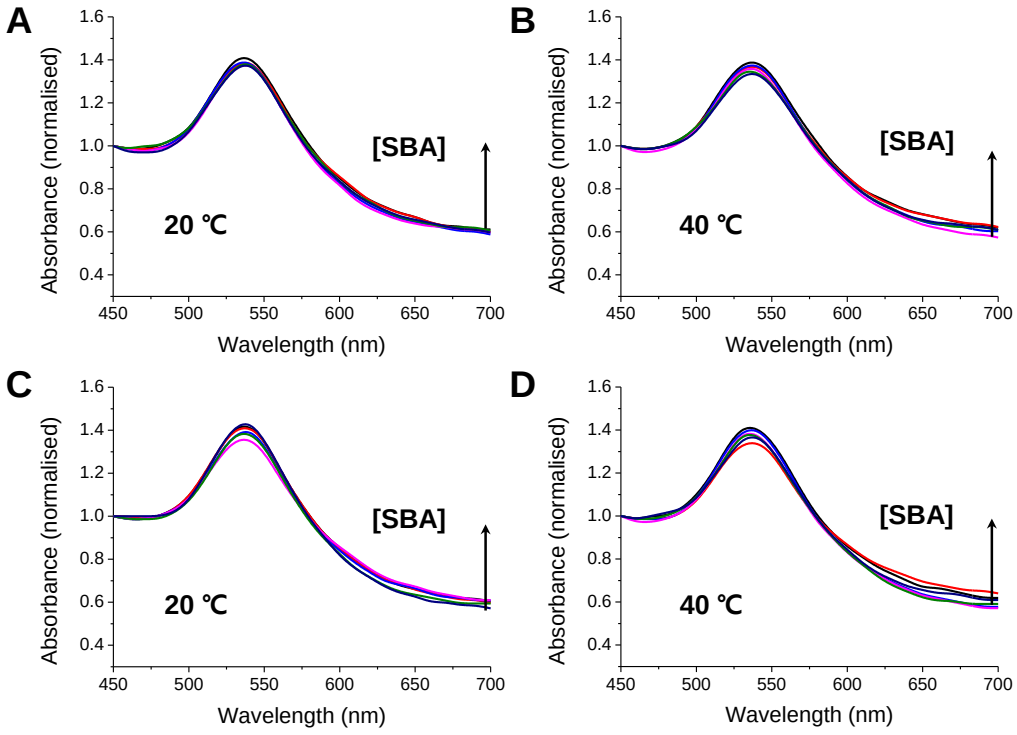

Figure 3.8 UV-Vis traces of different nanoparticle formulations in presence of serial dilution of SBA (0 – 0.01 mg mL^{-1}) after 30 minutes incubation. Gold particles (60 nm) had [$pHEA_{15}$-Gal]:[$pNIPAM_{25}$] 2:8 at 20 °C A) and 40 °C B); [$pHEA_{15}$-Gal]:[$pNIPAM_{25}$] 5:5 at 20 °C C) and 40 °C D). An increase in Abs_{700} and decrease in Abs_{540} is indicative of binding. All curves normalise so Abs_{450} = 1. Arrow indicates increase concentration.

With 8:2 molar ratio of $pHEA_{15}$-Gal and $pNIPAM_{25}$ coating, addition of SBA at either 20 or 40 °C leads to a clear change in colour from red to blue, with a shift in the Abs_{max} to longer wavelengths. This indicated that the $pNIPAM_{25}$ provided an insufficient steric block due to short polymer chain length and that the Gal-residues were accessible at both temperatures as shown in Figure 3.9A and B. This shows that as well as density, the relative chain lengths of the polymers are crucial to get the dynamic surface coatings.

Switching to the $pNIPAM_{50}$ (8:2 molar ratio of $pHEA_{15}$-Gal:$pNIPAM_{50}$) coating, and again exposing to SBA showed no interaction with SBA after 30 minutes incubation at 20 °C showing that this polymer was sufficiently bulky to limit access to the Gal residues (Figure 3.9C). Upon increasing the temperature to 40 °C, in the presence of SBA, there was a small, but significant shift in the UV-Vis spectra of Figure 3.9D with an increase at 700 nm and decrease at 540 nm indicative of lectin binding and aggregation. This clearly demonstrated that the concept of responsive gating to glycan access could be achieved, but that the surface coating has to be precisely tuned to achieve the balance required. Further optimisation studies revealed that changing the ratio of $pHEA_{15}$-Gal : $pNIPAM_{50}$ from 8:2 to 9:1 provided the optimum balance between glycan affinity (i.e. aggregation) and switchability.

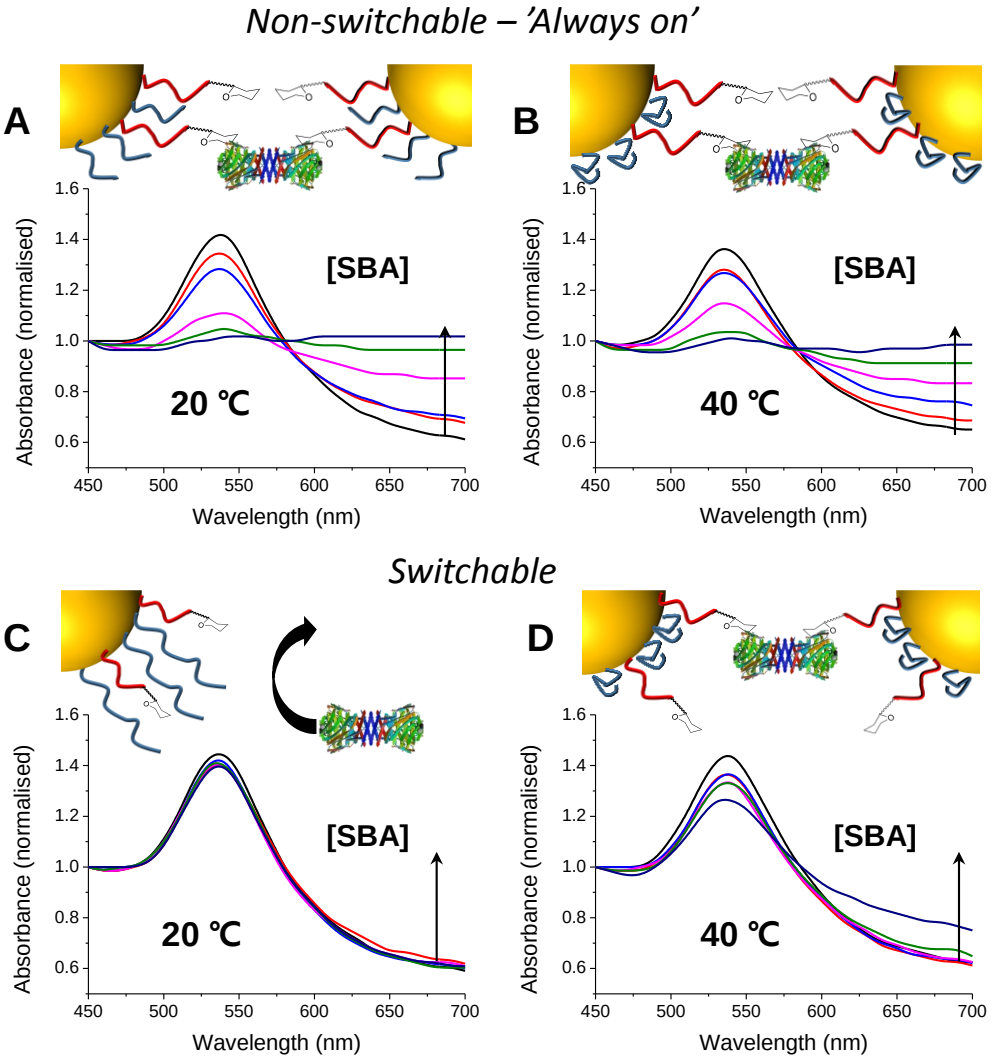

Figure 3.9 UV-Vis traces of different nanoparticle formulations in presence of serial dilution of SBA (10 – 1 μg mL^{-1}) after 30 minutes incubation. All particles (60 nm) had [$pHEA_{15}$-Gal]:[$pNIPAM_x$] 8:2. $pNIPAM_{25}$ at 20 °C A) and 40 °C B); $pNIPAM_{50}$ at 20 °C C) and 40 °C D). An increase in Abs_{700} and decrease in Abs_{540} is indicative of binding. All curves normalise so Abs_{450} = 1. Arrow indicates increase concentration.

To ensure the changes seen were due to particle aggregation (indicative of lectin-cross-linking), SBA binding was investigated using dynamic light scattering and transmission electron microscopy (TEM) Figure 3.10. The optimised nanoparticle formulation (above) was incubated with SBA at both 20 and 40 °C for 30 minutes and the observed hydrodynamic diameters shown in Figure 3.10A and B. At 20 °C, in the presence of various concentrations of SBA, there was no change in hydrodynamic diameter from the initial 60 nm. At 40 °C, with no SBA added, the particles were stable with the initial diameter of ~ 80 nm (due to some surface reconfiguration compared to at 40 °C) being retained, in agreement with the UV-Vis data. Following 30 minutes of incubation there was a clear dose-dependent increase in the aggregate size as [SBA] was increased, again supporting the hypothesis that the pNIPAM is gating access to the glycan. TEM analysis was also conducted to provide direct evidence of temperature triggered lectin/particle agglutination. Figure 3.10C shows nanoparticles plus SBA at 20 °C, which are clearly well-dispersed and Figure 3.10D shows the aggregates which form upon heating to 40 °C only in the presence of SBA.

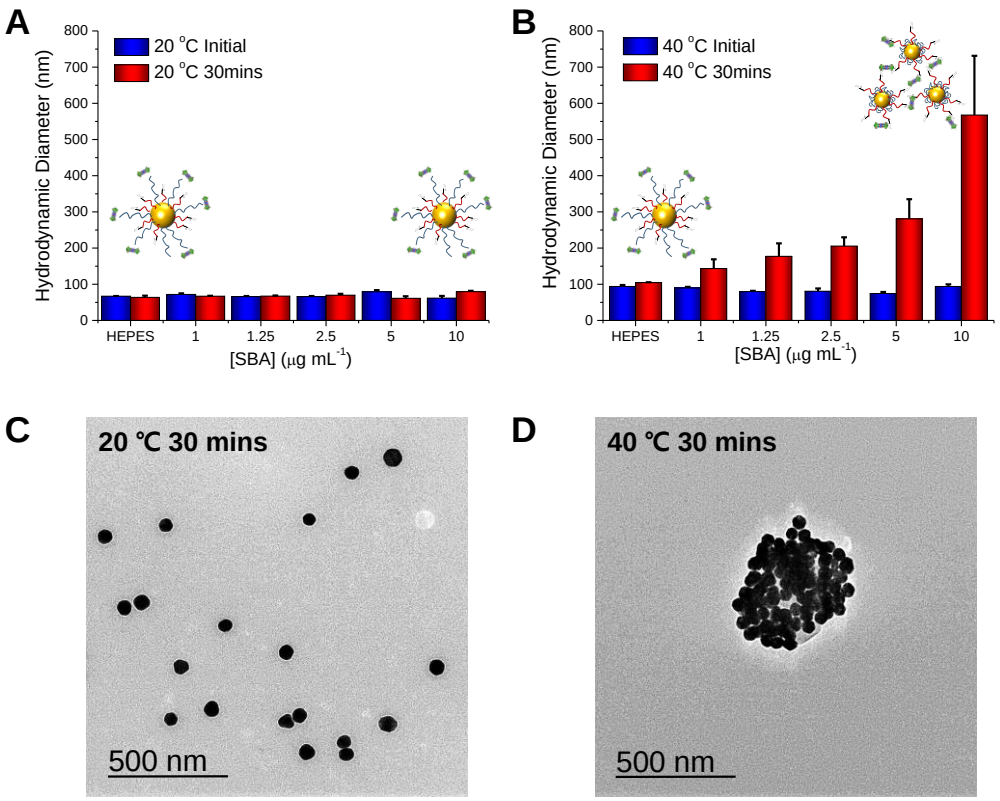

Figure 3.10 Dynamic light scattering (DLS) analysis of thermally gated lectin binding. $pHEA_{15}$-Gal:$pNIPAM_{50}$ ratio 9:1 @$AuNP_{60}$. A) Hydrodynamic diameter at 20 °C initially, and after 30 minutes incubation with SBA; B) Hydrodynamic diameter at 40 °C, initially and after 30 minutes incubation with SBA. All results are mean from a minimum of 3 independent repeats. TEM images of these particles after addition of SBA (10 μg mL^{-1}): C) at 20 °C for 30 mins; D) at 40 °C following 30 minutes incubation.

As a final test of the system, the optimised nanoparticle formulation (with the 9:1 ratio of $pHEA_{15}$-Gal:$pNIPAM_{50}$) was interrogated with a panel of lectins, with different binding specificities[32] at both 20 °C and 40 °C. SBA, Wheat germ agglutinin (WGA), *Ulex europaeus* agglutinin (UEA) and *Ricinus communis* agglutinin 120 (RCA_{120}) were employed. At 20 °C there was no measurable change in UV-Vis spectra of Figure 3.11 upon incubation with SBA, WGA, UEA or RCA_{120} lectins, indicating that the glycan is sterically shielded against all the lectins.

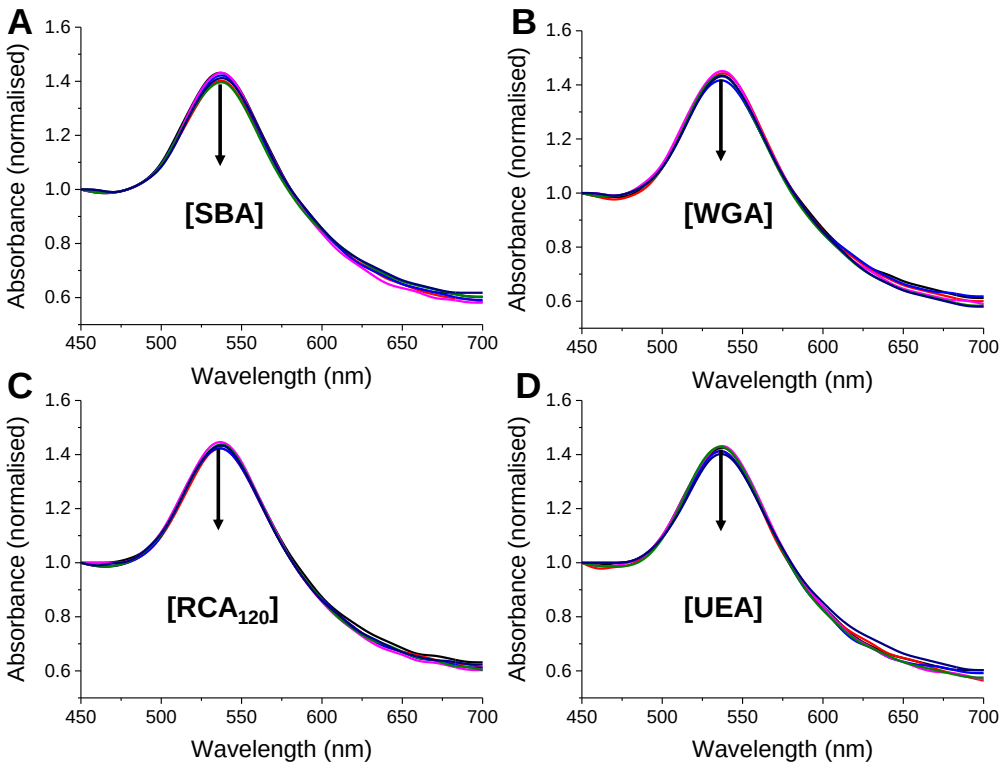

Figure 3.11 Assessment of specificity of thermally gated nanoparticles to a panel of lectins. Lectin concentration is 1 – 10 μg mL^{-1}. A – D) show UV-Visible traces (normalised to Abs_{450}) following 30 minutes incubation at 20 °C with indicated lectin. Arrow indicates increase concentration.

Increasing the temperature to 40 °C, however, lead to clear changes in the UV-Vis spectra for SBA, RCA_{120} and WGA as would be expected with their known affinities for Gal (or GalNAc/GluNAc for WGA) as shown in Figure 3.12. The control lectin UEA, which has specificity for fucose residues did not bind at any temperature, proving the specificity of the interaction and that temperature-induced aggregation is not a factor. A partial isotherm showing the relative changes is included in the supporting information as a measure of the relative affinity, in the order SBA>WGA~RCA_{120}>>>UEA.

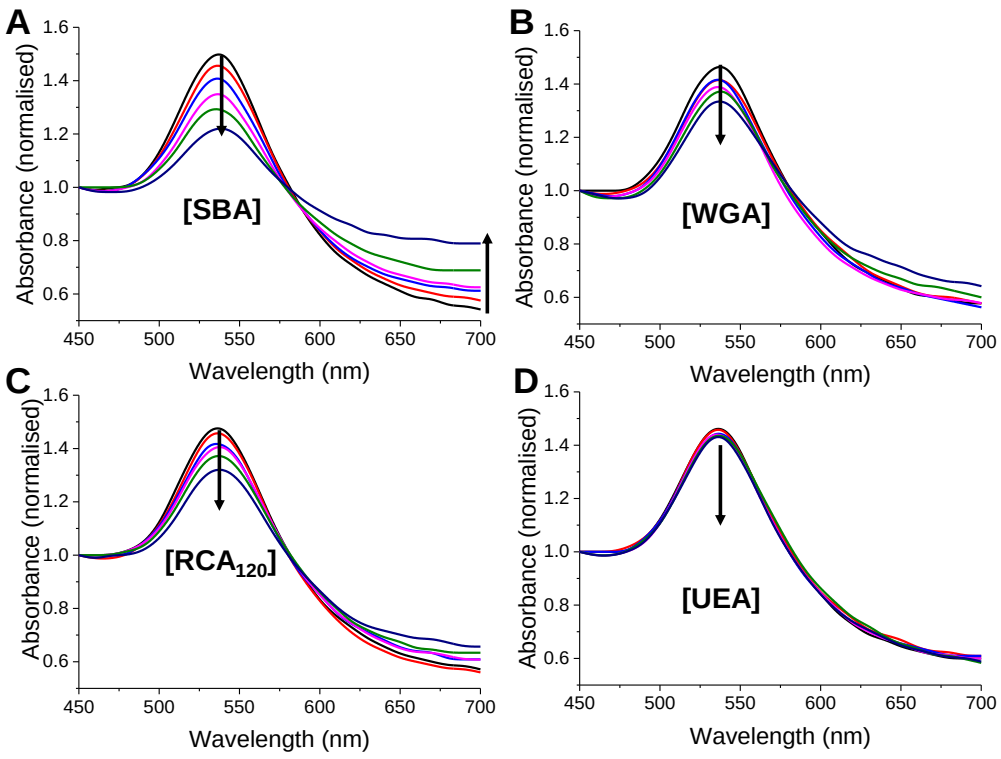

Figure 3.12 Assessment of specificity of thermally gated nanoparticles to a panel of lectins. Lectin concentration is 1 – 10 μg mL^{-1}. A – D) show UV-Visible traces (normalised to Abs_{450}) following 30 minutes incubation at 40 °C with indicated lectin. Arrow indicates increase concentration.

To test the specificity of the glyco-particle interactions, and rule out non-specific protein binding, control experiments were conducted using Bovine serum albumin (BSA) as a non-carbohydrate binding protein (Figure 3.13). Non responsive, galactosylated pHEA coated particles were incubated with a serial dilution of BSA and the UV-Vis spectra recorded, showing no change. Accordingly, the same experiment was undertaken with the pNIPAM containing particles at both low and high temperature (i.e. where we see activation towards lectin binding). No change was seen indicating there was no aggregation induced by non-specific effects. The ability to control glycan expression would be a powerful tool for studying the role of multivalency intracellularly, where the glycan is only exposed when trafficked to the desired location, potentially provided spatiotemporal control. They could also be used as new biomolecular logic gates.

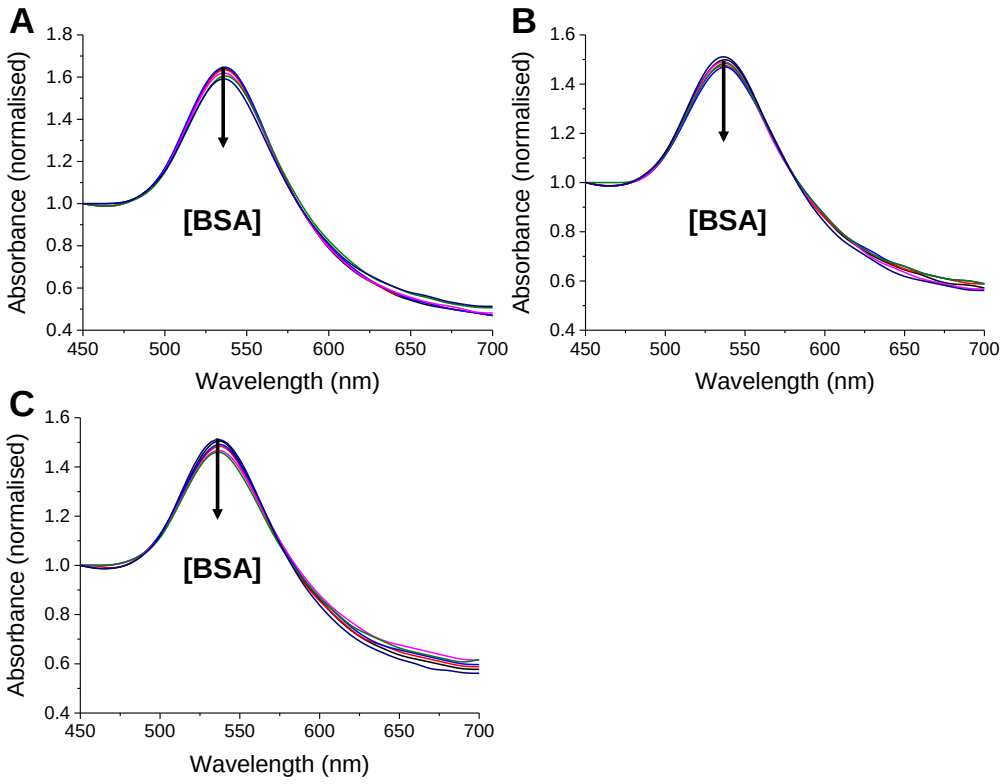

Figure 3.13 Control experiments for non-specific interactions with non-carbohydrate binding protein, BSA. A) $pHEA_{15}$-Gal@Au_{60} at 20 °C; B) $pHEA_{15}$-Gal (9)-$pNIPAM_{50}$(1) @Au_{60} at 20 °C; C) $pHEA_{15}$-Gal (9)-$pNIPAM_{50}$(1) @Au_{60} at 40 °C.

3.5 Conclusions

In summary, we have demonstrated a new concept in glyco-engineering where responsive polymer surfaces, rather than external enzyme expression levels, control the display of sugars on the surface of a nanoparticle, which could be considered a simple cell mimetic. The ‘gate’ pNIPAM had to be added in a relatively low ratio compared to the glycan-bearing polymer to ensure a binary on/off effect, with significant lectin binding above the pNIPAM LCST observed. The specificity of the GlycoAuNP was confirmed against a panel of lectins, with glycan expression only being induced above the critical temperature. The complex function of this relatively simple system with in-built optical outputs (AuNP colour changes) is highly versatile and presents a new method to dynamically control glycan expression using fully synthetic systems. By controlling presentation on the AuNP surface with an external trigger, we can envisage this being used as a tool to probe glycan function under very controlled environments, including intracellularly and could be considered a molecular ‘AND’ gate. Furthermore, the pNIPAM collapse could be replaced with a range of other stimuli responsive polymers, to enable biochemical rather than temperature trigger to probe more complex cellular environments.

3.6 Experimental Section

3.6.1 Materials

All chemicals were used as supplied unless otherwise stated. Methanol, hexane, hydrochloric acid, dichloromethane, toluene, acetone, tetrahydrofuran and diethyl

ether were purchased from Fisher Scientific at laboratory reagent grade. Deuterochloroform (99.9 atom % D), Deuteromethanol (99.5 atom % D), 4,4'-azobis(4-cyanovaleric acid) (> 97.0 %), dodecane thiol (≥ 98.0 %), potassium phosphate tribasic (reagent grade, ≥ 98.0 %), carbon disulfide (≥ 99.9 %), 2-bromo-2-methylpropionic acid (98.0 %), *N*-isopropylacrylamide (97.0 %), hydroxyethylacrylamide (97.0 %), *N*-(3-dimethylaminopropyl)-*N'*-ethylcarbodiimide hydrochloride (98.0 %), ethanolamine (≥ 99.0 %), magnesium sulfate (≥ 99.5 %) and mesitylene (analytical standard) were all purchased from Sigma-Aldrich. 4-(Dimethylamino)pyridine (99.0 %), pentafluorophenol (99.0 %) and trimethylamine (99.0 %) were purchased from Acros. Clear, polystyrene, flat-bottom, half-area 96-well microtiter plates were purchased from Greiner Bio-one. 10 mmol 4-(2-Hydroxyethyl)piperazine-1-ethanesulfonic acid, *N*-(2-Hydroxyethyl)piperazine-*N'*-(2-ethanesulfonic acid) (HEPES) buffer containing 0.15 M NaCl, 0.1 mM $CaCl_2$ and 0.01 mM $MnCl_2$ (pH 7.5, HEPES) was prepared in 200 mL of milliQ water (with a resistance of 18.2 MΩ cm). Gold nanoparticle solutions for 40 nm (0.296 mmol L^{-1}) and 60nm (0.288 mmol L^{-1}) were purchased from BBI Solutions. Soybean Agglutinin, *Ricinus Communis* Agglutinin, *Ulex Europaeus* Agglutinin, Wheat Germ Agglutinin and Bovine serum albumin were purchased from Vector Labs. D-Galactosamine Hydrochloride was purchased from Carbosynth Ltd.

3.6.2 Analytical and physical methods

^{1}H, ^{13}C and ^{19}F NMR spectra were recorded for analysis of monomer conversions and polymer compositions on Bruker HD-300 and HD-500 spectrometer using deuterated solvents obtained from Sigma-Aldrich. All chemical shifts are reported in ppm (δ)

relative to tetramethylsilane (TMS). FTIR spectra were acquired using a Bruker Vector 22 FTIR spectrometer with a Golden Gate diamond attenuated total reflection cell. A total 64 (or 128) scans with resolution of 4 cm^{-1} were collected. Samples were pre-dried as a thin film for FTIR analysis. SEC analysis was conducted on Varian 390-LC MDS system equipped with a column, two PL-AS RT/MT auto sampler, a PL-gel 3 mm (50 × 7.5 mm) guard column, two PL-gel 5 mm (300 × 7.5 mm) mixed-D columns using dimethylformamide (DMF) with 1 mg mL^{-1} LiBr at 50 °C as the eluent at a flow rate of 1.0 mL min^{-1}. The GPC system was equipped with ultraviolet (UV) (set at 280 nm) and differential refractive index (DRI) detections. Narrow molecular weight poly(methyl methacrylate) (PMMA) standards (200-1.0 × 10^6 g mol^{-1}) were used for calibration using a second order polynomial fit. Polymer solutions at 1 mg mL^{-1} were prepared in the eluent and filtered through 0.45 mm filters prior to injection. UV-vis spectra were recorded in a disposable cuvette using a Cary 60 UV-vis spectrometer from Agilent at 25 °C. Lower critical solution temperatures of free pNIPAM and pNIPAM nanoparticles were also analyzed using an Agilent Cary 60 UV-vis spectrometer equipped with a temperature controller at 700 nm with a heating/cooling rate of 1 °C min^{-1}. The cloud point of pNIPAM and pNIPAM nanoparticles were determined by normalising the turbidimetry curve such that the values were in the range of 0 to 1, and the transition temperature was defined as being the temperature corresponding to a normalised absorbance of 0.5. A polymer concentration of 1.0 mg mL^{-1} was used in all experiments. DLS measurements were performed using a Nano-Zs from Malvern Instruments, UK running DTS software (4 mW, He-Ne laser, λ = 633 nm) and an avalanche photodiode (APD) detector. The scattered light was measured at an angle of 173° for DLS measurement. The temperature was stabilized to ± 0.1 °C of the set temperature. All samples were prepared at the concentration of

0.057 mg mL^{-1} gold nanoparticles. Hydrodynamic diameter were determined using the manufacturer's software. Absorbance measurements of the nanoparticles incubated with lectin were recorded on a BioTek SynergyTM HT multi-detection microplate reader obtained using Gen5 1.11 multiple data collection and analysis software. The size and morphology of the synthesized gold nanoparticles and polymer coated gold nanoparticles were estimated by JEOL 2100FX transmission electron microscopy (TEM) at an accelerating voltage 200 kV. A drop of sample solution was deposited onto a copper grid and the water was evaporated under air. No staining was applied. The x-ray photoemission spectroscopy (XPS) data were collected at the Warwick Photoemission Facility, University of Warwick, more details of which are available at reference.[33] The samples investigated in this study were deposited on to Cu foil, mounted on to a sample bar and loaded in to a Kratos Axis Ultra DLD spectrometer which possesses a base pressure of ~ 5×10^{-10} mbar. XPS measurements were performed in the main analysis chamber, with the sample being illuminated using an Al kα x-ray source. The measurements were conducted at room temperature and at a take-off angle of 90° with respect to the surface parallel. The core level spectra were recorded using a pass energy of 20 eV (resolution approx. 0.4 eV). The spectrometer work function and binding energy scale were calibrated using the Fermi edge and $3d_{5/2}$ peak recorded from a polycrystalline Ag sample immediately prior to the commencement of the experiments. The data were analysed in the CasaXPS package, using Shirley backgrounds, mixed Gaussian-Lorentzian (Voigt) lineshapes. For compositional analysis, the analyser transmission function has been determined using Ag, Au and Cu foils to determine the detection efficiency across the full binding energy range.

3.6.3 Synthetic procedures

Synthesis of 2-(dodecylthiocarbonothioylthio)-2-methylpropanoic acid (DMP)

Dodecane thiol (4.00 g, 4.73 mL, 19.76 mmol) was added dropwise to a stirred suspension of K_3PO_4 (4.20 g, 19.76 mmol) in acetone (60 mL) over 25 minutes. CS_2 (4.10 g, 3.24 mL, 53.85 mmol) was added and the solution turned bright yellow. After stirring for ten minutes 2-bromo-2-methylpropionic acid (3.00 g, 17.96 mmol) was added and a precipitation of KBr was noted. After stirring for 16 hour, the solvent was removed under reduced pressure and the residue was extracted into CH_2Cl_2 (2 × 200 mL) from 1M HCl (200 mL). The organic extracts were washed with water (200 mL) and brine (200 mL) and further dried over $MgSO_4$. The solvent was removed under reduced pressure and the residue was purified by recrystallization in hexane.

^{1}H NMR (300 MHz, $CDCl_3$) δ_{ppm}: 3.31 (2H, t, $J_{12\text{-}11}$= 7.34 Hz, H^{12}); 1.76 (6H, s, H^{13}); 1.70 (2H, m, H^{11}); 1.41 (2H, m, H^{10}); 1.28 (16H, br. s, $H^{2\text{-}9}$); 0.90 (3H, t, $J_{1\text{-}2}$= 6.79 Hz, H^1).

^{13}C NMR (500 MHz, $CDCl_3$) δ_{ppm}: 220.98 (C^{13}); 176.63 (C^{16}); 55.44 (C^{14}); 37.09 (C^{12}); 31.92, 29.64, 29.56, 29.45, 29.35, 29.24, 29.11, 22.70 ($C^{2\text{-}9}$); 28.96 (C^{10}); 27.81 (C^{11}); 25.27 (C^{15}); 14.13 (C^1).

IR cm^{-1}: 2916 (alkyl-H stretch); 1710 (C=O stretch); 1068 (S-(C=S)-S stretch).

HRMS (ESI +) m/z: 365.1632 $[M+H]^+$; expected 365.1637 ($C_{17}H_{33}O_2S_3$).

Polymerization of *N*-isopropylacrylamide using 2-(dodecylthiocarbonothioylthio)-2-methylpropanoic acid (DMP*)*

Polymers with three different molecular weights were synthesised in typical procedure. *N*-isopropylacrylamide (1 g, 8.84 mmol), 2-(dodecylthiocarbonothioylthio)-2-methylpropanoic acid (64.45 mg, 177 μmol), and 4,4'-azobis(4-cyanovaleric acid) (ACVA) (9.9 mg, 35.3 μmol) were dissolved in methanol/toluene (1 : 1; 4mL) in a glass vial containing a stir bar giving [monomer] : [chain transfer agent] : [initiator] = 50 : 1 : 0.2. Mesitylene (150 μL) was added as an internal reference and the mixture was stirred (5 mins). An aliquot of this starting mixture was removed for ^{1}H NMR analysis. The vial was fitted with a rubber septum and degassed by bubbling with nitrogen gas (30 mins). The vial was then placed in an oil bath thermostated at 70 °C. After 35 minutes, the reaction mixture was opened to air and quenched in liquid nitrogen. An aliquot was removed and conversion determined by ^{1}H NMR. The remainder was precipitated into diethyl ether (45 mL). The polymer was re-precipitated and purified from THF to diethyl ether three times. The product was purified three times by precipitation from toluene into diethyl ether, isolated centrifugation, and dried under vacuum overnight to give a yellow solid. The overall monomer conversion was determined from the ^{1}H NMR spectrum by measuring the decrease in intensity of the vinyl peaks associated with the monomer relative to mesitylene. Conversion (NMR): 86 %; M_n (theoretical), 5200 g mol^{-1}; M_n (SEC), 7100 g mol^{-1}; M_w/M_n (SEC), 1.10.

Synthesis of pentafluorophenyl 2-(dodecylthiocarbonothioylthio)-2-methylpropanoic acid (PFP-DMP)

2-(dodecylthiocarbonothiolythio)-2-methylpropanoic acid (0.50 g, 1.37 mmol), N-(3-dimethylaminopropyl)-N'-ethylcarbodiimide hydrochloride (EDC) (0.39 g, 2.05 mmol) and 4-(dimethylamino)pyridine (DMAP) (0.25 g, 2.05 mmol) in 40 mL dichloromethane (DCM) was stirred for 20 minutes under N_2. Pentafluorophenol (0.78 g, 4.24 mmol) in 5 mL DCM was added. The reaction was stirred overnight at room temperature. The reaction was washed successively with 3 M HCl (50 mL), 1 M $NaHCO_3$ (50 mL) and 0.5 M NaCl (50 mL). The reaction was then dried over $MgSO_4$, filtered and then concentrated in vacuum.

^{1}H NMR (300 MHz, $CDCl_3$) δ_{ppm}: 3.24 (2H, t, $J_{12\text{-}11}$= 7.70 Hz, H^{12}); 1.79 (6H, s, H^{13}); 1.65 (2H, m, H^{11}); 1.32 (2H, m, H^{10}); 1.18 (16H, br. s, $H^{2\text{-}9}$); 0.81 (3H, t, $J_{1\text{-}2}$= 6.42 Hz, H^1).

^{13}C NMR (500 MHz, $CDCl_3$) δ_{ppm}: 219.94 (C^{13}); 169.62 (C^{16}); 55.41 (C^{14}); 37.17 (C^{12}); 31.92, 29.63, 29.55, 29.43, 29.35, 29.26, 29.09, 22.70 ($C^{2\text{-}9}$); 28.92 (C^{10}); 27.82 (C^{11}); 25.43 (C^{15}); 14.12 (C^1).

^{19}F NMR (300 MHz, $CDCl_3$) δ_{ppm}: -151.5 (d, 2F, ortho F); -157.7 (t, F, para F); -162.4 (t, 2F, meta F).

IR cm^{-1}: 2923 (CH_2); 1779 (C_6F_5C=O); 1073 (S-(C=S)-S).

Polymerization of hydroxyethylacrylamide usting pentafluorophenyl 2-(dodecylthiocarbonothioylthio)-2-methylpropanoic acid (PFP-DMP)

In a typical reacation, hydroxyethylacrylamide (HEA) (0.50 g, 4.34 mmol), pentafluorophenyl 2-(dodecylthiocarbonothiolythio)-2-methylpropanoic acid (PFP-DMP) (0.154 g, 0.289 mmol), 4,4'-azobis(4-cyanovaleric acid) (ACVA) (0.0162 g, 0.058 mmol) were dissolved in 50 : 50 toluene : methanol (4 mL). Mesitylene (150 μL) was added as an internal reference. An aliquot was taken for NMR analysis in MeOD. The solution was degassed under N_2 for 30 mins. The reaction was stirred at 70 °C for 90 mins. An aliquot was taken for NMR analysis for NMR analysis in MeOD. The reaction was rapidly cooled in liquid nitrogen and precipitaed into diethyl ether. The polymer was reprecipitaed into diethyl ether from methanol twice to yield a yellow polymer product which was dried under vacuum. Conversion (NMR): 93 %; M_n (theoretical), 2100 g mol^{-1}; M_n (SEC), 4800 g mol^{-1}; M_w/M_n (SEC), 1.10.

End group modification of PFP-polyhydroxyethylacrylamide using galactosamine

In a typical reacation, PFP-pHEA (50 mg, 0.024 mmol), galactosamine (25.2 mg, 0.117 mmol) were dissolved in 5 mL DMF with 0.05 M triethylamine (TEA). The reaction was stirred at 50 °C for 16 hrs. The polymer was precipitated into diethyl ether from methanol three times and dried under vacuum. IR indicated loss of C=O stretch corresponding to the PFP ester.

General procedure for the synthesis of polymer-coated gold nanoparticles

Approximately 1 mg of the pNIPAM or desired thiol-terminated pHEA-Gal was added to a microcentrifuge tube, and dissolved in 100 μL of high-purity water. For the thiol-terminated pNIPAM, ethanolamine (50 mol equiv of pNIPAM) was also added. 900 μL of the citrated-stabilized gold nanoparticle solution was added to this tube (40 nm: 0.296 mmol L^{-1}, 60 nm: 0.288 mmol L^{-1} total gold concentration), which was then agitated 30 mins in the absence of light. To remove excess polymer, the particles were centrifuged and following careful decantation of the supernatant, the particles were then re-dispersed in 1 mL of high-quality water and the centrifugation-resuspension process repeated for a total of 3 cycles. After the final cycle the particles were dispersed in 1 mL of high-quality water for future use. Assuming complete incorporation of the citrate coated gold particles into the final polymer coated particles the total concentration of gold in the final solution was 0.296 mmol L^{-1}, 0.058 mg mL^{-1} and 0.288 mmol L^{-1}, 0.057 mg mL^{-1}.

Gold nanoparticle functionalisation using a mixture of pHEA-Gal and pNIPAM (9 : 1 molar ratio)

100 μL of total polymer solution with different molar ratio between pHEA-Gal (0.90 mg, 0.43 μmol, 90 μL) and thiol-terminated DP50 pNIPAM (0.25 mg, 0.048 μmol, 10 μL) and was added to 900 μL of 60 nm gold nanoparticles. Left for 30 minutes at room temperature and centrifuged to remove any attached polymer and resuspended in water.

Lectin induced aggregation studies by absorbance

A stock solution of the lectin was made up (0.1 mg mL^{-1} for SBA) in 10 mM HEPES buffer with 0.15 M NaCl, 0.1 mM $CaCl_2$ and 0.01 mM $MnCl_2$. 25 μL serial dilution was made up in the same buffer in a 96-well micro-titre plate. 25 μL of the multi-polymer functionalised gold nanoparticle were added to each well. Initial and after 30 minutes, both absorbance spectrum were recorded from 450 nm – 700 nm with 10 nm intervals at 20 °C and 40 °C, respectively.

3.7 References

1 M. Ambrosi, N. R. Cameron and B. G. Davis, *Org. Biomol. Chem.*, 2005, **3**, 1593–1608.

2 J. J. Lundquist and E. J. Toone, *Chem. Rev.*, 2002, **102**, 555–578.

3 C. R. Bertozzi and Kiessling, L. L., *Science*, 2001, **291**, 2357–2364.

4 S. G. Spain, M. I. Gibson and N. R. Cameron, *J. Polym. Sci. Part A: Polym. Chem.*, 2007, **45**, 2059–2072.

5 S. Ordanini, N. Varga, V. Porkolab, M. Thépaut, L. Belvisi, A. Bertaglia, A. Palmioli, A. Berzi, D. Trabattoni, M. Clerici, F. Fieschi, A. Bernardi, *Chem. Commun.*, 2015, 51, 3816–3819.

6 S.-J. Richards, M. W. Jones, M. Hunaban, D. M. Haddleton and M. I. Gibson, *Angew. Chem., Int. Ed.*, 2012, **51**, 7812–7816.

7 P. I. Kitov, J. M. Sadowska, G. Mulvey, G. D. Armstrong, H. Ling, N. S. Pannu, R. J. Read and D. R. Bundle, *Nature*, 2000, **403**, 669–672.

8 M. L. Huang, R. A. A. Smith, G. W. Trieger and K. Godula, *J. Am. Chem. Soc.*, 2014, **136**, 10565–10568.

9 S. S. Pinho and C. A. Reis, *Nat. Rev. Cancer*, 2015, **15**, 540–555.

10 K. W. Moremen, M. Tiemeyer and A. V. Nairn, *Nat. Rev. Mol. Cell Biol.*, 2012, **13**, 448–462.

11 C. S. Mahon, M. A. Fascione, C. Sakonsinsiri, T. E. McAllister, W. B. Turnbull and D. A. Fulton, *Org. Biomol. Chem.*, 2015, **13**, 2756–2761.

12 Y. Ruff, E. Buhler, S. J. Candau, E. Kesselman, Y. Talmon and J. M. Lehn, *J. Am. Chem. Soc.*, 2010, **132**, 2573–2584.

13 O. Ramström, S. Lohmann, T. Bunyapaiboonsri and J.-M. Lehn, *Chemistry*, 2004, **10**, 1711–1715.

14 M. Ebara, M. Yamato, T. Aoyagi, A. Kikuchi, K. Sakai and T. Okano, *Biomacromolecules*, 2004, **5**, 505–510.

15 S. R. Abulateefeh, S. G. Spain, J. W. Aylott, W. C. Chan, M. C. Garnett and C. Alexander, *Macromol. Biosci.*, 2011, **11**, 1722–1734.

16 I. Cobo, M. Li, B. S. Sumerlin and S. Perrier, *Nat. Mater.*, 2015, **14**, 143–159.

17 M. A. C. Stuart, W. T. S. Huck, J. Genzer, M. Müller, C. Ober, M. Stamm, G. B. Sukhorukov, I. Szleifer, V. V. Tsukruk, M. Urban, F. Winnik, S. Zauscher, I. Luzinov, S. Minko, *Nat. Mater.*, 2010, **9**, 101–113.

18 D. J. Phillips and M. I. Gibson, *Polym. Chem.*, 2015, **6**, 1033–1043.

19 M. I. Gibson and R. K. O'Reilly, *Chem. Soc. Rev.*, 2013, **42**, 7204–7213.

20 D. J. Phillips, G.-L. Davies and M. I. Gibson, *J. Mater. Chem. B*, 2015, **3**, 270–275.

21 S. Won, D. J. Phillips, M. Walker and M. I. Gibson, *J. Mater. Chem. B*, 2016, **4**, 5673-5682.

22 F. Mastrotto, P. Caliceti, V. Amendola, S. Bersani, J. P. Magnusson, M. Meneghetti, G. Mantovani, C. Alexander and S. Salmaso, *Chem. Commun.*, 2011, **47**, 9846–9848.

23 F. Dalier, F. Eghiaian, S. Scheuring, E. Marie and C. Tribet, *Biomacromolecules*, 2016, **17**, 1727–1736.

24 K. Saha, S. S. Agasti, C. Kim, X. Li and V. M. Rotello, *Chem. Rev.*, 2012, **112**, 2739–2779.

25 M. J. Marin, A. Rashid, M. Rejzek, S. A. Fairhurst, S. A. Wharton, S. R. Martin, J. W. McCauley, T. Wileman, R. A. Field and D. A. Russell, *Org. Biomol. Chem.*, 2013, **11**, 7101–7107.

26 L. Otten, D. Vlachou, S.-J. Richards and M. I. Gibson, *Analyst*, 2016, **141**, 4305–4312.

27 C. I. Biggs, M. Walker and M. I. Gibson, *Biomacromolecules*, 2016, **17**, 2626–2633.

28 S.-J. Richards and M. I. Gibson, *ACS Macro Lett.*, 2014, **3**, 1004–1008.

29 C. Boyer, V. Bulmus, T. P. Davis, V. Ladmiral, J. Liu and S. Perrier, *Chem. Rev.*, 2009, **109**, 5402–5436.

30 R. Lotan, H. W. Siegelman, H. Lis and N. Sharon, *J. Biol. Chem.*, 1974, **249**, 1219–1224.

31 M. I. Gibson, D. Paripovic and H.-A. Klok, *Adv. Mater.*, 2010, **22**, 4721–4725.

32 A. M. Wu, E. Lisowska, M. Duk and Z. Yang, *Glycoconjugate J.*, 2009, **26**, 899–913.

33 http://go.warwick.ac.uk/XPS

Chapter 4

4. Triggerable Multivalent Glyco-Nanoparticles for Probing Carbohydrate-Carbohydrate Interactions

4.1 Chapter summary

In this chapter, multivalent glyco-nanostructures are developed where the surface-expression of the disaccharide lactose can be triggered by an external stimulus by the selective collapse of a response polymer ‘gate’. A gold nanoparticle core enables colourimetric signal outputs to be generated upon aggregation of the particles which enables two different carbohydrate-carbohydrate interactions to be probed, unlike the more commonly used carbohydrate-protein interactions.

4.2 Abstract

Carbohydrate-carbohydrate interactions, CCIs, are crucial in biological signaling but have much lower affinities than carbohydrate-protein interactions. Multivalent presentation of carbohydrates is essential to study CCIs to overcome their extremely low affinity, which is lower than even carbohydrate-lectin interactions. Here we use multivalent glyco-nanostructures where the expression of lactose at the particle surface is 'gated' by an external stimulus, and a gold nanoparticle core provides intrinsic colourimetric signal outputs to probe the CCIs. Careful macromolecular engineering of a responsive polymer 'gate' enables the lactose moieties to be blocked, until a stimulus is introduced, exposing the glycan in a manner comparable to how nature uses enzymes to regulate glycan expression. The system was used to probe both Lactose-Lactose and Lactose-monosialodihexosylganglioside (GM-3) glycolipd interactions to demonstrate regulation and specificity. This externally addressable system overcomes a challenge of studying self-self-interactions, where spontaneous cross-linking occurs, and will enable the exploitation of CCIs for biotechnological applications.

4.3 Introduction

Cells from across all kingdoms of life are coated with glycans (polysaccharides, glycolipids, glycoproteins) which provide both internal and external cues for recognition, disease state, signal transduction and more.[1] The protein 'readers' of glycans are termed lectins, which engage in relatively weak interactions with individual glycans with mM affinity.[2,3] To overcome this, glycans are presented on

cells in a multivalent format, enabling a non-linear increases in binding affinity (often to < nM), termed the 'cluster glycoside effect'[4] leading to dramatic increases in affinity.[4] Inspired by this, synthetic materials bearing multiple carbohydrates have been developed which also have high affinity[5] and can compete for native ligands in anti-adhesion therapy,[6-8] or as biosensors.[9,10]

Whilst carbohydrate-lectin interactions have been extensively studied and a huge variety of tools exist to probe them, carbohydrate-carbohydrate interactions (CCI) where the sugars directly engage with each other are much less studied.[11] Initial stages of cell-cell recognition are driven by glycosphingolipid CCI's[12] and the aggregation of marine sponges is driven by sulfated glycan CCI's.[13,14] The affinity of CCIs is extremely weak, even compared to carbohydrate-lectin interactions (~mM) and require divalent metal ions to bridge the glycans; multivalent presentation is essential to enable significant interaction forces to be generated.[11,15,16] Murthy et al have synthesized lactose-functional β-cyclodextrin which engages with monosialodihexosylganglioside (GM-3) glycolipid *via* a CCI to enable successful delivery of doxorubicin and may explain the lactose 'trojan horse' effect for gaining entry into mammalian cells.[17] Dendritic and nanoparticle based systems, normally based on lactose have been synthesized and evaluated for CCIs.[11,16,18] These extremely weak interactions have been measured using solution NMR,[19] interfacial techniques such as Langmuir-Blodget[18] and scanning probe microscopy[20] and also by surface plasmon resonance (SPR).[14] Seeberger and co-workers have developed multivalent 4 nm silica glyco nanoparticles to study GM3-Gg3 interactions.[16] Penades and co-workers have used glycan-functional gold nanoparticles with SPR to demonstrate strong CCI multivalent effects.[15] Russel and coworkers used PEG-lactose functional gold particles for the plasmonic detection (red-blue colour change) of CCIs,[21] enable

simple and accessible read-outs, which have also found application in biosensing.[10]

A challenge in studying CCIs is that many of these are self-self interactions, e.g. lactose-lactose. Therefore, it is highly desirable to prevent spontaneous interactions between synthetic multivalent systems, by introducing an inducible 'trigger' such that the glycan is presented with temporal, or spatial control; in Nature this is achieved by expression of glycosyltransferases which install the glycan as and when required, depending on internal/external stimuli such as disease state.[22,23] There are many examples of stimuli-responsive polymers,[24] capable of changing their form (e.g. coli-globule transition) in response to redox,[25] light[26] and metal ions.[27] Mastrotto *et al* have used the reversible collapse of poly(*N*-isopropyl acrylamide) to present folate on particle surfaces for cellular delivery.[28] Won et al demonstrated responsive polymers can provide a reversible steric 'shield' to present glycans at gold nanoparticle surfaces ensuring lectin binding only occurs when the system is activated.[29]

Herein we describe dynamic nanomaterials where the surface expression of glycans can be externally triggered, to induce a carbohydrate-carbohydrate interaction. We show that polymeric gates can effectively block a (shorter) polymer bound glycan and present it at the surface of a gold nanoparticle on demand, and exploit the coupling of gold particle SPRs to monitor the interaction colourmetrically under the control of a small temperature change. By engineering an inducible trigger, these systems will facilitate the study and exploitation of CCIs in biotechnological fields.

4.4 Result and Discussion

Our design principle requires a non-responsive polymer bearing the glycans, and a responsive polymer to act as the reversible gate, poly(hydroxyethyl acrylamide) (pHEA) and poly(*N*-isopropylacrylamide) (pNIPAM) were respectively chosen for this.[29] pNIPAM was polymerized using CTA-2 2-(dodecylthiocarbonothioylthio)-2-methylpropionic acid). pHEA was polymerized using CTA-1 (pentafluorophenyl 2-(dodecylthiocarbonothioylthio)-2-methylpropionic acid) which enables installation of amino-glycans onto the chain-end by displacement of the reaction PFP group.[30] PFP-pHEA$_{15}$ was quantitatively functionalised by addition of either 2-amino-2-deoxy-D-galactose (GalNH$_2$) or β-1-aminopropyl,D-lactose (LacNH$_2$), which was synthesized in 4 step procedure from lactose using a well-defined method similar to that already reported.[31, 32]

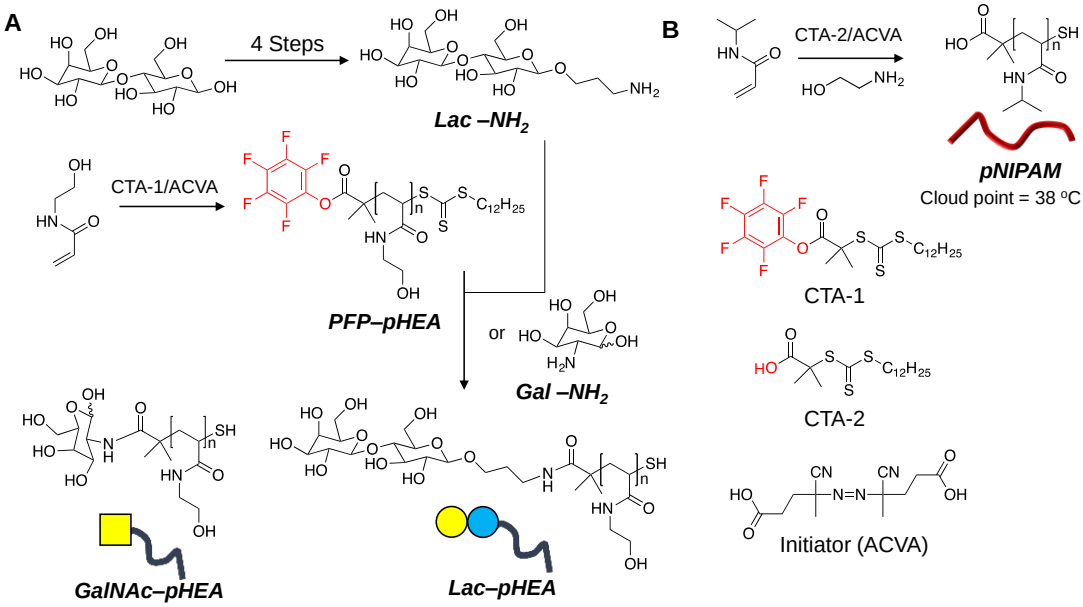

Scheme 4.1 Synthesis of a non-responsive/responsive polymer. A) Synthesis of glycosylated pHEA; B) Synthesis of pNIPAM. Initiator = 4,4′-Azobis(4-cyanovaleric acid).

Trithiocarbonate RAFT end-groups of pNIPAM undergo reaction with nucleophiles (e. g. ethanolamine) to transform to thiol functionality and addition of the glycans also results in cleavage of the RAFT agent of pHEA producing a terminal thiol suitable for conjugation to the surface of citrate-stabilized gold nanoparticles due to the high affinity between sulfur and gold as shown in Scheme 4.2. Finally, both non-responsive glycopolymer and temperature responsive polymer were conjugated on particles together to obtain the gating accessibility of glycans in certain circumstances.

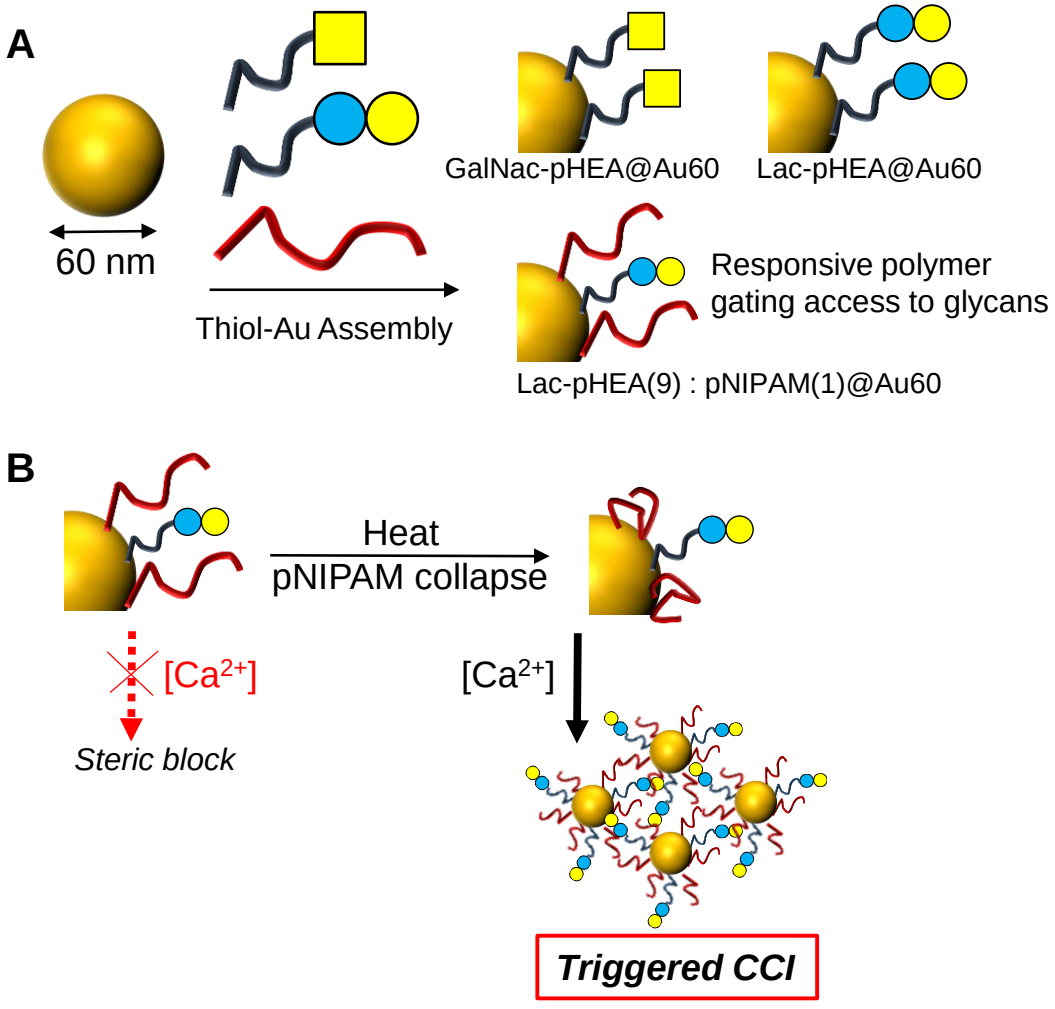

Scheme 4.2 Concept of gated glycoparticles. A) Homo-and hetero-genous coating of gold nanoparticles; B) concept of thermo-responsive polymer gate to control expression of lactose at the nanoparticle surface.

To ensure that the glycan-bearing polymer (pHEA) can be effectively 'hidden' by the responsive polymer (pNIPAM) the targeted degrees of polymerization were 15 and 50 respectively.[29] SEC analysis suggest slightly higher molecular weights than NMR for the theoretical molecular weight of pHEA and pNIPAM. These two different polymers were well-defined, with a narrow dispersity (Đ <1.1) as shown in Table 4.1 and Figure 4.1.

Table 4.1 Polymer synthesis and characterisation.

Polymer	**[M]:[CTA]:[I] (-)**	**Conversion[(a)] (%)**	**$M_{n(Theo)}$[(b)] (g mol^{-1})**	**$M_{n(SEC)}$[(c)] (g mol^{-1})**	**M_w/M_n (-)**	**CP[(d)] (°C)**
PFP-pHEA$_{15}$	15:1:0.2	93 %	2100	4800	1.10	-
pNIPAM$_{50}$	50:1:0.2	86 %	5200	7100	1.10	38

pNIPAM$_{xxx}$ / pHEA$_{xxx}$ = poly(*N*-isopropylacrylamide) / poly(hydroxyethyl acrylamide) where average degree of polymerization indicated by xxx; (a) determined by ^{1}H NMR; (b) From [M]:[CTA] and ^{1}H NMR; (c) Compared to PS standards; (d) cloud point determined by turbimimetry at 1.0 mg mL^{-1}.

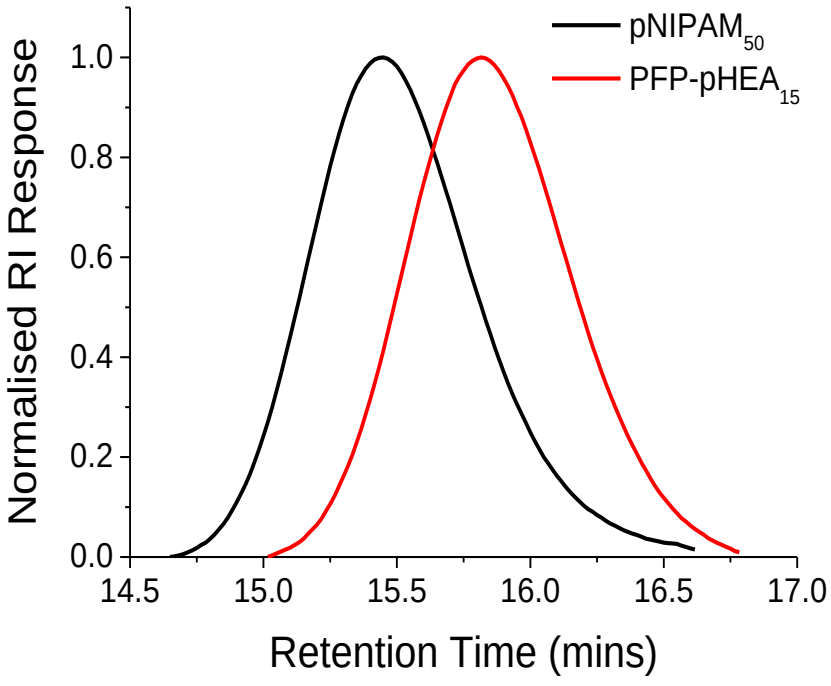

Figure 4.1 SEC analysis of polymers.

IR spectroscopies in Figure 4.2 confirmed installation of the two different glycan into pHEA. The disappearance of C=O stretch peak (at around 1750 cm^{-1}) corresponding to the carbonyl of PFP end-group shows that the pentafluorophenol end-group is removed successfully after reaction with galactosamine/lactosamine by an amide bond.

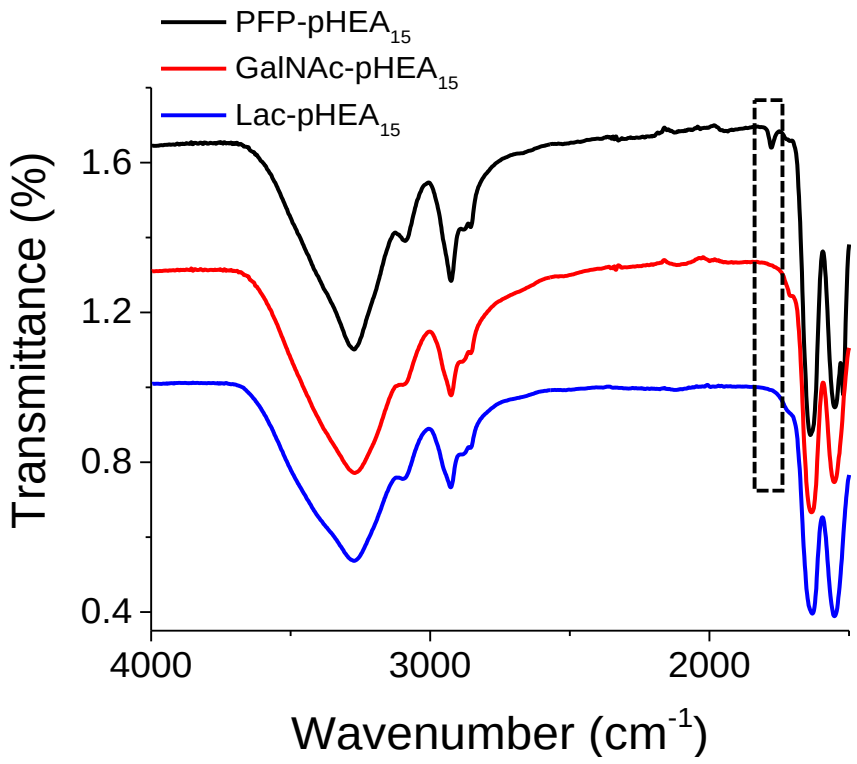

Figure 4.2 Infrared spectra of PFP-$pHEA_{15}$ (black), GalNAc-$pHEA_{15}$ (red) and Lac-$pHEA_{15}$ (blue). Box indicate region where PFP ester group would be found.

60 nm gold nanoparticles (Au_{60}) were coated with the indicated (Figure 4.3 and Table 4.2) ratios of each polymer to generate particles bearing either pure glycan coatings, or mixed glycan/responsive polymer coatings. The resulting nanoparticles were purified from excess polymer by repeated centrifugation/resuspension cycles and characterised by UV-Visible spectroscopy and dynamic light scattering. Polymer coating was confirmed by the shift of the SPR_{MAX} peak to red shifted longer

wavelength. Dynamic light scattering showed an increase in diameter from 58 to ~ 70 nm upon particle coating with mono-modal distributions obtained. TEM analysis was also employed to provide the polymer coating directly, TEM images clearly show the presence of an approximately 3 nm polymer 'halo' surrounding each individual gold nanoparticle (Figure 4.3C/D).

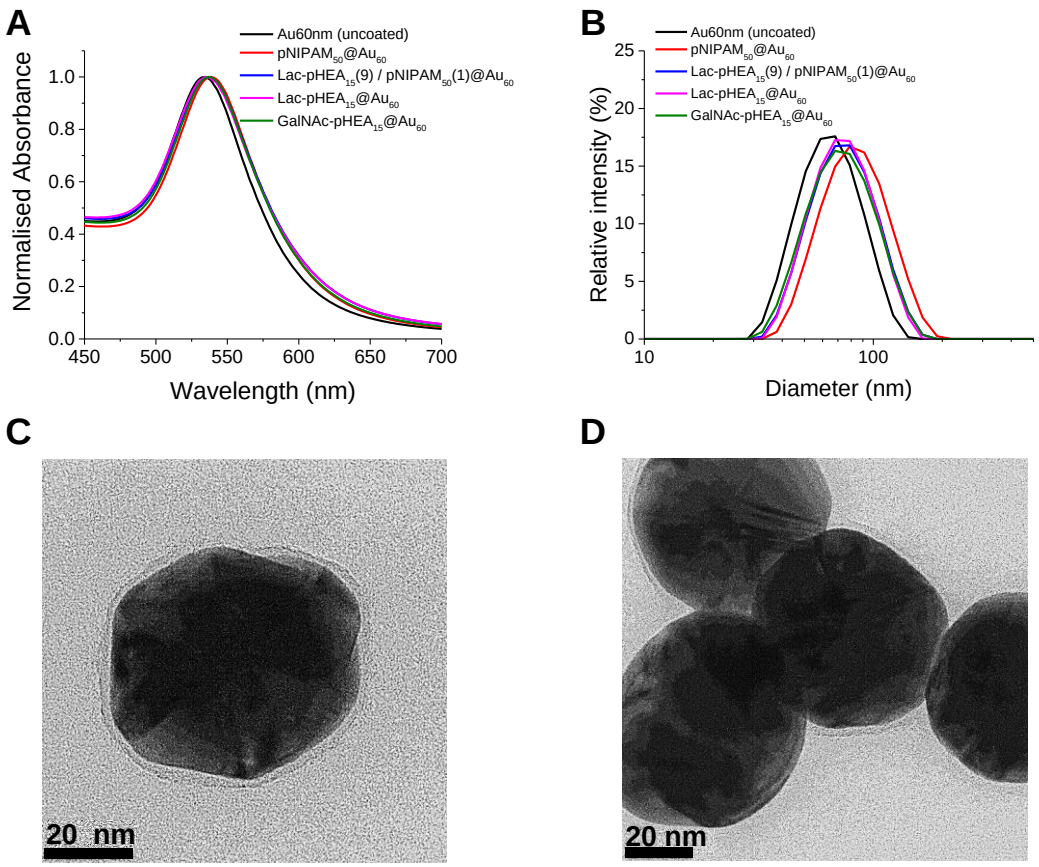

Figure 4.3 Characterisation of polymer functionalised 60 nm gold nanoparticle A) UV-Vis spectra; B) DLS analysis; C) Transmission electron microscope (TEM) image of Lac-pHEA$_{15}$ (9) / pNIPAM$_{50}$ (1) coated 60 nm gold nanoparticles at 20 ^{o}C showing polymer 'halo'; D) at 40 ^{o}C in presence of Ca^{2+} when aggregated.

Table 4.2 Nanoparticle characterisation.

Particle	SPR [nm][(a)]	Diameter [nm][(b)]	Cloud point [°C][(c)]	Zeta-potential [mV][(d)]
Au60	534	58	-	-41[(e)]
pNIPAM$_{50}$@Au$_{60}$	538	75	59	-15
Lac-pHEA$_{15}$(9)/pNIPAM$_{50}$(1)@Au$_{60}$	538	67	52	-14
Lac-pHEA$_{15}$@Au$_{60}$	537	66	-	-11
GalNAc-pHEA$_{15}$@Au$_{60}$	537	66	-	-9

(a) Surface plasmon resonance band; (b) determined by DLS; (c) determined in water by UV-Vis spectroscopy; (d) conducted in HEPES buffer unless noted; (e) conducted in water. Total gold particle concentration (0.0255 mg mL^{-1}).

UV-Vis spectroscopy was used to determine the cloud point (CP) of homopolymer and polymer coated nanoparticles in different media (pure water, HEPES buffer, 100 mM of Ca^{2+} in HEPES) defined as being the point of 50 % transmittance. All particles CP data are shown in turbidity curves of Figure 4.4 and Table 4.2. (Note, the cloud point is distinct from, and is the macroscopic effect associated with, an LCST). pNIPAM$_{50}$ showed a cloud point of 38 °C at 1 mg mL^{-1}. It is notable that once pNIPAM immobilised on the nanoparticle the actual transition temperature will vary,[33] hence a full concentration dependant study on this well-known polymer was not undertaken.[25] pNIPAM$_{50}$ containing particles had cloud points above 50 °C, this is sufficiently high degree to prevent the false positive signal (unwanted particle aggregation). Actual pNIPAM$_{50}$ chain collapse occurs around 38 ^{o}C, slightly below at certain reaction temperature (40 ^{o}C) for carbohydrate-carbohydrate interaction. The desired temperature will be safely placed between room temperature and Lac-pHEA$_{15}$/pNIPAM$_{50}$ coated particle's CP (52 °C). This is essential for the present work and all CP value shown here represents macroscopic aggregation.[33]

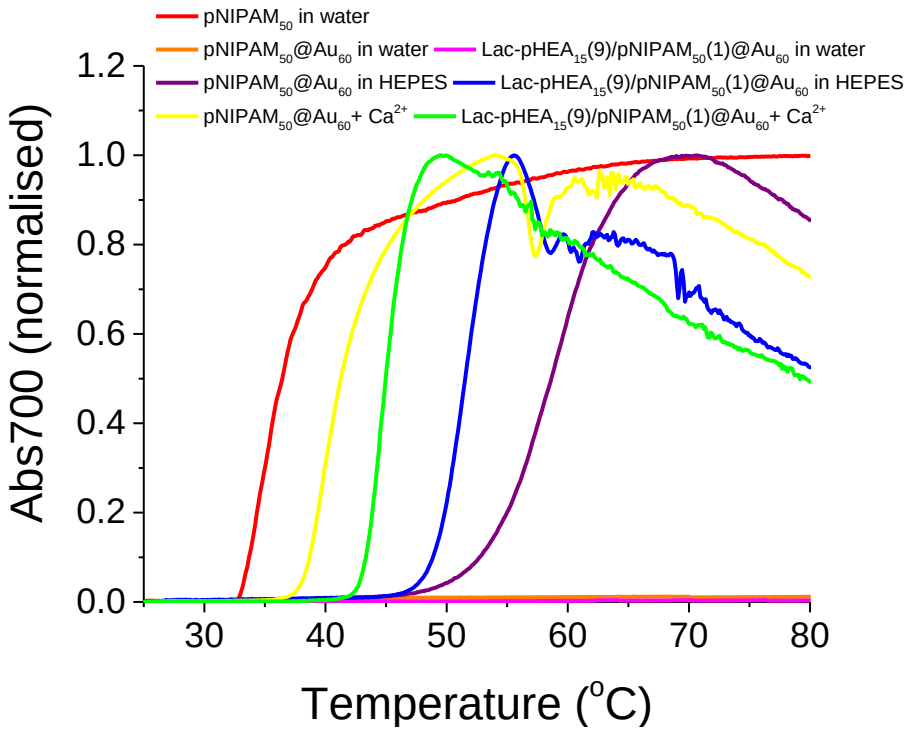

Figure 4.4 Turbidimetry scans (absorbance at 700 nm) of pure $pNIPAM_{50}$ (1.0 mg mL^{-1}) and polymer functionalised gold nanoparticles (0.0255 mg mL^{-1}) in different solution.

There was also a corresponding increase in the zeta potential (less negative) of particles in different media as shown in Figure 4.5 and Table 4.3. Citrate stabilized bare gold nanoparticle in the pure water has strong negative charge less than -40 mV and negative charge of particles was slightly increased of homogeneous or heterogeneous polymer coating. These values are significantly increased in HEPES buffer solution with various salt ions, moreover zeta potential of polymer coated gold nanoparticles are increased higher again in HEPES solution with 100 mM of Ca^{2+} due to decrease of electrostatic repulsion force by salt screen effect. The particles overall had a net-negative charge as is widely reported for coating by this method.[34] However, there was no significant shift in UV-vis absorption peaks even after hours incubation (data not shown), indicating the particles remain stable in buffered saline solutions with high concentration of Ca^{2+}.

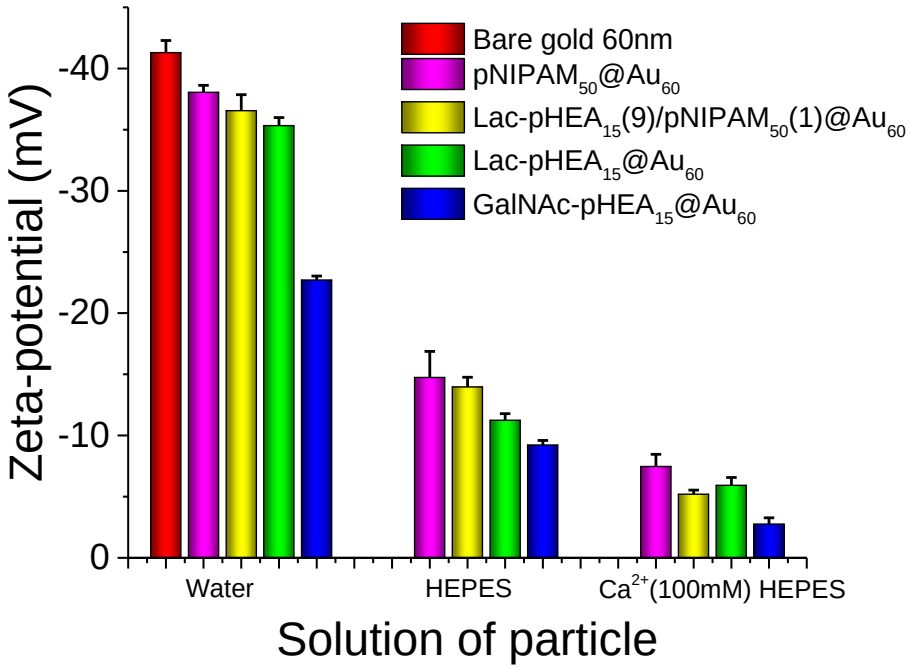

Figure 4.5 Zeta-potential analysis of nanoparticles in water, in HEPES without Ca 2^{+}, and in HEPES containing Ca^{2+} (100 mM). Polymer functionalised gold nanoparticles (0.0255 mg mL^{-1}).

Table 4.3 Solution properties of polymer coated gold nanoparticles.

Particle	**Cloud point $_{Ca2+}$ [°C] [a)]**	**Zeta-potential$_{water}$ [mV] [b)]**	**Zeta-potential $_{Ca2+}$ [mV] [c)]**
Bare gold 60 nm	-	-41	-
pNIPAM@Au60	42	-38	-7
Lac-pHEA(9)/pNIPAM(1)@Au$_{60}$	45	-37	-5
Lac-pHEA@Au$_{60}$	-	-35	-5
GalNAc-pHEA@Au$_{60}$	-	-23	-3

[a)]Cloud point was measured in HEPES buffer containing 100 mM Ca^{2+} upon heating from 25 °C to 80 °C, 0.0255 mg mL^{-1} total particle concentration. The cloud point of particles defined as being the point of 50% transmittance by UV-Vis spectroscopy; Zeta-potential of nanoparticles measured in [b)]water and [c)]HEPES buffer containing 100 mM Ca^{2+}.

With this panel of nanoparticles bearing both responsive/non-responsive units and two different glycans to hand, control experiments were undertaken to demonstrate glycan-driven interactions at the particle surface. Lac-pHEA$_{15}$@Au$_{60}$ and GalNac-pHEA$_{15}$@Au$_{60}$ (i.e. non-responsive homogenous coatings) were exposed to 0.1 to 100 mM of Ca^{2+}. Ca^{2+} is the primary divalent ion which bridges glycans of appropriate stereochemistry to enable the CCI.[35,36] Following 30 min incubation Lac-pHEA@Au60 showed distinct shifts in its UV-Visible spectra with the SPR$_{MAX}$ decreasing and Abs$_{700}$ increasing, consistent with cross-linking, Figure 4.6.[37,38] Conversely, addition of Ca^{2+} to GalNAc-pHEA$_{15}$@Au$_{60}$ showed very minor spectral changes with essentially zero aggregation. In order to ensure specificity of particles, the interaction of Ca^{2+} with two different particles was evaluated by plotting the Abs$_{700}$ against Ca^{2+} concentration. Figure 4.6C shows Lac-pHEA$_{15}$@Au$_{60}$ exhibiting a clear dose-dependent binding isotherms in the Ca^{2+} concentration range.

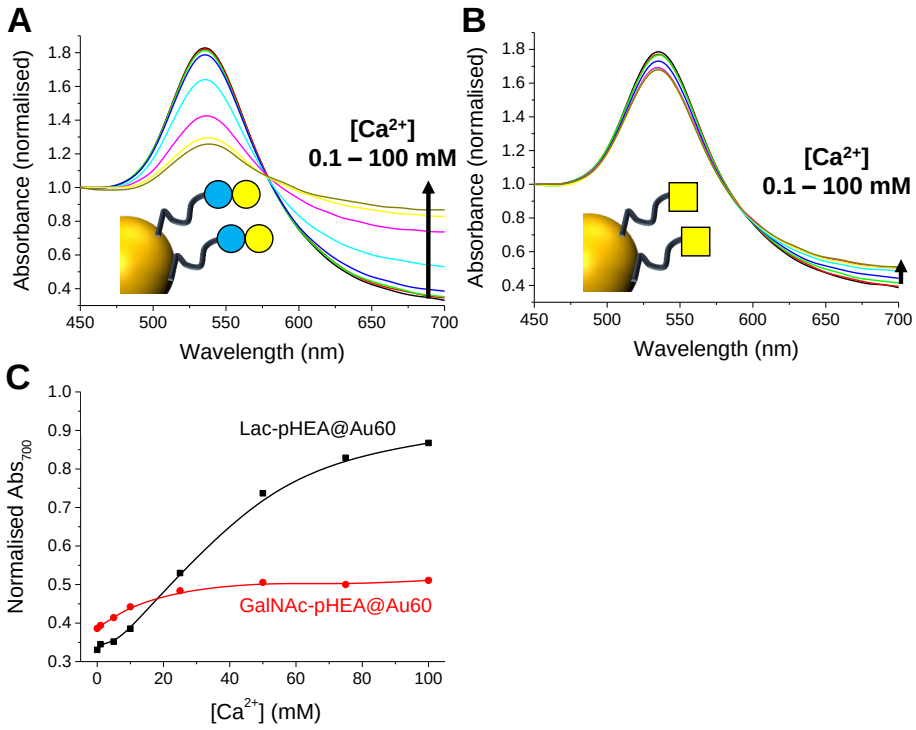

Figure 4.6 Calcium and lectin triggered aggregation of homogenous glyco-nanoparticles. A) Lac-pHEA$_{15}$@Au$_{60}$ with Ca^{2+}; B) GalNAc-pHEA$_{15}$@Au$_{60}$ with SBA; C) Binding Isotherm with Ca^{2+} gradient.

TEM analysis confirmed these observations (Figure 4.7). TEM images of Lac-pHEA$_{15}$ coated gold nanoparticles were acquired by simple preparation method. A drop of nanoparticle samples solution with or without 100 mM of Ca^{2+} was deposited onto a copper grid and the water was evaporated under room temperature until fully dried without any staining. Figure 4.7A shows spherical gold nanoparticles were well-dispersed due to the colloidal stability by polymer coating without Ca^{2+}. By contrast, there is a clear aggregated gold nanoparticles complex where containing Ca^{2+} as shown in Figure 4.7B. GalNAc particles does not undergo self-CCIs and hence ruled out non-specific interactions due to the changes in ionic strength of the buffers.

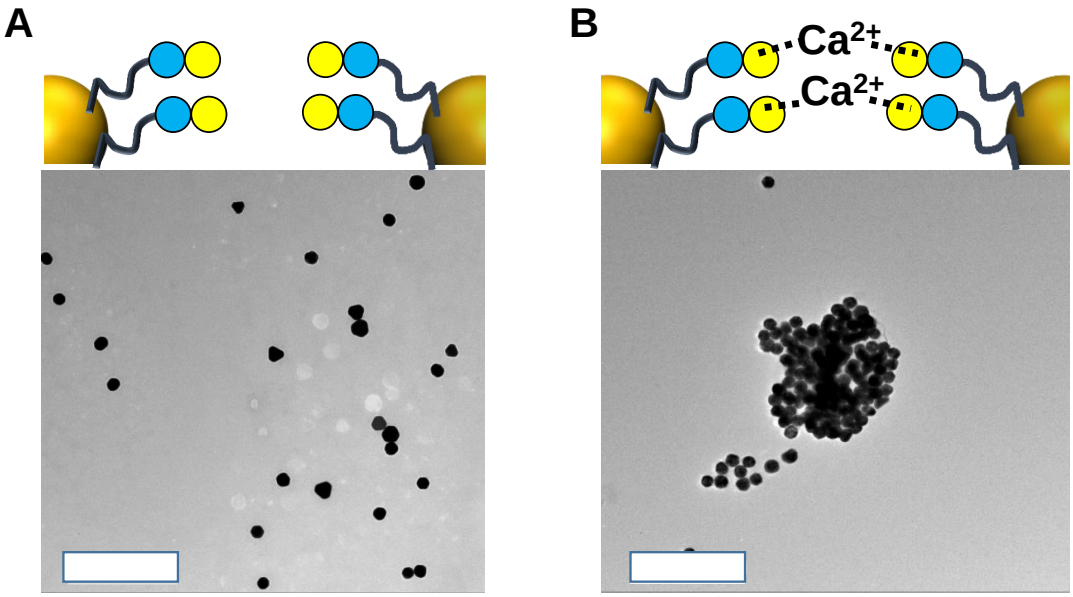

Figure 4.7 Calcium and lectin triggered aggregation of homogenous glyco-nanoparticles. TEM analysis of Lac-pHEA$_{15}$@Au$_{60}$ A) without and B) with Ca^{2+}. Scale bar = 500 nm.

To further corroborate the link between glycan presentation and aggregation, a lectin-mediated (carbohydrate-protein) interaction was also studied. Soy bean agglutinin (SBA) was chosen as it has high affinity for GalNAc but lower affinity for lactose (i.e. opposite response to CCI expected).[39] A serial dilution of SBA was added to both nanoparticles from 10 – 100 nM and UV-Vis spectra recorded (Figure 4.8). SBA requires some calcium to be present in the binding mix, but at concentrations which did not cause CCI aggregation. Lac-pHEA$_{15}$@Au$_{60}$ showed no aggregation but GalNAc-pHEA$_{15}$@Au$_{60}$ underwent strong dose-dependent binding to SBA with a decrease in SPR$_{MAX}$ and increase in ABS$_{700}$. These control experiments confirmed the differential presentation of glycans on the nanoparticle surface and the highly specific nature of the both the CCI and lectin mediated interactions and that the subtle end-group modifications provide sufficient density on the particle surface to induce a cluster-glycoside enhancement.

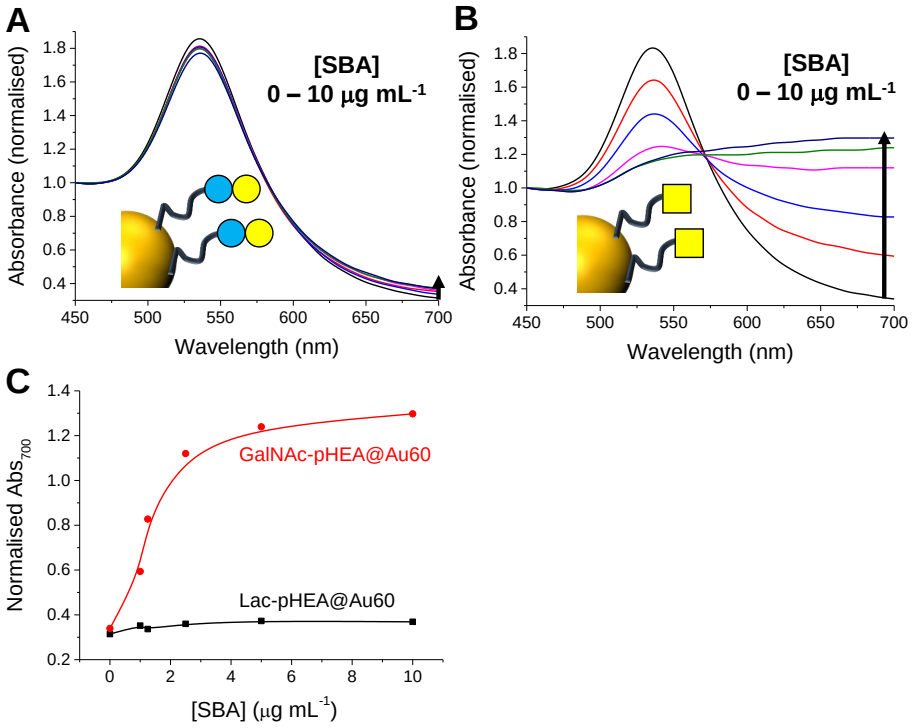

Figure 4.8 Calcium and lectin triggered aggregation of homogenous glyco-nanoparticles. A) Lac-pHEA$_{15}$@Au$_{60}$ with SBA; B) GalNAc-pHEA$_{15}$@Au$_{60}$ with SBA; C) Binding isotherm with SBA gradient.

For further control experiment, Mn^{2+} was used, also a divalent cation which can drive CCI. Similar results were obtained as we expected (Figure 4.9), the Lac-pHEA$_{15}$@Au$_{60}$ show a clear dose-dependent response with remarkable changes in the UV-vis spectra and binding isotherms in the Mn^{2+} concentration range, whereas Gal-pHEA$_{15}$@Au$_{60}$ do not show any significant changes from both data. This result indicating that a divalent cation has a selectivity toward lactose terminal glycans.

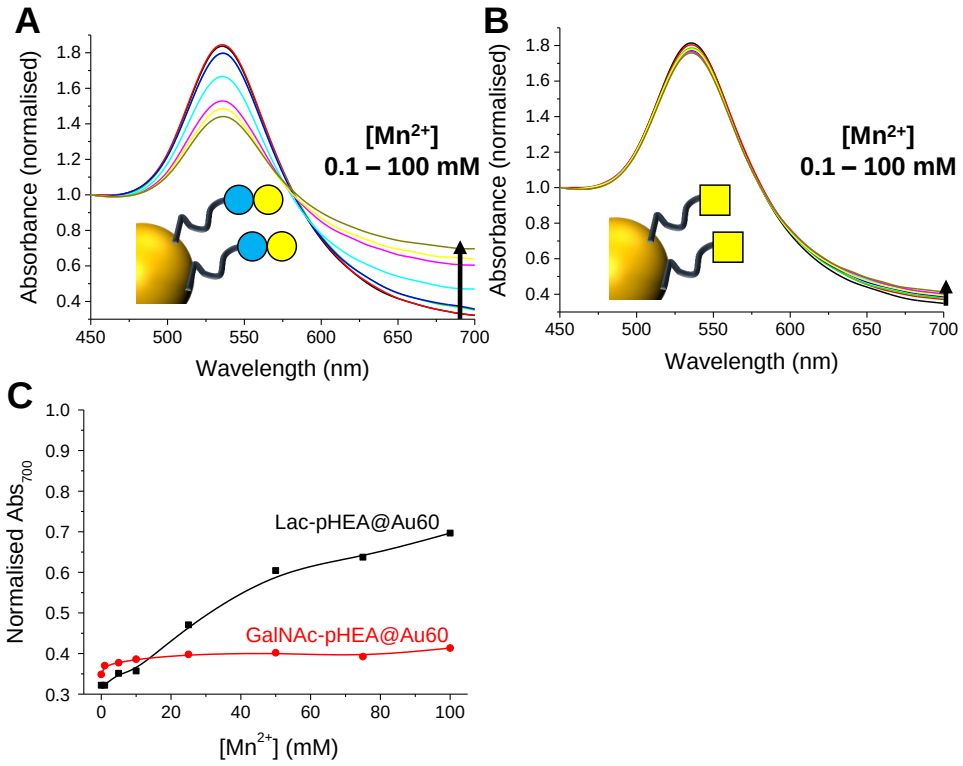

Figure 4.9 UV-Vis traces of different glycol-nanoparticle in presence of serial dilution of manganese (Mn^{2+}) after 30 minutes incubation at room temperature. A) Lac-pHEA$_{15}$@Au$_{60}$ with Mn^{2+}; B) GalNAc-pHEA$_{15}$@Au$_{60}$; C) Binding isotherm with Mn^{2+} gradient.

The above data demonstrated that Lac-Lac CCIs could be induced on polymer-coated nanoparticle surfaces but also highlights the challenge of their study; when lactose-functional materials are placed in the biological buffers spontaneous self-aggregation is always going to occur. This complicates detailed studies, especially in cell based

assays as the expression of lactose is static, not controllable, but has been reported to drive cell uptake by unknown mechanisms.[17] To evaluate steric gating to mediate these interactions Lac-pHEA$_{15}$: pNIPAM$_{50}$ ratio 9 : 1 @Au60 was monitored for calcium-mediated aggregation at 20 °C. At this temperature, the pNIPAM is fully extended and provides a steric block to CCIs, preventing aggregation even at 100 mM Ca^{2+}, Figure 4.10. Time-dependant studies by monitoring Abs$_{700}$ showed only a very slow change. TEM revealed no evidence of aggregation for both in the presence and absence of Ca^{2+} in particle solution. Hence it can be seen that just 10 mol% of pNIPAM on the particle surface can sterically block CCIs, and is 'gate closed'.

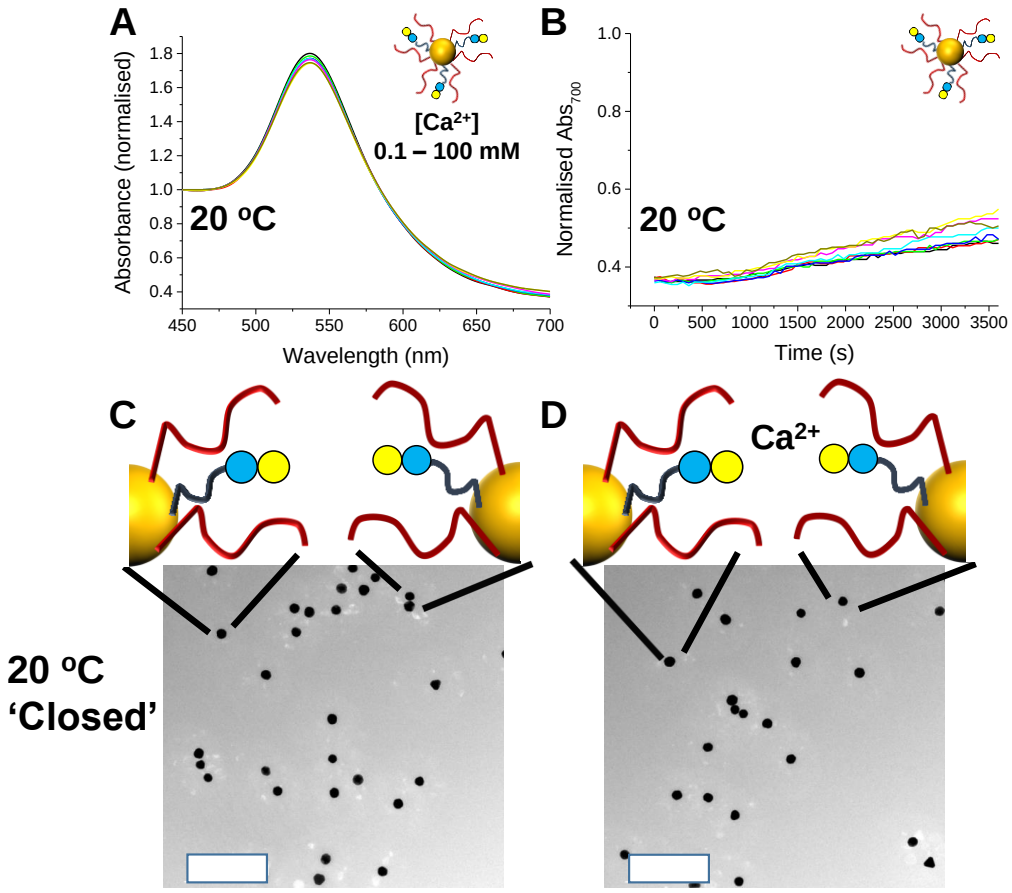

Figure 4.10 Temperature–controlled gating off lactose expression at Lac-pHEA$_{15}$: pNIPAM$_{50}$ ratio 9 : 1 @Au$_{60}$ surfaces. Ca^{2+} addition at 20 °C showing full UV-vis A) and time-dependence B). Ca^{2+} addition at 40 °C showing full UV-Vis C) and time-dependence D).

Identical experiments as above were conducted, but this time at 40 °C which is above the chain collapse temperature of pNIPAM, but below the threshold for them to aggregate (avoiding false positives, see Table 4.2), Figure 4.11C/D. Addition of Ca^{2+} lead to a clear increase in Abs_{700} and time-dependant monitoring of these showed rapid aggregation significantly faster and to a greater extent than for at 20 °C. TEM confirmed the formation of aggregates in the presence of Ca^{2+} at 40 ºC, but that in the absence of Ca^{2+} (even at 40 °C) there were no non-specific particle-particle interactions. It should be highlighted that this is the first example of using an external trigger (temperature) to control a CCI interaction and provides a dynamic tool for studying this area of glycoscience.

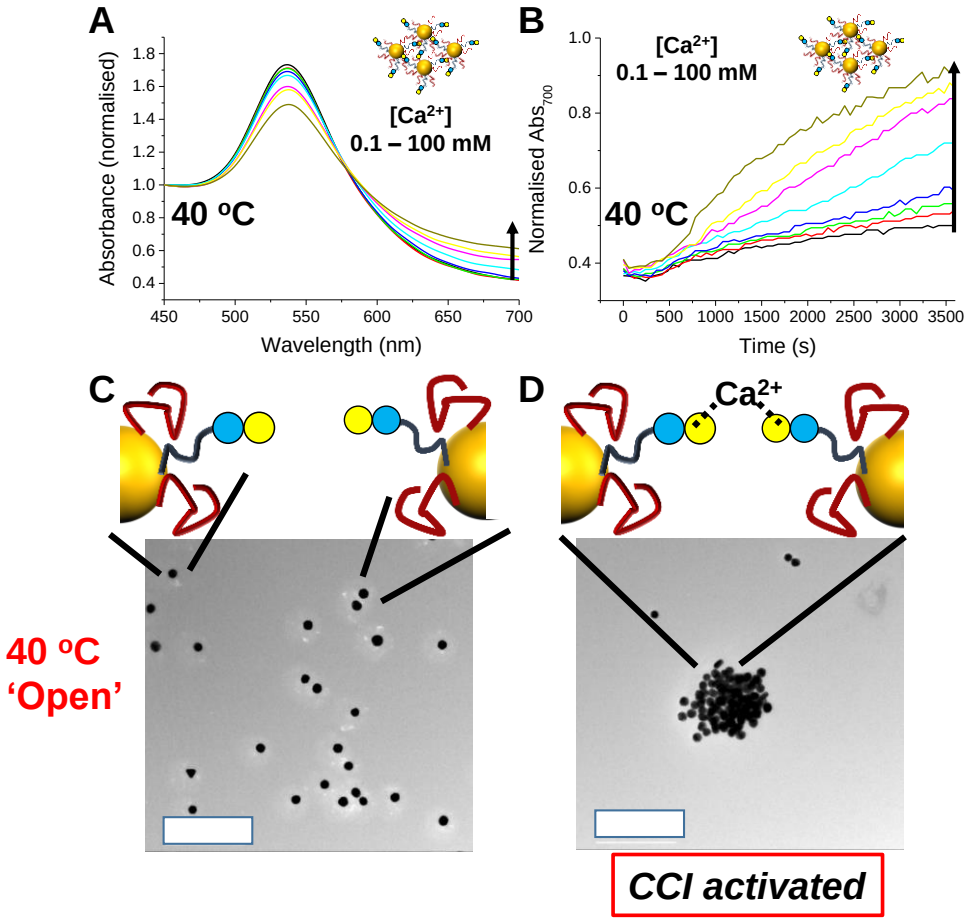

Figure 4.11 TEM analysis of Lac-$pHEA_{15}$(9)/$pNIPAM_{50}$(1)@Au_{60} to prove need for both collapse of the steric block and Ca^{2+}. 20 ºC without A) and with B) 100 mM Ca^{2+}. 40 ºC without C) and with D) 100 mM Ca^{2+}.

To further demonstrate the potential utility of these responsive nanoparticles, an assay was devised to mimic cell-surface hetero-CCI interactions; namely lactose-GM-3.[40] In short, a polystyrene plate was modified by physiosorption of monosialodihexosylganglioside (GM-3) glycolipid to create a cellular membrane mimic substrate. This was then incubated with both static, and dynamic nanoparticles and binding evaluated by UV-Vis and high-resolution scanning electron microscopy (SEM) after washing, Scheme 4.3.

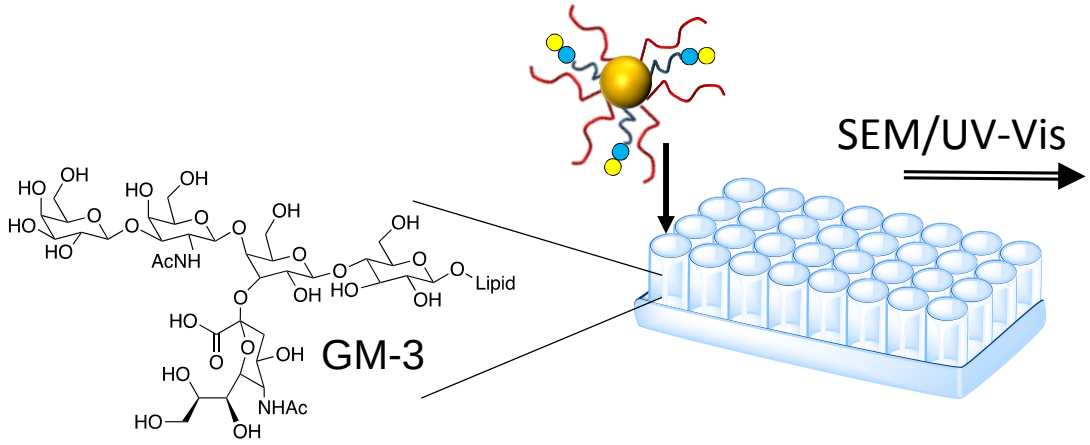

Scheme 4.3 Schematic illustration of experimental concept and GM-3 structure.

Due to the low concentration (a monolayer) low UV-Vis signals were obtained but the presence of the SPR peak at ~ 550 nm was present when Lac-pHEA@Au_{60} was incubated with calcium at 20 ºC, but no SPR peak was seen for the other static particles Figure 4.12A. Figure 4.12B shows the dynamic particles, Lac-$pHEA_{15}$(9)/$pNIPAM_{50}$(1)@Au_{60}, at both 20 and 40 ºC showing Nanoparticles were only bound at the higher temperature, when the gate is 'open'. SEM corroborated the observations from UV-Vis. Figure 4.12C/D show that for the static nanoparticles significant capture of particles by GM-3 only occurred for lactose not GalNAc functional particles, demonstrating the specific nature of the interaction. Figure 4.12E

show the dynamic nanoparticles with 'gate closed' at 20 ºC (no binding) and Figure 4.12F with 'gate open' at 40 ºC with significant Lac-GM-3 interactions occurring. This model system clearly demonstrates the potential for dynamic glycoparticles for cell/interfacial based assays to probe CCI function.

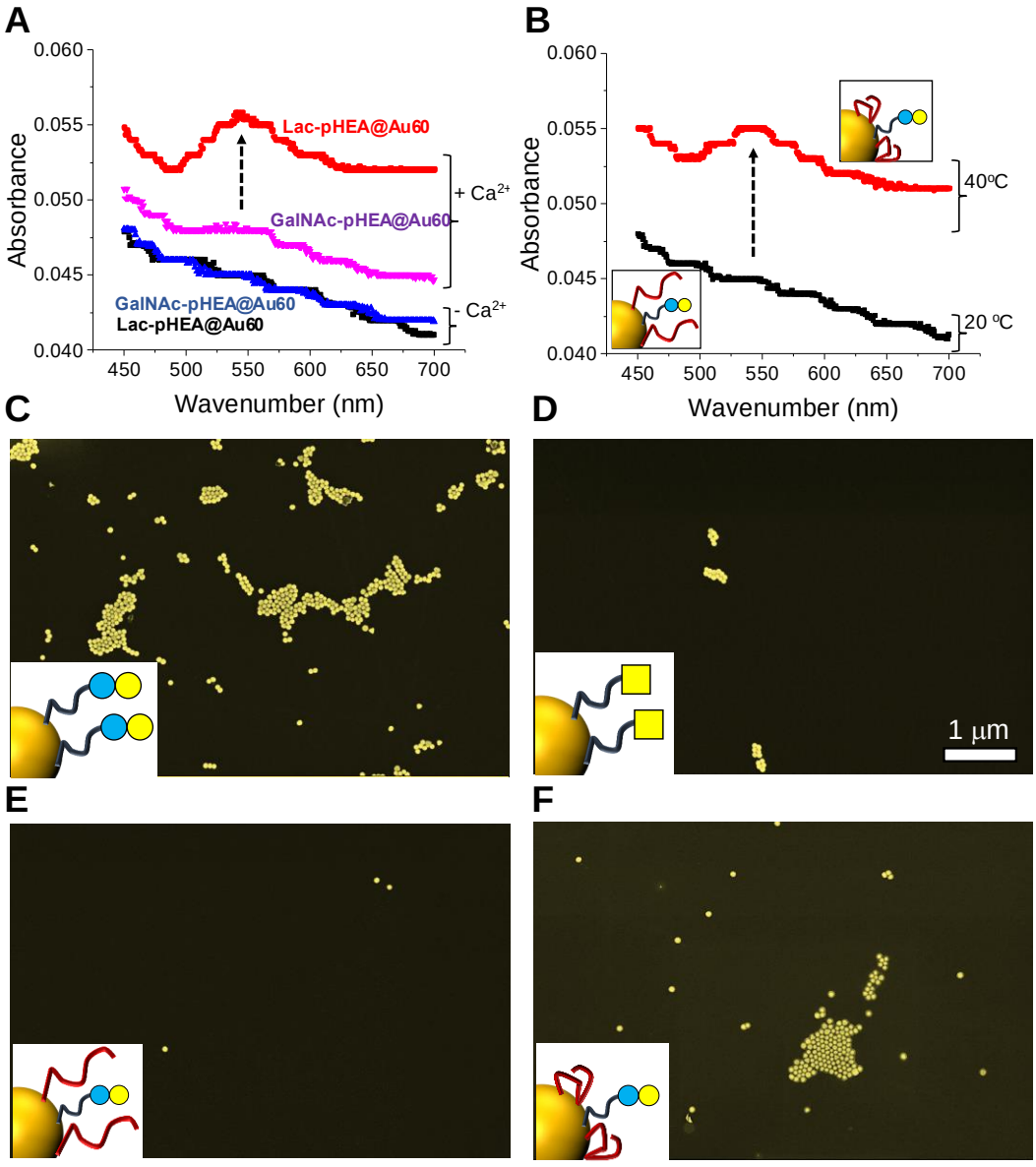

Figure 4.12 Interactions between glyco nanoparticles and GM-3 functional surface. UV-Vis analysis of GM-3 surface after incubation with particles, A) with 'static' nanoparticles at fixed temperature and B) with dynamic nanoparticles, in presence of Ca^{2+} at variable temperatures. SEM's of C) Lac-pHEA$_{15}$@Au$_{60}$ at 20 ºC; D) GalNAc-pHEA$_{15}$@Au$_{60}$ 20 ºC; E) Lac-pHEA$_{15}$(9)/pNIPAM$_{50}$(1)@Au$_{60}$ at 20 ºC; F) Lac-pHEA$_{15}$(9)/pNIPAM$_{50}$(1)@Au$_{60}$ at 40 ºC. False colour applied to SEM for clarity (non-coloured images are presented in the appendix 1).

4.5 Conclusions

Herein we demonstrate the first example of stimuli-responsive, 'triggerable' multivalent glyconanoparticles for the study of carbohydrate-carbohydrate interactions, unlike the widely studied carbohydrate-lectin interactions. At the surface of 60 nm gold nanoparticles non-responsive poly(hydroxyethyl acrylamide) was used to anchor lactose and responsive poly(*N*-isopropylacrylamide) which can undergo thermally-triggered chain collapse also added. The responsive polymer, below its transition temperature, blocked any lactose-lactose interactions *via* steric shielding, but upon application of a temperature stimulus the chain collapses and exposes the lactose. Lactose-lactose interactions could then be measured, as a function of calcium concentration, which is essential for this process. The polymer molecular weights were tuned such that upon carbohydrate-carbohydrate interaction, the gold nanoparticles will aggregate, leading to changes in their surface plasmon resonance band and hence providing a read-out of the interaction by UV-Vis spectroscopy. The hetero Lac-GM-3 interaction was also probed by this method, using a complimentary surface-binding assay to mimic a cell-surface interaction. This new method enables temporal control of when the glycans are expressed on the nanoparticle surface, comparable to enzymatic control in Nature. Crucially, unwanted spontaneous carbohydrate-carbohydrate interactions are entirely prevented, ensuring that recognition (and hence aggregation) only occurs under the operators control and hence will facilitate the study and exploitation of multivalent carbohydrate-carbohydrate interactions, which are underrepresented compared to carbohydrate-lectin interactions.

4.6 Experimental Section

4.6.1 Materials

All chemicals were used as supplied unless otherwise stated. Methanol, hexane, hydrochloric acid, dichloromethane, toluene, acetone, tetrahydrofuran, chloroform, ethyl acetate, petroleum ether and diethyl ether were purchased from Fisher Scientific at laboratory reagent grade. Deuterochloroform (99.9 atom % D), deuteromethanol (99.5 atom % D), deuterium oxide (99.9 atom % D), 4,4'-azobis(4-cyanovaleric acid) (> 97.0 %), dodecane thiol (≥ 98.0 %), potassium phosphate tribasic (reagent grade, ≥ 98.0 %), carbon disulfide (≥ 99.9 %), 2-bromo-2-methylpropionic acid (98.0 %), *N*-isopropylacrylamide (97.0 %), hydroxyethylacrylamide (97.0 %), *N*-(3-dimethylaminopropyl)-*N'*-ethylcarbodiimide hydrochloride (98.0 %), *N*,*N*-dimethylformamide (99.8%), 3-bromo-1-propanol (97.0 %), boron trifluoride diethyl etherate (46.5 % BF_3 basis), sodium bicarbonate (99.5 %), sodium chloride (99.5 %), sodium azide (99.5 %), calcium chloride (≥ 96.0 %), manganese(II) chloride (99.0 %), ethanolamine (≥ 99.0 %), magnesium sulfate (≥ 99.5 %) and mesitylene (analytical standard) were all purchased from Sigma-Aldrich. 4-(Dimethylamino)pyridine (99.0 %), pentafluorophenol (99.0 %), trimethylamine (99.0 %) and sodium methoxide solution(30 wt. % in methanol) were purchased from Acros. Clear, polystyrene, flat-bottom, half-area 96-well microtiter plates and 96-well high binding microtitre plates were purchased from Greiner Bio-one. 10 mmol HEPES buffer containing 0.15 M NaCl, 0.1 mM $CaCl_2$ and 0.01 mM $MnCl_2$ (pH 7.5, HEPES) was prepared in 200 mL of milli-Q water (with a resistance of 18.2 MΩ cm). Pre formulated phosphate buffered saline tablets dissolved in 200 mL of milli-Q water

(with a resistance of 18.2 MΩ cm) to give 0.137 NaCl, 0.0027 M KCl, 0.01 M Na_2HPO_4, 0.0018 M KH_2PO_4 and pH = 7.4. Gold nanoparticle solutions for 60nm (0.288 mmol L^{-1}) were purchased from BBI Solutions. Amberlite IR-120 hydrogen form, ion exchange resin was purchased from Alfa Aesar. Soybean Agglutinin (SBA) was purchased from Vector Labs. D-Galactosamine hydrochloride, β-D-Lactose octaacetate and GM-3-Ganglioside were purchased from Carbosynth Ltd.

4.6.2 Analytical and physical methods

^{1}H, ^{13}C and ^{19}F NMR spectra were recorded for analysis of monomer conversions and polymer compositions on Bruker HD-400 and HD-500 spectrometer using deuterated solvents obtained from Sigma-Aldrich. All chemical shifts are reported in ppm (δ) relative to tetramethylsilane (TMS). FTIR spectra were acquired using a Bruker Vector 22 FTIR spectrometer with a Golden Gate diamond attenuated total reflection cell. A total 64 (or 128) scans with resolution of 4 cm^{-1} were collected. Samples were pre-dried as a thin film for FTIR analysis. SEC analysis was conducted on Varian 390-LC MDS system equipped with a column, two PL-AS RT/MT auto sampler, a PL-gel 3 mm (50 × 7.5 mm) guard column, two PL-gel 5 mm (300 × 7.5 mm) mixed-D columns using dimethylformamide (DMF) with 1 mg mL^{-1} LiBr at 50 °C as the eluent at a flow rate of 1.0 mL min^{-1}. The GPC system was equipped with ultraviolet (UV) (set at 280 nm) and differential refractive index (DRI) detections. Narrow molecular weight poly(methyl methacrylate) (PMMA) standards (200-1.0 × 10^6 g mol^{-1}) were used for calibration using a second order polynomial fit. Polymer solutions at 1 mg mL^{-1} were prepared in the eluent and filtered through 0.45 mm filters prior to injection. UV-vis spectra were recorded in a disposable cuvette using a Cary 60 UV-vis spectrometer

from Agilent at 25 °C. Lower critical solution temperatures of free PNIPAM and pNIPAM nanoparticles were also analyzed using an Agilent Cary 60 UV-vis spectrometer equipped with a temperature controller at 700 nm with a heating/cooling rate of 1 °C min^{-1}. The cloud point of pNIPAM and pNIPAM nanoparticles were determined by normalising the turbidimetry curve such that the values were in the range of 0 to 1, and the transition temperature was defined as being the temperature corresponding to a normalised absorbance of 0.5. A polymer concentration of 1.0 mg mL^{-1} was used in all experiments. DLS and Zeta potential measurements were performed using a Nano-Zs from Malvern Instruments, UK running DTS software (4 mW, He-Ne laser, λ = 633 nm) and an avalanche photodiode (APD) detector. The scattered light was measured at an angle of 173° for DLS measurement. The temperature was stabilized to ± 0.1 °C of the set temperature. All samples were prepared at the concentration of 0.051 mg mL^{-1} gold nanoparticles. Hydrodynamic diameter were determined using the manufacturer's software. Absorbance measurements of the nanoparticles incubated with lectin were recorded on a BioTek SynergyTM HT multi-detection microplate reader obtained using Gen5 1.11 multiple data collection and analysis software. The size and morphology of the synthesized gold nanoparticles and polymer coated gold nanoparticles were estimated by JEOL 2100FX transmission electron microscopy (TEM) at an accelerating voltage 200 kV. A drop of sample solution was deposited onto a copper grid and the water was evaporated under air. No staining was applied. Scanning Electron Microscopy (SEM): The samples were contacted to the stub using silver paint for SEM analysis. They were then carbon coated to provide a thin conductive covering in the region of a few nm. They were imaged using a Zeiss Gemini 500 SEM, using a 5 keV beam and the in-Lens detector.

4.6.3 Synthetic procedures

Synthesis of 2-(dodecylthiocarbonothioylthio)-2-methylpropanoic acid (DMP)

Dodecane thiol (4.00 g, 4.73 mL, 19.76 mmol) was added dropwise to a stirred suspension of K_3PO_4 (4.20 g, 19.76 mmol) in acetone (60 mL) over 25 minutes. CS_2 (4.10 g, 3.24 mL, 53.85 mmol) was added and the solution turned bright yellow. After stirring for ten minutes 2-bromo-2-methylpropionic acid (3.00 g, 17.96 mmol) was added and a precipitation of KBr was noted. After stirring for 16 hour, the solvent was removed under reduced pressure and the residue was extracted into CH_2Cl_2 (2 × 200 mL) from 1M HCl (200 mL). The organic extracts were washed with water (200 mL) and brine (200 mL) and further dried over $MgSO_4$. The solvent was removed under reduced pressure and the residue was purified by recrystallization in hexane.

^{1}H NMR (500 MHz, $CDCl_3$) δ_{ppm}: 3.31 (2H, t, $J_{12\text{-}11}$= 7.32 Hz, H^{12}); 1.76 (6H, s, H^{13}); 1.70 (2H, m, H^{11}); 1.41 (2H, m, H^{10}); 1.28 (16H, br. s, $H^{2\text{-}9}$); 0.90 (3H, t, $J_{1\text{-}2}$= 6.79 Hz, H^1).

^{13}C NMR (500 MHz, $CDCl_3$) δ_{ppm}: 220.97 (C^{13}); 176.62 (C^{16}); 55.43 (C^{14}); 37.09 (C^{12}); 31.92, 29.64, 29.56, 29.45, 29.35, 29.24, 29.11, 22.70 ($C^{2\text{-}9}$); 28.96 (C^{10}); 27.81 (C^{11}); 25.27 (C^{15}); 14.13 (C^1).

IR cm^{-1}: 2916 (alkyl-H stretch); 1710 (C=O stretch); 1068 (S-(C=S)-S stretch).

HRMS (ESI +) m/z: 365.1632 $[M+H]^+$; expected 365.1637 ($C_{17}H_{33}O_2S_3$).

Polymerization of *N*-isopropylacrylamide using 2-(dodecylthiocarbonothioylthio)-2-methylpropanoic acid (DMP)

N-isopropylacrylamide (1 g, 8.84 mmol), 2-(dodecylthiocarbonothioylthio)-2-methylpropanoic acid (64.45 mg, 177 μmol), and 4,4'-azobis(4-cyanovaleric acid) (ACVA) (9.9 mg, 35.3 μmol) were dissolved in methanol/toluene (1 : 1; 4mL) in a glass vial containing a stir bar giving [monomer] : [chain transfer agent] : [initiator] = 50 : 1 : 0.2. Mesitylene (150 μL) was added as an internal reference and the mixture was stirred (5 mins). An aliquot of this starting mixture was removed for ^{1}H NMR analysis. The vial was fitted with a rubber septum and degassed by bubbling with nitrogen gas (30 mins). The vial was then placed in an oil bath thermostated at 70 °C. After 35 minutes, the reaction mixture was opened to air and quenched in liquid nitrogen. An aliquot was removed and conversion determined by ^{1}H NMR. The remainder was precipitated into diethyl ether (45 mL). The polymer was re-precipitated and purified from THF to diethyl ether three times. The product was purified three times by precipitation from toluene into diethyl ether, isolated centrifugation, and dried under vacuum overnight to give a yellow solid. The overall monomer conversion was determined from the ^{1}H NMR spectrum by measuring the decrease in intensity of the vinyl peaks associated with the monomer relative to mesitylene. Conversion (NMR): 86 %; M_n (theoretical), 5200 g mol^{-1}; M_n (SEC), 7100 g mol^{-1}; M_w/M_n (SEC), 1.10.

Synthesis of pentafluorophenyl 2-(dodecylthiocarbonothioylthio)-2-methylpropanoic acid (PFP-DMP)

2-(dodecylthiocarbonothiolythio)-2-methylpropanoic acid (0.50 g, 1.37 mmol), N-(3-dimethylaminopropyl)-N'-ethylcarbodiimide hydrochloride (EDC) (0.39 g, 2.05 mmol) and 4-(dimethylamino)pyridine (DMAP) (0.25 g, 2.05 mmol) in 40 mL dichloromethane (DCM) was stirred for 20 minutes under N_2. Pentafluorophenol (0.78 g, 4.24 mmol) in 5 mL DCM was added. The reaction was stirred overnight at room temperature. The reaction was washed successively with 3 M HCl (50 mL), 1 M $NaHCO_3$ (50 mL) and 0.5 M NaCl (50 mL). The reaction was then dried over $MgSO_4$, filtered and then concentrated in vacuum.

^{1}H NMR (500 MHz, $CDCl_3$) δ_{ppm}: 3.24 (2H, t, $J_{12\text{-}11}$= 7.48 Hz, H^{12}); 1.79 (6H, s, H^{13}); 1.67 (2H, m, H^{11}); 1.31 (2H, m, H^{10}); 1.19 (16H, br. s, $H^{2\text{-}9}$); 0.81 (3H, t, $J_{1\text{-}2}$= 6.56 Hz, H^1).

^{13}C NMR (500 MHz, $CDCl_3$) δ_{ppm}: 219.94 (C^{13}); 169.62 (C^{16}); 55.42 (C^{14}); 37.17 (C^{12}); 31.92, 29.63, 29.55, 29.43, 29.35, 29.12, 29.09, 22.70 ($C^{2\text{-}9}$); 28.92 (C^{10}); 27.82 (C^{11}); 25.43 (C^{15}); 14.13 (C^1).

^{19}F NMR (400 MHz, $CDCl_3$) δ_{ppm}: -151.54 (d, 2F, ortho F); -157.74 (t, F, para F); -162.34 (t, 2F, meta F).

IR cm^{-1}: 2923 (CH_2); 1779 (C_6F_5C=O); 1073 (S-(C=S)-S).

Polymerization of hydroxyethylacrylamide usting pentafluorophenyl 2-(dodecylthiocarbonothioylthio)-2-methylpropanoic acid (PFP-DMP)

In a typical reacation, hydroxyethylacrylamide (HEA) (0.50 g, 4.34 mmol), pentafluorophenyl 2-(dodecylthiocarbonothiolythio)-2-methylpropanoic acid (PFP-DMP) (0.154 g, 0.289 mmol), 4,4'-azobis(4-cyanovaleric acid) (ACVA) (0.0162 g, 0.058 mmol) were dissolved in 50 : 50 toluene : methanol (4 mL). Mesitylene (150 μL) was added as an internal reference. An aliquot was taken for NMR analysis in MeOD. The solution was degassed under N_2 for 30 mins. The reaction was stirred at 70 °C for 90 mins. An aliquot was taken for NMR analysis for NMR analysis in MeOD. The reaction was rapidly cooled in liquid nitrogen and precipitaed into diethyl ether. The polymer was reprecipitaed into diethyl ether from methanol twice to yield a yellow polymer product which was dried under vacuum. Conversion (NMR): 93 %; M_n (theoretical), 2100 g mol^{-1}; M_n (SEC), 4800 g mol^{-1}; M_w/M_n (SEC), 1.10.

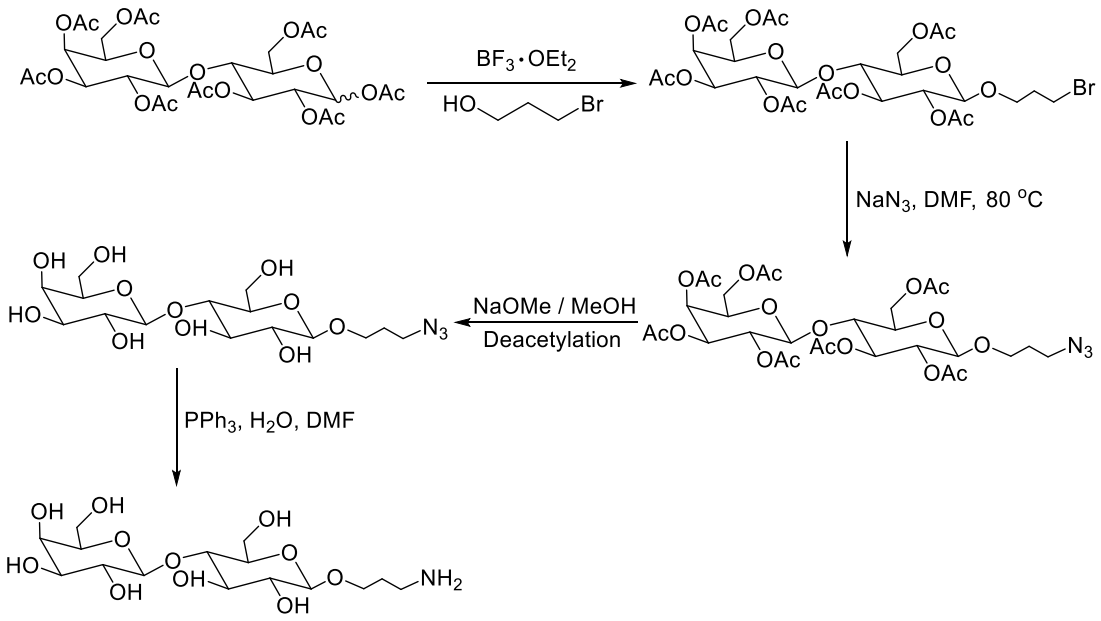

Scheme 4.4 Synthesis of amino-propyl modified lactose.

Synthesis of 1-(3-bromopropoxy) 2,2',3,3',4',6,6'-hepta-*O*-acetyl-β-lactoside

β-D-Lactose octaacetate (5.0 g, 7.37 mmol) was dissolved in dry CH_2Cl_2 (40 mL) with stirring. 3-bromo-1-propanol (1.54 g, 11.07 mmol) was added to a solution at rt for 1 h under an N_2 atmosphere. The reaction mixture was cooled at 0 °C, and $BF_3{\cdot}OEt_2$ (3.64 mL, 29.45 mmol) was added. The reaction mixture was stirred at 0 °C for 24 h, and filtered over a filter paper. The filtrate was diluted with EtOAc (100 mL), and the organic layer was washed with satd $NaHCO_3$ and satd NaCl, dried over $MgSO_4$, then filtered and concentrated in vacuuo. The residue was purified by chromatography (silica gel, 1:2 pet ether-EtOAc) to give a compound 1 (1.72 g, 38%) as a colourless syrup.

^{1}H NMR (500 MHz, $CDCl_3$) δ_{ppm}: 5.37 (1H, d, J = 3.20 Hz, Gal-4); 5.23 (1H, t, J = 9.46 Hz, Glc-3); 5.13 (1H, dd, J = 10.38, 8.09 Hz, Gal-2); 4.98 (1H, dd, J = 10.53, 3.51 Hz, Gal-3); 4.91 (1H, dd, J = 9.31, 8.09 Hz, Glc-2); 4.54 (1H, d, J = 1.68, Glc-1); 4.51

(1H, d, *J* = 2.29, Glc-6); 4.49 (1H, d, *J* = 2.59, Gal-1); 4.18-4.08 (3H, m, Glc-6, Gal-6, Gal-6); 3.99-3.95 (1H, m, -CH_2-); 3.89 (1H, t, *J* = 7.02 Gal-5); 3.81 (1H, t, *J* = 9.31 Glc-4); 3.71-3.48 (5H, m, Glc-5, -CH2-); 2.18 (3H, s, Ac); 2.15 (3H, s, Ac); 2.08 (3H, s, Ac); 2.07 (3H, s, Ac); 1.99 (3H, s, Ac).

^{13}C NMR (500 MHz, $CDCl_3$) δ_{ppm}: 170.40, 170,37, 170.17, 170.09, 169.77, 169.74, 169.08 (COCH3); 101.09 (Gal-1); 100.80 (Glc-1); 76.27, 72.70, 71.65, 71.00, 70.70, 69.11, 67.34, 66.60, 61.97, 60.81; 21.07, 20.90, 20.82, 20.76, 20.65, 20.53 ($COCH_3$).

HRMS (ESI +) m/z: 779.1367 $[M+Na]^+$; expected 779.1368 ($C_{29}H_{41}BrO_{18}Na$).

Synthesis of 1-(3-azidopropoxy) 2,2',3,3',4',6,6'-hepta-*O*-acetyl-β-lactoside

Compound 1 (1.0 g, 1.32 mmol) was added to a suspension of NaN_3 (0.429 g, 6.60 mmol) in dry DMF (15 mL) at 80 °C for 16 h with stirring. The reaction mixture was concentrated in vacuuo, and the residue was diluted with $CHCl_3$ (50 mL). The organic layer was washed with H_2O and brine, dried over MgSO4, filtered, and concentrated in vacuuo to give a compound 2 (0.75 g, 75 %) as a colourless syrup.

^{1}H NMR (500 MHz, $CDCl_3$) δ_{ppm}: 5.37 (1H, d, *J* = 3.05 Hz, Gal-4); 5.22 (1H, t, *J* = 9.31 Hz, Glc-3); 5.11 (1H, dd, *J* = 10.38, 8.09 Hz, Gal-2); 4.96 (1H, dd, *J* = 10.38 3.36 Hz, Gal-3); 4.93 (1H, dd, *J* = 9.46, 8.09 Hz, Glc-2); 4.54 (1H, d, *J* = 1.68, Glc-1); 4.51 (1H, d, *J* = 2.29, Glc-6); 4.50 (1H, d, *J* = 2.59, Gal-1); 4.18-4.08 (3H, m, Glc-6, Gal-6, Gal-6); 3.95-3.91 (1H, m, CH); 3.89 (1H, t, *J* = 6.87 Gal-5); 3.82 (1H, t, *J* = 9.61 Glc-4); 3.65-3.33 (5H, m, Glc-5, -CH2-); 2.18 (3H, s, Ac); 2.15 (3H, s, Ac); 2.09 (3H, s, Ac); 2.07 (3H, s, Ac); 1.99 (3H, s, Ac).

^{13}C NMR (500 MHz, $CDCl_3$) δ_{ppm}: 170.40, 170.37, 170,16, 170.09, 169.77, 169.66,

169.09 ($COCH_3$); 101.10 (Gal-1); 100.59 (Glc-1); 76.25, 72.76, 72.68, 71.65, 70.99, 70.70, 69.11, 66.60, 61.93, 60.80; 47.95($CH_2CH_2N_3$); 20.87, 20.82, 20.72, 20.65, 20.53 ($COCH_3$).

HRMS (ESI +) m/z: 742.2283 $[M+Na]^+$; expected 742.2277 ($C_{29}H_{41}N_3O_{18}Na$).

Synthesis of 1-(3-azidopropoxy) β-lactoside

Compound 2 (700 mg, 0.97 mmol) was deacetylated with large excess of NaOMe in MeOH (30 % soln, 20 mL) in THF/MeOH (3:1, 80 mL) for overnight with stirring (not exceeding 10 °C). The reaction mixture was neutralized by acidic amberlite ion exchange resin. The residue was filtered and condensed in vacuuo to give a compound 3 (240 mg, 34 %) as a colourless solid.

^{1}H NMR (500 MHz, CD_3OD) δ_{ppm}: 4.37 (1H, d, *J* = 7.63 Hz, Gal-1); 4.30 (1H, d, *J* = 7.93 Hz, Glc-1); 4.00 (1H, m, CH); 3.90 (1H, dd, *J* = 12.36, 2.14 Hz, Glc-6); 3.83 (1H, dd, *J* = 10.53, 4.12 Hz, Glc-6); 3.80 (1H, d, *J* = 3.97, Gal-4); 3.73-3.64 (4H, m, Gal-6, Gal-6, -CH2-); 3.61-3.41 (9H, m, Gal-5, Gal-3, Gal-2, Glc-4, Glc-3, Gal-2, Glc-5, -CH2-); 3.26 (1H, t, *J* = 8.39, Glc-2).

^{13}C NMR (500 MHz, CD_3OD) δ_{ppm}: 103.69 (Gal-1); 102.91 (Glc-1); 79.18, 75.69, 75.05, 75.01, 73.43, 73.33, 71.16, 68.90, 66.23, 61.08, 60.49; 48.10 (CH_2N_3).

HRMS (ESI +) m/z: 448.1541 $[M+Na]^+$; expected 448.1538 ($C_{15}H_{27}N_3O_{11}Na$).

Synthesis of 1-(3-aminopropoxy) β-lactoside

To a mixture of compound 3 (200 mg, 0.47 mmol) in DMF (10 mL), PPh_3 (246.55 mg, 0.940 mmol) was added at 0 °C. The mixture was stirred at rt for 2 h. H_2O (1.0 mL) was added and the reaction mixture was stirred at rt for 22 h until showing white precipitation (Ph_3PO). The reaction mixture filtered and concentrated in vacuuo to give final product.

^{1}H NMR (500 MHz, D_2O) δ_{ppm}: 4.40 (1H, d, *J* = 8.09 Hz, Gal-1); 4.34 (1H, d, *J* = 7.78 Hz, Glc-1); 3.99-3.95 (1H, m, -CH2-); 3.84 (1H, d, *J* = 3.20 Hz, Gal-6); 3.78 (1H, m, Gal-4); 3.80 (1H, d, *J* = 3.97, Gal-4); 3.76-3.61 (6H, m, Gal-6, Gal-5, Glc-6, Glc-6, Glc-4, -CH2-); 3.59-3.43 (6H, m, Gal-3, Glc-4, Glc-3, Glc-5, Glc-2, Gal-2); 3.07 (2H, t, *J* = 6.87, -CH2-).

^{13}C NMR (500 MHz, D_2O) δ_{ppm}: 102.91 (Gal-1); 102.03 (Glc-1); 78.38, 75.35, 74.77, 74.34, 72.80, 72.10, 70.99, 69.64, 68.50, 67.90, 61.00, 60.46; 36.87 ($CH_2CH_2NH_2$).

HRMS (ESI +) m/z: 400.1815 $[M+H]^+$; expected 400.1813 ($C_{15}H_{30}NO_{11}$).

End group modification of PFP-polyhydroxyethylacrylamide using galactosamine/lactosamine

In a typical reacation, PFP-pHEA (50 mg, 0.024 mmol), galactosamine (25.2 mg, 0.117 mmol) were dissolved in 5 mL DMF with 0.05 M triethylamine (TEA). The reaction was stirred at 50 °C for 16 hrs. The polymer was precipitated into diethyl ether from methanol three times and dried under vacuum. IR indicated loss of C=O stretch corresponding to the PFP ester.

General procedure for the synthesis of polymer-coated gold nanoparticles

Approximately 1 mg of the pNIPAM or desired thiol-terminated GalNac-pHEA / Lac-pHEA was added to a microcentrifuge tube, and dissolved in 100 μL of high-purity water. For the thiol-terminated pNIPAM, ethanolamine (50 mol equiv of pNIPAM) was also added. 900 μL of the citrated-stabilized gold nanoparticle solution was added to this tube (60 nm: 0.288 mmol L^{-1}, 0.057 mg mL^{-1} total gold concentration), which was then agitated 30 mins in the absence of light. To remove excess polymer, the particles were centrifuged and following careful decantation of the supernatant, the particles were then re-dispersed in 1 mL of high-quality water and the centrifugation-resuspension process repeated for a total of 3 cycles. After the final cycle the particles were dispersed in 1 mL of high-quality water for future use. Assuming complete incorporation of the citrate coated gold particles into the final polymer coated particles the total concentration of gold in the final solution was 0.259 mmol L^{-1}, 0.051 mg mL^{-1}.

Gold nanoparticle functionalisation using a mixture of pNIPAM and Lac-pHEA (1 : 9 molar ratio)

100 μL of total polymer solution with different molar ratio between thiol-terminated DP50 pNIPAM (0.25 mg, 0.048 μmol, 10 μL) and Lac-pHEA (0.90 mg, 0.43 μmol, 90 μL) was added to 900 μL of 60 nm gold nanoparticles. Left for 30 minutes at room temperature and centrifuged to remove any attached polymer and resuspended in water.

Calcium and lectin induced aggregation studies by absorbance

A stock solution of the Ca^{2+} or SBA was made up (0.1 mg mL^{-1} for SBA) in 10 mM HEPES buffer with 0.15 M NaCl, 0.1 mM $CaCl_2$ and 0.01 mM $MnCl_2$. 25 μL serial Ca^{2+} (0.1 to 100 mM) or SBA (0 to 10 μg mL^{-1}) dilution was made up in the same buffer in a 96-well micro-titre plate. 25 μL of the multi-polymer functionalised gold nanoparticle (0.051 mg mL^{-1} in water) were added to each well. Initial and after 30 minutes, both absorbance spectrum were recorded from 450 nm – 700 nm with 10 nm intervals at 20 °C and 40 °C, respectively.

Carbohydrate-carbohydrate interaction surface binding assays

Greiner high binding 96-well plates (half volume) were incubated for 17 h with solutions of GM-3 (180 μL of 0.1 mg mL^{-1} in PBS) per well. After incubation, unbound GM-3 was removed by washing vigorously with Milli-Q water, after which the plates were dried and stored at 4 °C. 50 μL of gold nanoparticle solution (0.255 mg mL^{-1} in water) and 5 μL of Ca^{2+} solution (5 M in HEPES) were then added to 96-well plates functionalised with GM-3 and incubated at room temperature and 40 °C for 1 h, respectively. After removing the unbound gold nanoparticles by extensively washing with Milli-Q water, the absorbance in each well was measured between 450 and 700 nm in 1 nm steps. Finally, each well was prepared for SEM analysis.

4.7 References

1 C. R. Bertozzi and L. L. Kiessling, *Science*, 2001, **291**, 2357–2364.

2 T. K. Dam and C. Fred Brewer, *Glycobiology*, 2009, **20**, 270–279.

3 M. Ambrosi, N. R. Cameron and B. G. Davis, *Org. Biomol. Chem.*, 2005, **3**, 1593–1608.

4 J. J. Lundquist and E. J. Toone, *Chem. Rev.*, 2002, **102**, 555–578.

5 L. L. Kiessling and J. C. Grim, *Chem. Soc. Rev.*, 2013, **42**, 4476–4491.

6 P. I. Kitov, J. M. Sadowska, G. Mulvey, G. D. Armstrong, H. Ling, N. S. Pannu R. J. Read and D. R. Bundle, *Nature*, 2000, **403**, 669–672.

7 S.-J. Richards, M. W. Jones, M. Hunaban, D. M. Haddleton and M. I. Gibson, *Angew. Chemie - Int. Ed.*, 2012, **51**, 7812–7816.

8 C. R. Becer, M. I. Gibson, J. Geng, R. Ilyas, R. Wallis, D. A. Mitchell and D. M. Haddleton, *J. Am. Chem. Soc.*, 2010, **132**, 15130–15132.

9 L. Otten, D. Vlachou, S.-J. Richards and M. I. Gibson, *Analyst*, 2016, **141**, 4305–4312.

10 M. J. Marin, A. Rashid, M. Rejzek, S. A. Fairhurst, S. A. Wharton, S. R. Martin, J. W. McCauley, T. Wileman, R. A. Field and D. A. Russell, *Org. Biomol. Chem.*, 2013, **11**, 7101–7107..

11 J. M. de la Fuente and S. Penadés, *Glycoconj. J.*, 2004, **21**, 149–163.

12 I. Bucior, S. Scheuring, A. Engel and M. M. Burger, *J. Cell Biol.*, 2004, **165**,

529–537.

13 E. Vilanova, G. R. C. Santos, R. S. Aquino, J. J. Valle-Delgado, D. Anselmetti, X. Fernández-Busquets and P. A. S. Mourão, *J. Biol. Chem.*, 2016, **291**, 9425–9437.

14 S. R. Haseley, H. J. Vermeer, J. P. Kamerling and J. F. Vliegenthart, *Proc. Natl. Acad. Sci. U. S. A.*, 2001, **98**, 9419–9424..

15 M. J. Hernáiz, J. M. De La Fuente, Á. G. Barrientos and S. Penadés, *Angew. Chem. Int. Ed.*, 2002, **41**, 1554–1557.

16 C.-H. Lai, J. Hütter, C.-W. Hsu, H. Tanaka, S. Varela-Aramburu, L. De Cola, B. Lepenies and P. H. Seeberger, *Nano Lett.*, 2016, **16**, 807–811.

17 D. Benito-Alifonso, S. Tremel, B. Hou, H. Lockyear, J. Mantell, D. J. Fermin, P. Verkade, M. Berry and M. C. Galan, *Angew. Chemie - Int. Ed.*, 2014, **53**, 810–814.

18 N. Seah, P. V. Santacroce and A. Basu, *Org. Lett.*, 2009, **11**, 559–562.

19 J. I. Santos, A. C. de Souza, F. J. Cañada, S. Martín-Santamaría, J. P. Kamerling and J. Jiménez-Barbero, *Chem. Bio. Chem.*, 2009, **10**, 511–519.

20 A. Carvalho de Souza, J. F. G. Vliegenthart and J. P. Kamerling, *Org. Biomol. Chem.*, 2008, **6**, 2095–2102.

21 A. J. Reynolds, A. H. Haines and D. A. Russell, *Langmuir*, 2006, **22**, 1156–1163.

22 S. S. Pinho and C. A. Reis, *Nat. Rev. Cancer*, 2015, **15**, 540–555.

23 K. W. Moremen, M. Tiemeyer and A. V. Nairn, *Nat. Rev. Mol. Cell Biol.*, 2012, **13**, 448–462.

24 M. A. C. Stuart, W. T. S. Huck, J. Genzer, M. Müller, C. Ober, M. Stamm, G. B. Sukhorukov, I. Szleifer, V. V. Tsukruk, M. Urban, F. Winnik, S. Zauscher, I. Luzinov and S. Minko, *Nat. Mater.*, 2010, **9**, 101–113.

25 D. J. Phillips and M. I. Gibson, *Chem. Commun.*, 2012, **48**, 1054–1056..

26 O, Bertrand and J.-F. Gohy, *Polym. Chem.*, 2016, **44**, 5539–5553.

27 D. J. Phillips, I. Prokes, G.-L. Davies and M. I. Gibson, *ACS Macro Lett.*, 2014, **3**, 1225–1229..

28 F. Mastrotto, P. Caliceti, V. Amendola, S. Bersani, J. P. Magnusson, M. Meneghetti, G. Mantovani, C. Alexander and S. Salmaso, *Chem. Commun.*, 2011, **47**, 9846–9848.

29 S. Won, S.-J. Richards, M. Walker and M. I. Gibson, *Nanoscale Horiz.*, 2017, **3**, 1593–1608.

30 S.-J. Richards and M. I. Gibson, *ACS Macro Lett.*, 2014, **3**, 1004–1008.

31 H. Kato, H. Uzawa, T. Nagatsuka, S. Kondo, K. Sato, I. Ohsawa, M. Kanamori-Kataoka, Y. Takei, S. Ota, M. Furuno, H. Dohi, Y. Nishida and Y. Seto, *Carbohydr. Res.*, 2011, **346**, 1820–1826.

32 R. Šardzik, G. T. Noble, M. J. Weissenborn, A. Martin, S. J. Webb and S. L. Flitsch, *Beilstein J. Org. Chem.*, 2010, **6**, 699–703.

33 M. I. Gibson and R. K. O'Reilly, *Chem. Soc. Rev.*, 2013, **42**, 7204–7213.

34 Z. Zhang, S. Maji, A. B. da F. Antunes, R. De Rycke, Q. Zhang, R. Hoogenboom and B. G. De Geest, *Chem. Mater.*, 2013, **25**, 4297–4303.

35 C. E. Bugg, *J. Am. Chem. Soc.*, 1973, **95**, 908–913.

36 W. J. Cook and C. E. Bugg, *J. Am. Chem. Soc.*, 1973, **95**, 6442–6446.

37 S.-J. Richards, L. Otten and M. I. Gibson, *J. Mater. Chem. B*, 2016, **4**, 3046–3053.

38 R. Elghanian, J. J. Storhoff, R. C. Mucic, R. L. Letsinger and C. A. Mirkin, *Science (80-.)*, 1997, **277**, 1078–1081.

39 A. M. Wu, E. Lisowska, M. Duk and Z. Yang, *Glycoconj. J.*, 2009, **26**, 899–913.

40 R. V. Murthy, H. Bavireddi, M. Gade and R. Kikkeri, *Chem. Med. Chem.*, 2015, **10**, 792–796.

Chapter 5

5. Conclusions

A great deal of interest in the integration of gold nanoparticles with responsive materials (polymer) is emerging for biological and biomedical applications. Due to the versatility of these nanostructures in biosensing and biorecognition among other areas, they are continuously being elucidated for a deep understanding of their functions, stimuli responsivity and the precise mechanism of their association generating signal outputs by environmental alteration or in the presence of specific target materials.

In this work, firstly, we have demonstrated that temperature-responsive behaviour of poly(*N*-isopropylacrylamide) (pNIPAM) and pNIPAM functionalised gold nanoparticles for both fundamental studies on their aggregation behavior but also demonstrated a new platform for dynamic display of glycans, similar to 'logic gates' and the dynamic expression of glycans on cell surfaces. Smart polymer pNIPAM with a thiol-functional terminal group was synthesized *via* RAFT polymerization grafting onto the surface of pre-formed gold nanoparticles, exploiting the affinity and ease of thiol-gold self-assembly. Versatile 'modular' approaches to accessing many different thermo-responsive nanomaterials was introduced in Chapter 2.

4 different mixing strategies were employed to fine-tune the transitions temperatures *via* co-operative assembly, rather than through tedious co-polymerizaton; i) different polymers on the same sized particles, ii) mixture of polymers on same sized particles, iii) same polymer on different sized particles and iv) different polymers on different

sized particles. In each case, the blending strategy enable the exact transition temperature to be tuned by simply mixing. Using TEM it shown that different sized nanoparticles preferentially interacted with each other, rather than themselves. This strategy may have applications in fine-tuning thermal responses for diagnostic or delivery applications and to improve out basic understanding of responsive nanostructures.

Secondly, we have developed a temperature-switchable colourimetric sensing system to dissect protein-carbohydrate interactions. Two different functional polymers were co-grafted on the surface of gold nanoparticles. The multifunctionality of particles is based on the molecular recognition of galactose modified poly(hydroxyethyl acrylamide) (pHEA) and the thermo-sensitivity based on the coil-to-globule phase transition of pNIPAM.

pNIPAM chains act as a reversible blocking agent, longer stretched linear pNIPAM chain shields lectin accessing to shorter Gal-pHEA chain below the LCST of the pNIPAM due to steric hindrance. Conversely, the galactosyl residues of pHEA is exposed by shrunken globular pNIPAM structure upon heating above LCST, this triggers crosslinking of particles exhibiting dramatic visible red-to-blue colour change of solution as a result of lectin-carbohydrate interactions. Quantitative detection of lectins associated with relative changes in particle aggregation can be simply monitored by a shift in the surface plasmon resonance peak (SPR) using UV-Vis spectroscopy. To get the optimum performance of particles as a biosensor, we optimised crucial parameters; i) size of core gold nanoparticles, ii) chain length of pNIPAM as a blocking agent and iii) molar ratio between Gal-pHEA and pNIPAM. 9 : 1 molar ratio of Gal-pHEA and pNIPAM grafted 60nm sized gold nanoparticles have shown excellent dose dependent detection of target lectin with high sensitivity

(8.5 nM for SBA) and selectivity.

Thirdly, we have successfully demonstrated that previous strategy with larger glycans (disaccharides) can be used to probe technically challenging low affinity carbohydrate-carbohydrate interactions. Whilst the literature on protein-carbohydrate interactions is vast, carbohydrate-carbohydrate interactions are often ignored. The surface of 60 nm gold nanoparticles was decorated with both shorter non-responsive disaccharides lactose modified pHEA and longer responsive pNIPAM which can undergo thermally-triggered coil to globule conformation transformation.

Multivalent glyco-nanostructures where the expression of lactose at the particle surface can be triggered by an external temperature rise above the LCST of pNIPAM, and a gold nanoparticle core provides intrinsic colourimetric signal outputs by divalent calcium ion mediated lactose-lactose binding events, as confirmed by measuring the surface plasmon resonance (SPR) band using UV-Vis spectroscopy. TEM analysis was also conducted to support direct evidence of particle aggregation in the presence of calcium ion. Furthermore, these particles were subsequently employed to measure the interactions between the cancer-associated glycosphingolipds GM-3 and lactose, using a complimentary surface-binding assay to mimic a cell-surface interaction. The morphology of particle adsorption on glycolipids surface through Lactose-GM-3 interactions were directly observed by SEM analysis. This method enables governing the expression of glycans which can control carbohydrate-carbohydrate interactions at desired condition compared to enzymatic control in Nature.

In conclusion, these findings provide unique optical properties and thermo-responsive behaviour of polymer/gold hybrid nanoparticles in depth. Hopefully, these studies including switchable controlled specific targeting function of polymer tethered gold

nanoparticles in response to external temperature changing (by simply changing the temperature of media) will open up new horizons to the developments of precision multi-functional nanoparticles for *in vitro* and *in vivo* bio applications in the future.

Appendices

Appendix 1

Supplementary Information: Chapter 3

Additional Characterisation

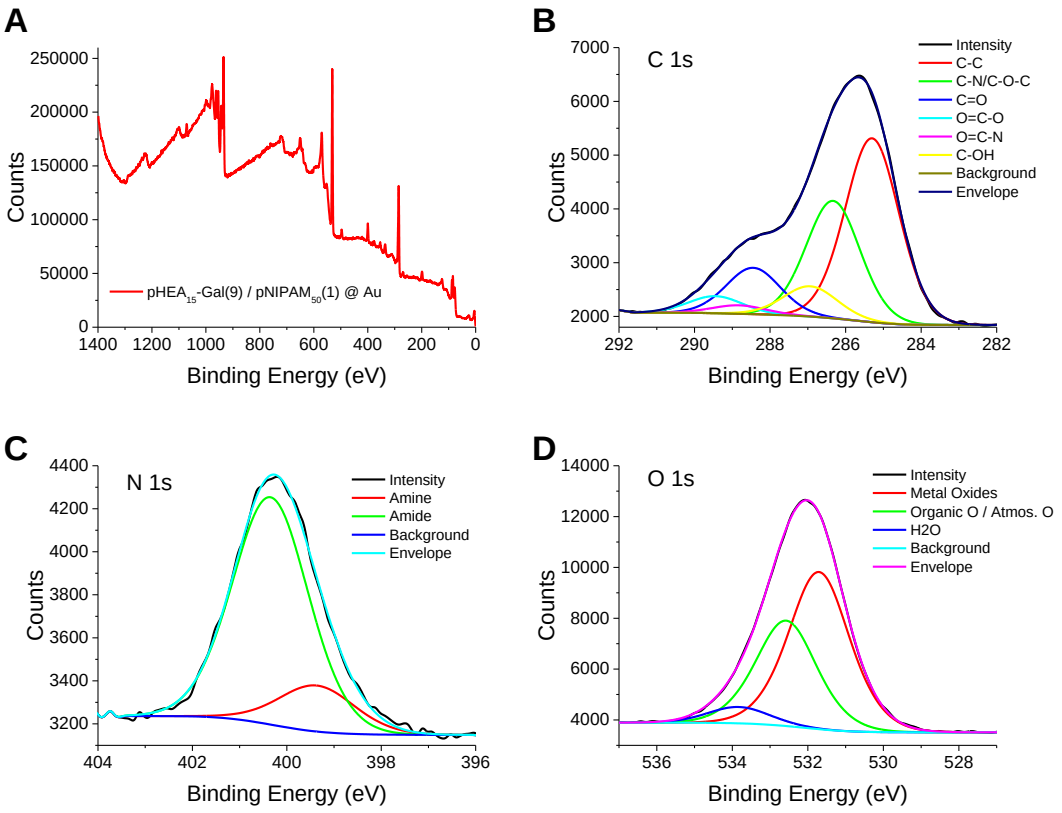

Figure S1.1 X-ray photoelectron spectroscopy analysis of $pHEA_{15}$-Gal(9) / $pNIPAM_{50}$(1) functionalised 60 nm gold nanoparticles. A) Full survey scans B) Carbon (C1s) peak, C) Nitrogen (N1s) peak and D) Oxygen (O1s) peak.

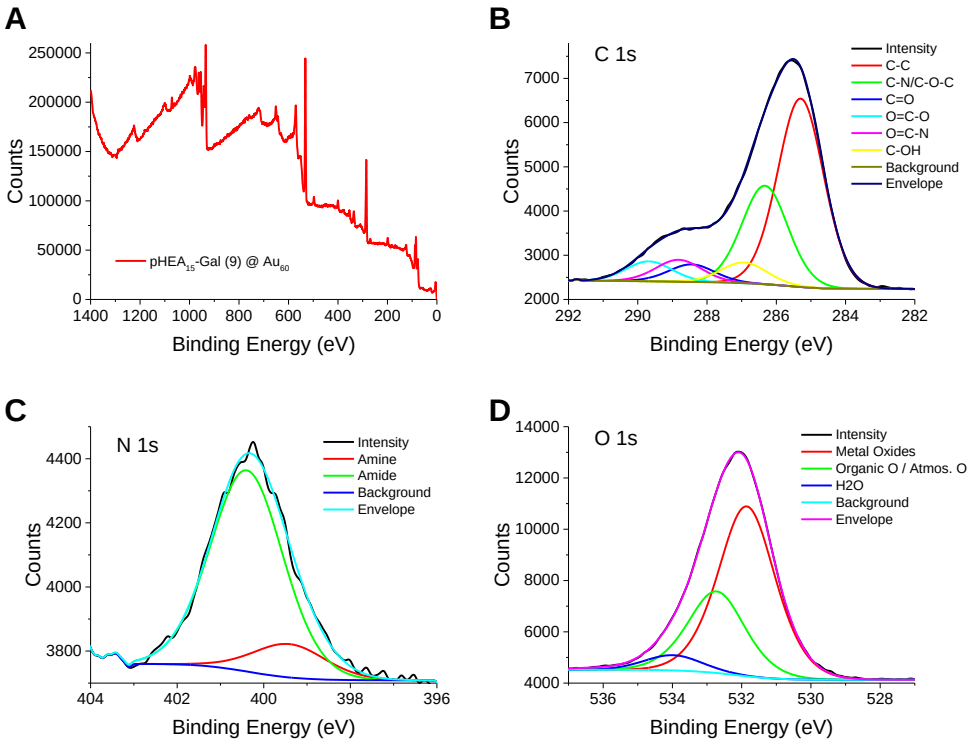

Figure S1.2 X-ray photoelectron spectroscopy analysis of $pHEA_{15}$-Gal(9) functionalised 60 nm gold nanoparticles. A) Full survey scans B) Carbon (C1s) peak, C) Nitrogen (N1s) peak and D) Oxygen (O1s) peak.

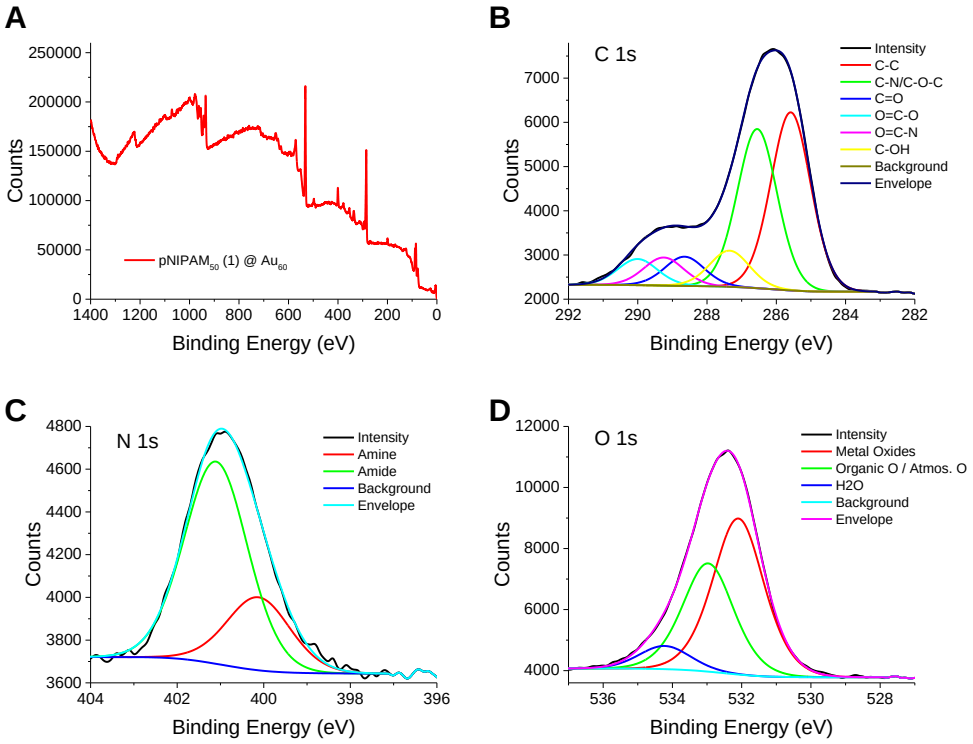

Figure S1.3 X-ray photoelectron spectroscopy analysis of $pNIPAM_{50}$(1) functionalised 60 nm gold nanoparticles. A) Full survey scans B) Carbon (C1s) peak, C) Nitrogen (N1s) peak and D) Oxygen (O1s) peak.

Supplementary Information: Chapter 4

Additional Characterisation

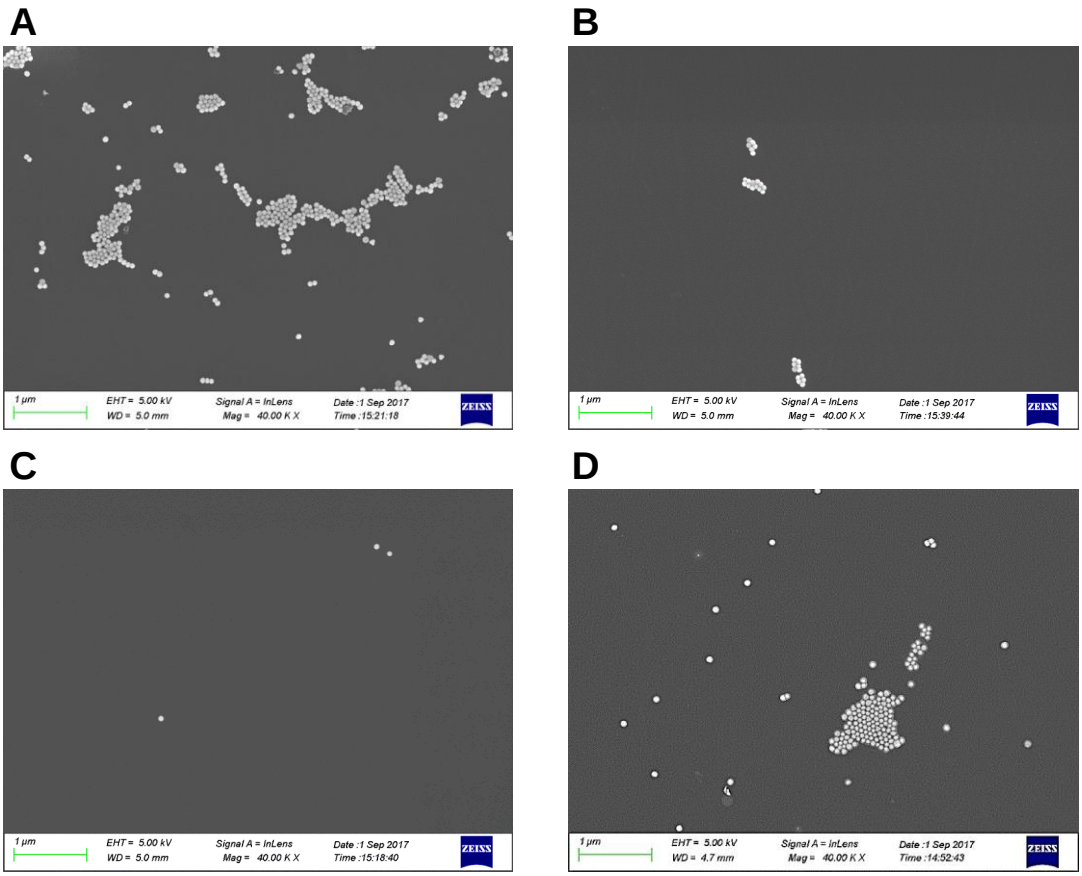

Figure S1.2 Non-coloured SEM image of A) Lac-pHEA$_{15}$@Au60 at 20 ºC; B) GalNAc-pHEA$_{15}$@Au60 20 ºC; C) Lac-pHEA$_{15}$(9)/pNIPAM$_{50}$(1)@Au60 at 20 ºC; D) Lac-pHEA$_{15}$(9)/pNIPAM$_{50}$(1)@Au60 at 40 ºC.

Appendix 2

‘Unsuccessful’ experiments

The increase in drug-resistant bacteria is one of the biggest threats to global health, food security, and development today due to human and animal infections caused by drug-resistant bacteria are harder to treat than those caused by non-resistant bacteria. The concept of this experiment is a development of nanoparticles responsive to drug-resistant bacteria enzymes. The target enzyme is beta-lactamases (β-lactamases), also known as penicillinase, which are produced by bacteria providing multi-resistance to antibiotics such as penicillins, cephalosporins, and carbapenems. β-lactamase exhibits antibiotic resistance by breaking the β-lactam ring (a four-atom ring) in the molecular structure of antibiotics through hydrolysis, which ultimately deactivates the molecule’s antibacterial properties, as shown in Figure S2.1.

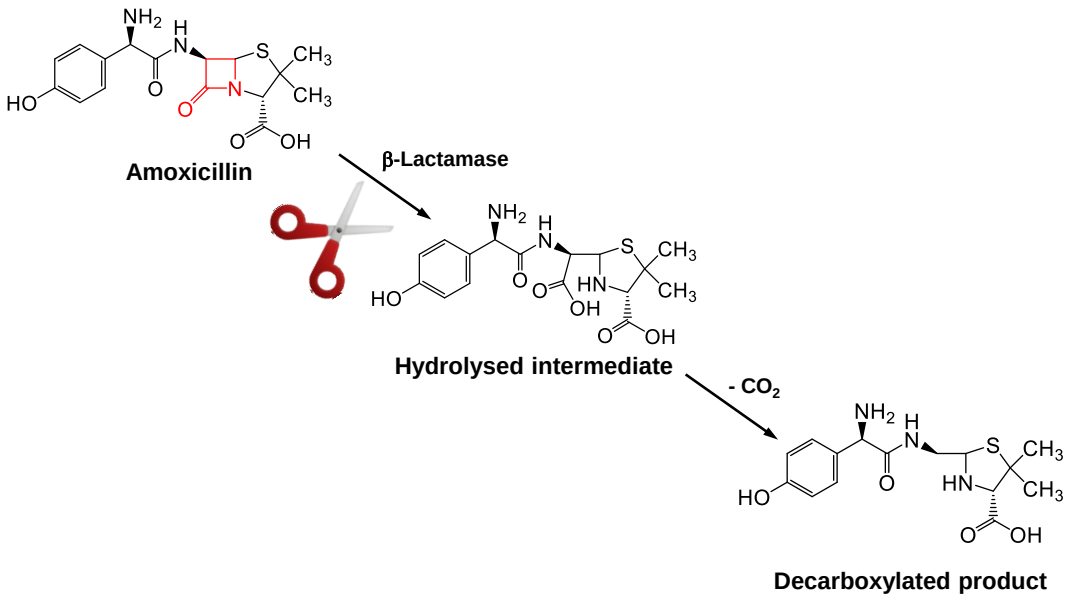

Figure S2.1 The action of β-lactamase and decarboxylation of the intermediate.

In this study, amoxicillin and penicillinase were used as a model antibiotics and enzyme. The enzyme action of β-lactamase involving hydrolysis and decarboxylation of the intermediate are successfully confirmed by mass spectroscopy analysis.

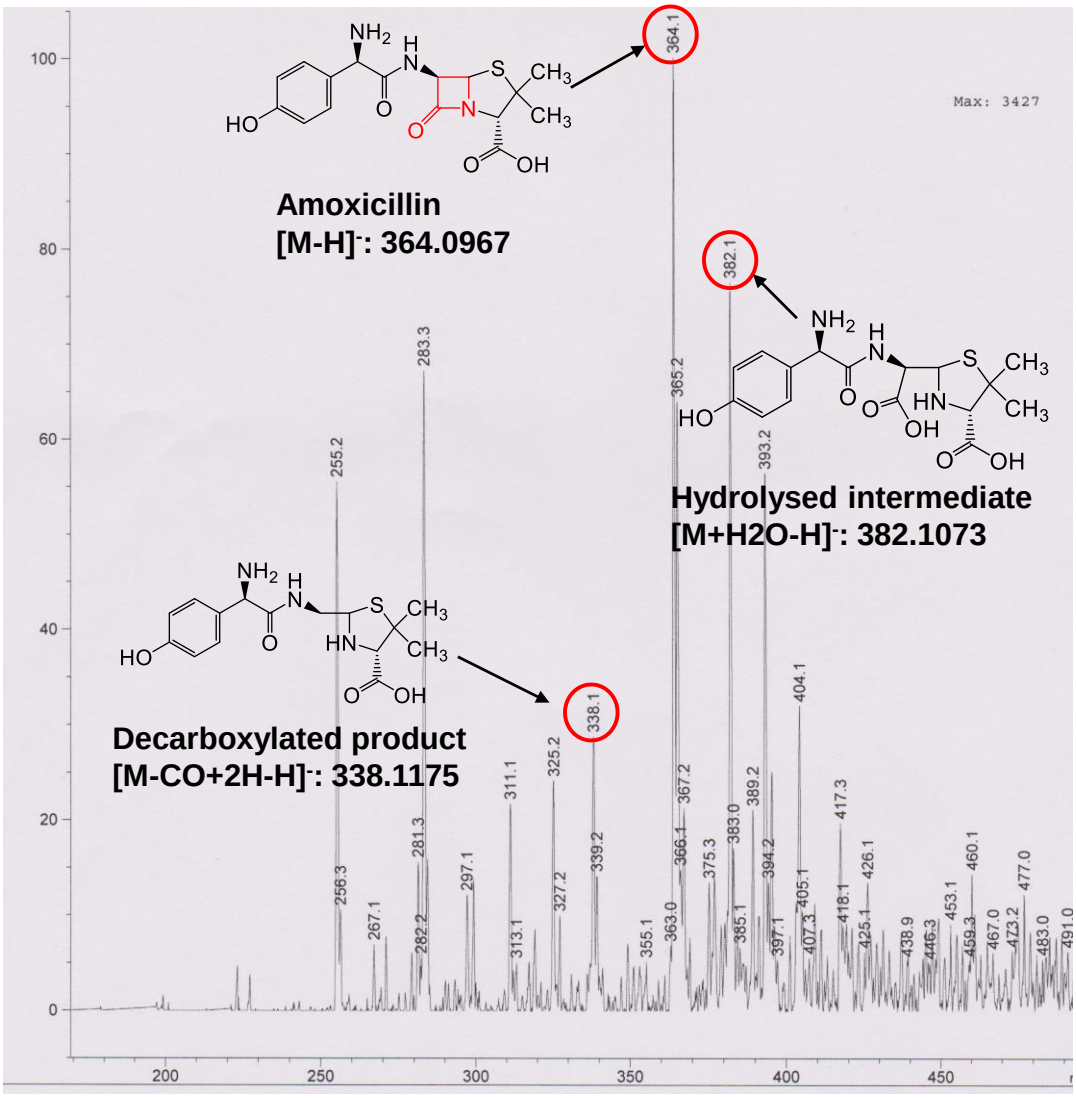

Figure S2.2 Mass spectrum (negative mode) of amoxicillin (1 mg mL^{-1}) upon addition of β-lactamase (15-30 units) for 30 mins incubation at room temperature.

Next, antibiotics conjugated thermo-responsive polymers were synthesized to investigate the phase transition properties in the presence of enzyme. Two different molecular weight of pentafluorophenyl (PFP) ester modified poly(*N*-isopropyacryl amide) (PFP-pNIPAM) were synthesized *via* RAFT polymerization. Polymers have

narrow molecular weight distributions as confirmed by SEC analysis (Figure S2.3B and Table S2.1), and then fluorophenyl esters end group was subsequently reacted with primary amines (-NH2) in the amoxicillin to form a stable amoxicillin conjugated pNIPAM through amide bond.

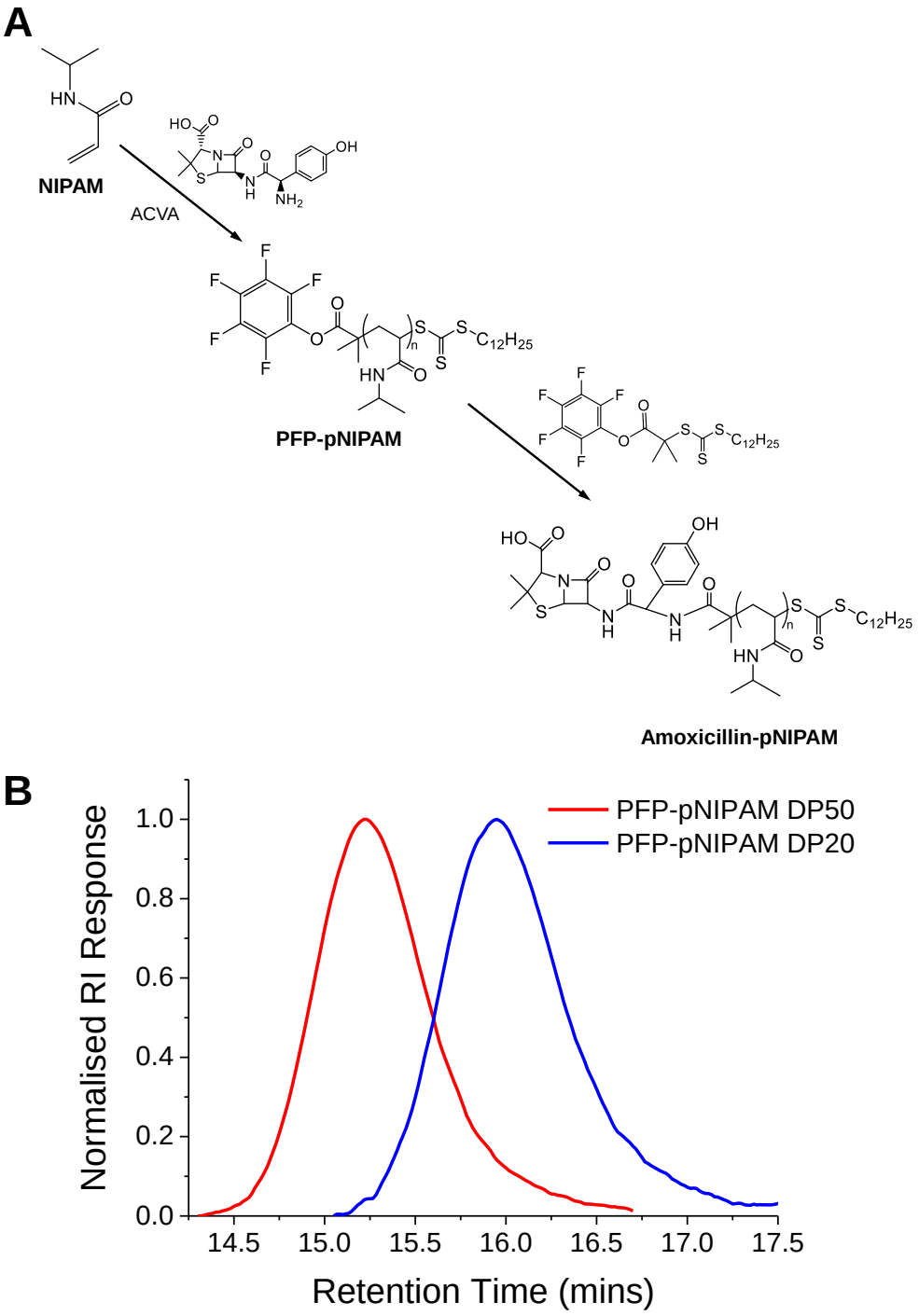

Figure S2.3 A) Synthetic route to amoxicillin conjugated pNIPAMs; B) SEC analysis of polymers.

Table S2.1 Polymer synthesis and characterisation.

Polymer	[M]:[CTA]:[I] (-)	Conversion[(a)] (%)	$M_{n(Theo)}$[(b)] (g mol^{-1})	$M_{n(SEC)}$[(c)] (g mol^{-1})	M_w/M_n (-)
PFP-pNIPAM$_{20}$	20:1:0.2	89 %	2000	3200	1.10
PFP-pNIPAM$_{50}$	50:1:0.2	90 %	5100	7000	1.12

PFP-pNIPAM$_{xxx}$ = pentafluorophenyl poly(*N*-isopropylacrylamide) where average degree of polymerization indicated by xxx; (a) determined by ^{1}H NMR; (b) From [M]:[CTA] and ^{1}H NMR; (c) Compared to PS standards.

Infrared analysis of pNIPAM was conducted before and after reaction of PFP end-group with amoxicillin. Disappearance of C=O at around 1777 cm^{-1} attributable to the carbonyl associated with the PFP end-group being removed as shown in Figure S2.4.

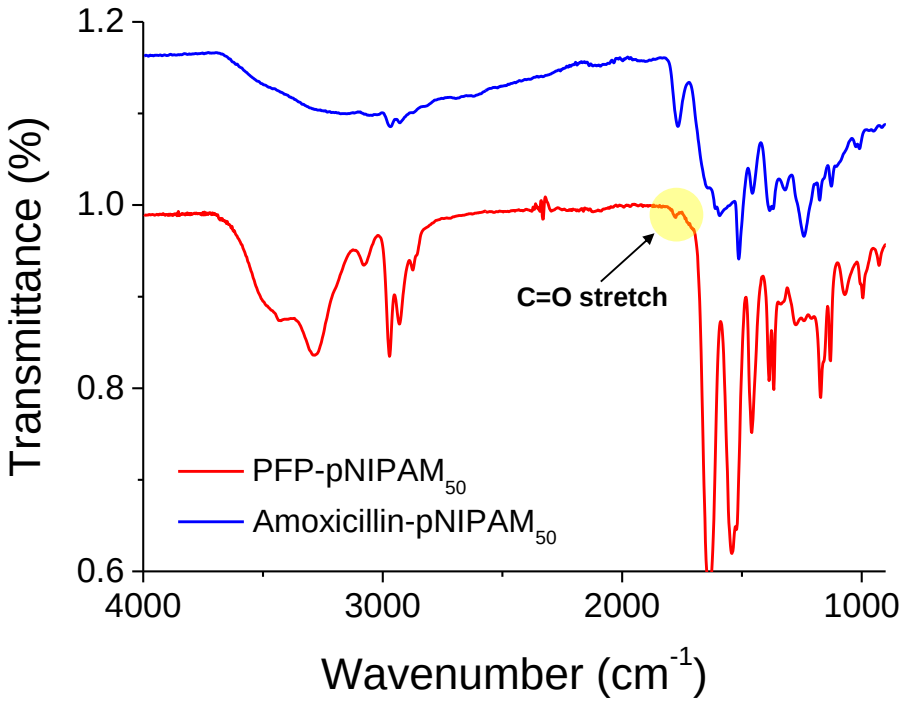

Figure S2.4 Infrared spectra of PFP-pNIPAM (red) and Amoxicillin-pNIPAM (blue).

In order to characterise the temperature response of synthetic polymers, the cloud point (CP) of each polymer was determined by UV-vis spectrometer. Independent transition curves of turbidimetry scans Figure S2.5 and Table S2.2 showed both amoxicillin modified pNIPAM with DP50 and pNIPAM with DP20 have higher CPs than CPs of PFP-pNIPAMs. Moreover, short amoxicillin conjugated pNIPAM with DP20 has no transition temperature upon heating up to 75 ^{o}C, the polymer chain may have increased solubility and hydrophilicity associated with end group modification. Therefore, amoxicillin conjugated pNIPAM with DP50 was used for further study to probe the enzyme effects on the transition temperature of antibiotic modified temperature responsive polymer.

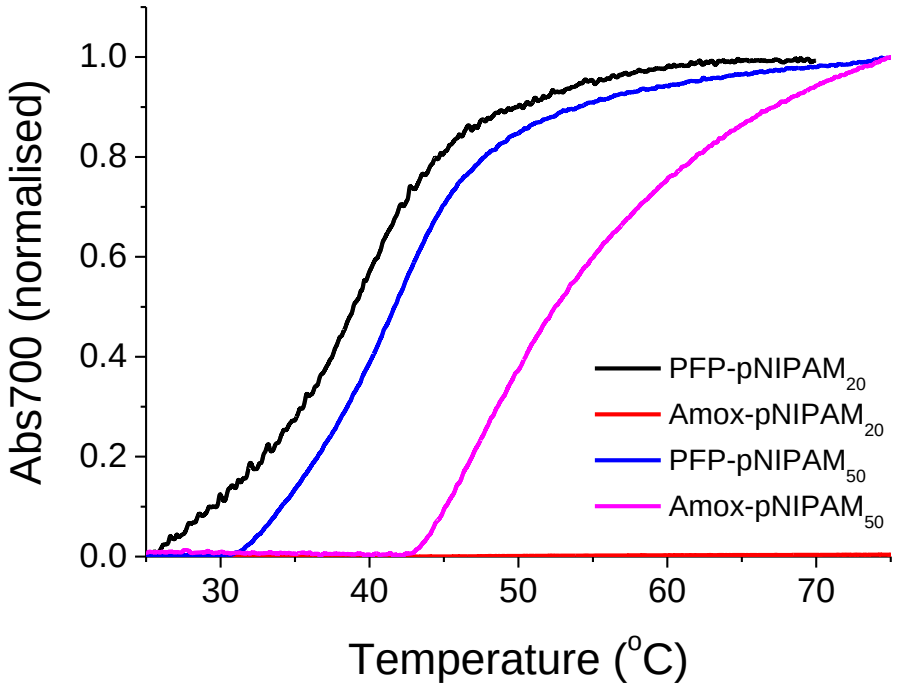

Figure S2.5 Turbidimetry scans (absorbance at 700 nm) of two different molecular weight of PFP-pNIPAMs and Amoxicillin-pNIPAMs (total concentration of polymer solution 1.0 mg mL^{-1}).

Table S2.2 Cloud points of polymers.

Polymer	Cloud point [°C][a)]
PFP-pNIPAM$_{20}$	39
Amoxicillin-pNIPAM$_{20}$	-
PFP-pNIPAM$_{50}$	42
Amoxicillin-pNIPAM$_{50}$	52

[a)]Cloud points were measured in water upon heating from 25 °C to 75 °C, 1.0 mg mL^{-1} total polymer concentration.

Finally, enzyme induction study was conducted using both PFP-pNIPAM$_{50}$ (as a control experiment) and amoxicillin conjugated pNIPAM$_{50}$. The cloud point of polymer solution is measured in the absence of the β-lactamase and in the presence of 15-30 units of β-lactamase for 30 minutes incubation at room temperature without any further purification. From turbidimetry scans Figure S2.6 and Table S2.3, there were no changes of transition temperature of PFP-pNIPAM with or without enzyme. β-lactamase had no affects at all to PFP-pNIPAM polymer which doesn't contain the β-lactam ring, as expected. The cloud point of Amox-pNIPAM$_{50}$ has an increased transition temperature of 55 ^{o}C in the presence of enzyme, this value was 5 degree higher than transition temperature without enzyme. The shift of cloud point may result from the alteration of hydrophilicity of polymer chain due to the enzyme lysed amoxicillin.

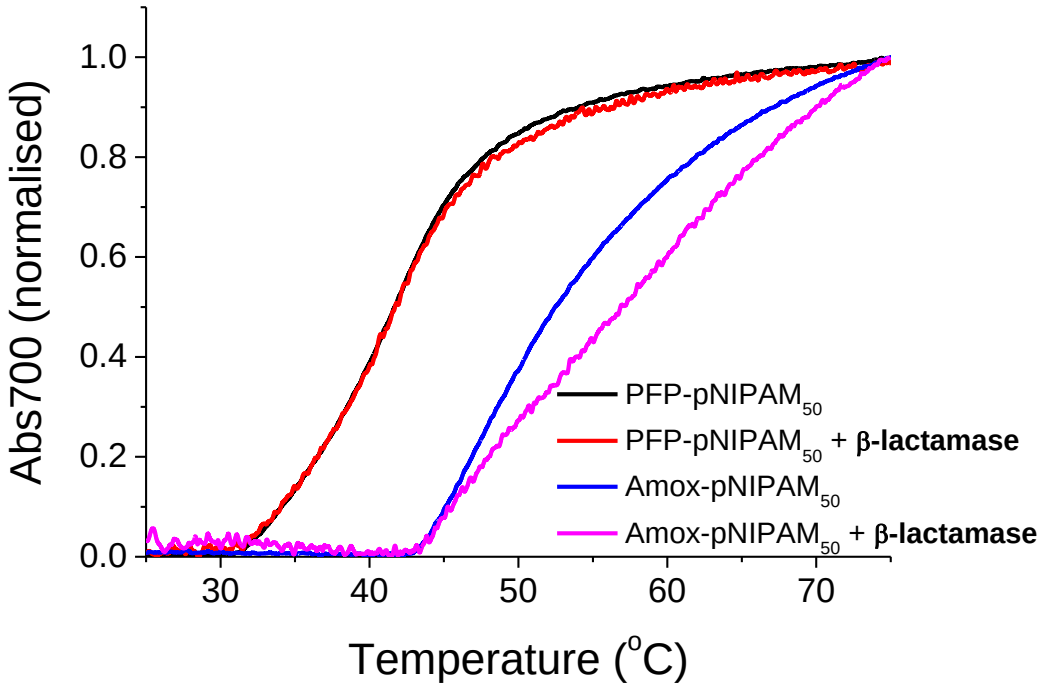

Figure S2.6 Turbidimetry scans (absorbance at 700 nm) of PFP-pNIPAM$_{50}$ and Amoxicillin-pNIPAM$_{50}$ with or without β-lactamase (total concentration of polymer solution 1.0 mg mL^{-1}).

Table S2.3 Cloud points of polymers.

Polymer	**Cloud point [°C][a)]**
PFP-pNIPAM$_{50}$	42
PFP-pNIPAM$_{50}$ + β-lactamase	42
Amoxicillin-pNIPAM$_{50}$	52
Amoxicillin-pNIPAM$_{50}$ + β-lactamase	57

[a)]Cloud points were measured in water upon heating from 25 °C to 75 °C, 1.0 mg mL^{-1} total polymer concentration with or without β-lactamase.

We observed the transition temperature of antibiotic modified pNIPAM is increase by enzyme reaction associated with hydrophilicity/hydrophobicity of polymer chain. However, from previous work in the chapter 2, the similar molecular weight of pNIPAM coated gold nanoparticle has higher transition temperature (e.g. CP of $pNIPAM_{50}$ coated 40 nm sized gold nanoparticle is 80^{o}C) than pure polymer its own. Consequently, polymer functionalised particles has extremely higher or even no transition temperature which unable particles to generate aggregation mediated colourimetric visible signal outputs. These problems are current challenges facing the use of antibiotics functionalised gold nanoparticles as an enzymatic biosensor. It is noteworthy that several crucial factors (conditions) have to be considered and optimised such as polymer chain length, core particle size, enzyme concentration, incubation time, hydrophilicity/hydrophobicity of antibiotics, enzyme toxicity of gold nanoparticles for the future 'success' of the enzymatic biosensor.

Appendix 3

Publications

This appendix contains published works that I have been involved in during my PhD.

1 **S. Won**, D. J. Phillips, M. Walker and M. I. Gibson, 'Co-operative transitions of responsive-polymer coated gold nanoparticles; precision tuning and direct evidence for co-operative aggregation', *J. Mater. Chem. B.*, 2016, 4, 5673-5682.

2 **S. Won**, S.-J. Richards, M. Walker and M. I. Gibson, 'Externally controllable glycan presentation on nanoparticle surfaces to modulate lectin recognition', *Nanoscale Horiz.*, 2017, 2, 106-109.

3 **S. Won**, S. Hindmarsh and M. I. Gibson, 'Triggerable multivalent glyconanoparticles for probing carbohydrate-carbohydrate interactions', *ACS Macro lett.*, 2018, 7, 178-183.